# THE EXTERNAL MANIPULATION OF COLLAGEN TYPE I USING INORGANIC IONS AND TOPOGRAPHICAL CUES

by

EMMA MORGAN MCCARTHY

A thesis submitted to
The University of Birmingham
for the degree of
DOCTOR OF PHILOSOPHY

School of Chemical Engineering
College of Engineering and Physical Sciences
The University of Birmingham
November 2019

UNIVERSITY OF
BIRMINGHAM

## University of Birmingham Research Archive

### e-theses repository

This unpublished thesis/dissertation is copyright of the author and/or third parties. The intellectual property rights of the author or third parties in respect of this work are as defined by The Copyright Designs and Patents Act 1988 or as modified by any successor legislation.

Any use made of information contained in this thesis/dissertation must be in accordance with that legislation and must be properly acknowledged. Further distribution or reproduction in any format is prohibited without the permission of the copyright holder.

**Abstract**

Collagen is a crucial component of tissue. It is a main protein of the extracellular matrix and functions as a cellular support, aiding cell-matrix signalling. As it supports cells, its orientation and structure are highly important; any alterations in collagen formation and assembly cause an alteration in tissue type. Collagen is a hierarchical protein, forming intercellularly before being released into the extracellular matrix where collagen molecules self-assemble. The simplest form of collagen is a triple helix, with a repeating amino acid structure predominately made of Gly-X-Y (where X and Y are usually proline and hydroproline respectively). This triple helix forms the collagen molecule, which self-assembles and super twists into microfibrils, fibrils and then fibres within the extracellular space. As there are many stages to collagen formation, it can be externally manipulated at many points to produce changes to the overall matrix structure and function. Within this thesis, the influence of inorganic ions and surface topography are investigated within the context of exploring how metal-on-metal implants effect collagen matrix formation, the fundamentals of how early stage collagen mineralisation occurs and how collagen fibrils' alignment can be influenced for wound dressings. It was found that cobalt ions, a main constituent of metal-on-metal implants are detrimental to matrix assembly. It was also found that calcium and phosphate (two of the main components of bone mineral) individually cause a conformational change in the molecular structure of collagen, ultimately preventing fibril formation to occur, but together allow for native fibril assembly. Although introducing chemicals into the collagen environment resulted in a drastic change in assembly, altering the surface chemistry did not. However, surface topography plays a large part in collagen alignment, with a nano-pattern of ridge to gap ratio 1.5 and a depth of 1000 nm resulting in 60% collagen alignment perpendicular to the ridge edge. The results within this thesis show that when creating a medical device, or wound dressing, it is important to factor in any changes to the extracellular matrix as they fundamentally control cellular function through support and facilitation of cell signalling. Therefore, by investigating how to externally manipulate collagen, better ways to treat trauma, such as scarring, and a better understanding of how devices, such as implants, can influence the surrounding tissue can be understood.

To my friends and family;
for without their continual support I would
not have been able to achieve half of what I
have

# ACKNOWLEDGEMENTS

I would to thank my supervisors Professor Liam M. Grover and Doctor Pola Goldberg Oppenheimer for their continual support, advice and invaluable knowledge, without which this project would not have been possible.

I am forever indebted to all the researchers within the Grover and Oppenheimer groups for their knowledge, incredible advice and useful discussions, all which made this interdisciplinary project that bit easier. I am additionally thankful to Doctor Megan Cooke and Doctor Hayley Floyd who set the groundwork for multiple aspects of this project. I am also grateful to all the researchers who helped me understand a wide range of instruments, in particular Mr James Craig, who aided all circular dichroism work and gave critical insight towards the interpretation of results.

This project would not be possible without both the Engineering and Physical Sciences Research Council and the National Institute for Health Research for their financial support provided throughout this research project. I am also thankful to the Physical Sciences for Health Centre for Doctoral Training for giving me this opportunity, alongside the support of my cohort.

Finally, I am eternally grateful to my parents, family and friends for their love and support throughout not only my doctorate but throughout all of my studies.

# CONTENTS


**1 Introduction** **1**

1.1 The Role of the Extracellular Matrix within the Body . . . . . 1

1.1.1 Composition and Biochemistry of the ECM . . . . . 2

1.2 Composition of Collagen Type I . . . . . 6

1.3 Collagen Molecule Hydration . . . . . 13

1.4 Characterisation of Collagen Type I . . . . . 15

1.5 External Influence of Collagen Type I . . . . . 20

1.5.1 Chemical Influence . . . . . 20

1.5.2 Physico-Chemical Influence . . . . . 24

1.5.3 Physical Influence . . . . . 26

1.6 ECM and Tissue Function . . . . . 30

1.6.1 Dermal ECM . . . . . 30

1.6.2 Tendon ECM . . . . . 30

1.6.3 Skeletal Muscle ECM . . . . . 31

1.6.4 Cardiovascular ECM . . . . . 32

1.7 Thesis Aims . . . . . 32

**2 General Theory and Methodology** **34**

2.1 Physical Theory and Methodology . . . . . 34

2.1.1 Collagen Hydrogels . . . . . 34

2.1.2 Atomic Force Microscopy (AFM) . . . . . 34

2.1.3 X-Ray Fluorescence (XRF) . . . . . 38

2.1.4 Rheology . . . . . 39

2.1.5 Differential Scanning Calorimetry (DSC) . . . . . 43

2.1.6 Raman Spectroscopy . . . . . 43

2.1.7 Principal Component Analysis (PCA) . . . . . 45

2.1.8 Circular Dichroism . . . . . 46

2.1.9 Zeta Potential . . . . . 47

2.1.10 Fibrillogenesis . . . . . 48

2.1.11 Scanning Electron Microscopy (SEM) . . . 49
2.1.12 Fabrication of Polydimethylsiloxane (PDMS) Surfaces . . . 50
2.1.13 Surface Free Energy (SFE) . . . 51
2.1.14 Patterned IP-DIP Fabrication . . . 54
2.2 Biological Methodology . . . 55
2.2.1 MC3T3 Cell Culture . . . 55
2.2.2 TrypanBlue Assay . . . 55
2.2.3 alamarBlue Assay . . . 56
2.2.4 Confocal Fluorescent Imaging of MC3T3 cells . . . 56
2.2.5 Extraction and Culture of Primary Human Corneal Fibroblasts . . . 57
2.2.6 Sample Preparation and Confocal Fluorescent Imaging of Corneal Fibroblasts on Patterned IP-DIP . . . 58
2.3 General Statistics . . . 58
2.3.1 Determining Sample Size . . . 58
2.3.2 T-Test . . . 59
2.3.3 One-Way ANOVA . . . 59

**3 Influence of Cobalt Ions on Collagen Matrix Formation 61**
3.1 Introduction . . . 62
3.2 Methodology . . . 64
3.2.1 Cobalt Doped Collagen Hydrogels (CoCol gels) . . . 64
3.2.2 X-Ray Fluorescence (XRF) . . . 65
3.2.3 Rheological Analysis . . . 65
3.2.4 Molecular Mechanics . . . 65
3.2.5 Confocal Fluorescent Imaging . . . 66
3.3 Results . . . 66
3.3.1 Cobalt Influence on Local Collagen Structure . . . 66
3.3.2 Bulk Collagen Matrix Effects from Cobalt Ions . . . 68
3.3.3 Cellular Response due to CoCol Gel Structure . . . 71
3.3.4 Cobalt-Collagen Molecular Mechanics . . . 73
3.4 Discussion . . . 75
3.5 Conclusion . . . 80

**4 The Effect of Calcium and Phosphate on Collagen Assembly 82**
4.1 Introduction . . . 83
4.2 Methodology . . . 85
4.2.1 Ionic Buffers . . . 85
4.2.2 Freeze Drying . . . 86

4.2.3 Dynamic Light Scattering (DLS) . . . 86
4.3 Results . . . 87
4.3.1 The Influence of Calcium and Phosphate Ions on Collagen Assembly 87
4.3.2 Investigation of the Early Mineralisation of Collagen . . . 99
4.4 Discussion . . . 102
4.5 Conclusion . . . 105

**5 Influence of Surface Chemistry and Topographical Cues on Collagen Matrix Formation 107**
5.1 Introduction . . . 108
5.2 Methodology . . . 111
5.2.1 Patterned Surfaces . . . 111
5.2.2 Alignment Measurements . . . 111
5.2.3 Surface Free Energy (SFE) of IP-DIP . . . 112
5.3 Results . . . 112
5.3.1 Influence of Surface Chemistry . . . 112
5.3.2 Topographical Influences . . . 117
5.3.3 Topographical Influence on Cell Alignment . . . 122
5.3.4 Understanding the Driving Forces Behind Alignment . . . 126
5.4 Discussion . . . 128
5.5 Conclusion . . . 131

**6 Conclusions and Future Aspects 132**
6.1 Chapter Summary and Future Perspectives . . . 132
6.1.1 Influence of Cobalt Ions on Collagen Assembly . . . 132
6.1.2 Calcium and Phosphate Influence on Collagen Formation . . . 133
6.1.3 Topographical Influence on Collagen Assembly . . . 136
6.2 Overall Conclusion . . . 139

**7 Appendix I 140**

**8 Appendix II 151**

**9 Appendix III 155**

# LIST OF FIGURES

1.1 A cartoon showing that the ECM is comprised of water, matrix proteins and proteoglycans. All components are essential for both cellular support and tissue function. Not to scale. . . . . 3

1.2 Hierarchical process of collagen type I formation. Collagen begins as a triple helix, forming within the endoplasmic recticulum. It is then modified in the Golgi aparatus to form a collagen molecule, which is excreted from the cell. Here, the molecule self assembles to form a collagen fibril. Multiple fibrils then self assemble to form a collagen fibre. Schematic not to scale. . . . . 7

1.3 (A) Collagen triple helix, where each colour indicates a separate amino acid chain. (B) Colouration of one $\alpha$ chain where glycine is shown in blue, proline in red and hydroxyproline in pink all linked via peptide bonds. Image acquired from [1] used under the Creative Commons Attribution License (CC-BY-4.0). . 8

1.4 Hypothesised transportation of procollagen molecules from the ER lumen to the Golgi apparatus. ERGIC vesicles form a large capsule with the aid of TANGO, SEC23/24 and SEC13 complexes. They form either one large capsule which transports the procollagen or a tunnel for procollagen migration to the Golgi. Adapted from [2] with permission from Copyright © 2015 Annual Reviews. . . 10

1.5 Atomic force microscopy image of collagen fibrils in bone showcasing characteristic D-spacing on fibrils. Scale bar is 1 $\mu$m. Adapted from [3] with permission from Copyright © 2012, American Chemical Society. . . . . 12

1.6 Not to scale cartoon depicting lateral and plan view hydration levels of a collagen molecule. (A) Structural water bridges forming between peptide bonds on separate chains on each third residue. (B) Cleft water forming within the gaps of each $\alpha$-chain with increased hydration, forming a triple helix of water within the collagen triple helix. (C) Monolayer formed from primary and secondary water layers. Primary hydration occurs when water molecule bind with polar residues with secondary hydration forming with non-polar residues. This forms an uneven outer hydration layer. . . . . 15

2.1 Schematic showing an AFM cantilever with attached tip. Cantilever deflected due to the forces between the tip and the surface forming an image signal which creates the overall image. . . . . 35
2.2 Schematic showing the inside of working AFM with laser path. . . . . 36
2.3 X-ray produced from an x-ray source expels an electron from an inner orbital. The vacancy produced is filled by an electron in a higher orbital. Any surplus energy is released as a fluorescence radiation and detected by a detector in the XRF. . . . . 39
2.4 Schematic depicting parallel plate frequency-dependent oscillatory rheology on a collagen hydrogel. . . . . 41
2.5 Schematic representing the interaction of stress and strain when looking at an elastic material (Hookean), a viscoelastic material and a viscous material (Newtonian). . . . . 42
2.6 Schematic of Rayleigh scattering and Raman scattering. Changes in energy levels are described as in Equation 2.4. . . . . 44
2.7 Schematic showing (A) circularly polarised light consisting of two out of phase light beams. (B) When plane-polarised light is passed through a circularly dichroic medium it is converted into elliptically polarized light which contributes to a CD signal. . . . . 47
2.8 Schematic showing the sessile drop method for determining contact angle between a liquid and solid surface, where $\theta$ is the contact angle. . . . . 52
2.9 CAD file created in eDrawings showing a ridge width of 850 nm, a gap width of 550 nm (giving a ridge to gap ratio of 1.5) and a depth of 1000 nm . . . . . 54
2.10 Schematic showing the dip-in laser lithography configuration used to created photolithography patterned surfaces in an IP-DIP photoresist. . . . . 55

3.1 Mechanical abrasion of the protective oxide layer of a MOM implant introduces the underlying metal to the surrounding tissue fluid. This causes cobalt and chromium ions to be released into the surrounding tissue causing inflammation which may lead to unexpected implant failure. $Co^{2+}$ refers to cobalt ions produced and $Cr^{3+}$ refers to the chromium ions produced from electrochemical corrosion. . . . . 62

3.2 (A) AFM height images of CoCol gels at concentrations 0, 67, 133 and 200 ppm over a 10 x 10 $\mu m^2$ area. (B) Fibril density calculated through measuring the number of fibrils per 2.1 $\mu m^2$. Fibrils were separated into three categories, low (4-6 fibrils), medium (7-10 fibrils) and high (11-13 fibrils) with fibril number tallied to obtain area frequency. Length of D-spacing (C) and fibril diameter (D) of collagen at each cobalt concentration, measured from 30 randomly selected fibrils over three AFM repeats. NS refers to a non-significant result * refers to a P-value $\leq 0.05$, ** refers to a P-value $\leq 0.01$ and *** refers to a P-value $\leq 0.001$. N = 75 across 3 biological samples, error bars refer to ± standard deviation. Scale bar is 2 $\mu$m in length. . . . . 67

3.3 Visual depiction of the reduction in structural integrity when increasing the concentration of cobalt ions in a collagen hydrogel. Scale bar is 10 mm. . . . . 68

3.4 XRF fluorescent measurements depicting the dispersion of cobalt throughout the bulk of a 200 ppm CoCol gel. (A) Scan depicting relative cobalt dispersion throughout the entire area, (B) spectrum indicating cobalt is being measured (highlighted peak). (C) A scan depicting an example of two objects showing relative high and low cobalt intensity. (D) An example of spectra of both object 1 and object 2 used within average concentration increase measurements. Here object 1 and 2 are the spectra of object 1 and 2 in part (C). (E) Average counts from five areas with high cobalt concentration and five areas with low cobalt concentration, * indicates a P value $\leq 0.05$. N = 5, error bars refer to ± standard deviation. Scale bar is 3 mm in length. . . . . 69

3.5 (A) G' and (B) G" from a frequency sweep of CoCol gels at increasing cobalt concentration ranging from 0.01 - 10 Hz. Sweep was taken with a strain of 0.01 determined from a strain sweep of 200 ppm CoCol gel sample. (C) Percentage weight decrease over five hours of collagen hydrogels doped with varying concentrations of cobalt. N = 3, error bars refer to ± standard deviation. . . . . 70

3.6 Confocal fluorescent images of MC3T3s stained with calcein AM and propidium iodide seeded onto both the surface of CoCol gels (A) and grown within cobalt infused media (B). Green cells indicate live cells, red indicate dead cells. (C) TrypanBlue assay quantifying both live and dead cells seeded onto CoCol gels. (D) alamarBlue assay of MC3T3 cells cultured on CoCol gels and in cobalt infused media. *** referes to a P value $\leq 0.001$. N = 3, error bars refer to ± standard deviation. Scale bar is 200 $\mu$m. . . . . 72

3.7 (A) DSC measurements between a 0 ppm and 200 ppm sample indicating a reduction in energy required to remove bulk water. (B) Raman spectroscopy using an immersion lens of both 0 ppm and 200 ppm CoCol gels, (C) scores plot of the first two principal components determined via PCA, (D) loadings plot of the first principal component indicating the largest change in variance at 869 $cm^{-1}$ and 1000 $cm^{-1}$. For DSC N = 3, for Raman and PCA N = 30. . . . . 74
3.8 Schematic diagram depicting the cross-section of the binding sites of water with a collagen fibril. (A) Four water molecules per three collagen residues. (B) Polar and non-polar bound water layers surrounding the collagen fibril. Image is not to scale. . . . . 78
3.9 Schematic diagram depicting the potential binding sites of collagen with cobalt (not to scale). (A) Binding of cobalt to the collagen fibril directly. (B) Binding of cobalt to the first hydration layer. (C) Cobalt binding to the collagen fibril via a carboxylic bond. (D) Cobalt binding to the collagen fibril via a hydroxyl bond. (E) Cobalt binding to collagen at the carboxylic terminal. (F) Cobalt forming a water bridge between two collagen molecules. . . . . 79

4.1 Mineralisation process of calcium (Ca) and phosphate ($PO_4$) ions aggregating to form mineralised collagen. (A) $Ca^{2+}$ and $PO_4^{3-}$ ions within the surrounding environment. (B) $Ca^{2+}$ and $PO_4^{3-}$ ions aggregate to form Posner Clusters (0.1 - 1 nm). (C) Posner clusters aggregate to form amorphous calcium phosphate (ACP) particles (30 - 100 nm). (D) ACP becomes crystalline, in which it forms a platelet morpholoy (50 nm x 25 nm x 23 nm). (E) Crystalline calcium phosphate nanocrystals incorporated into and mineralising collagen fibrils. Image adapted from [4]. . . . . 84
4.2 (A) Circular dichroism measurements of collagen in excess calcium chloride ($CaCl_2$), excess sodium phosphate ($PO_4^{3-}$) and excess calcium phosphate at a Ca:$PO_4$ ratio of 1:1 (Ca:$PO_4$ 1:1). (B) Ratio of positive to negative (Rpn) peaks of circular dichroism data shown in (A). (C) Dynamic light scattering measurements of collagen in excess $CaCl_2$, excess $PO_4^{3-}$ and excess Ca:$PO_4$ 1:1. It has been assumed that the collagen molecule size is located at approximately 100 nm. (D) Quantification of the dynamic light scattering measurements shown in (C). (E) Zeta potential measurements at a pH of 3.9 of collagen in excess $CaCl_2$, excess $PO_4^{3-}$ and excess Ca:$PO_4$ 1:1. ** refers to a P value $\leq$ 0.01, * refers to a P value of $\leq$ 0.05 and NS refers to a non-significant result. N = 3, error bars refer to $\pm$ standard deviation. . . . . 88

4.3 (A) Absorbance of 3 mg $mL^{-1}$ collagen taken over the range 300 - 700 nm, peak was taken to be at a wavelength of 380 nm. (B) Fibrillogenesis of 2, 1.5, 1 and 0.5 mg $mL^{-1}$ collagen, with 2 mg $mL^{-1}$ giving the most expected response. All scans were baselined to that of uncross-linked collagen at each corresponding concentration. N = 3, error bars refer to ± standard deviation. . . . . 90
4.4 (A) Fibrillogenesis repeats of 2 mg $mL^{-1}$ when initial method was undertaken. This involved small volumes of NaOH being added to buffer within a 96-well individually. (B) Fibrillogenesis repeats of 2 mg $mL^{-1}$ using alternative method. This method involved adding NaOH to a working buffer stock prior to addition of both to the 96-well. (C) Average of (B) with standard deviation. N = 12 for (A) and N = 8 for (B), (C). Error bars refer to ± standard deviation. . . . . 91
4.5 (A) Varying concentrations of NaOH (12-26 $\mu$L $mL^{-1}$) required for gelation to occur. (B) Absorbance scan between 300-700 nm of varying concentrations of KCl to determine what concentration of ion was optimal. (C) Absorbance scan between 300-700 nm of 0.1 mM ion with 2 mg $mL^{-1}$ collagen to ensure wavelength used for fibrillogenesis was optimal. N = 3. . . . . 92
4.6 Fibrillogenesis of (A) $CaCl_2$, (B) sodium phosphate solution and (C) calcium phosphate solution at a ratio of Ca:$PO_4$ 1:1. N = 3, error bars refer to ± standard deviation. . . . . 93
4.7 Fibrillogenesis measurements of (A) $CaCl_2$, (B) KCl, (C) $MgCl_2$, and (D) NaCl at a concentration of 0.1 mM added to 2 mg $mL^{-1}$ collagen. Growth phase of collagen in excess KCl, $CaCl_2$, $MgCl_2$ and NaCl. *** refers to a P value $\leq$ 0.001, * refers to a P value $\leq$ 0.05, NS refers to a statistically non significant result. N = 3, error bars refer to ± standard deviation. . . . . 94
4.8 (A) AFM images of 2 mg $mL^{-1}$ collagen with added KCl, $CaCl_2$, $MgCl_2$ and NaCl at a concentration of 0.1 mM. (B) Fibril diameter measured from triplicates of each AFM image. *** refers to a P value of $\leq$ 0.001. N = 75 across 3 biological repeats, error bars refer to ± standard deviation. Scale bar is 2 $\mu$m. . . . . 95
4.9 (A) Growth phase of $CaCl_2$, sodium phosphate solution (Na:$PO_4$) and calcium phosphate solution (Ca:$PO_4$)at a ratio of 1:1. (B) Growth phase measurements of Ca:$PO_4$ with decreasing ratios of phosphate. Fibrillogenesis profiles used to measure ratio growth phase can be found in Appendix I Figures 7.2 and 7.11. *** refers to a P value of $\leq$ 0.001, ** refers to a P value of $\leq$ 0.01, * refers to a P value of $\leq$ 0.05, NS refers to a statistically non-significant result. N = 3, error bars refer to ± standard deviation. . . . . 96

4.10 (A) AFM images of 2 mg $mL^{-1}$ collagen with added $CaCl_2$ and calcium phosphate in a ratio of Ca:$PO_4$ 1:1 at a concentration of 0.1 mM. (B) Fibril diameter measured from triplicates of each AFM image. *** refers to a P value of $\leq$ 0.001. N = 75 across 3 biological samples, error bars refer to $\pm$ standard deviation. Scale bar is 2 $\mu$m. . . . . 97
4.11 Fibrillogenesis measurements of (A) $CaCl_2$, (B) EDTA, (C) Ca:EDTA at a ratio of 1:1. (D) Quantification of growth phase measurements for $CaCl_2$, Ca:$PO_4$ at a ratio of 1:1, EDTA, Ca:EDTA at a ratio of 1:1. *** refers to a P value of $\leq$ 0.001, ** refers to a P value of $\leq$ 0.01, NS refers to a statistically non-significant result. N = 3, error bars refer to $\pm$ standard deviation. . . . . 98
4.12 Maximum absorbance measurements of collagen with excess calcium at a concentration of 2 mM and phosphate at a concentration ranging from 0 - 2 mM. N = 3, error bars refer to $\pm$ standard deviation. . . . . 99
4.13 Fibrillogenesis of (A) Ca:$PO_4$ at a ratio of (A) 1:0, (B) 1:0.6 and (C) 1:1 all with calcium at a concentration of 2 mM. Growth phase (D) and plateau time (E) of each ratio. ** refers to a P value of $\leq$ 0.01, NS refers to a statistically non significant result. N = 3, error bars refer to $\pm$ standard deviation. . . . . 100
4.14 (A) AFM images of control collagen, Ca:$PO_4$ at a ratio of 1:0.6 and Ca:$PO_4$ at a ratio of 1:1 at a higher calcium concentration of 2 mM. (B) Fibril diameter measured from AFM images of each sample. ** refers to a P value of $\leq$ 0.01, NS refers to a statistically non significant result. N = 75 across 3 biological samples, error bars refer to $\pm$ standard deviation. Scale bar is 2 $\mu$m. . . . . 101
4.15 Schematic showing (A) an unaffected collagen molecule, (B) a collagen molecule distorted by calcium ions and (C) a collagen molecule distorted by Posner's clusters. Not to scale. . . . . 103

5.1 Structure of collagen within the cornea. Hash network of fibres at the anterior part of the eye which are regularly spaced to allow exterior light into the retina. Cartoon is not to scale. Blue lines represent collagen fibrils and yellow lines represent light. Shades only represent different layers of collagen fibrils. . . . . 110
5.2 (A) XRF image of PDMS half sputtercoated with gold. Scale bar is 1000 $\mu$m. (B) SEM image of PDMS half sputtercoated with gold. Coating of gold is sufficient enough to result in a change in surface chemistry. Scale bar is 100 $\mu$m. 113

5.3 (A) Contact angle mean for each surface using pure water. (B) Zisman plot using diiodomethane ($CH_2I_2$), ethylene glycol ($C_2H_6O_2$) and pure water ($H_2O$) for each of the chemically altered surfaces. *** refers to a P value $\leq 0.001$ and ** refers to a P value $\leq 0.01$.
N = 30, 5 measurements of both left and right side angles across 3 biological repeats. Error bars refer to ± standard deviation. . . . . 114
5.4 SEM images of 0.5 mg $mL^{-1}$ collagen deposited onto a (A) silicon wafer, (B) PDMS, (C) PDMSPlasma, (D) PDMSAu and (E) PDMSAPTES. PDMS and PDMSPlasma produced globular collagen rather than fully formed fibrils. The gold on PDMS formed an uneven layer changing the topography of the surface. (F) Percentage aligned of fibrils, measured from the horizontal, of 0.5 mg $mL^{-1}$ collagen deposited onto a silicon wafer, PDMS, PDMSPlasma, PDMSAu and PDMSAPTES. It was found that there was no significant difference in collagen assembly with respect to surface free energy, however PDMSAu, a surface with a topographical change, did provide a significant increase in organised collagen. * refers to a P value $\leq 0.05$, NS refers to a non-significant result. N = 3, error bars refer to ± standard deviation. Scale bar is 5 $\mu$m. . . . . 116
5.5 AFM images of each surface to ensure that the dimensions were the same as those created in the CAD file. Scale bar is 5 $\mu$m. . . . . 118
5.6 SEM images of 1 mg $mL^{-1}$ collagen deposited onto each patterned structure. Images taken in vacuum with a 5 kV beam. Scale bar is 5 $\mu$m. Ridge width (R), gap width (G) and depth (D) are as follows: 1.# (R) 700 nm, (G) 1000 nm, 2.# (R) 1000 nm, (G) 700 nm, 3.# (R) 550 nm, (G) 850 nm, 4.# (R) 850 nm, (G) 550 nm. #.1 (D) 1000 nm, #.2 (D) 500 nm, #.3 (D) 200 nm. . . . . 119
5.7 Percentage of fibrils aligned between 80-110° at depths of (A) 200 nm, (B) 500 nm, (C) 1000 nm. Red circles indicate biological repeats that are within 10° of each other, green circles indicate biological repeats that were statistically significant from the control. (D) Average percentage of fibrils at perpendicular alignment with respect to structural roughness.There is no correlation so roughness does not effect alignment organisation. ** refers to a P value $\leq 0.01$, * refers to a P value $\leq 0.05$ and NS refers to a non-significant result. N = 75 across 3 biological samples for (A), (B), and (C). N = 3 for (D). Error bars refer to ± standard deviation. . . . . 120
5.8 SEM images of varying concentrations of collagen on pattern structures with an RTG ratio of (A) 1.4 and (B) 1.5. Images taken in vacuum with a 5 kV beam. Scale bar is 5 $\mu$m. . . . . 121

5.9 Quantification of percentage of fibrils aligned between 80 - 110° of the ridge edge. Alignment measured from SEM images of varying concentrations of collagen deposited onto pattern structures with a RTG ratio of (A) 1.4 and (B) 1.5. *** refers to a P value ≤ 0.001, ** refers to a P value ≤ 0.01, * refers to a P value ≤ 0.05. N = 75 across 3 biological samples. Error bars refer to ± standard deviation. . . . . 122
5.10 (A) Contact angle mean for both silicon wafer and IP-DIP non-patterned surface using pure water. (B) Zisman plot using diiodomethane ($CH_2I_2$), ethylene glycol ($C_2H_6O_2$) and pure water ($H_2O$) for silicon and IP-DIP. *** refers to a P value ≤ 0.001. N = 30, 5 measurements of both left and right side angles across 3 biological repeats. Error bars refer to ± standard deviation. . . . . 123
5.11 ESEM image of 1 mg $mL^{-1}$ collagen deposited onto (A) patterned IP-DIP and (B) non-patterned IP-DIP. (C) Quantification of the percentage of fibrils aligned between 80 - 110° of the ridge edge. ** refers to a P value ≤ 0.01, *** refers to a P value ≤ 0.001. N = 75 across 3 biological samples. Error bars refer to ± standard deviation. Scale bar is 2 $\mu$m. . . . . 124
5.12 Fluorescent and brightfield images taken of corneal fibroblasts cultured for 48 hrs on patterened and non-pattered IP-DIP in the presence of collagen and without. Cells were stained with both Phalloidin (red) and DAPI (blue), however the DAPI dye stained the IP-DIP pattern very strongly preventing the visualization of cellular DNA. IP-DIP patterning was vertical as shown within brightfield images. Scale bar is 150 $\mu$m. . . . . 125
5.13 SEM images taken of collagen aligned on patterns with ridge to gap ratios of 1.3, 1.4 and 1.6 at depths of 500, 750 and 1000 nm to see whether ridge to gap ratio or depth is more influential for collagen alignment. Scale bar is 5 $\mu$m. . . . 127
5.14 Quantification of percentage of fibrils aligned between 80 - 110° of the ridge edge. Alignment measured from SEM images of varying concentrations of collagen deposited onto pattern structures with an RTG ratio of (A) 1.3 (B) 1.4 and (C) 1.6. As there is no significant difference between the perpendicular alignment of collagen with respect to the depth we can conclude that ridge to gap ratio is the most influential factor in collagen alignment. N = 75 across 3 biological samples. Error bars refer to ± standard deviation. . . . . 128

7.1 Fibrillogenesis profiles used to calculate growth phase measurements (only average shown). (A) Control collagen, (B) potassium chloride, (C) calcium chloride, (D) magnesium chloride, (E) sodium chloride, (F) sodium carbonate, (G) sodium sulphate, (H) sodium acetate. $t_{lag}$ refers to the lag time, $t_p$ refers to the time point when the plateau time begins and $\Delta t$ refers to the time at which collagen fibril formation ends. N = 3. . . . . 141

7.2 Fibrillogenesis profiles indicating how growth phase was measured for decreasing ratios of Ca:$PO_4$. (A) Ca:$PO_4$ 1:1, (B) Ca:$PO_4$ 1:0.75, (C) Ca:$PO_4$ 1:0.5, (D) Ca:$PO_4$ 1:0.25, (E) Ca:$PO_4$ 1:0.125, (F) Ca:$PO_4$ 1:0.0625, (G) Ca:$PO_4$ 1:0.03125. $t_{lag}$ refers to the lag time, $t_p$ refers to the time point when the plateau time begins and $\Delta t$ refers to the time at which collagen fibril formation ends. N = 3. . . . . 142

7.3 Fibrillogenesis profiles indicating how growth phase was measured for (A) $CaCl_2$, (B) NaCl, (C) NaCl + $CaCl_2$, (D) sodium phosphate, and (E) Ca:$PO_4$ 1:1. $t_{lag}$ refers to the lag time, $t_p$ refers to the time point when the plateau time begins and $\Delta t$ refers to the time at which collagen fibril formation ends. N = 3. . . . 143

7.4 Fibrillogenesis profiles indicating how growth phase was measured for collagen doped with (A) EDTA and (B) Ca:EDTA. $t_{lag}$ refers to the lag time, $t_p$ refers to the time point when the plateau time begins and $\Delta t$ refers to the time at which collagen fibril formation ends. N = 3. . . . . 143

7.5 Fibrillogenesis profiles indicating how growth phase was measured for collagen doped with a higher concentration of Ca (2 mM), (A) Ca:$PO_4$ 1:0, (B) Ca:$PO_4$ 1:0.6, and (C) Ca:$PO_4$ 1:1.. $t_{lag}$ refers to the lag time, $t_p$ refers to the time point when the plateau time begins and $\Delta t$ refers to the time at which collagen fibril formation ends. N = 3. . . . . 144

7.6 Control indicating that the addition of both sodium chloride (NaCl) and calcium chloride ($CaCl_2$) does not result in any change in fibrillogenesis. N = 3, error bars refer to ± standard deviation. . . . . 144

7.7 Fibrillogenesis assays indicating that changing the anion does not result in a change in fibrillogenesis profile. (A) NaCl, (B) $Na_2CO_3$, (C) $Na_2SO_4$, (D) $C_2H_3NaO_2$. N = 3, error bars refer to ± standard deviation. . . . . 145

7.8 (A) Growth phase measurements for anion experiments. Plateau measurements for (B) cations and (C) anions. N = 3, error bars refer to ± standard deviation. 146

7.9 (A) AFM images of collagen and excess NaCl, $Na_2CO_3$, $Na_2SO_4$, $C_2H_3NaO_2$. (B) Fibril diameter measured from triplicates of each AFM images. *** refers to a P value $\leq 0.001$. N = 75 across 3 biological samples. Error bars refer to ± standard deviation. . . . . 147

7.10 Examples of how measurements of fibrils were taken from AFM images to determine fibril diameter. Lines drawn across fibrils, on AFM images acquired from triplicate samples, were measured in ImageJ at random in order to establish mean fibril diameter and standard deviation. N = 75 across 3 biological samples. 148
7.11 Fibrillogenesis profiles for decreasing ratios of $Ca:PO_4$. (A) $Ca:PO_4$ 1:1, (B) $Ca:PO_4$ 1:0.75, (C) $Ca:PO_4$ 1:0.5, (D) $Ca:PO_4$ 1:0.25, (E) $Ca:PO_4$ 1:0.125, (F) $Ca:PO_4$ 1:0.0625, (G) $Ca:PO_4$ 1:0.03125. N = 3, error bars refer to ± standard deviation. . . . . 149
7.12 Circular dichroism (CD) titration of calcium chloride ($CaCl_2$) and sodium phosphate ($Na:PO_4$) added at large volumes to collagen to determine approximate number of surface binding sites of each molecule. CD measurements for the peak at 221 nm (A) and for 197 nm (B). To further gain the number of available binding sites for $CaCl_2$ and $Na:PO_4$ more measurements in a smaller range were taken. (C) CD measurements for the peak at 221 nm for the smaller range. (D) CD measurements for the peak at 197 nm for the smaller range. N = 3. . . . . 150

8.1 Fluorescent images of corneal fibroblasts cultured onto patterned and non-patterned IP-DIP in the presence of collagen. Three culture repeats were imaged with a total of four patterns per repeat. Two patterns within repeat 1 were lost in the cell fixing process. Red staining is Phalloidin and blue staining is DAPI. DAPI stained the IP-DIP pattern very strongly preventing the visualization of cellular DNA. Scale bar is 150 $\mu$m. . . . . 152
8.2 Brightfield images of corneal fibroblasts cultured onto patterned and non-patterned IP-DIP in the presence of collagen. Three culture repeats were imaged with a total of four patterns per repeat. Two patterns within repeat 1 were lost in the cell fixing process. Scale bar is 150 $\mu$m. . . . . 153
8.3 Fluorescent and brightfield images of corneal fibroblasts cultured onto patterned and non-patterned IP-DIP without the presence of collagen. Although there were three culture repeats seeded, only two pattern repeats from one culture repeat was not lost in the cell fixing and washing process. Red staining is Phalloidin and blue staining is DAPI. Scale bar is 150 $\mu$m. . . . . 154

# LIST OF TABLES

5.1 Surface free energy measurements calculated from Zisman plots for silicon, PDMS, PDMSPlasma, PDMSAu and PDMSAPTES . . . . . 115
5.2 AutoCAD parameters for etching specific patterns into silicon wafers . . . . . 117
5.3 Measured parameters from AFM images of etched silicon patterned surfaces 118
5.4 Surface free energy measurements calculated from Zisman plots for silicon and IP-DIP . . . . . 124

| Abbreviation | Name |
|---|---|
| ECM | Extracellular Matrix |
| GAG | Glycosaminoglycan |
| TGF-$\beta$ | Transforming Growth Factor - $\beta$ |
| MMP | Metalloproteinase |
| ER | Endoplasmic Reticulum |
| P4H | Prolyl 4-Hydroxylase |
| PDI | Protein Disulphide Isomerase |
| HSP47 | Heat Shock Protein 47 |
| TANGO | Transport ANd Golgi Organisation |
| ERGIC | ER-Golgi-Intermediate Compartment |
| BMP-1 | Bone Morphogenetic Protein-1 |
| ADAMTS | A Disintegrin and A Metalloproteinase with Thrombospondin repeats |
| LOX | Lysyl Oxidase |
| BAPN | $\beta$-AminoPropioNitrile |
| FACIT | Fibril-Associated Collagen with Interrupted Triple helices |
| SLRP | Small Leucine-rich Repeat Proteoglycans |
| DNA | Deoxyribonucleic Acid |
| TEM | Transmission Electron Microscopy |
| SEM | Scanning Electron Microscopy |
| p$I$ | Isoelectric Point |
| CM | Compressive Modulus |
| CSE | Compressive Strain Energy |
| PS | Polystyrene |
| PSox | Oxidized Polystyrene |
| DHT | Dehydrathermal treatment |
| UV | Ultraviolet |
| HA | Hydroxyapatite |
| PEF | Pulsed Electric Field |
| PBS | Phosphate Buffer Solution |
| AFM | Atomic Force Microscopy |

| Abbreviation | Name |
|---|---|
| XRF | X-Ray Fluorescence |
| DSC | Differential Scanning Calorimetry |
| PCA | Principle Component Analysis |
| CD | Circular Dichroism |
| SE | Secondary Electron |
| BSE | Back-Scattering Electron |
| EDS | Energy-Dispersive X-ray Spectroscopy |
| PDMS | Polydimethylsiloxane |
| PDMSPlasma | Polydimethylsiloxane Plasma treated |
| PDMSAu | Polydimethylsiloxane Gold sputtercoated |
| PDMSAPTES | Polydimethylsiloxane treated with APTES |
| APTES | (3-Aminopropyl)triethoxysilane |
| SFE | Surface Free Energy |
| $\alpha$-MEM | $\alpha$-Minimum Essential Medium |
| DPBS | Dulbecco's Phosphate Buffered Saline |
| CoCrMo | Cobalt-Chromium-Molybdenum |
| MOM | Metal-On-Metal |
| CoCol | Cobalt doped Collagen hydrogels |
| DMEM | Dulbecco's Modified Eagles Medium |
| G' | Storage Modulus |
| G" | Loss Modulus |
| ACP | Amorphous Calcium Phosphate |
| DLS | Dynamic Light Scattering |
| EDTA | Enthylenediaminetetraacetic Acid |
| FIB | Focus-Ion Beam |
| ESEM | Environmental Scanning Electron Microscopy |
| PGMEA | Propylene Glycol Monomethyl Ether Acetate |
| SFE | Surface Free Energy |
| RTG | Ridge to Gap |

# CHAPTER 1

# INTRODUCTION

## 1.1 The Role of the Extracellular Matrix within the Body

The extracellular matrix (ECM) is essential for cellular structural support and provides both biomechanical and biochemical signals for all tissue types [5, 6]. It is comprised of 300 proteins, mostly collagen and glycoproteins; the formation and composition of these proteins determines each tissue function [5–7]. In addition to proteins, the ECM also contains proteoglycans which resist compressive forces of the surrounding environment by hydrating the tissue and providing swelling pressure [8]. Cellular components interact with the ECM during tissue development, with cell adhesion mediated by receptors within the ECM, such as integrins [5, 7]. Integrins are a family of cell-surface receptors that facilitate attachment to the ECM. They are integral to cell survival, development, proliferation and apoptosis [9]. This integrin adhesion provides a platform for cell migration through cytoskeletal coupling [5, 7]. It also provides attachment sites for cells to use for detection of mechanical disruptions. Any mechanical alteration results in remodelling of the ECM to ensure it is both structurally and functionally viable [10]. Most cells must be bound to the ECM in order to proliferate. Matrix-cell adhesion regulates cellular shape, a prerequisite for anchorage-dependent cell proliferation [9].

As tissues are continually restructuring, the ECM undergoes constant modification and

remodelling through both enzyme and non-enzyme processes. Each modification provides the correct tensile, elasticity and compressive strength crucial for each tissue type. For example, tissue within the skin requires an ECM with random orientation to allow for distortion in multiple directions, unlike bone ECM which needs to be more ordered. The ECM determines tissue function not only through changes in mechanical properties but also through binding growth factors and cell-surface receptors to allow cell–cell signalling to occur [5, 7]. Tissue function is controlled by the regulation of growth factors and receptors released, the pH and hydration level of the surrounding environment. Unique topographies and compositions of the ECM are created through a dynamic physical and chemical interaction with the various cells in the micro-environment. These factors relate to the water, proteoglycans and proteins within the ECM, dictating the microenvironment [11].

### 1.1.1 Composition and Biochemistry of the ECM

There are two types of ECM. One surrounds the cells and forms a connective tissue matrix, as explained above. The other is specialised and forms the basement membrane separating the bulk tissue from the epithelium [7], as shown by the schematic in Figure 1.1. Both create a three-dimensional structure which is comprised of macromolecules.

Each of these macromolecules is chemically and structurally specific for each tissue type. There are multiple macromolecules groups: fibrillar proteins, non-fibrillar proteins and proteoglycans [11]. Fibrous proteins within the ECM are collagenous (formed from collagen types) or non-collagenous (such as fibronectin) [12–14]. The most abundant protein within the ECM is collagen, consisting of 30% of the total ECM composition. Collagens provide tensile strength and regulate and support both cell adhesion and migration thereby directing tissue development [7, 14, 15]. Collagens are created and secreted by fibroblasts residing in the surrounding tissue and has both fibrillar and non-fibrillar forms [7, 16].

There are multiple types of fibrillar collagens which all have different chemical com-

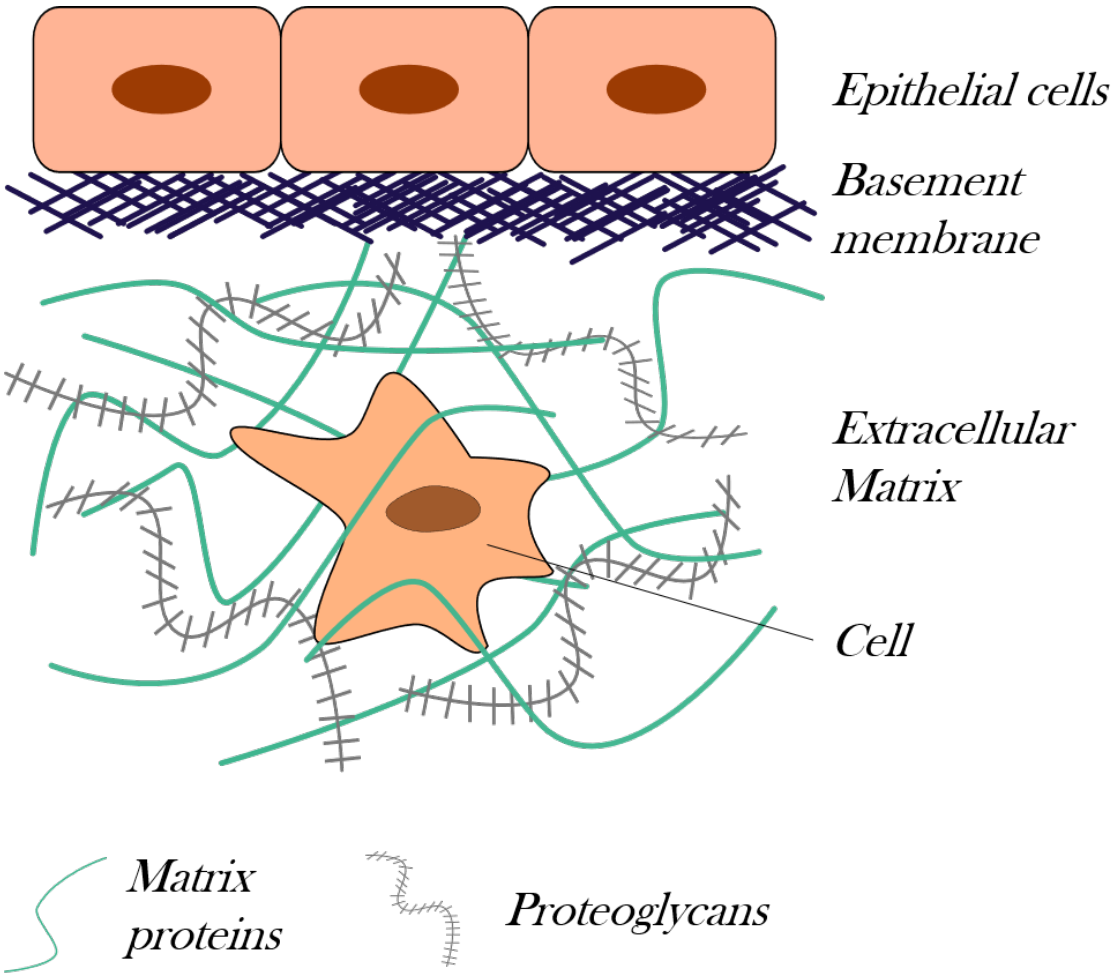



Figure 1.1: A cartoon showing that the ECM is comprised of water, matrix proteins and proteoglycans. All components are essential for both cellular support and tissue function. Not to scale.

positions tailored for each specific tissue type. Type I collagen triple helix comprises of two $\alpha(1)$ chains and one $\alpha(2)$ chain. In comparison to this, Type II and Type III consist of three $\alpha(1)$ chains. Each chemical composition of the $\alpha$ chain is specific to each collagen type. These changes in triple helical structure mean that Type II is found only in cartilage, vitreous humour and intervertebral disk tissue, with Type III present in most connective tissues, in particular lungs, skin and blood vessels [17].

Type V is classed as a regulatory fibrillar collagen, regulating the fibrillogenesis process of collagen type I and III. Type V collagen has three different triple helix isoforms – two $\alpha(1)$, one $\alpha(2)$ chains; three $\alpha(1)$ chains; one $\alpha(1)$, one $\alpha(2)$ and one $\alpha(3)$ chains. Each triple helix configuration is specific for the unique role of collagen type V in the tissue,

with each amino acid chain comprised of residues specific for collagen type V. For example, in the cornea collagen type V is found in the heterotrimeric form of two $\alpha(1)$ and one $\alpha(2)$ chains allowing it to co-assemble with collagen type I [18]. This regulates collagen type I fibrillogenesis to ensure optimal matrix organisation within the cornea [19].

Non-fibrillar collagens predominately form networks as well as attaching to fibrillar collagen surfaces for regulation. For example, Type XIV is a fibril-associated collagen with interrupted triple helices (FACIT) and attaches to Type II collagen to regulate collagen Type II fibril diameter [17]. Collagen Type IV is a non-fibrillar collagen that is mostly found in the basement membrane. It has a triple helix consisting of two $\alpha(1)$ and one $\alpha(2)$ chains. The Type IV collagen molecules attach to each other to form a complex network of proteins. This creates the basement membrane which separates epithelial and endothelial cells. It differs from fibrillar collagen as one domain within the C-terminal of the triple helix is not removed during the post-translational stage, with molecules linking at the triple helix terminals rather than in parallel. It also lacks one of the predominant amino acid residues present within fibrillar collagens (further description into fibrillar collagen Type I triple helix structure and formation can be found in Section 1.2) [20].

Bridges between structural ECM components are formed through non-collagenous multidomain gylcoproteins, such as laminin or elastin [11, 14]. Not only do they reinforce the structural network but also provide a connection between the ECM and, both cells and soluble molecules within the extracellular space [11]. Glycoproteins interact with epithelial cells acting as ligands for cell integrins. Cell functions such as adhesion, proliferation and differentiation are regulated through the glycoproteins due to the signals they transmit [7].

Proteoglycans, a separate component of the ECM, take the form of a hydrated gel and fill the majority of the extracellular space surrounding a cell within tissue. They predominately have hydrating, buffering, force-resisting and binding properties and interact with the subsequent fibrous proteins to aid mechanical and biochemical processes [5, 7, 11]. These properties are due to the biochemical and hydrodynamic characteristics of the gly-

cosaminoglycan (GAG) chain within the molecules which bind with water contributing to both compressive resistance and hydration [11]. These chains are long, linear chains of disaccharide repeats with an overall negative charge. They are subdivided dependent on the structure of the GAG chains as well as the density and distribution of these chains along the protein core [11].

Both the deposition and formation of the ECM is regulated via growth factors, cytokines and mechanical signals mediated via cell surface receptors [9, 14]. Growth factors stimulate cells causing them to increase either the production of ECM or the synthesis of ECM degradation enzymes. For example, transforming growth factor-beta (TGF-$\beta$) regulates ECM production (both enhancing and reducing) during wound healing [9]. TGF-$\beta$ not only stimulates the production of ECM across many cell types [9, 21–23], but also other extracellular components such as hyaluronic acid and tenascin. Although growth factors influence ECM synthesis, ECM-growth factor binding influences and controls their activity. By binding to multiple growth factors, the ECM is able to store and sequester the growth factors guaranteeing activation within the vicinity of cells and reducing the likelihood of degradation. The main advantages to the binding and release of growth factors by the ECM is the increase in overall activity of growth factors, the localisation of their activity to the immediate surrounding environment and the alteration of the intensity of specific growth factor activity [9].

Remodelling is an integral part of maintaining ECM structure and function [24]. ECM degradation is maintained by metalloproteinases (MMPs), a family of zinc dependent proteolytic enzymes [14, 24–26]. They are homologous proteins which can be separated into six groups: collagenases, matrilysins, stromelysins, gelatinases, membrane-type metalloprotieases and other MMPs (which are $Zn^{+}$ and $Ca^{2+}$ dependent). They are comprised of an N-terminal propeptide, a C-terminal and a catalytic domain and are secreted as inactive proenzymes from the cell. They are able to cleave multiple components of the ECM, including proteins, proteoglycans and growth factors, resulting in matrix degradation [9, 14, 25].

As collagen is the main structural protein of the extracellular matrix, and orientation and assembly determines overall tissue function, its external manipulation is the main focus of this thesis.

## 1.2 Composition of Collagen Type I

The functional properties of most connective tissues are determined by the multiscale organisation of the component molecules. Collagen is one of the major building blocks of connective tissues, and there are 29 different types of collagen within the body [27, 28]. Collagen type I is the most abundant collagen type and is synthesized within mature fibroblasts. This synthesis begins in the endoplasmic reticulum (ER) with the formation of procollagen chains [29–32]. Once three of these chains form a triple helix, the molecule undergoes post translational modification in the Golgi apparatus (Golgi) before being secreted into the extracellular space [2]. Collagen then self-assembles through multiple hierarchical stages: from the molecular scale as procollagen to the macro-scale as a fully formed collagen fibre, as shown in Figure 1.2.

A procollagen chain is a polypeptide consisting of a 300 repeating amino acid triplet sequence Gly-X-Y, where X and Y are usually proline and 4-hydroxyproline respectively [27, 33, 34]. Once a procollagen chain is formed, three then self-assemble into a right handed triple helix through interchain hydrogen bonds, forming a procollagen molecule, as shown in Figure 1.3A [28, 31, 33, 35]. This triple helix is a 300 nm long heterotrimer, comprising of two procollagen $\alpha(1)$ chains and one procollagen $\alpha(2)$ chain [28, 30, 33]. The $\alpha(2)$ chain is important for the stability and degradation of the heterotrimer, with a lack of the $\alpha(2)$ chain resulting in disruption of later stage collagen development [36]. Glycine is the simplest amino acid that is incorporated into protein structures, with only one hydrogen atom in it's centre [37]. As glycine is the smallest amino acid, it is the only residue in the Gly-X-Y triple able to reside in the centre position of the triple helix. Hydrogen bonds link the amino acids together, with a peptide bond forming between

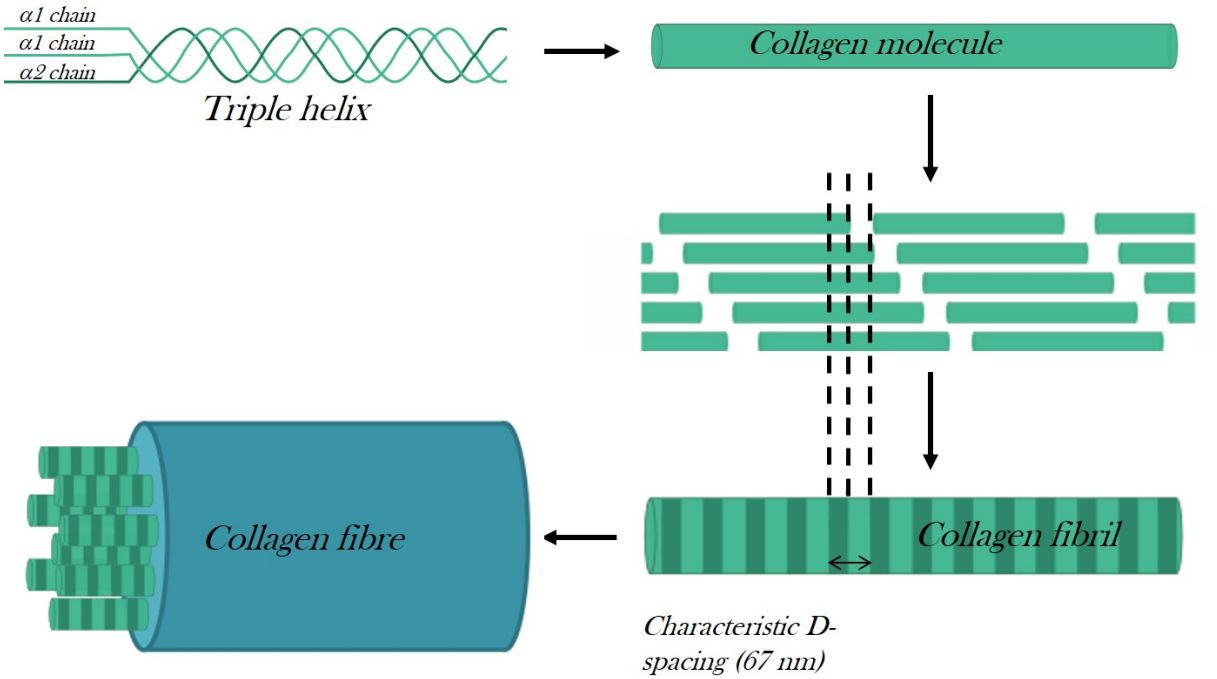



Figure 1.2: Hierarchical process of collagen type I formation. Collagen begins as a triple helix, forming within the endoplasmic recticulum. It is then modified in the Golgi aparatus to form a collagen molecule, which is excreted from the cell. Here, the molecule self assembles to form a collagen fibril. Multiple fibrils then self assemble to form a collagen fibre. Schematic not to scale.

Gly-X, X-Y and Y-Gly. The angle of the C-N bond in the peptide link between glycine and proline/hydroxyproline allows for helical formation [38]. The ordering of the Gly-X-Y region can be shown in Figure 1.3B.

To form a procollagen molecule within the ER, other domains alongside the procollagen chain are required for trimerization to occur. These domains are non-collagenous peptide sections located adjacent to the Gly-X-Y domains to allow for ease of assembly [39]. Two stages are required for trimerization: specific chain recognition for correct chain stoichiometry and stable nuclear formation to favour triple-helical folding. Both the C- and N- terminal of the procollagen chains contributes to triple-helical folding, with the C-propeptide domain (terminal) initiating the trimerization process. Trimerization causes triple helix formation at defined sites, ensuring that there is no misalignment of collagen chains at the triple-helical folding stage [28, 30, 39]. Triple helix formation acts as a zipper within the ER, moving from the C-terminus to the N-terminus [27].

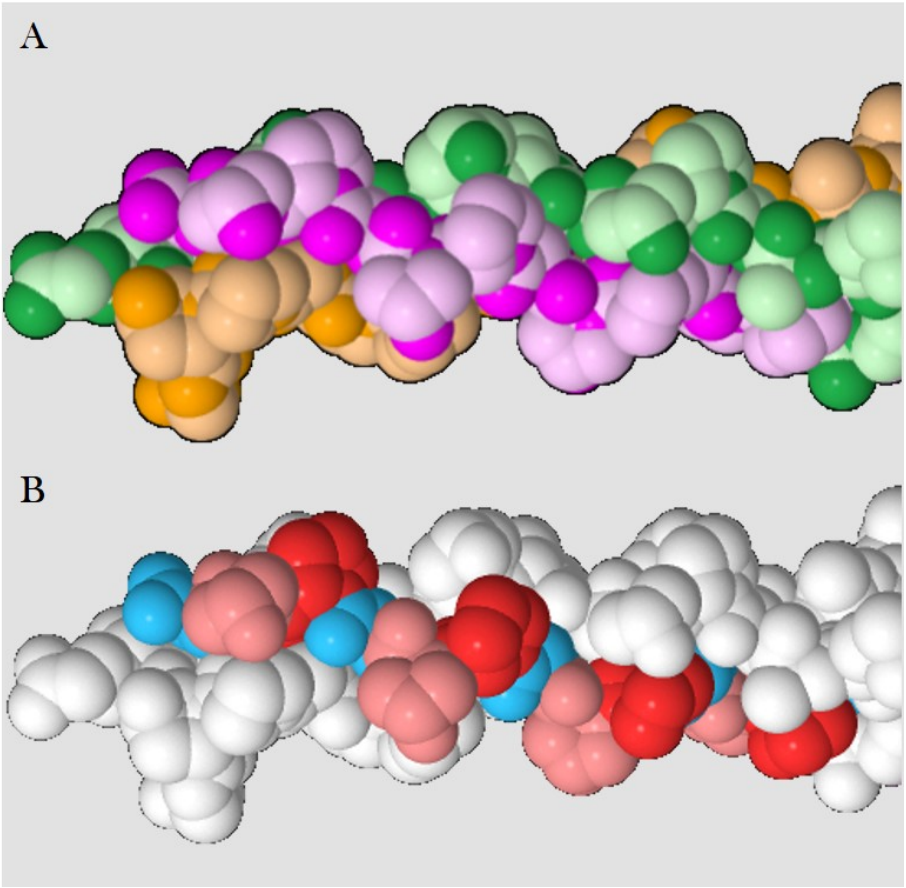



Figure 1.3: (A) Collagen triple helix, where each colour indicates a separate amino acid chain. (B) Colouration of one $\alpha$ chain where glycine is shown in blue, proline in red and hydroxyproline in pink all linked via peptide bonds. Image acquired from [1] used under the Creative Commons Attribution License (CC-BY-4.0).

After trimerization and chain recognition has occurred, various proteins are required to control the triple-helix formation to ensure the complete formation of the procollagen molecule. One of these proteins is prolyl 4-hydroxylase (P4H). This protein catalyses the formation of 4-hydroxyproline via hydrolysing of specific proline residues. This selective binding to $\alpha$ chains not yet folded into a triple helix plays a crucial role in preventing premature helical formation and final helical folding [40, 41]. Another one of these proteins is protein disulphide isomerase (PDI). PDI is activated via the N-terminal domain and forms intra- and inter-molecular disulphide bonds between procollagen $\alpha$ chains. These bonds have to be trans-conformational for triple helical formation. If the procollagen $\alpha$ chains have cis conformation the triple helical formation process is hindered [27]. Once procollagen molecules have formed within the ER, a protein called heat-shock protein 47

(HSP47) binds to the Gly-X-Y repeating units to prevent premature molecule agglomeration [42, 43]. This only occurs when there is an arginine residue in the Y position rather than a hydroxyproline (Gly-X-Arg) [42]. If HSP47 did not stop premature molecule agglomeration, collagen aggregates would form intracellularly [27]. This stabilizes the triple helix until a pH drop in the local environment, on transit from the ER to the Golgi apparatus (Golgi), causes the HSP47 to dissociate [28, 30, 33].

Post-modifications of procollagen molecules occur in the Golgi. This means that the proteins need to be transported from the ER to the Golgi. Transportation of proteins from the ER to the Golgi apparatus is mediated by COPII vesicles. COPII vesicles are comprised of 6 proteins, which exchange amino acids between each other to bind and release specific cargo [2]. However, these vesicles usually have a diameter of 60-90 nm so are too small to transport a collagen molecule (procollagen of size 300 nm) [2, 28, 30, 44]. Procollagen does not bind to the COPII proteins, yet studies have shown that COPII is integral for procollagen transportation [45–48]. Therefore, an intermediate protein is required to bind to procollagen and COPII, which allows COPII to grow to accommodate procollagen [2].

These intermediate proteins are called TANGOs (Transport ANd Golgi Organization) [2, 48–50]. They are able to bind to the SEC23/24 protein (within COPII vesicles) and to procollagen molecules [2, 49, 51]. This creates an inner shell for transportation, with evidence showing that SEC13 (another one of the six COPII vesicles) is able to expand the outer shell of the COPII vesicle [2, 47]. This is still an incomplete model with there being underlying issues such as a failure to identify all of the mediation proteins within this process, and how the inner and outer shells within the enlarged vesicle relate to each other [2]. Another hypothesis is that ERGIC (ER-Golgi-Intermediate Compartment) membranes accumulate at the site of transportation and join together to create a large capsule, as shown in Figure 1.4 [2]. The TANGO, SEC23/24 and SEC 13 complex is still required at the neck of the growing capsule [2, 52]. Once the capsule has begun forming there are two distinct possibilities: either the ERGIC vesicles form a complete capsule

and transport procollagen to the Golgi, or a tunnel is formed between the ER and the Golgi with ERGIC acting as the tunnel walls [2].

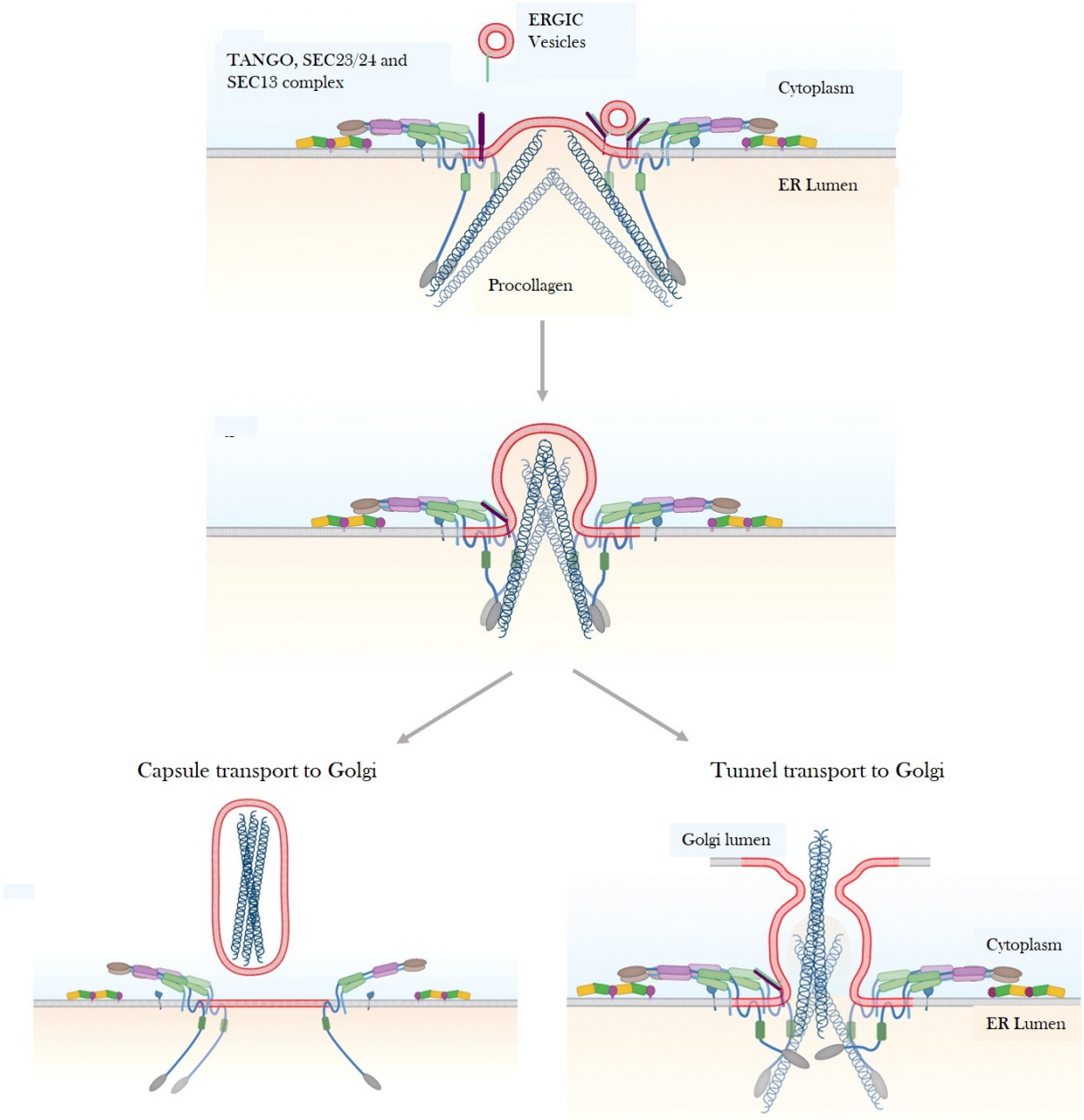



Figure 1.4: Hypothesised transportation of procollagen molecules from the ER lumen to the Golgi apparatus. ERGIC vesicles form a large capsule with the aid of TANGO, SEC23/24 and SEC13 complexes. They form either one large capsule which transports the procollagen or a tunnel for procollagen migration to the Golgi. Adapted from [2] with permission from Copyright © 2015 Annual Reviews.

It is still unknown how procollagen is transported within the Golgi. It has been hypothesised that procollagen remains in the Golgi cisterna and is transported via cisterna

maturation [2, 53]. Cisterna maturation is the dilation of cisternae on the Golgi wall, which is assumed to encompass the procollagen molecules and transport them around the Golgi [54].

Once the procollagen molecule is within the Golgi the removal of procollagen C- and N-terminals can begin. C-terminal processing of the procollagen is performed predominately by bone morphogenetic protein-1 (BMP-1)/Tolloid like proteinases [28, 55]. BMP-1/Tolloid-like proteinases are regulated by procollagen C-proteinase enhancers (PCPE)-1 and-2, which are extracellular matrix proteins. The removal of C-terminal propeptides from procollagen molecules is a rate-limiting step of fibril formation and therefore the regulation of BMP1 within the Golgi is extremely important [56]. N-terminal processing is carried out by metalloproteinases belonging to a set of large multidomain proteins called ADAMTS (A Disintegrin and A Metalloproteinase with Thrombospondin repeats) [28, 57]. These multidomain metalloproteinases are zinc-dependent [56]. Although the ADAMTS family contains many members, only ADAMTS-2, -3 and -14 are required for N-terminal processing [28].

After Golgi processing, procollagen molecules are secreted from the cell. The plasma membrane recesses of the Golgi are able to increase in diameter accommodating the large procollagen molecules [58, 59]. This allows the newly synthesised molecules (tropocollagen) to be released from the cell into the surrounding extracellular space [30–32, 44, 60].

Tropocollagen self-assembles extracellularly with other tropocollagen molecules to form microfibrils. Both hydrogen and covalent bonds are formed between tropocollagen molecules to stabilise microfibrils. Hydrogen residues in glycine form the hydrogen bonds between the carboxyl groups of proline in adjacent molecules. Hydrogen bonds are also formed between hydroxyl groups in the hydroxylysine residues to further stabilise the tropocollagen molecules. Covalent bonds form when a methylamine group becomes an aldehyde group in both lysine and hydroxylysine residues by lysyl oxidase. The aldehyde groups form covalent cross-links with other aldehyde groups in adjacent molecules [61]. Molecules then pack into parallel lines with a quarter-staggered array and supertwist in

the axial direction [32, 62]. This structure packs into a quasi-hexagonal array in the equatorial plane to form a fibril. A variable number of these microfibrils aggregate to form the collagen fibrils causing a variation in fibril diameter [61]. The staggered array causes both overlapping and gap regions within the microfibrils. This produces an oscillating surface topography of repeating bands along the entire fibril length. The overlapping region is referred to as D-spacing, and any changes from the average length seems to indicate a change in collagen formation. D-spacing is averagely 67 nm in length, shown from X-ray diffraction and scanning electron microscopy, although it is dependent on tissue type [28]. An example of D-spacing is shown in Figure 1.5.

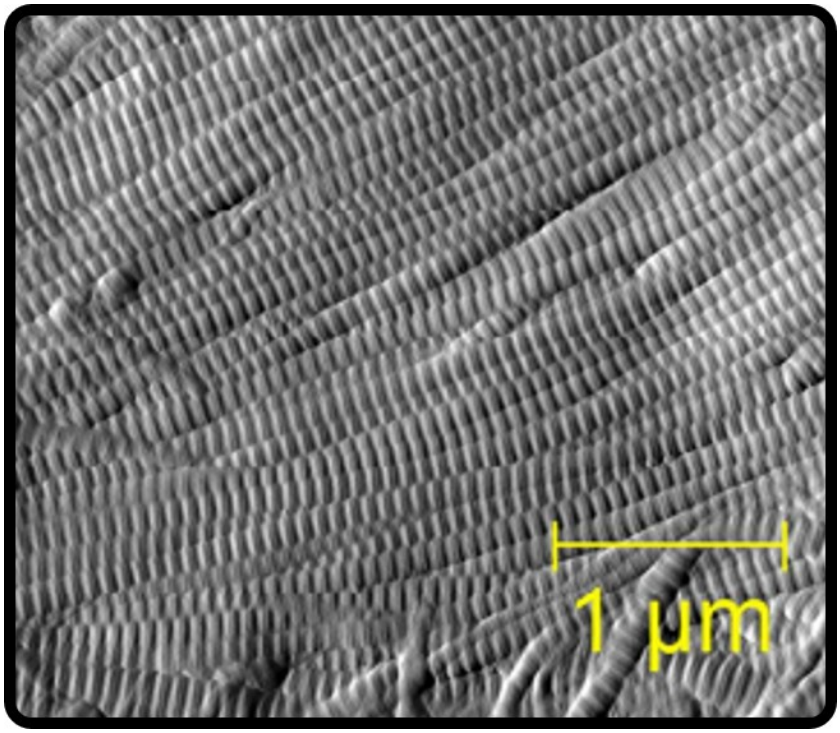



Figure 1.5: Atomic force microscopy image of collagen fibrils in bone showcasing characteristic D-spacing on fibrils. Scale bar is 1 $\mu$m. Adapted from [3] with permission from Copyright © 2012, American Chemical Society.

Collagen fibres are formed through covalent cross-links between mature collagen fibrils. The formation of these cross-links is predominately initiated by members of the lysyl oxidase family [28, 63]. Within the family there are five main contributors: lysyl oxidase (LOX), lysyl oxidase-like (LOXL), LOXL2, LOXL3, and LOXL4. All members have highly homologous C-terminal regions, containing a catalytic domain alongside a

cytokine receptor domain [28]. LOX causes both telopeptide lysine and hydroxylysine precursors to convert to telopeptide aldehyde, allysine and hydroxyallysine respectively. Alongside this, BMP1/Tolloid proteinases continue to regulate the cross-linking and assembly. BMP1 processes the proline-rich region of LOX to allow for multiple forms of the mature enzyme to produce cross-links. Another enzyme, transglutaminase, is also involved in cross-linking. It forms an isopeptide bond between the $\gamma$-carboxyaminde group of specific peptidyl glutamine residues and the $\epsilon$-amino group of peptidyl lysines. Mainly allysine, alongside other precursors, spontaneously condense with other allysines or unreacted lysines in order to form both intra- and intermolecular covalent cross-links. Some of these covalent links can mature into a trivalent form, for example pyridinolines or pyrroles. Cross-link formation is limited by compounds such as $\beta$-aminopropionitrile (BAPN) and penicillamine. By inhibiting LOX and its derivatives from catalysing aldehyde formation, BAPN prevents cross-links from being formed [28, 32]. Multiple fibres then bundle together within connective tissue and are stabilised through interactions with FACIT collagens and small leucine-rich repeat proteoglycans (SLRPs). These interactions allow for tensile forces to be absorbed by the collagen structure and can range in size dependent on final tissue type [11].

## 1.3 Collagen Molecule Hydration

Protein-water interactions are crucial for protein conformation, folding, stability and function [64, 65]. The high content of hydroxyproline within the main bulk of the collagen molecule facilitates water interaction with the molecule, due to the hydroxyl group present within the residue [65, 66]. There are two forms of water within a collagen matrix; bulk water and surface water [64]. The water that is bound to collagen differs from that of bulk water within the matrix [66]. This is due to the three stages of collagen hydration; structural water bridges, cleft water and surface water [64].

Structural water bridges form between the $\alpha$ chains within the triple helix (Fig-

ure 1.6A). They occur when collagen reaches a humidity of 0.065 grams of water/grams of protein (g/g) [64, 67]. These bridges form between the amide carbonyl groups between peptide bonds in separate chains and link every three protein residues [64, 65, 68]. Carbonyl groups from glycine and hydroxyproline only are involved in inter-chain hydration; two sites for hydroxyproline and one for glycine. These groups however, are still less hydrated than the hydroxyl group in hydroxyproline [65]. This hydration link allows for triple helix stability and conformation [64].

Cleft water begins to form at higher hydration levels. Water molecules link together to form chains which lie in the gaps (or clefts) between the collagen $\alpha$ chains within the molecule and form in the direction of the fibre, as shown in Figure 1.6B. When combined with structural water bridges, the hydration layer forms a triple helix that lies within and between the triple helix of the collagen. This occurs only at a hydration layer higher than 0.26 g/g [64, 67]. As hydration levels increase, cleft water begins to form a monolayer surrounding the collagen molecule (consisting of 18 water chains), hydrating the entire molecule surface [67].

The hydration monolayer surrounding the collagen molecule consists of primary and secondary hydration, occurring at a higher hydration of 1.62 g/g, and is also known as surface water [64, 67]. Primary hydration (0.794 g/g) occurs next to hydrophilic surfaces with secondary (0.83 g/g) occurring adjacent to hydrophobic surfaces. Therefore, half of the hydration is associated with polar surfaces on the collagen molecule and the other half non-polar. Primary hydration will form first with polar residues, followed by secondary hydration forming an uneven monolayer, as shown in Figure 1.6C. This layer is important for self-assembly of collagen molecules into fibrils [66].

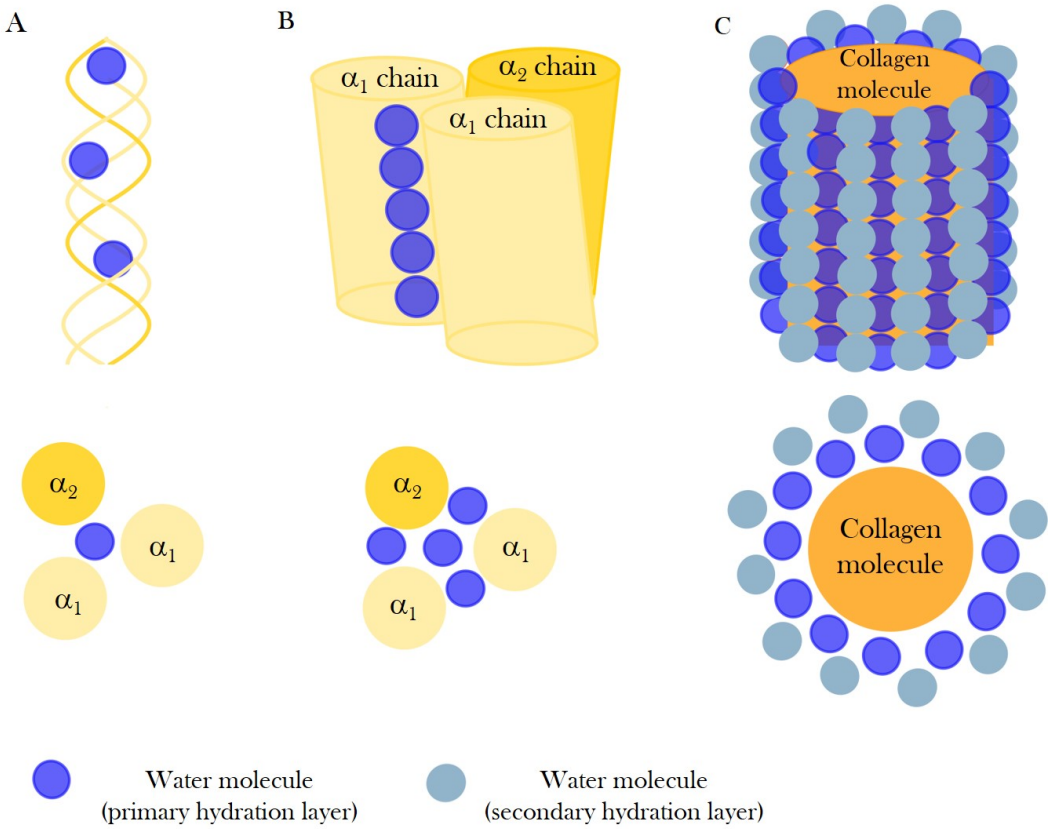



Figure 1.6: Not to scale cartoon depicting lateral and plan view hydration levels of a collagen molecule. (A) Structural water bridges forming between peptide bonds on separate chains on each third residue. (B) Cleft water forming within the gaps of each $\alpha$-chain with increased hydration, forming a triple helix of water within the collagen triple helix. (C) Monolayer formed from primary and secondary water layers. Primary hydration occurs when water molecule bind with polar residues with secondary hydration forming with non-polar residues. This forms an uneven outer hydration layer.

## 1.4 Characterisation of Collagen Type I

Molecular characterisation of collagen was predominately obtained via X-ray diffraction imaging [69]. Initial X-ray diffraction studies by Herzog, Jancke and Gonell in 1921 and 1925 indicated the presence of collagen fibres [69–71]. However, they were unable to interpret the diffraction pattern. This was achieved by Astbury in 1940, when he stretched the collagen fibre to see the underlying collagen components [69, 72]. His diffraction pattern had an intensity distribution that matched that of a helical structure, previously established by Cohen and Bear in 1953 [69, 73]. Astbury was able to establish that collagen had a distinct diffraction pattern with a meridional arc at 2.86 Å [72, 74]. This

was further confirmed with chemical studies occurring at the same time. Bowes and Kenten [75] first investigated the full amino-acid composition of collagen in 1948. They used titration curves to establish both the acidic and basic components of the amino acids. This was advantageous over individual amino-acid analysis as it gave insight into how each residue interacted and how the amino-acids linked within the collagen molecule. They were able to determine that the side-chain groups of both dicarboxylic acids and basic residues were free, and that there was a small number of terminal groups. They also were able to account for 99% of all nitrogen within the collagen molecule [75, 76].

Within the 1950s there were many discoveries into the formation of secondary biological protein structures including the alpha-helix, beta-sheet and the structure of DNA [77–79]. These formations, alongside the development of new technologies, provided the foundations for the collagen triple helix structure [76]. Pauling and Corey created the first model in which collagen was comprised of three amino acid chains instead of one [74]. The fibre-axis spacing of 2.86 Å (previously shown by Astbury [72]) indicated a cis configuration of the amide groups within the polypeptide chain. By looking at x-ray investigations, the length of the amide group within the chain matched that of the fibre-axis spacing [74]. However, previous studies into alpha-keratin structure showed that helical structures had a meridional arc of 5.1 Å, indicative of diagonal spacing [80]. This was impossible to achieve with the current x-ray diffraction patterns of collagen. However, by having three polypeptide chains, in a cis-cis-trans formation, they would interact in a way which allows for intramolecular hydrogen bonds and a fibre-axis residue length of 2.86 Å. Also, by looking at the density of dehydrated collagen and x-ray diffraction pattern, Pauling and Corey were able to establish that each chain consisted of three residues per unit of the molecule [74].

The triplet sequence of amino acids was first discovered by Schröeder *et al* [81]. By using ion exchange chromatography on a gelatin sample it was found that it comprised mainly of glycine, proline and hydroxyproline. Chromatography was used as it allowed for the gelatin to be separated into a series of discrete peptide zones. Some of these zones

were still too large to establish individual amino acids, so conversion to dinitrophenyl derivatives allowed for further fractionation. A method previously developed by Moore and Stein [82] allowed for peptide fractionation of this manner, although the processes needed to be maintained at $37.5^o$ to ensure complete peptide separation. Following on from this work, Ramachandran and Kartha [83] developed the order of amino acids and how these amino acid chains interacted with each other. Although their initial sequence was incorrect, it allowed for Rich and Crick to develop the correct Gly-X-Y structure, with proline and hydroxyproline in position X and Y respectively [84]. They believed that the original structural model was incorrect as it was stereochemically unsatisfactory, with a short carbon-carbon line alongside it's inconsistency with the work of Schröeder *et al* [81]. By creating potential chains and coiling them into both right and left handed helical arrangements, they found that the right handed helix allowed for hydrogen bonds to form between chains. This was confirmed by similarity of x-ray diffraction work from Schroeder *et al* and consistency with stereoisomer stability [84]. Gross first proposed the idea of a subunit of collagen in 1956 which, when aggregated together, formed a collagen fibril. The study used electron microscopy of collagen at different pH values to characterise the precipitated collagen. Highly dilute solutions allowed for images of individual collagen molecules, determining both their length and diameter. It was also determined that the solution in which the collagen precipitated caused a variation in both fibril form and width [85].

Trimerization of type I collagen was intitially investigated in 1973 by Monson and Bornstein [86]. By extracting procollagen from embryonic chick cranial-bone, evidence was provided to show how procollagen exists as a triple-stranded molecule bonded by disulphide links. Through radioactive labelling each of the procollagen chains, pulse-chase experiments determined how the formation of procollagen chains occurred *in vitro*. Chromatography on CM-cellulose was also used to indicate that procollagen chains co-valently linked, creating a triple helical strucutre with there being a ratio of pro$\alpha(1)$ and pro$\alpha(2)$ of 2:1 [86]. This work was further investigated by Fessler *et al* [87] to see

whether inhibiting enzymes prevented the formation of disulphide links. They found that N-terminal regions linked via disulphide bonds regardless of the folding states of the rest of the procollagen chain. However, this caused dimerization rather than trimerization of the procollagen chains.

The importance of P4H in collagen formation was first established by Peterkofsky and Udenfriend [41]. Through previous work [40], it was found that there was a lag phase between proline hydrolysation and hydroxyproline. Radioactive markers were attached to both the proline and hydroxyproline and measured after hydrolysis. The experiment indicated how proline hydroxylase was required in order to hydrolyse hydroxyproline at the same time as proline [40, 41]. HSP47 was initially identified within chick embryos by Nagata *et al* in 1986 [88]. Gel electrophoresis revealed that there was an unexpected protein which corresponded to HSP47. Localisation of HSP47 in the ER was proved by immunofluorescence and immunoelectron microscopy in 1987 by Saga *et al*, who also confirmed the pH dependence of HSP47 through binding assays [89]. Further insight into sequence signalling of the protein and the N-terminal of procollagen chains developed in subsequent years [90, 91], with research continuing into the exact binding mechanisms of HSP47 to procollagen molecules.

The first structural analysis of the polypeptide was reported by Yonath and Traub [92] in 1969, through x-ray diffraction. After this many theoretical investigations were undertaken to further understand the primary structure of collagen [93, 94]. Building on the theoretical work, diffraction investigations involving synthesized peptides helped understand the formation and stabilization of procollagen peptides [95].

D-spacing is a fundamental characteristic created during collagen fibril formation. The presence of D-spacing was originally observed by Rigby *et al* in 1959 [96]. They saw undulating structures spanning a rat tail tendon under light microscopy. Diamant *et al* [97] continued this work and showed the same repeating pattern, instead using polarised light microscopy. The first discovery of D-spacing using SEM was made by Millington and Brown in 1970 [98]. Through imaging separate characteristics of skin they observed

the phenomena of D-spacing but did not know how it arose. A comparison between x-ray diffraction and electron microscopy was undertaken by Hulmes *et al* [99]. They were able to confirm that the D-spacing averaged at the expected 67 nm in periodicity. Confirmation of the regular D-spacing on AFM was first measured by Baselt *et al* in 1993 [100]. They were able to image native rat tail collagen type I to the same detail that is obtained through electron microscopy. From here, development into combining techniques to obtain better quantitative values of D-spacing alongside observation of how different environments affect the D-spacing have been investigated. Ushiki *et al* found that inclination angle of subfibrils had an effect on the D-spacing, with a $15^o$ spiral angle causing a D-spacing of 63 nm, showing how the average may not be the most appropriate indicator of collagen formation [101]. Erickson *et al* have combined AFM and two-dimensional fast Fourier transforms in order to quantitatively characterize nanoscale features of collagen, including D-spacing lengths [102].

The first work regarding collagen fibril cross-linking was conducted through investigations into lathyritic chick embryos, undertaken by Levene *et al* in 1959 [103]. Lathytic diseases causes tremors, paraplegia and muscular weakness. This work and work following found that the incorporation of more BAPN caused greater deformities in collagen formation [104–107]. In comparison, the discovery of lysyl oxidase in collagen cross-linking was first discovered by Bornstein *et al* in 1965 [108]. Chromatography on phosphocellulose was undertaken and the quantity of lysine in cross-links between varying $\alpha$ chains was established. From here, investigations involving reduction in lysyl oxidase activity were undertaken to see how this effected collagen formation [109]. Other members of the LOX family were not discovered until much later. All of the members were discovered through cDNA, with LOXL being the first of the extended family to be discovered in 1993 by Kenyon *et al* [110]. The next family member to be discovered was LOXL2, an oxidase found at high levels in reproductive tissues. LOXL2 was found in 1999 by Jourdan-Le Saux *et al* [111]. Both LOXL3 and LOXL4 were discovered in 2001 by Maki *et al* and Ito *et al* respectively [112, 113]. More recent work has involved inhibiting collagen cross-

links by introducing new selective inhibitors of LOXL2/3 to an *in vitro* model [114–116]. Further work into the function of members of the lysyl oxidase family *in vivo* has been mainly focused on collagen's involvement in tumour growth and regulation [117–121].

## 1.5 External Influence of Collagen Type I

### 1.5.1 Chemical Influence

Collagen fibril self-assembly is a thermally driven proces. The formation of fibrils is highly dependent on pH, ionic strength and temperature with native fibrils, forming within a pH range of 5.0 - 8.5, temperature range of 15 - 37 $^{o}$C and ionic strength range of 0.1 - 0.8 [122–124]. The pH value of the solution in which the collagen is dispersed effects the stability of the collagen fibrils, which in turn influences both D-spacing and fibril diameter [122, 125]. Therefore, it is important to understand how different pH and ionic environments effect characteristic properties of collagen formation (such as D-spacing, fibrillogenesis profiles and fibril diameter). Temperature effects the hydrophobic interactions which in turn affects the kinetics of fibril formation alongside pH and ionic strength [126].

Harris *et al* [127] showed that a buffer with pH of 2.5 (glycine·HCl) prevented collagen molecules from aggregating regardless of the concentration of buffer used. This suggests that pH value has a large influence on aggregation of collagen molecules to form fibrils. However, when in the presence of high concentration NaCl (500 mM), partial aggregates can be detected via transmission electron microscopy (TEM). This, however, indicates that the presence of certain ions can aid initial molecular aggregation. When the pH of the buffer is further increased (pH 4) with the presence of NaCl, partial unbanded aggregates form, which have a flecked rather than smooth appearance. In the presence of phosphate buffer (pH 7), collagen molecules aggregate to display characteristic D-spacing with aligned clustering. If this is also in the presence of high NaCl concentrations (100 - 500 mM), fibrils with D-spacing are observed alongside fully formed collagen fibres. This overall indicates that pH value is an integral part of collagen formation, with compounds

such as NaCl contributing to final fibril formation and alignment to form fibres [127].

Li *et al* [122] investigated the kinetics of collagen type I fibril formation at varying pH values to determine how the pH of the surrounding environment influenced collagen morphology. Initially, turbidity measurements were conducted to understand how the pH of the medium effected fibril formation. Turbidity measurements of solutions measure absorbance in the z-axis over a select time period [122]. When collagen assembles, the resulting solution changes from translucent to opaque in the z-axis, so formation of the collagen matrix can be observed via absorbance [128]. The study found that pH values ranging between 8.0 - 9.2 produce the greatest level of absorbance, and therefore allow for a higher level of aggregation. Fibrils also form between pH values of 6.9 - 8.0 but with a lower overall absorbance. Collagen dispersed in buffer at pH values of 6.6 and 10.5 produce relatively weak gels with low absorbance and low rate of fibril formation. Morphological experiments (conducted via TEM and scanning electron microscopy (SEM)) indicate how low pH values cause a wide range of fibril sizes, with smaller aggregates not forming characteristic D-spacing. However, when the pH of the medium is increased, fibrils become uniform and begin to form a matrix. TEM and SEM measurements also provided insight into how pH effects fibril diameter. A pH of 6.0 gives no detectable fibrils, however, after three days small fibrils of 85 nm diameter can be detected with a medium of pH 6.6. Although the rate at which fibrils form between pH values of 6.9 - 8.0 vary, the final fibril diameter across the range is consistent at approximately 200 nm [122]. D-spacing is also unaffected within the pH range of 6.9 - 8.0, with an average D-spacing of approximately 62 nm, correlating with expected values [122, 129–132]. Low pH values show an increase in fibril diameter, as shown by Wood *et al* [124], however the more basic the pH of the medium the thinner the fibril diameter, as shown by Roeder *et al* [133].

Electrostatic interactions between collagen molecules and fibrils will have an effect on the formation of larger fibrils and fibres [122, 134, 135]. Collagen molecules are more likely to aggregate at their isoelectric point (p$I$) as they are less soluble. This occurs at pH 9.3 [135], yet is effected by the presence of ions within the solution. If ionic strength

is increased then the pI value shifts to a lower pH [136]. If the ionic strength is increased, causing a pH shift between 5.3 - 7.3 (through, for example, increasing KCl content) the p$I$ also shifts to the pH region. Yet, if a complex such as $CaCl_2$ is present the p$I$ favours more basic pH conditions [136]. This indicates that the aggregation of collagen molecules into fibrils is controlled significantly by electrostatic interactions. The Debye length, ($\kappa^{-1}$), needs to be taken into account when discussing electrostatic interactions. This length measures the net electrostatic effect of a colloidal particle within a medium containing free ions/charges. It indicates the distance to which the electrostatic effect of the colloidal particles can be observed and decays exponentially with distance. It is dependent on both the concentration of charges within the solution but also on their size [137, 138]. It is expressed as,

$$\kappa = (\frac{N_A e^2}{\epsilon_0 \epsilon_r k_B T} \sum_{i=1}^{n} C_i Z_i^2)^{\frac{1}{2}} \tag{1.1}$$

where $N_A$ is Avogadro's constant, $e$ is the elementary charge, $\epsilon_0$ is the permittivity of free space, $\epsilon_r$ is the relative permittivity of the solution, $k_B$ is the Botlzmann constant, $T$ is the absolute temperature, $C_i$ is the molar concentration of the $i$-th ion (mol $L^{-1}$) and $Z_i$ is the charge number of the $i$-th ion [122].

The theoretical maximum of the Debye length of collagen within a pure water medium, is ∼970 nm. However, Li *et al.* determined that when collagen is within an electrolyte rich medium the Debye length reduces to $\leq$ 0.6 nm. The distance between two collagen molecule surfaces (i.e. between two tropocollagen monomers) in fully hydrated collagen fibrils is ∼0.5 nm. Therefore, electrostatic interactions between collagen molecules within an electrolyte medium are only important when the collagen molecules are aggregated into fibrils, as the distance between the collagen molecule surfaces is less than 0.6 nm [122].

When the pH of collagen approaches the p$I$ value the molecule charge is reduced, minimizing repulsion and favouring aggregation. Overall, fibril formation of similar D-spacing and diameter is formed within a pH range of 6.9 - 9.2, although the rate of fibril

formation varies within this range. A pH value of 9.2, matching that of the p$I$ value for collagen, has the highest rate of molecule aggregation [122]. This is because the collagen molecules have an overall net charge, which increases their electrostatic attraction to neighbouring fibrils. Any changes in pH value will alter the charge on the side groups and therefore alter the likelihood of electrostatic interaction [126].

The mechanical properties of a collagen matrix are determined by fibril formation. Therefore, the chemical environment in which the collagen matrix forms will alter the mechanical properties. Achilli *et al* used turbidity measurements to evaluate how the local environment effected collagen fibrillogenesis. Collagen is unable to form fibrils at a temperature of 4 ℃, yet is able to fully gel at a temperature of 21 ℃ after three days. Achilli *et al* also found that a pH of 7 obtained a higher absorbance and faster kinetic formation than that of pH 10 [126]. Collagen matrices at higher pH seem to be more compact regardless of ionic strength (shown via SEM imaging) [126, 139]. This is most likely due to an increased formation of net electrostatic interactions between charged side groups, increasing attraction and causing tighter packing of the network. When collagen is at a pH of 10, an increase in ionic strength and decrease of temperature result in a higher compressive modulus (CM) and compressive strain energy (CSE). CSE here was defined as the integral between 0 – 40% strain [126]. However, a pH of 7 does not significantly change the CM or CSE regardless of temperature and ionic concentration. It has been shown in multiple studies that the higher the pH the stiffer the collagen matrix [126, 139, 140]. This may be due to the higher level of packing observed at higher pH, contributing more to an increase in collagen matrix stiffness, CM and CSE rather than it being dependent on another characteristic such as fibril diameter. Overall, it seems that a neutral pH stabilises the mechanical properties of the collagen matrix, with neither temperature nor ionic strength altering CM and CSE. Yet, in basic conditions, temperature has a significant effect on mechanical strength, greatly increasing the mechanical properties of the matrix at a temperature of 4 ℃ [126].

Alterations in the surface chemistry of a substrate can change how collagen adsorbs

onto its surface. By enhancing the hydrophilicity of a surface, the organisation and mechanical properties of adsorbed collagen can be changed. Pamula *et al* demonstrated this by evaluating how collagen structure changes when placed on polystyrene (PS) and oxidized polystyrene (oxidized by oxygen plasma discharge, PSox). PSox is more hydrophilic than PS due to the increase in surface oxygen concentration. This results in a slower initial adsorption onto the PSox in comparison to the PS surface. Throughout all stages of adsorption, the hydrophobic PS surface resulted in collagen aggregates. In comparison, the more hydrophilic surface resulted in a smooth initial layer followed by a mesh like structure of collagen at longer adsorption times. This in turn altered the overall mechanical properties of the collagen matrix, with a more hydrophilic surface allowing for a higher mechanical stability of the collagen structure [141]. Denis *et al* also found that a more hydrophobic surface resulted in aggregates of collagen on the substrate surface [142]. They found in multiple studies that more collagen adsorbed onto hydrophobic surfaces in comparison to hydrophilic surfaces [142, 143]. It was concluded that surface chemistry determined the level of adsorption, with both surface chemistry and topography determining orientation and organisation [142]. This property was also confirmed by Elliott *et al*, who indicated that hydrophobic areas caused large collagen fibril structures. More specifically, they determined that a water contact angle of $>78^\circ$ is essential for large collagen fibril assembly. Collagen fibril density increased with this angle until reaching a maximum density at a contact angle of $87^\circ$. If the water contact angle is $< 63^\circ$ there will not be any collagen fibril assembly [144]. In this way surface chemistry is able to dictate adsorption of collagen molecules and therefore initial organisation of the self-assembly process essential to collagen fibril formation.

### 1.5.2 Physico-Chemical Influence

Physical treatments can be implemented during fibril formation which alter the chemical composition of collagen, and in turn it's physical properties.

Dehydrothermal (DHT) treatment is a treatment which causes free carboxyl and amine

groups within the collagen triple helixes to form amide bonds. This results in more cross-linked collagen, enhancing properties such as elastic modulus, tensile strength, thermal stability and resistance to enzyme degradation [145]. During the treatment, collagen is placed under vacuum and exposed to high temperatures (110 ℃) to remove any water within the structure [145, 146]. Ber *et al* found that exposing collagen to DHT resulted in a increase in strain, toughness and overall elongation of collagen structure. They also found that DHT decreased the hydrophilicity of collagen structures, however the treatment did not effect the biocompatibility of collagen, instead enhancing cell adhesion and growth [146]. Ratanavaraporn *et al* found that DHT treated collagen could be used as a skin substitute. During this treatment, freeze dried collagen samples were subjected to temperatures of 140 ℃ under vacuum. They found that DHT treated collagen had a higher compressive modulus, increasing with an increasing exposure to DHT treatment. They also found that the longer the DHT treatment, the higher the rate of cellular proliferation, indicating as well that DHT treated collagen increases cellular proliferation [147].

Another technique which can increase the cross-linking of collagen is exposure to ultra-violet (UV) light. As UV irradiation causes bonds to form within aromatic phenylalanine and tyrosine residues within collagen, it is able to increase the cross-linking of the collagen structure without compromising the bioactivity of the matrix. This, therefore, links protein molecules without changing the binding sites crucial for cell recognition [148]. Another benefit to irradiating collagen with UV is that it will also sterilise the collagen, killing microorganisms by disrupting their DNA [148, 149]. Irradiation at short wavelengths of 184.9 and 253.7 nm result in an excitation of molecular oxygen, forming ozone [150]. This ultimately changes the number of amino acids within the triple helix [151]. This improves hydrophilicity of substrates by exciting oxygen groups, such as hydroxyl and carboxyl groups, maintaining biocompatibility as these groups interact with cell receptors [150]. Davidenko *et al* irradiated collagen with UV at a wavelength of 254 nm to cross-link collagen scaffolds. This allowed them to have customizable mechanical properties while not compromising biocompatibility. They found that exposure to UV at this short wave-

length increased the elastic modulus of the collagen structure. This is important as when cells traverse over collagen they bend individual collagen struts, so the higher the elastic modulus the easier it is for cells to traverse across the structure [148]. However, although UV increases cross-linking, it also destabilizes collagen molecules. Kontomaris *et al* found that UV exposure reduces the height of the D-spacing within collagen alongside reducing overall fibril diameter. There was also a reduction in Young's modulus from both the overlap region and gap region of D-spacing. Kontomaris *et al* hypothesised that this was due to scission of the polypeptide chain from UV irradiation [152].

Gamma-ray ($\gamma$) radiation is another way to cross-link collagen without the addition of external chemicals. However, if collagen is exposed to too much $\gamma$-radiation, there is a significant reduction in bioactivity due to multiple structural alterations. Not only is the collagen more cross-linked, but more scissions occur throughout the structure. Increase in cross-linking occurs when the sample is hydrated, however, when dehydrated, scissions are more common [145]. Predominately, $\gamma$-radiation causes degradation of collagen, reducing its mechanical properties and increasing the likelihood of enzymatic digestion. However, the influence of $\gamma$-radiation on collagen is important as it is a common sterilizing technique for medical devices and treatments [153]. Tyan *et al* found that the critical $\gamma$-radiation exposure to both moderate collagen bioactivity and amide degradation is 10 KGy [154].

### 1.5.3 Physical Influence

Collagen fibre orientation and diameter are important for matrix assembly and in turn cellular attachment and growth [155–159]. Physical techniques can be implemented to manipulate these characteristics and create a specialised matrix.

Electrospinning is a technique which forms small diameter fibres and deposits them onto a surface. The technique uses a thin needle, into which a polymer solution is injected, producing thin fibres, and controls deposition via an electric field. An electrically charged jet is produced when the critical voltage is hit; here, the surface tension is superseded by the charge imbalance. The jet produced is directed through the electric field

and becomes thinner due to evaporation of the solvent. The result is a highly porous network of non-woven fibres. Specific fibre alignment can also be achieved by rotating the underlying surface [14]. Electrospinning is a technique which can alter the distance between needle and surface, voltages, collagen concentration and electric field strength to produce tailored, specific collagen scaffolds [160].

Linear, parallel alignment of fibres can be obtained by rotating the deposition surface during electrospinning. Matthews *et al* found that a rotation speed of 4500 rpm resulted in optimal results [160]. Initial collagen concentration directly influences final fibre diameter, in which a critical collagen concentration of 0.083 $\text{gmL}^{-1}$ allows for large diameter while still producing fibrils [160, 161]. Bending modulus of individual fibres decreases with an increase in electrospun collagen fibre diameter. Although electrospinning denatures the collagen molecule (measured via circular dichroism) [162, 163], bending modulus values of produced fibres are comparable to native collagen at similar diameters, as found by Yang *et al*. They hypothesised that this is due to the alignment of each individual molecules within the axial direction, caused by the spinning process. As the collagen molecules align, there is an increase in the potential number of intermolecular interactions resulting in a bending modulus similar to native collagen [163]. Electrospun collagen scaffolds are also able to enhance cellular infiltration into the scaffold network, which can be tailored by altering parameters of the electrospinning process [160, 161].

Collagen molecules are dipolar, and therefore have an electric charge. When there is no electric field, the dipoles of the collagen molecules are randomly dispersed, however, if subject to an electric field these dipoles begin to orientate [164].

Applying an electric field to collagen composites can improve collagen alignment and therefore improve mechanical properties. Ficai *et al* exposed a collagen/hydroxyapatite (HA) composite to an electric field over 1 hr, testing the influence of two fields; pulsatory (0.93 $\text{Vcm}^{-1}$) and superposed (direct field of 0.67 $\text{Vcm}^{-1}$ and pulsatory field of 0.93 $\text{Vcm}^{-1}$). They found that when the collagen/HA composite was exposed to a pulsatory field, fibril orientation and compactness matched that of compact bone. Pulsatory

electric field exposure was superior to that of the superposed field. This is because the direct field also migrates collagen molecules, causing collision of HA particles and collagen molecules during the orientation of the pulsatory phase. They also hypothesised that pulsatory fields cause a higher level of collagen orientation as it matches the electrical stimuli caused during osteogenesis [164]. Collagen is a piezoelectric material (induces charge under mechanical stress [165]) so mechanical stimuli caused by cells during the collagen deposition and mineralisation induces an electrical surface charge. This electric field caused by piezoelectricity matches that of a pulsatory field, so therefore aids collagen orientation [164].

Alahakoon *et al* also used a pulsed electric field (PEF) to change the thermal stability of collagen within connective tissues. They found that introducing connective tissues to a PEF caused a significant reduction in the denaturation temperature. Furthermore, treatment of a PEF resulted in an increase in connective tissue porosity [166].

PEFs have also been shown to influence the production of collagen and other ECM proteins from fibroblasts. Multiple healthcare treatments, used for accelerating wound healing and chronic pain management, take advantage of the influence electric fields have on biological processes, such as increasing fibroblast cell proliferation [167–172]. Nguyen *et al* showed that collagen expression is increased with applied PEFs. Furthermore, they indicated that intracellular matrix protein concentration doubles with electric field stimulation. They showcased that the short time voltage pulses were more effective at increasing intracellular matrix protein concentration. Overall, the introduction of PEFs caused an increase in the production of intracellular proteins and therefore an increase in expressed ECM proteins [173].

Electric fields can also be used to regulate the proline expressed in both intra- and extracellular protein. McLeod *et al* found that the level of proline within protein produced by fibroblasts was dependent on sinusoidal electric currents. It was also dependent on the orientation of the cells within the electric field. By reducing the current, they were able to reduce the amount of newly synthesized ECM and therefore reduce the amount of

proline present. It was only cells that were aligned with the electric field that produced this decrease in proline production [174].

As a magnetic field is produced by a moving electric charge, it follows that collagen can also be influenced by magnetic fields [175]. A magnetic field can be used to achieve alignment of collagen fibres over large areas, orientating perpendicular to the magnetic field. Each collagen molecule has a small negative diamagnetic susceptibility, which allows them to be influenced by a magnetic field [176, 177]. When collagen molecules self-assemble into fibres, each small negative diamagnetic susceptibility accumulates to create one large enough to induce alignment perpendicular to the magnetic field [177].

Several studies have shown that a strong magnetic field of 1 T, applied during gelation, is able to increase alignment at a normal to the magnetic field [177–180]. Erikson *et al* were able to achieve a 0.7 T magnetic field influence over collagen gels by pulling collagen solution into glass capillaries. They saw an increase in anisotropy factor from 1.02 to 1.76 when collagen was exposed to a magnetic field [181]. Not only can this influence collagen alignment, but in turn can alter cellular orientation. Kotani *et al* were able to alter the orientation of osteoblasts within a magnetic field from parallel with the field to perpendicular with the addition of collagen fibres [182].

Collagen fibres can also be aligned through the use of topographical surfaces. Glass-Brudzinski *et al* used patterned titanium surfaces to orientate both cells and collagen. These titanium surfaces were patterned with sets of grooves that ranged in both width and depth. They found that both cells and collagen aligned parallel to grooves, with smooth titanium surfaces producing only random orientation [183]. Mendonça *et al* found that a smooth surface allowed for fibroblasts to maintain their morphology more than a rough surface. This correlated to an increase in collagen production, with a 10% increase in collagen from fibroblasts cultured on a rough surface. They did not however investigate whether this changed any characteristics or alignment of the collagen produced [184]. Multiple studies investigate the influence of the topographical surface on cell adhesion and culture, yet there are few investigations into how this influences the ECM [185–189].

## 1.6 ECM and Tissue Function

The organisation of ECM within tissue determines its biophysical properties. Structure and composition of the extracellular matrix vary dependent on tissue type resulting in varied tissue characteristics. By providing specific biochemical and mechanical cues the extracellular matrix provides each tissue type with its function. Any changes in the ECM can result in the tissue not functioning properly, leading to disease [190]. More structural information on the ECM of bone and of the cornea is explained in depth in Chapter 4 Section 4.1 and Chapter 5 Section 5.1 respectively. Within these chapters the understanding and manipulation of the collagen network is developed and discussed in more detail. The specific organisation and composition of ECM for a range of tissues, and how this relates to tissue function, is outlined below.

### 1.6.1 Dermal ECM

ECM within the skin is formed of a randomised network of collagen fibres in a basket-weave-style configuration [191]. Collagen fibres lie perpendicularly to each other intersecting at an approximately 90° angle to each other [192]. As collagen is the main stress-bearing component of the skin, the orientation and organisation of its network determines the skin's mechanical properties. Thinner collagen bundles are found nearer the surface of the skin, with bundles becoming thicker deeper into the dermis. Throughout the dermis, collagen is densely packed, accounting for most of the space within the dermis [193].

### 1.6.2 Tendon ECM

ECM within tendon is predominately collagen type I [194, 195]. Collagen bundles within tendon align along the long axis of the tissue, in the direction of loading [195, 196]. This provides good uniaxial mechanical strength for the tissue. Tendon collagen fibrils can have diameters ranging from a few nm to 300 nm and grow in length up to a few millimetres [195]. These fibrils then self-assemble to form fascicles and, when interspersed

with non-collagenous matrix components, finally form the whole tendon [194, 195]. Fascicles and fibrils form a helical structure, with an undulating "crimp" appearance which allows them to be flexible [194]. Some tendons also store energy via stretching to improve the efficiency of motion. These energy storing tendons are less stiff with more elasticity caused by changes in collagen cross-linking and ECM composition [195]. Strain is transferred through the tendon through loading and extension of the individual collagen units and via shearing between different stages in collagen hierarchy. Small changes in ECM composition, therefore, will alter the mechanical properties of the tendon tissue [194, 195].

### 1.6.3 Skeletal Muscle ECM

There are three subsections of ECM within skeletal muscle. That which resides around the muscle cell (endomysial), that which resides around a group of muscle cells (perimysial) and that which resides around the whole muscle (epimysial). Endomysial ECM forms a highly ordered matrix which deforms non-linearly with increasing length of sarcomere. The geometry of this network allows for a load-bearing matrix, transmitting any force applied by shear [197]. Perimysial ECM is less understood, however studies seem to indicate ECM forming both traverse and longitudinally to muscle fibres [198, 199]. The traverse ECM has been linked to cell signalling, with the connection points potentially relating to focal adhesion. Large collagen bundles within the perimysial ECM form coils, indicative of providing strain relief, a function required in load-bearing tissue. Epimysium ECM is comprised of larger collagen bundles than perimysial ECM, with a "crimp" pattern (similar of that to tendon ECM). It has been found that there is a link between age and increase in epimysium ECM stiffness, shedding light on the biomechanical properties of muscle tissue and age. Overall, the ECM within skeletal muscle is extremely stiff and nonlinear to allow for passive load-bearing of the tissue [197].

### 1.6.4 Cardiovascular ECM

Cardiovascular tissue is highly reliant on chemical and genetic signals between cells and the surrounding environment [200]. Integral to the communication of these signals is the ECM by providing both chemical signal factors and structural support [200, 201]. By providing chemical and mechanical signals the ECM ensures that cell transformation and migration occurs in the correct spatiotemporal order. The ECM is also important during angiogenesis, providing a structural scaffold to stabilize and promote tube formation. In particular, collagen within the ECM provides mechanical properties needed for each vessel wall within the tissue [200]. As the heart is a muscle, the ECM is organised similar to that of skeletal muscle ECM, with perimysium and epimysium components. The organisation of these components, in particular the perimysium, organises cardiac myocytes (muscle cells) which in turn determines the mechanical properties of the heart [202].

## 1.7 Thesis Aims

Studies within the literature indicate how collagen can be influenced across multiple length scales by both external chemical and physical parameters. The overall aim of this thesis is to influence collagen type I triple helix, microfibril and fibril formation by introducing chemistries and physical changes in surface parameters, thereby manipulating collagen assembly and orientation externally. Each external influence relates to a biomedical problem or bioprocess, and investigates how changes to the local environment influences collagen formation from the molecular scale to the macro-scale. Chapters within this thesis cover the following points:

- To investigate how the composition of materials used in metal-on-metal implants influence collagen fibril formation on the nano- and macro-scale, alongside collagen bulk mechanics, and in turn how these changes to the collagen structure influence cellular proliferation and viability.

- To understand the fundamental interactions between inorganic calcium and phosphate ions present at early stage collagen mineralisation, and how these ions interact individually with collagen formation and assembly, from the molecular scale to the macro-scale.

- To investigate how alterations in the nanotopography of a surface can organise and control collagen fibril formation and orientation, and how this in turn influences cellular orientation in the context of corneal scarring from laceration. Surfaces were physically altered to have a nanopattern of ridges and grooves of select widths, with the groove depth being either at 200, 500 or 1000 nm.

# CHAPTER 2

# GENERAL THEORY AND METHODOLOGY

## 2.1 Physical Theory and Methodology

### 2.1.1 Collagen Hydrogels

Cultrex rat tail collagen type I (AMS Biotechnology Europe Marketplace, UK) supplied at a concentration of 5 mg $mL^{-1}$ in 0.6% acetic acid, was initially diluted down to 3 mg $mL^{-1}$ using phosphate buffer solution (PBS) stock (NaCl: 0.137 M, KCl: 0.003 M, $Na_2HPO_3$: 0.008 M, $KH_2PO_4$: 0.0015 M). To create this stock, two Oxoid$^{TM}$ PBS tablets were dissolved in 200 mL of distilled water. Collagen was further diluted down to the desired concentrations using PBS or distilled water and neutralised with 1 M sodium hydroxide (NaOH, Sigma-Aldrich, UK). Samples were incubated within a humidified incubator until gelation had occurred.

### 2.1.2 Atomic Force Microscopy (AFM)

Atomic force microscopy (AFM) does not rely on a charged surface so there is no limitation to the surface being imaged, nor its local environment. A force-sensing cantilever is mounted on the scanning device which moves in the xyz plane. At one end of the cantilever is a tip which is positioned above the sample (Figure 2.1). The tip needs to be close to the surface of the sample to create a potential energy between the two. Cantilevers can

be described as a spring, and therefore can be described by Hooke's Law:

$$F = -ks \tag{2.1}$$

the force $F$ required to extend the spring is dependent on the distance, $s$, that it is extended. The spring constant, $k$, determines stiffness of the cantilever and likelihood of deformation with surface topographical changes.

The imaging signal produced from an AFM is either the force $F$ or a value derived from this force. AFM can measure force from both long and short-range contributions due to the components of $F$. Short-range contributions are measured from chemical forces within the range of a few nanometres. Long-range contributions are measured from forces such as van der Waals, magnetic and electrostatic forces, which range up to 100 nm. To sense tip - sample forces, the force sensor needs to be relatively flexible in one axis, and rigid in the other two. In most cases the cantilever is flexible in the z-axis. Cantilever deflection is commonly measured by bouncing a laser off the cantilever and measuring any deflection. [203, 204]

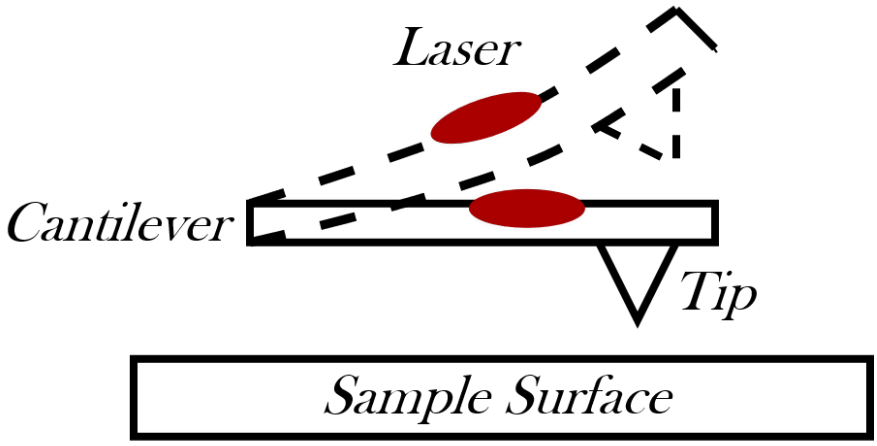



Figure 2.1: Schematic showing an AFM cantilever with attached tip. Cantilever deflected due to the forces between the tip and the surface forming an image signal which creates the overall image.

Within AFM, the laser beam is reflected from the cantilever onto a mirror and then reflected onto a detector. Any small change in the z-position of the cantilever results

in a large deflection on the photo-detector. The photo-detector is separated into four quadrants which are compared to each other to determine the deflection signal. The top and bottom quadrants determine any changes in vertical deflection. This corresponds to interaction forces. The left- and right-hand sides of the photo-detector determine any lateral twisting of the cantilever. A schematic of an AFM is shown in Figure 2.2 [205].

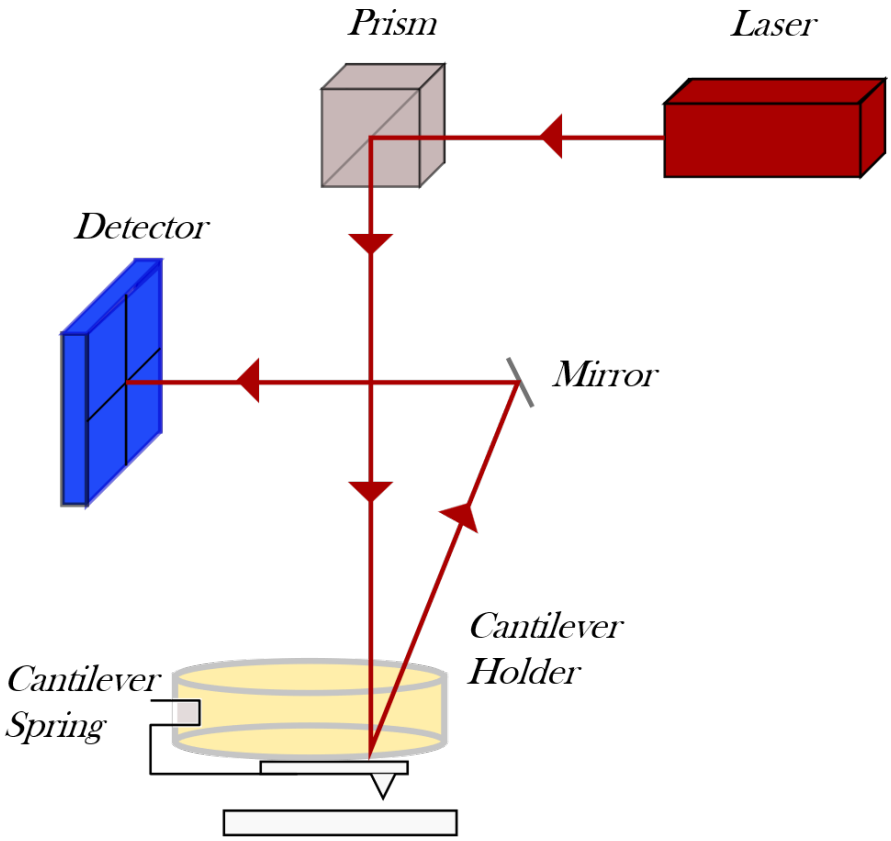



Figure 2.2: Schematic showing the inside of working AFM with laser path.

There are two operating modes for AFM; static and dynamic. Static AFM measurements use the force $F$ as the imaging signal. In this instance, the force is described by any deflection of the cantilever, and expressed as:

$$q' = \frac{F}{k} \tag{2.2}$$

where, $q'$ is the cantilever deflection. As the cantilever will deflect more than any sample/tip deformation, the specified range of $k$ is useful for choosing the correct tip for

each sample [204]. Static AFM, otherwise known as contact mode, measures the repulsive forces between the sample and the tip. Any deflection of the cantilever is due to surface topography as changes in force are caused by surface height variations. Tapping mode, or dynamic mode, is commonly used when samples are more likely to be susceptible to tip damage, for example biological samples. The tip oscillates near to resonant frequency and contacts the surface on each oscillation. This allows the oscillation amplitude, and therefore the energy associated with each oscillation, to be greater than the energy required to remove the tip from the sample preventing it from getting stuck. As tapping mode produces high resolution images for biological samples it was the main technique used for imaging changes in collagen gels [206].

Collagen gels were prepared as indicated in Section 2.1.1, however samples were completely dehydrated to avoid any external dragging. Collagen gel was deposited onto a snow cleaned silicon wafer using an adjustable micropipette. Snow cleaning utilizes compressed liquid carbon dioxide to clean a surface. Dehydration of the collagen gel resulted in the formation of a thin collagen layer on the solid substrate. The sample was dehydrated in an incubator for 24 hrs and washed three times with distilled water. A 10 x 10 $\mu m^2$ area of each sample was imaged using a NanoWizard®4 NanoScience Atomic Force Microscope (JPK Instruments, DE) with intermittent contact (tapping) mode. A PointProbe®Plus Non-Contact/Tapping Mode - High Resonance Frequency - Reflex Coating probe (Nanosensors, CH) with a force constant of 42 N $m^{-1}$ and a frequency of 330 kHz was used. Fibril density was determined through ImageJ [207] by counting the number of fibrils visible in a 5000 $pixel^2$ area. For each concentration, images of 3 samples were acquired and fibrils counted over 36 areas for each image. Density was classed as low (4-6 fibrils), medium (7-10 fibrils) and high (11-13 fibrils). Fibril diameter and D-spacing was also measured using ImageJ. N=75, with 25 fibrils, measured at random from AFM images, over 3 biological repeats. A justification of this number can be found in Section 2.3.1. Images of three repeats were taken and a two-way paired t-test performed on the data.

### 2.1.3 X-Ray Fluorescence (XRF)

XRF is a technique predominately used to determine the chemical composition of materials. X-rays produced from a source irradiate the sample, causing elements within the sample to emit fluorescent X-ray radiation. These X-rays have discrete energies and so can be mapped to a specific element. The intensity of the emitted energies can also determine the quantity of each element within the sample. There is an inverse proportion between wavelength and energy, given by:

$$E\lambda = hc \tag{2.3}$$

$$E = h\nu \tag{2.4}$$

where $E$ is the energy in keV, $\lambda$ is the wavelength in nm, $h$ is Planck's constant (6.62607004 x $10^{-34}$m$^2$kgs$^{-1}$), $c$ is the speed of light (2.99792458 x $10^8$ ms$^{-1}$) and $\nu$ is the frequency in Hz [208].

When X-ray radiation comes into contact with matter, Compton scatter, Rayleigh scatter and fluorescence is produced. Compton scatter and Rayleigh scatter occur when the scattered radiation causes an energy loss or no energy loss respectively. Fluorescence occurs when the X-ray radiation is partially absorbed, producing a fluorescent beam. All interactions are dependent on the thickness, density and chemical composition of the materials [208].

By taking the classical model of an atom, with a nucleus comprised of protons and neutrons surrounded by orbitals of electrons, we can understand how fluorescent radiation is produced from interacting X-rays. Electron energy is dependent on the orbital that it occupies. If an X-ray beam has enough energy to overcome the electron's binding energy it can expel the electron from its orbital (Figure 2.3). This produces a vacancy in the orbital, causing the atom to be in an unstable excited state with higher energy. For the atom to return to a stable state, an electron from an outer shell must occupy the vacancy. The energy surplus produced by the electron moving into a lower orbital is released from

the atom as an X-ray. As electron energies are discrete the X-ray energy produced will be dependent on the atom orbital configuration. Therefore, a collection of X-rays within a certain range will produce a fingerprint for each element. In this way, XRF can measure the fluorescence produced and use it to determine the chemical composition of a sample and the quantity of each element within that sample [208].

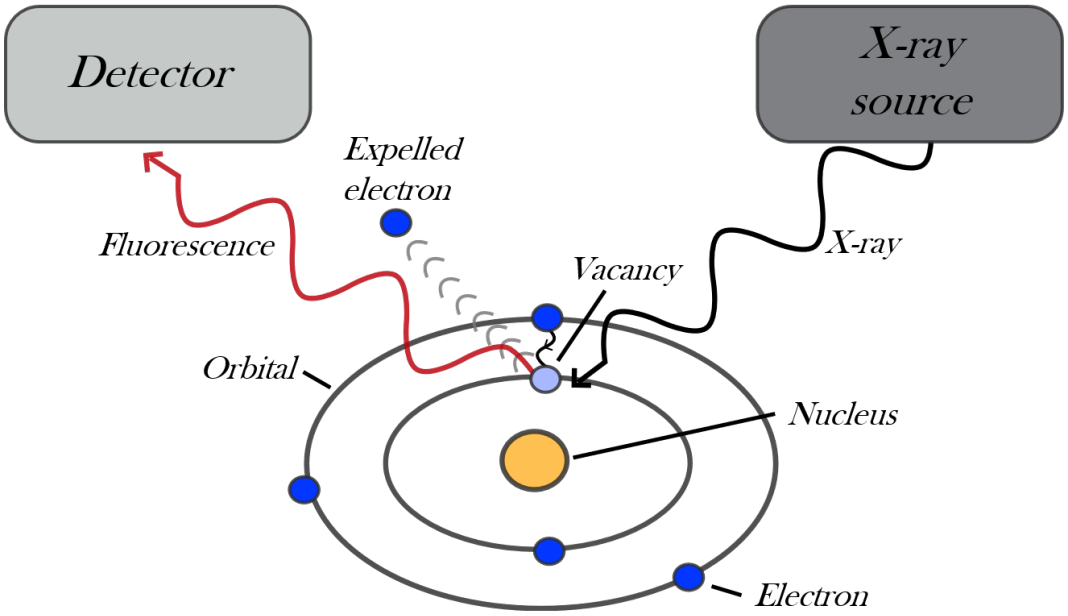



Figure 2.3: X-ray produced from an x-ray source expels an electron from an inner orbital. The vacancy produced is filled by an electron in a higher orbital. Any surplus energy is released as a fluorescence radiation and detected by a detector in the XRF.

Samples were analysed in high resolution using a tornado M4 XRF (Bruker, UK), an energy dispersive system, with the ability to detect elements ranging from sodium to uranium. A scan area of 5.5 x 5.5 $mm^2$ was measured with a spot size of 25 $\mu$m under an x-ray beam of 50 kV and 400 $\mu$A under atmospheric conditions.

### 2.1.4 Rheology

The flow and deformation of a material can be quantified by measuring its rheology. Most materials have aspects of elasticity and viscosity and are therefore referred to as viscoelastic materials. Elasticity is described by Hooke's law via classical theory. Hooke's Law indicates the direct proportionality between stress and strain due to deformation and in-

dependent of the rate of strain. Viscosity is described by Newton's Law via hydrodynamic theory, where the stress is directly proportional to the rate of strain and independent of strain itself. Viscoelastic polymers respond elastically when a force is applied rapidly and respond viscously when the force is applied slowly. The applied force is proportional to both the deformation and the rate of deformation. As the elastic component is described by Hooke's law, there is a full recovery after deformation. As the viscosity is described by Newton's law of viscosity, any deformation does not recover [209].

Viscoelastic properties of materials are analysed using both static (creep and stress relaxation tests) and dynamic measurements. Stress relaxation tests measure the amount of stress required to maintain the applied strain over a period of time. This is achieved by deforming a specific volume of the material rapidly [209].

Dynamic mechanical tests measure the response of the material when exposed to cyclic stresses. A viscoelastic material will have a strain within the range $\frac{\pi}{2} > \delta > 0$. Amplitude attenuation of the cyclic strain and delay of the strain wave are characteristic properties of each viscoelastic material. By applying a cyclic stress, the complex modulus $E^*$ can be resolved into two components: the storage modulus $E'$ and the loss modulus $E''$. The storage modulus is described as the ratio between the strain and the in-phase stress with respect to strain and relates to the elastic component of the material. The loss modulus is the ratio between the strain and $\frac{\pi}{2}$ out-of-phase stress with respect to strain and represents the viscous component of the material. The complex modulus $E^*$ is described using the equation:

$$|E^*| = \frac{\frac{\Delta F}{S \times Lt}}{\Delta L} \tag{2.5}$$

where $\Delta F$ is the loading force, $S$ is the area of the specimen deformed, $Lt$ is the length of the specimen and $\Delta L$ is the dynamic displacement.

$E'$ and $E''$ and the loss tangent are defined as:

$$E^* = E' + iE'' \tag{2.6}$$

$$E' = |E^*|cos\delta \tag{2.7}$$

$$E'' = |E^*|sin\delta \tag{2.8}$$

$$tan\delta = \frac{E'}{E''} \tag{2.9}$$

with these parameters often measured using frequency-dependent dynamic rheological testing [209].

When determining the viscoelastic properties of hydrogels, a parallel plate in oscillatory mode is used as shown in Figure 2.4.

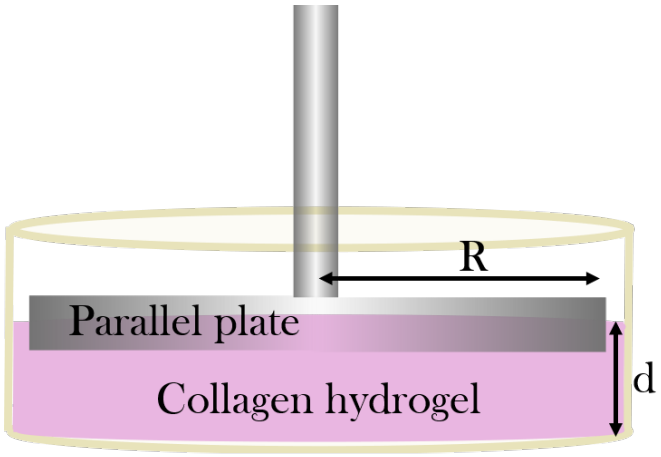



Figure 2.4: Schematic depicting parallel plate frequency-dependent oscillatory rheology on a collagen hydrogel.

The torque of the gel is measured at constant angular displacement and oscillating frequency. In this system, shear strain ($\gamma$) and shear stress ($\tau$) are determined as:

$$\gamma = F_\gamma \omega \tag{2.10}$$

$$\tau = F_\tau T \tag{2.11}$$

where $F_\gamma$ is the shear strain factor $\left(\frac{R}{d}\right)$, $F_\tau$ the shear stress factor $\left(\frac{2}{\pi R^3}\right)$; $\omega$ the angular displacement; $T$ the force produced from torque; $R$ the radius of the plate, usually fixed and $d$ the shear gap. As gels experience shear, the complex shear modulus ($G^*$), shear

storage modulus ($G'$) and shear loss modulus ($G''$) are defined as:

$$G^* = G' + iG'' \tag{2.12}$$

$$|G^*| = \frac{\tau}{\gamma} \tag{2.13}$$

$$G' = |G^*|cos\delta \tag{2.14}$$

$$G'' = |G^*|sin\delta \tag{2.15}$$

where $\delta$ is the phase angle between strain and stress. As before, the shear storage modulus represents the elastic component of the material and the shear loss modulus represents the viscous component [209]. A schematic of the relationship between stress and strain between a perfectly elastic, viscoelastic and viscous material can be shown in Figure 2.5.

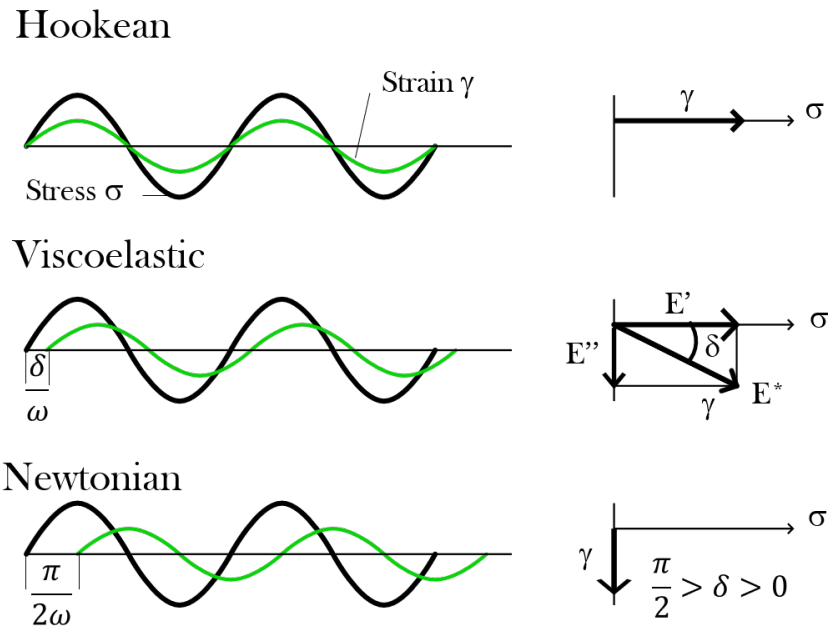



Figure 2.5: Schematic representing the interaction of stress and strain when looking at an elastic material (Hookean), a viscoelastic material and a viscous material (Newtonian).

Collagen gels, at a concentration of 1 mg $mL^{-1}$ and a volume of 2.4 $mL^3$, were prepared in petri dishes. Samples were maintained at 37 ℃ for 5 min prior to measurement to maintain gelation. An AR-G2 rheometer (TA Instruments, DE, USA) was used to obtain

rheological measurements, using parallel plate geometry with a gap of 1 mm. Wall slip was minimised through the use of a sandblasted plate and samples remained in the petri dishes throughout the duration of the experiment. In order to establish the limit of the linear viscoelastic region, strain sweeps at a frequency of 1 Hz were taken. Frequency sweeps were performed at a frequency range of 0.01-10 Hz at the lowest strain measured.

### 2.1.5 Differential Scanning Calorimetry (DSC)

Calorimetry is the study of heat exchange. All chemical reactions involve the exchange of heat, calorimetry is a technique which measures these processes. Differential scanning calorimetry not only measures changes in heat, but also heat flow rates and characteristic temperatures of reactions [210]. The technique works by measuring any changes to the difference of the heat flow rate with respect to a reference sample while undergoing a controlled linear temperature program [210, 211]. When the sample temperature is altered, usually due to a chemical reaction, there is a change in the difference of heat flow rate resulting in a measurement [210]. As each sample had a high water content, any changes shown from DSC measurements related to energy released from the evaporation of bound water.

A Mettler Toldeo DSC 1 (Mettler Toledo, CH) was used to analyse samples of 0 ppm and 200 ppm CoCol gels at a collagen concentration of 1 mg $mL^{-1}$. Each sample was weighed into a 46 $\mu$L aluminium DSC pan (Mettler Toledo, CH), capped with an aluminium DSC lid (Mettler Toledo, CH) and sealed with a press (Mettler Toledo, CH). This was calibrated with indium and zinc standards. Experiments were conducted under a nitrogen flow rate of 50 mL $min^{-1}$ and samples were heated from 25 ℃ to 135 ℃ after gelation at a rate of 5 ℃ $min^{-1}$.

### 2.1.6 Raman Spectroscopy

Raman uses a photon of light to produce a fingerprint of scattered radiation. It utilises inelastic scattering of monochromatic light (through use of a single wavelength laser)

either from the visible range, near ultraviolet or near infrared. Raman spectroscopy is able to study rotational and vibrational modes in a system. As Raman yields a lot of information, it is usually used for chemical identification, characterisation and effect of bonding and environment on a sample [212].

Scattered radiation from the irradiated sample produces both Rayleigh scattering and a small amount of Stokes and Anti-Stokes Raman scattering as depicted in Figure 2.6. The difference in wavelength of the scattered photon (Raman scattering) provides the structural and chemical information of the sample. These changes in wavelength are associated with the vibrational, rotational and electronic level transitions. If there is no change in wavelength then Rayleigh scattering has occurred [213].

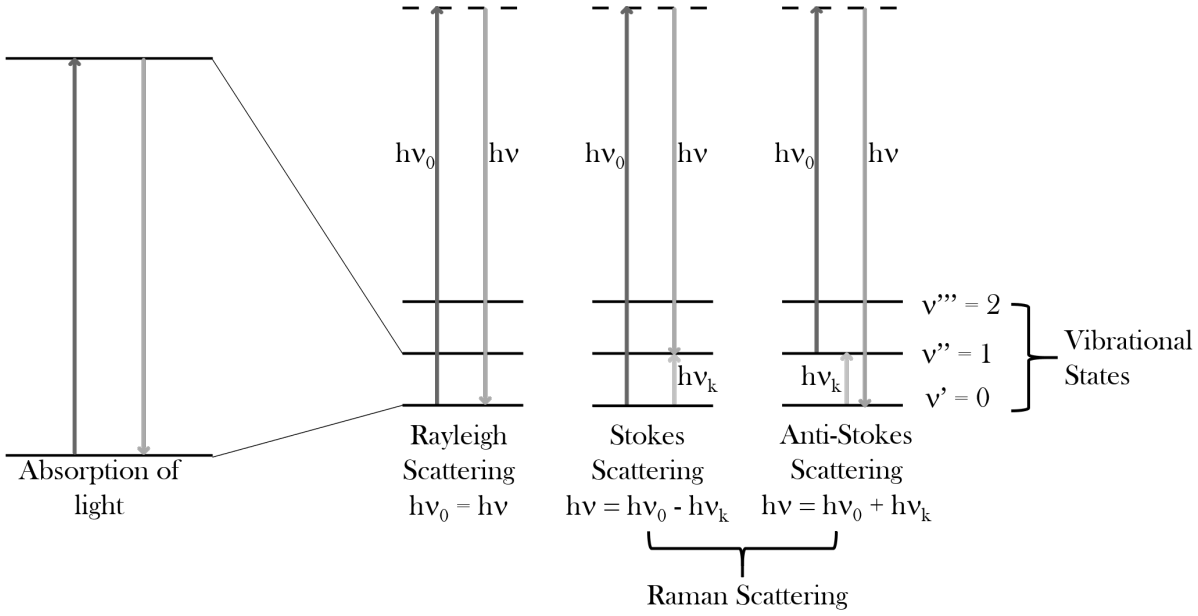



Figure 2.6: Schematic of Rayleigh scattering and Raman scattering. Changes in energy levels are described as in Equation 2.4.

Samples of 1 mg $mL^{-1}$ were measured using a 50x lens via an inVia Qontor Confocal Raman (Renishaw, UK). An extended scan over a spectral range of 100-4500 $cm^{-1}$ was taken at 30 random positions throughout each sample. The 785 nm laser was used with the pinhole in at 10% power to obtain scans with a 30 s acquisition time. Cosmic ray removal was performed on each spectra using WiRE (Windows-based Raman Environment, Renishaw, UK). Averaging and normalising of the dataset was achieved using Microsoft

Office 365 Excel (2013). Reduction of the spectral range of 350-2650 $cm^{-1}$ was undertaken using Prism 5 (GraphPad Software, 2007) to isolate the fingerprint region and to remove any background effects.

### 2.1.7 Principal Component Analysis (PCA)

PCA is a method that takes a large multivariate data set and converts it into a new set of variables described as principal components. These components show the greatest differences within the original data set, with the principal component space being that of large data clusters [214].

Data in PCA is shown as a data matrix **X** comprised of rows termed "objects" (here this is the control collagen sample and the CoCol gel sample), and columns termed "variables" (here the Raman spectra produced from each). This creates two smaller matrices called **T** and **P'** which encompass the data patterns within **X**. Dominant patterns within the objects can be found by plotting the columns on **T**, with complementary variable patterns found from plotting the rows of **P'** [215].

To observe large differences more clearly, a plot of the first principal components against wavenumber is required. In this space any differences between clusters is indicated as a peak with high intensity. In this way, the wavenumber of peaks with high intensity within the first principal component plot correlates to a large change within the original data set [214]. A plot of the second principal components against wavenumber corresponds to the bets fit for the residuals. This continues throughout all the data set. The change in intensity shown is formed from the eigenvectors of the original data set matrix [216].

Raman spectra were imported and further analysed using Matlab software (R2017a). Prior to PCA analysis, all spectra were normalised and reduced to a spectral range of 350-2650 $cm^{-1}$ to remove any background effects. Once PCA was performed, principal components were chosen based on the highest fraction of variance. This allowed for scores and loadings values to be plotted with respect to wavelength to aid data interpretation.

### 2.1.8 Circular Dichroism

Circular dichroism (CD) uses circularly polarized light to determine the difference between how a molecule absorbs both the left- and right-hand components of circularly polarized light [217, 218]. Circularly polarized light consists of two plane-polarized beams of light that are 90° out of phase (shown in Figure 2.7A). The electric vector relating to these beams rotates about the axis of propagation of the wave, with the left- and right-hand circularly polarized light propagating in an anti-clockwise or clockwise rotation respectively. When plane-polarized light is passed through a circularly dichroic medium, the light is converted into elliptically polarized light due to the difference in absorption of the two circular components (Figure 2.7B) [217, 219]. The semimajor axis of the ellipsis is due to the sum of the magnitudes of the vectors when the two circular components are in the same direction. The semiminor axis is that of the vectors in the opposite direction. CD is characterised by the ratio of both the semimajor and semiminor axes, a tangent of an angle $\theta$, called the ellipticity. This ellipticity is directly proportional to CD [217]. The CD spectra consists of a series of bands which correspond to the electronic transition states of the molecule, from a ground state to an excited one. Each band is characteristic of the molecule being investigated [217].

A Chirascan (Applied Photophysics Ltd, UK) was used to determine circular dichroism of collagen molecules in the presence of calcium and phosphate. For excess calcium and phosphate, 0.05 mM of calcium chloride (Sigma-Aldrich, UK), sodium phosphate (sodium phosphate dibasic heptahydrate and sodium phosphate monobasic monohydrate at a ratio of 1:0.46) and Ca:$PO_4$ 1:1 (calcium chloride and sodium phosphate added together at a ratio of 1:1) were added to 0.1 mg $mL^{-1}$ of collagen. A cuvette with a path length of 1 mm, step size of 1 nm and 0.5 s time-per-point were used over a wavelength of 185-400 nm (three repeats taken for each sample). A circular dichroism scan of deionised water and air was taken as a baseline.

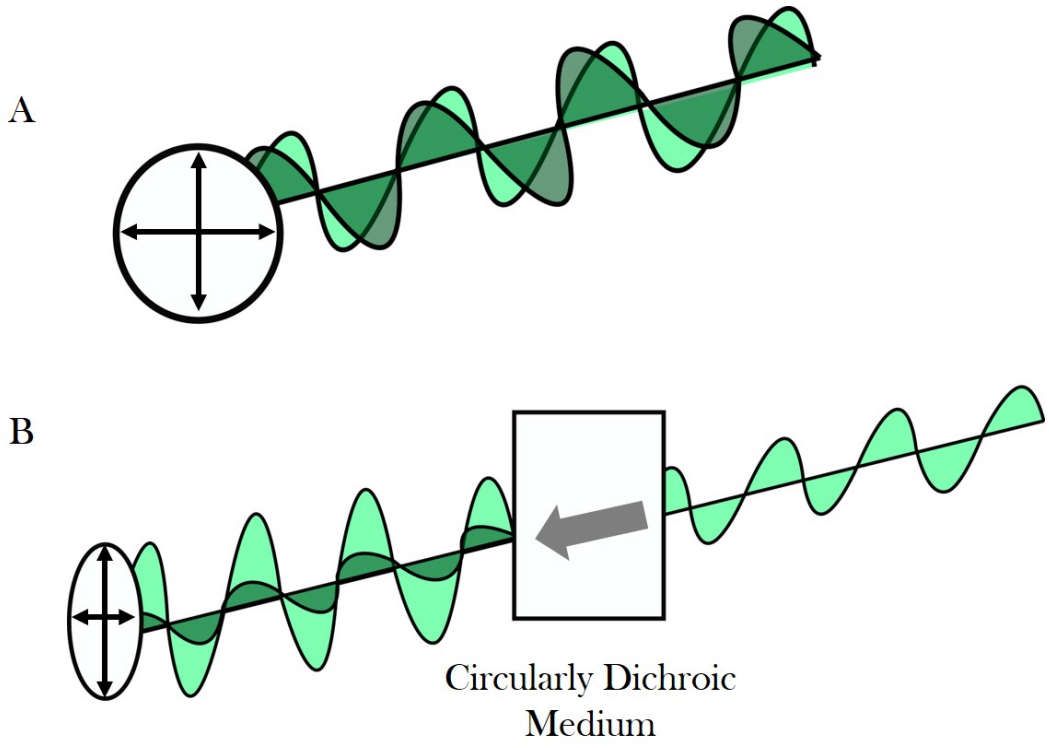



Figure 2.7: Schematic showing (A) circularly polarised light consisting of two out of phase light beams. (B) When plane-polarised light is passed through a circularly dichroic medium it is converted into elliptically polarized light which contributes to a CD signal.

### 2.1.9 Zeta Potential

Particles are surrounded by a layer of ions, opposite to their net charge, bound strongly to their surface. This layer is called the Stern layer. This is followed by a secondary diffuse layer consisting of associated ions which are loosely bound. This diffuse layer is also opposite in charge to the particle. Collectively these two layers form the electrical double layer. As the particle moves through the dispersant, due to Brownian motion, there is a distinction between the ions that are associated with the particle (in the diffuse layer) and those that remain within the bulk dispersant. This causes an electrostatic potential boundary. Through calculating the average potential in the surface of sheer between the diffuse layer and dispersant the zeta potential can be obtained [220, 221]. It is determined by the surface charge of the particle [221].

An electric field is applied across the sample and laser doppler velocimetry is used to measure the particle movement. The zeta potential is then calculated using the Henry

equation [221]:

$$U_e = \frac{2\epsilon\xi f(\kappa a)}{3\eta} \tag{2.16}$$

Where $U_e$ is the electrophoretic mobility, $\epsilon$ is the dielectric constant, $f(\kappa a)$ is the Henry function, $\kappa a$ is a measure of the ratio of the particle radius to the Debye length and $\eta$ is the absolute zero-shear viscosity of the medium [221].

A Zetasizer NanoSeries (Malvern, UK) was used to measure zeta potential of collagen and collagen with excess calcium chloride ($CaCl_2$), sodium phosphate ($PO_4^{3-}$) and calcium phosphate at a ratio of 1:1 (Ca:$PO_4$ 1:1) at a collagen concentration of 0.5 mg $mL^{-1}$ and buffer concentration of 0.1 mM. The dispersant used was water with a viscosity of 0.8872 cP and refective index of 1.330. Disposable folded capillary cells were initially flushed with ethanol prior to being washed 4x with pure water. Samples had a collagen concentration of 0.5 mg $mL^{-1}$ and an ionic concentration of 0.05 mM. Final pH of each solution ranged between 3.85 – 3.89.

### 2.1.10 Fibrillogenesis

Kinetic turbidity measurements of each sample provided collagen fibrillogenesis information. Turbidity measurements are separated into two methods: turbidimetry, which determines the transmission of light, and nephelometry, which determines the scattering of light within the sample. For fibrillogenesis studies, turbidimetry provides a qualitative study on how the solids (here collagen molecules/fibrils) within the solution are obstructing the transmittance of light through water [222]. This process relies heavily on the Beer-Lambert law, which relates the power of light to the concentration of the species in the medium and the path length of the beam in the medium [223]. It is expressed by the relation:

$$A = -log_{10}\frac{P}{P_0} = abc \tag{2.17}$$

where $A$ is the absorbance, $P$ is the radiant power, $a$ is the absorptivity, $b$ path length of the beam of light in the absorbing medium and $c$ is the concentration of the absorbing species [223].

As the path length and the power of the light are kept consistent, the absorption measured during the turbidity measurements will be in relation to the concentration of the species within the medium alone. Therefore, this process can be used to determine fibrillogenesis, as when there is an increase in fibril formation (and hence concentration) there is an increase in absorbance [224, 225].

A Spark multimode plate reader (Tecan, CH) was heated to 37 ℃ and a wavelength of 380 nm used to determine collagen fibrillogenesis. A collagen concentration of 2 mg $mL^{-1}$ was made by diluting the stock collagen concentration (5 mg $mL^{-1}$) with deionised water. This was placed in -20 ℃ for 15 min and then in 4 ℃ for 10 min. Various ions were added to deionised water to create a concentration of 0.1 mM. To each buffer the volume of NaOH (Sigma-Aldrich, UK) at 1 M required to induce collagen gellation was also added (130 $\mu$L NaOH for 5 mL of buffer). Each buffer was then vortexed for 5 s and 67 $\mu$L of each buffer placed into a 96 well-plate. Ionic buffer solution which did not have any NaOH included, treated in the same way, were also added to the 96 well-plate to allow for baselining. The 96 well-plate was then placed in -20 ℃ for 5 min and then in 4 ℃ for 10 min. To this a volume of 133 $\mu$L of 2 mg $mL^{-1}$ collagen, previously chilled, was added using a multi-channel micro-pipette. Absorbance measurements were taken every minute for a total of 90 min. Non-cross-linked collagen and ionic buffer was subtracted as a baseline in Microsoft Office 365 Excel (2013) and data plotted in Prism 5 (GraphPad Software, 2007). Growth phase measurements were taken from each fibrillogenesis profile, as shown in Appendix I Figures 7.1, 7.2, 7.3, 7.4 and 7.5.

### 2.1.11 Scanning Electron Microscopy (SEM)

Scanning electron microscopes use an incident electron beam to image surfaces. The electrons within the beam interact with the surface of the sample via both elastic and

inelastic scattering. Elastic scattering is when no energy is lost through interaction. Inelastic scattering is when energy is lost usually through ionization of the sample. Two different types of signals are produced when the beam traverses the surface. When the intensity of the signal is plotted against the probe position an image is formed. The first type of imaging is secondary electron (SEs) imaging, in which the secondary electrons released from ionization provide the signal [226]. They are produced from the first few layers of the sample and are relatively low in energy (0 – 50 eV) so give topographical information about the sample. The second type is back-scattering electron (BSEs) imaging, in which electrons that have been scattered multiple times within the sample create the signal. The amount of scattering is determined by the atomic number of the sample, so BSE imaging shows contrast between different chemical compositions [226, 227]. To get chemical information however, energy-dispersive X-ray spectroscopy (EDS) is required in which X-rays are detected from the decay of ionized atoms [226]. As topography was the main interest of all samples imaged by the SEM, only SE imaging was used.

A XL30 ESEM FEG (Philips) was used to image collagen deposited onto various surfaces. Images were acquired under 1.3 x $10^{-4}$ mBar vacuum with a 5 kV electron beam. The electron source is from a point-source cathode of tungsten with a surface layer of zirconia [228]. Collagen, at a volume of 5 $\mu$L, deposited onto a patterned silicon wafer was sputtercoated with gold at 20 mA for 10 s using an Agar Auto Sputter Coater (Agar Scientific, UK). Collagen deposited onto polydimethylsiloxane (PDMS) was sputtercoated with gold at 25 mA for 3 min. Copper tape was also required with PDMS samples due to the insulating properties of the polymer.

### 2.1.12 Fabrication of Polydimethylsiloxane (PDMS) Surfaces

Polydimethylsiloxane (PDMS) was created using Sylgard 184 (Merck, UK) at a ratio of 6:4. Samples were made in petri dishes and placed under vacuum to remove any air bubbles. Samples were then placed within a 60 ℃ oven until cured. Some PDMS samples were plasma treated (PDMSPlasma) using a piezobrush® PZ2 handheld plasma

device (Relyon Plasma, DE). The piezobrush® PZ2 uses corona discharge to ionize the surrounding air, creating a plasma temperature of $< 50$ ℃, with a maximum power consumption of 30 W. Without using an external gas supply it is able to plasma treat a surface at a treatment distance of 2 - 10 mm, and treatment width of 5 - 20 mm [229]. PDMS samples were exposed to the treatment for 9 mins in atmospheric conditions. Some PDMS samples were sputtercoated with gold (PDMSAu) at 40 mA for 30 s. Some PDMS plasma treated samples were also treated with (3-Aminopropyl)triethoxysilane (APTES) (Merck, UK). Samples were submerged in APTES at a pH of 3 for 30 mins. The pH of the APTES was then increased to 9, through the addition of NaOH (Sigma-Aldrich, UK), and left again for 30 mins. Excess APTES was then removed and the samples were placed within a 60 ℃ oven for 30 mins. They were then placed within a 100 ℃ furnace for 30 mins. 0.5 mg $mL^{-1}$ collagen gel at a volume of 10 $\mu$L was added using an adjustable micropipette to each PDMS and PDMS treated surface and left for 10 mins. Excess collagen gel was removed and samples placed within a 37 ℃ incubator until dehydrated. Samples were then washed three times with distilled water.

### 2.1.13 Surface Free Energy (SFE)

The most common way to determine surface free energy (SFE) is through the sessile drop method [230]. This method uses a sessile drop, whose shape is dependent on the equilibrium between gravity and surface tension, to determine surface tension [231]. An image is taken of a liquid droplet on a flat solid surface and the contact angle measured, as shown in Figure 2.8.

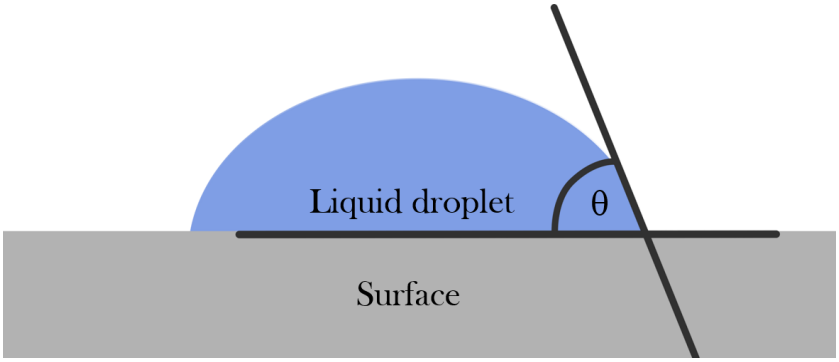



Figure 2.8: Schematic showing the sessile drop method for determining contact angle between a liquid and solid surface, where $\theta$ is the contact angle.

SFE can then be determined from the contact angle measured as follows. Young's equation shows the relationship between a liquid droplet on a flat solid surface [230, 232]:

$$\gamma_s = \gamma_{sl} + \gamma_l cos\theta \tag{2.18}$$

where $\gamma_l$ is the surface tension of liquid, $\gamma_s$ is the surface free energy of the solid, $\gamma_{sl}$ is the interfacial tension and $\theta$ is the contact angle between the liquid interface and the solid surface. As the last two parameters are unknown, we need to express $\gamma_{sl}$ in terms of $\gamma_l$. This can be done by expressing $\gamma_{sl}$ as a sum of facial tensions minus work of adhesion [230]:

$$W_a = \gamma_l(1 + cos\theta) \tag{2.19}$$

$W_a$ is additive so can be separated into different forces of adhesion. It is then assumed that SFE can also be separated into components which represent different surface interactions. SFE is expressed as [230]:

$$\gamma = \gamma^d + \gamma^p \tag{2.20}$$

where $d$ is the dispersion component and $p$ is the polar component.

Owens and Wendt separated SFE into its components and expressed $W_a$ as [233]:

$$(1 + cos\theta_i)\gamma_{li} = 2(\sqrt{\gamma_{li}^d \gamma_s^d} + \sqrt{\gamma_{li}^p \gamma_s^p}) \tag{2.21}$$

If there are multiple liquids, then there are multiple equations. For further derivation, Equation 2.21 is assumed to be linear within the square roots. This also allows for a linear fit of data acquired when measuring greater than two liquids. Through division of Equation 2.21 by $2(\sqrt{\gamma_{li}^d})$ we get [230]:

$$\frac{(1 + cos\theta_i)\gamma_{li}}{2\sqrt{\gamma_{li}^d}} = \sqrt{\gamma_s^d} + \sqrt{\frac{\gamma_{li}^p}{\gamma_{li}^d}}\sqrt{\gamma_s^p} \tag{2.22}$$

This equation is that of $y = mx + c$ where $m$ is the gradient and $c$ is the y-intercept. By plotting $y$ and $x$ values for more than one liquid on a solid surface and drawing a line of best fit $m$ and $c$ can be determined. By using the Equation 2.20, the sum of the square of both the $y$ intercept and gradient will give the SFE of the solid surface [230].

Pure water (Sigma-Aldrich, UK), diiodomethane (Sigma-Aldrich, UK) and ethylene glycol (Sigma-Aldrich, UK) were deposited using a micropipette at a volume of 10 $\mu$L onto each surface. Five images were acquired per technical repeat using an Andonstar A1-AV-200W USB narrow webcam-microscope, with magnifications ranging between 1-500x (purchased from www.ebay.co.uk). Real-time images were acquired as the webcam-microscope was connected via USB to a laptop. Three technical repeats were imaged for each surface. Contact angle of each liquid was measured using ImageJ [207], with both left and right tangents measured and the value averaged. 5 droplets were measured on each surface resulting in N=30. A justification of this number can be found in Section 2.3.1. Contact angle average measurements were taken from the contact angle of pure water only. A one-way ANOVA was performed on the data set to determine any statistical significance. Microsoft Office 365 Excel (2013) was used to change angle measurements from degrees into radians. Prism5 (GraphPad Software, 2007) was used to create lines of best fit, from which the y-intercept and gradient were obtained. SFE measurements were calculated through the addition of the square of the y-intercept and gradient.

### 2.1.14 Patterned IP-DIP Fabrication

Patterned surfaces created via photolithography were made using an IP-DIP photoresist using a NanoScribe Photonic Professional GT Two-Photon Laser Lithography System (NanoScribe, DE). Surface parameters (depth 1000 nm, ridge width 850 nm, gap width 550 nm and surface area 100 x 100 $\mu m^2$) were created using eDrawings software (Dassault Systèmes, FR, 2019) and saved as an STL file. This file is shown in Figure 2.9.

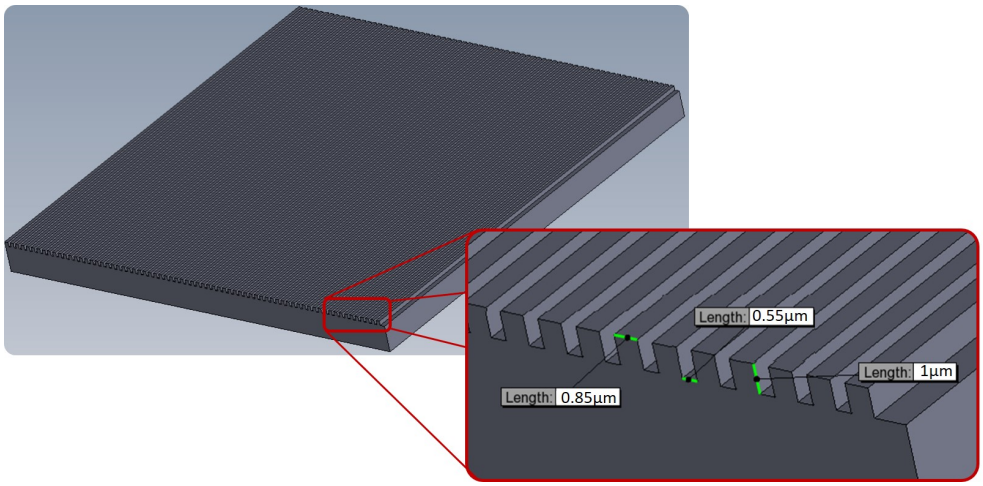



Figure 2.9: CAD file created in eDrawings showing a ridge width of 850 nm, a gap width of 550 nm (giving a ridge to gap ratio of 1.5) and a depth of 1000 nm

The STL file was converted into a GWL file for printing. A 63x (Oil/DiLL) objective was used with the dip-in laser lithography configuration as shown in Figure 2.10. 2-3 drops of the IP-DIP was placed on the centre of the glass substrate. The system was calibrated prior to printing. Once printing had been completed, the patterned IP-DIP were placed in propylene glycol monomethyl ether acetate (PGMEA) for 30 mins to remove any unpolymerized resist from the substrate. It was then immediately transferred into excess Novec engineering fluid and left for 2 mins to remove any residue left behind by the resist. An IP-DIP control (5 $mm^2$ surface area) was also created in this way, however there was no pattern on the photoresist. All IP-DIP surfaces were made by D. Kinahan, Dublin City University.

Collagen alignment measurements on patterned IP-DIP followed that of Section 2.1.11 and Section 5.2.2, with a gold sputtercoating of 20 mA for 10 s. Alignment of collagen on

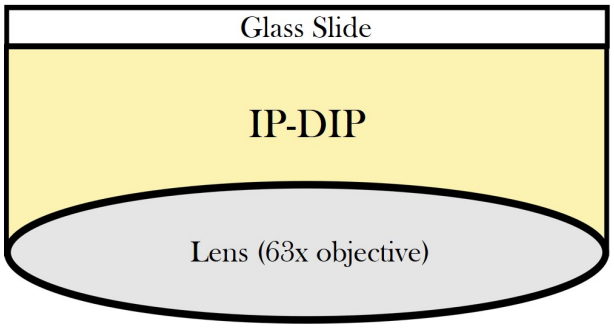



Figure 2.10: Schematic showing the dip-in laser lithography configuration used to created photolithography patterned surfaces in an IP-DIP photoresist.

non-patterned IP-DIP was measured by depositing 3 biological repeats of 1 mg $mL^{-1}$ collagen onto 3 separate areas of the non-patterned surface. It was again gold sputtercoated for 20 mA for 10 s, and imaged and analysed as stated before. Images were automatically edited for brightness and contrast using ImageJ.

## 2.2 Biological Methodology

### 2.2.1 MC3T3 Cell Culture

MC3T3-E1 (passage 23) osteoblast precursor cells were cultured in $\alpha$-minimum essential medium ($\alpha$-MEM) (Sigma-Aldrich, UK) supplemented with 1% penicillin-streptomycin (Sigma-Aldrich, UK), 4% L-glutamine (Sigma-Aldrich, UK) and 10% fetal bovine serum (Sigma-Aldrich, UK). Cells were maintained in a humidified incubator at 37 ℃ and 5% $CO_2$.

### 2.2.2 TrypanBlue Assay

Collagen type I was gelled within a 12-well plate following the method stated in Section 2.1.1. MC3T3 cell suspensions were seeded onto the gels at a concentration of 100,000 cells $mL^{-1}$. Samples were cultured for 3 days within a humidified incubator. In order to detach cells from the collagen hydrogel, 0.1% collagenase was added to each sample followed by incubation for an hour. To count cells, 100 $\mu$L of media was added

to 100 $\mu$L of TrypanBlue, to produce a diluting factor of 2, and both live and dead cells counted using a haemocytometer.

### 2.2.3 alamarBlue Assay

Collagen type I was gelled within a 12-well plate following the method stated in Section 2.1.1. MC3T3 cell suspensions were seeded onto the surface of the gels at a concentration of 200,000 cells mL$^{-1}$. After culturing for 3 days, culture medium was aspirated and 300 $\mu$L of alamarBlue stock was added to each sample. alamarBlue stock was made using fresh media and 10% alamarBlue dye (Thermo Fisher Scientific, UK). The samples were incubated at 37 ℃ for 4 h before 100 $\mu$L of the medium was removed and placed within a 96-well plate. This was read at an absorption of 570 nm using a Synergy HT plate reader (Biotek, UK).

### 2.2.4 Confocal Fluorescent Imaging of MC3T3 cells

Collagen type I gels were gelled within a 12-well uncoated 10 mm glass diameter MatTek dish at a concentration of 1 mg mL$^{-1}$ following the method stated in Section 2.1.1. MC3T3 cell suspensions were seeded at a density of 200,000 cells mL$^{-1}$ either onto the gel surface or the well base. All cells were cultured in $\alpha$-MEM (culture medium). After culturing within a humidified incubator at 37 ℃ and 5% $CO_2$, culture medium was aspirated and samples were washed with 400 $\mu$L of PBS. 2.5 $\mu$L mL$^{-1}$ of calcein AM (Thermo Fisher Scientific, UK) and 5 $\mu$L mL$^{-1}$ propidium iodide (Thermo Fisher Scientific, UK) were prepared in PBS to use as dye stock. 300 $\mu$L of dye stock was added to each well and incubated for 30 minutes. Images were taken on a FV10-ASW confocal microscope with a 10x lens with image dimensions of 800 x 800 pixels. Images were processed in ImageJ [207].

### 2.2.5 Extraction and Culture of Primary Human Corneal Fibroblasts

Corneal transplantation tissue, surplus to surgical requirement, was used to culture primary human corneal fibroblasts. Tissue was obtained under the ethics of *Ocular Microenvironment in Health and Disease* (LREC 06/Q2702/44). Experiments were conducted in accordance with the Declaration of Helsinki. Corneal stromal tissue was isolated by debridement of the endothelial and epithelial layers using an aseptic technique. The superficial lamella of the stroma was then debrided further. Stromal tissue from the corneoscleral rim was then removed, dissected into segments, and placed in a 6-well plate (Corning, USA) within complete media and stored in an incubator at 37 ℃ and 5% $CO_2$. Fibroblasts from the tissue were cultured until approximately a third of the well surface was populated (visually determined) prior to their first passage. Cell media was replaced every 2 – 3 days and comprised of RPMI-1640 medium (Sigma, UK) with 1% L-glutamine (Sigma-Aldrich, UK), 10% Fetal Bovine Serum (Sigma-Aldrich, UK) and 1 % penicillin-streptomycin (Sigma-Aldrich, UK).

When fibroblasts reached 90% confluency routine passage was performed. This was conducted by washing the cells three times with PBS solution, followed by the application of 1x Trypsin-EDTA for a maximum of 5 mins. The cell solution and Trypsin-EDTA were neutralised by adding an equal volume of media. To obtain a cell pellet the solution was centrifuged at 1500 rpm for 7 mins. Supernatant was aspirated and discarded, and the cell pellet resuspended in media. As experiments required a specific number of cells, a haemocytometer was used to count cells within the resuspended fresh media and distributed accordingly. Cellular extraction and culture was conducted by G. Butt, University of Birmingham.

### 2.2.6 Sample Preparation and Confocal Fluorescent Imaging of Corneal Fibroblasts on Patterned IP-DIP

Collagen, created using deionised water as a buffer, at a concentration of 1 mg $mL^{-1}$ was deposited onto the IP-DIP surface and left for 10 mins. Excess was removed with lint-free paper and left in a dehumidified incubator at 37 ℃ for 24 hrs. The collagen was then washed three times with deionised water to remove any salt crystals. Samples of patterned IP-DIP with and without collagen (in triplicates) were sterilised with ethanol and washed in Dulbecco's Phosphate Buffered Saline (DPBS, Sigma, UK). Samples were placed into a 6-well plate (Corning, USA) and structures were encapsulated within a 70 $\mu$L culture-insert well (ibidi GmbH, DE) into which 3,750 cells were seeded onto the surfaces. Total volume of cells and media was 50 $\mu$L. The cellular samples were incubated for 48 hrs within a humidified incubator at 37 ℃ and 5% $CO_2$. Cells were then fixed with Triton X-100 (Sigma, UK) and washed three times with DPBS for 10 mins. Cells were stained with Phalloidin-594 at a concentration of 25 $\mu$L $mL^{-1}$ (Cambridge Bioscience, UK) and DAPI at a concentration of 3.33 $\mu$L $mL^{-1}$ (Sigma, UK) and left at room temperature for 30 mins. Confocal images were taken on a FV10-ASW confocal microscope with a 40x lens with image dimensions of 800 x 800 pixels. Images were processed in ImageJ [207]. Cellular experiments were conducted by G. Butt, University of Birmingham.

## 2.3 General Statistics

### 2.3.1 Determining Sample Size

Power calculations were conducted to determine the sample size required for a 95% confidence interval. The sample size was calculated by using the equation below:

$$n = \frac{2(Z_\alpha + Z_{1-\beta})^2(\sigma)^2}{\Delta^2} \tag{2.23}$$

where $n$ is the required sample size, $Z_\alpha$ is a constant according to the accepted error,

$Z_{1-\beta}$ is a constant set by the power of the study, $\sigma$ is the standard deviation and $\Delta$ is the difference in means [234].

Using the above equation, a minimum sample size of 63.037 is required for fibril characteristic measurements, such as fibril diameter, fibril D-spacing and fibril alignment. Therefore, a total of 75 measurements, calculated from 25 fibrils over 3 biological repeats, were sufficient for calculating significant differences between sample sets.

Contact angle measurements of N=30, and biological repeats of N=3 were more than sufficient for calculating significant differences between sample sets. All data was found to be normally distributed, as determined via Minitab® statistical software (2019).

### 2.3.2 T-Test

A t-test is a statistic used to test the differences between the means of two independent, normally distributed groups. The null hypothesis of a t-test assumes that there is no difference between the means of two groups, with an alternative hypothesis assuming that one mean is greater than the other. By using the difference of two means and their variance, a t-test statistic can be generated [235, 236].

T-test assumptions require that the variance of both groups are equal, the data is normally distributed, and the data used is randomly selected. These assumptions must be upheld in order for a t-test to provide a meaningful statistic [235, 236]. As all data was normally distributed, this test was used to determine the significant difference between a sample mean and the control mean.

### 2.3.3 One-Way ANOVA

A one-way ANOVA is a statistic used to test the differences between the means of two or more independently, normally distributed groups. The null hypothesis of a one-way ANOVA assumes that the means across all the groups are equal. The alternative hypothesis assumes that there is a difference in mean values.

The one-way ANOVA statistic follows a set of assumptions. These are that the data is

normally distributed, the variance across all the groups are equal, and that the errors are independent of one another. These assumptions must be upheld to ensure that a one-way ANOVA provides a meaningful statistic [237, 238]. As all data was normally distributed, this test was used to determine the significant difference across a range of sample means.

# CHAPTER 3

# INFLUENCE OF COBALT IONS ON COLLAGEN MATRIX FORMATION

Data in this chapter was also presented in the published paper *Influence of Cobalt Ions on Collagen Gel Formation and Their Interaction with Osteoblasts*[ii]

Metal on metal implants, utilizing materials such as cobalt - chromium - molybdenum alloy, have long been used as arthroplasties due to their robustness and low dislocation rate. Debris and corrosion from these implants, however, has been found to cause inflammatory responses leading to unexpectedly high failure rates. Safety assessments of these materials traditionally relies on the use of simple two-dimensional assays, where cells are grown on the surface of the material over a relatively short period of time. It is now well known that the composition and stiffness of the extracellular matrix (ECM) has a critical effect on cell function. In this chapter the way in which cobalt ions influence the assembly of type I collagen, a key constituent of the ECM, has been evaluated. It was found that cobalt had a significant effect on the collagen matrix formation, resulting in local variations in collagen characteristics. An increase in heterogeneity caused a decrease in the bulk stiffness of the material. Moreover, when the collagen matrices contained cobalt ions, there was a significant change in cell interaction with the collagen matrix. Fluorescence images and biological assays showed a decrease in cell proliferation and viability with an increase in cobalt concentration. This chapter presents evidence that the cobalt ion complex interacts with the hydroxyl group present in the carboxylic terminal of the collagen fibril, preventing crucial stabilising bonds within collagen formation. This demonstrates that currently accepted toxicity assays are poor predictors of the longer-term biological performance of a material.

[ii] 10.1021/acsomega.8b01048

## 3.1 Introduction

Cobalt-chromium-molybdenum (CoCrMo) alloys have a high level of robustness and low risk of dislocation, which is why the material is commonly used for metal-on-metal (MOM) arthroplasties and implant resurfacing [239–241]. CoCrMo implants have a Young's Modulus of 230 GPa, higher than that of titanium (105 GPa) [242], resulting in its wide use as a cement type femoral stem material for implants [243]. CoCrMo implants also have comparible tensile strength (430 - 1028 MPa) and yeild strength (200 - 823 MPa) to that of titanium (1000 MPa and 910 MPa respectively) [242].

Although MOM implants have lower wear rates than metal-on-polyethylene implants, there is a 500-fold increase in small particle generation [244–246]. These small metallic particles cause inflammatory responses which can lead to unexpected implant loosening and bone resorption [247–250]. In addition to this, tribocorrosion of the implant introduces cobalt ions into the surrounding tissue as shown in Figure 3.1 [251, 252].

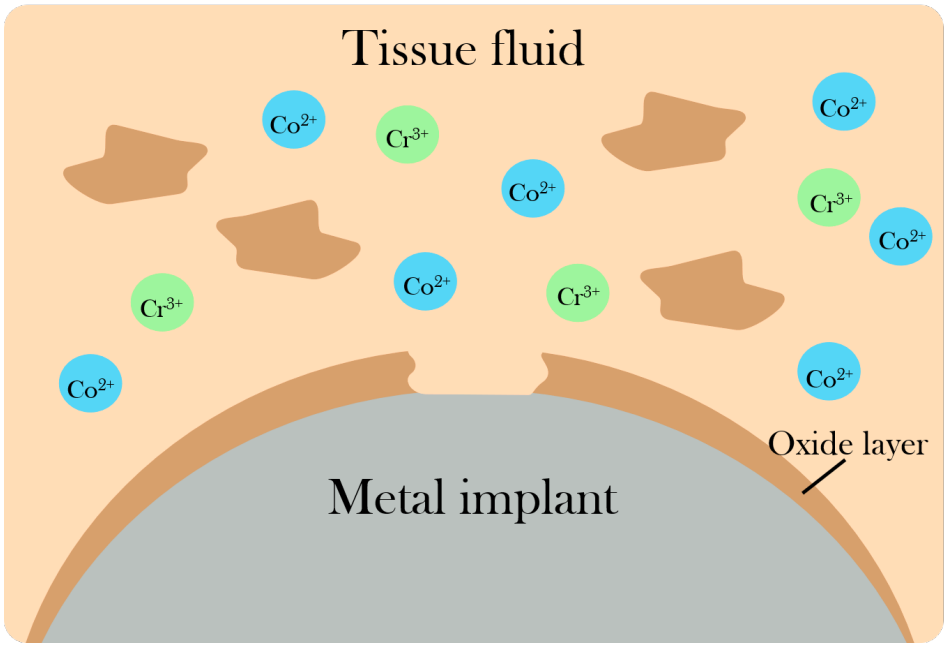



Figure 3.1: Mechanical abrasion of the protective oxide layer of a MOM implant introduces the underlying metal to the surrounding tissue fluid. This causes cobalt and chromium ions to be released into the surrounding tissue causing inflammation which may lead to unexpected implant failure. $Co^{2+}$ refers to cobalt ions produced and $Cr^{3+}$ refers to the chromium ions produced from electrochemical corrosion.

Tribocorrosion is a corrosion which occurs at the surfaces of articulating components of MOM implants. It is a consequence of both mechanical and electrochemical processes [252]. MOM implant surfaces are protected from electrochemical corrosion due to the presence of a passive surface oxide layer. CoCrMo alloys have a protective oxide layer that is 1 - 4 nm thick, formed by oxidation of both chromium and cobalt at the interface. Load bearing arthroplasties undergo repetitive mechanical movement which can disrupt the thin oxide layer through abrasion. This results in exposure of the underlying metal, leading to dissolution (an anodic reaction) and the formation of metal cations. The exposure of unoxidised metal causes a passive reaction producing an electron flow from the corrosion site to the metal surface (here acting as a cathode). Hydrolysis of any released metallic ions causes a local acidification which results in a migratory contribution to the mass transport of the ions away from the original source [253, 254]. In the case of CoCrMo alloys the free ions correlate to cobalt and chromium. These ions will remain in solution or precipitate within the surrounding extracellular tissue space alongside any wear debris. As cobalt is more soluble than chromium it is more likely to stay in ionic form and interact with both the surrounding tissue fluid and the extracellular matrix [252].

Most investigations regarding the effect of cobalt ions on surrounding tissue have predominately focused on two-dimensional cell cultures, with emphasis on direct interaction between macrophages and cobalt debris [255–257]. For example, cobalt ions have been found to interact with both nuclear proteins and DNA, causing cellular death [258]. Cobalt has an ionic radius of 0.74 Å [259], and consequently is able to cross the cytoplasmic membrane, accumulating in the cell nucleus and surrounding structures [258, 260, 261]. Studies have also shown that the addition of cobalt ions into cell media causes a decrease in proliferation of osteoblasts and a decrease in differentiation of mesenchymal stem cells to osteoblasts [262–265]. Although the direct influence between cobalt ions and various cell lines is well established, there has not been an investigation into how these ions influence the ECM or any ECM interactions. As the ECM drives cell interactions, any small changes in the three-dimensional ECM from cobalt ions will change the cellular response,

therefore two-dimensional investigations are not sufficient to understand the full process [266].

As stated in Section 1.1.1, the ECM is comprised mostly of collagen type I, a hierarchical protein which provides not only structural support to cells and surrounding tissue, but also influences the differentiation of surrounding cells [5, 7, 266–269]. As cobalt ions have a low ionic radius, they can interact with collagen fibres at much earlier stages of formation. This can hinder the formation process of collagen and potentially alter both the chemical and mechanical properties of the matrix. These changes will drastically affect cellular attachment and thereby tissue function.

This chapter investigates the influence of cobalt (II) ions on collagen matrix formation and cell interactions. This highlights the importance of how low ionic concentrations can have crucial implications on collagen matrix formation. A maximum cobalt concentration of 200 ppm was used as it is the highest recorded cobalt concentration found at an injury site [270]. Osteoblast cells were used to understand the cellular effects of any matrix formation changes without the influence of an inflammatory environment.

## 3.2 Methodology

### 3.2.1 Cobalt Doped Collagen Hydrogels (CoCol gels)

Cultrex rat tail collagen at a concentration of 3 mg $mL^{-1}$ was diluted down to the desired concentrations using either Dulbecco's Modified Eagles Medium (DMEM) (Sigma-Aldrich, UK) or cobalt infused DMEM as buffer. Cobalt infused DMEM was made using a cobalt (II) chloride (Sigma-Aldrich, UK) stock. This stock was made to a concentration of 72.67 mg $mL^{-1}$ using distilled water. Samples were made to a cobalt concentration of 0, 67, 133 or 200 ppm and neutralised with 1 M NaOH (Sigma-Aldrich, UK) at a concentration of 8 $\mu$L $mL^{-1}$ per sample. Samples were incubated for 3 hours to ensure gelation had occurred. These four concentrations were used throughout all cobalt doped collagen gel analysis.

### 3.2.2 X-Ray Fluorescence (XRF)

A 4.9 mL sample of 200 ppm CoCol gel was analysed *via* XRF. Scan areas were imaged for three cycles to improve the resolution. Analysis of the completed scan involved segmenting ten object regions with both high and low intensity profiles over the entirety of the image (five sections per intensity). Each object produced a spectrum which gave the intensity of cobalt present within that area. This intensity correlated to relative cobalt concentration. Differences between the height of the intensity peaks between high and low concentration regions were measured and averaged, giving an indication of relative concentration increase of cobalt ions throughout the bulk of the hydrogel. All other parameters followed that stated in Section 2.1.3.

### 3.2.3 Rheological Analysis

Samples of CoCol gels were measured under oscillatory rheology. The lowest value from strain sweeps was found to be 0.01, obtained from samples doped with 200 ppm of cobalt. Frequency sweeps were therefore performed at a strain of 0.01. All other parameters followed that stated in Section 2.1.4.

### 3.2.4 Molecular Mechanics

Data obtained from CoCol gels at 0 ppm and 200 ppm cobalt concentrations were used to determine molecular mechanics. Samples weighing 46 $\mu$g were analysed using differential scanning calorimetry (DSC) to determine energy loss changes. Two 1 mL CoCol samples (0 ppm and 200 ppm) were measured *via* Raman using a 60x water immersion lens to analyse the atomic bonds present. Principle component analysis was performed on this data set, which comprised of 60 spectra in total, 30 from each sample concentration to further analyse the Raman data. All samples were prepared using PBS buffer instead of DMEM to prevent any additional background signals. All other parameters followed that stated in Sections 2.1.5, 2.1.6, and 2.1.7.

### 3.2.5 Confocal Fluorescent Imaging

MC3T3 cells were seeded at a density of 200,000 cells $mL^{-1}$ onto the CoCol gel surface and cultured. Those seeded onto the base of the wells were cultured in culture medium doped with 67 ppm, 133 ppm and 200 ppm cobalt. Culturing methods and fluorescent staining information can be found in Section 2.2.4

## 3.3 Results

### 3.3.1 Cobalt Influence on Local Collagen Structure

Atomic force microscopy (AFM) was used to image and analyse the microsctructure of collagen when introduced to increasing concentrations of cobalt. The changes to matrix formation can be visualised in Figure 3.2A. These images indicate that there is an increase in heterogeneity of the matrix with the increasing addition of cobalt ions. Visually, adding a cobalt concentration of 200 ppm causes regions of agglomerated, dense collagen fibrils to emerge in comparison to 0 ppm; with 67 and 133 ppm causing less of a visual change. The agglomeration was quantified by measuring the fibril density per 2.1 $\mu m^2$, an area comprised from a grid covering each technical repeat, as shown in Figure 3.2B. When cobalt ions are added to the collagen matrix, there is a significant increase in collagen fibril density eluding to an increase in heterogeneity. There is also a decrease in low fibril number in comparison to 0 ppm further emphasising this change, indicative that cobalt ions alter the localised matrix structure. There was a significant increase in the length of the D-spacing of collagen fibrils with the addition of cobalt ions at 133 ppm and above, as shown by Figure 3.2C. As the length of the D-spacing on a fibril is determined by the end spacing between the fibril's molecules (see Figure 1.2), this increase indicates that cobalt is interacting at an early stage of collagen fibril formation. Therefore, this implies that the cobalt is interacting with the collagen in a position which interrupts parallel staggered alignment at higher concentrations. A concentration of 67 ppm is not sufficient to have

an effect on D-spacing showing that a certain concentration must be upheld to cause significant fibril formation changes. In comparison, any addition of cobalt ions causes a significant decrease in collagen fibril diameter, as shown in Figure 3.2D. This indicates that cobalt-collagen interaction is preventing crucial interactions between collagen molecules, reducing fibril thickness.

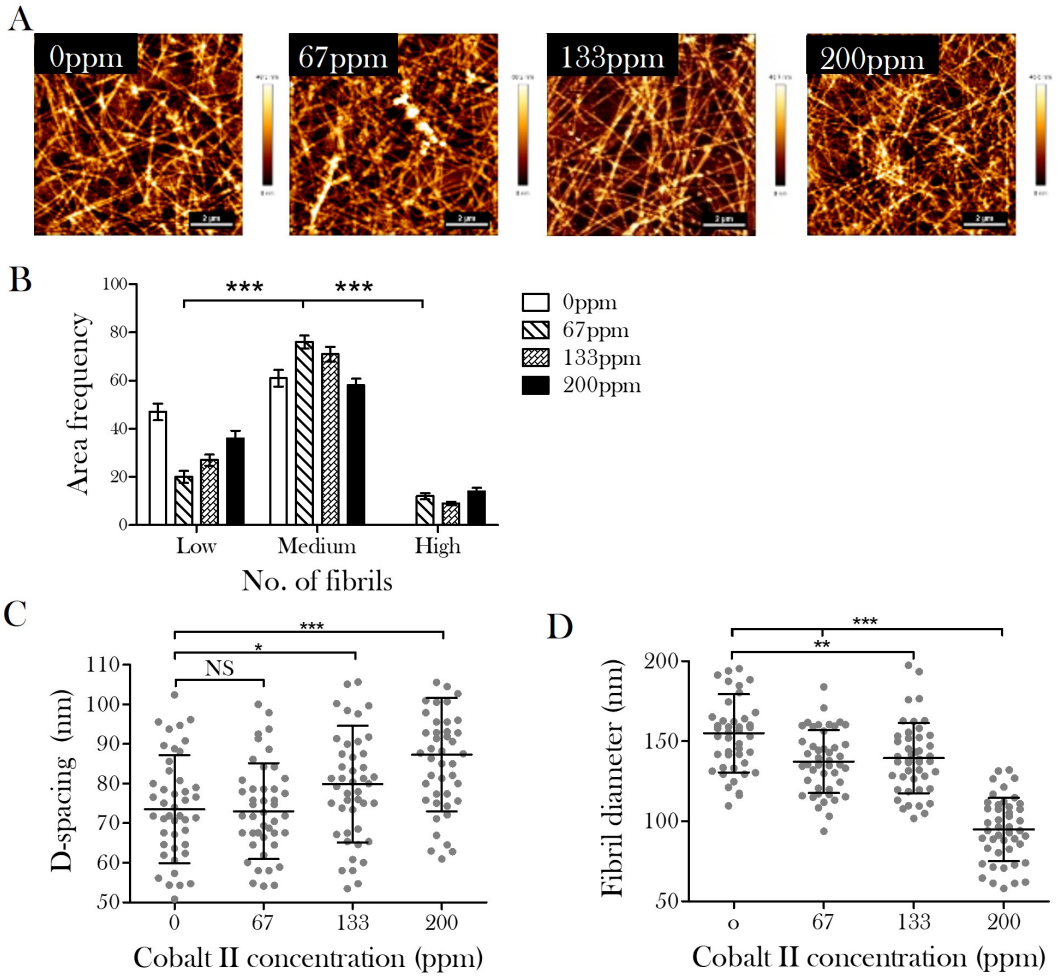



Figure 3.2: (A) AFM height images of CoCol gels at concentrations 0, 67, 133 and 200 ppm over a 10 x 10 $\mu m^2$ area. (B) Fibril density calculated through measuring the number of fibrils per 2.1 $\mu m^2$. Fibrils were separated into three categories, low (4-6 fibrils), medium (7-10 fibrils) and high (11-13 fibrils) with fibril number tallied to obtain area frequency. Length of D-spacing (C) and fibril diameter (D) of collagen at each cobalt concentration, measured from 30 randomly selected fibrils over three AFM repeats. NS refers to a non-significant result * refers to a P-value $\leq 0.05$, ** refers to a P-value $\leq 0.01$ and *** refers to a P-value $\leq 0.001$. N = 75 across 3 biological samples, error bars refer to $\pm$ standard deviation. Scale bar is 2 $\mu$m in length.

.

### 3.3.2 Bulk Collagen Matrix Effects from Cobalt Ions

When adding cobalt ions to a collagen matrix there is a visible reduction in the structural integrity of the hydrogel as shown in Figure 3.3. CoCol gels with increasing cobalt concentration have a bulk reduction in gel stability and produce an excess of water when physically disturbed. In addition to this, less force is required to break the CoCol gel with an increase in cobalt causing the gel to break into increasingly smaller pieces when the gel is handled or manipulated. This further indicates that cobalt ions perturbed the overall structure of matrix formation.

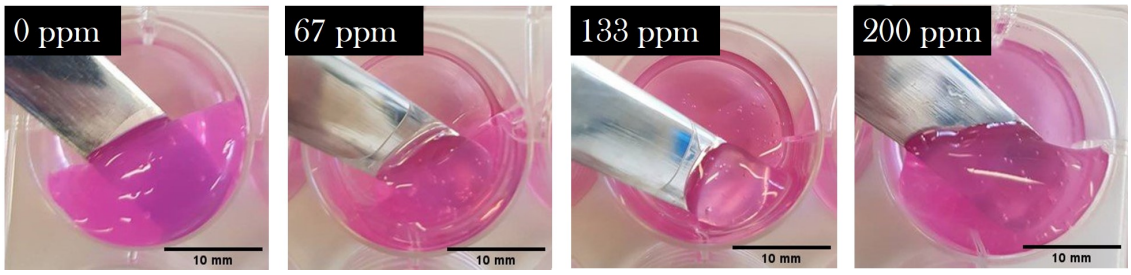



Figure 3.3: Visual depiction of the reduction in structural integrity when increasing the concentration of cobalt ions in a collagen hydrogel. Scale bar is 10 mm.

To investigate the cause of the high and low collagen fibril density regions found in the microstructre, the dispersion of cobalt ions throughout the bulk of the matrix was measured. XRF revealed that there were regions of localised high concentrations of cobalt ions, instead of a homogeneous dispersion throughout the hydrogel, as depicted in Figure 3.4A. Confirmation of cobalt intensity is shown in Figure 3.4B with the highlighted peak indicating cobalt. High and low relative intensities were measured by drawing regions of interest and analysing the spectra produced, an example is given by Figure 3.4C. By averaging the difference between cobalt peak intensities at relative high and low cobalt concentrations, there was found to be a three-fold increase in concentration at high intensity areas, as shown in Figure 3.4D;E. High intensity areas had an average count of 10 whereas low intensity areas had an average count of 3. This suggests that the increase in heterogeneity of collagen fibrils may be due to the uneven distribution of cobalt ions throughout the bulk of the matrix.

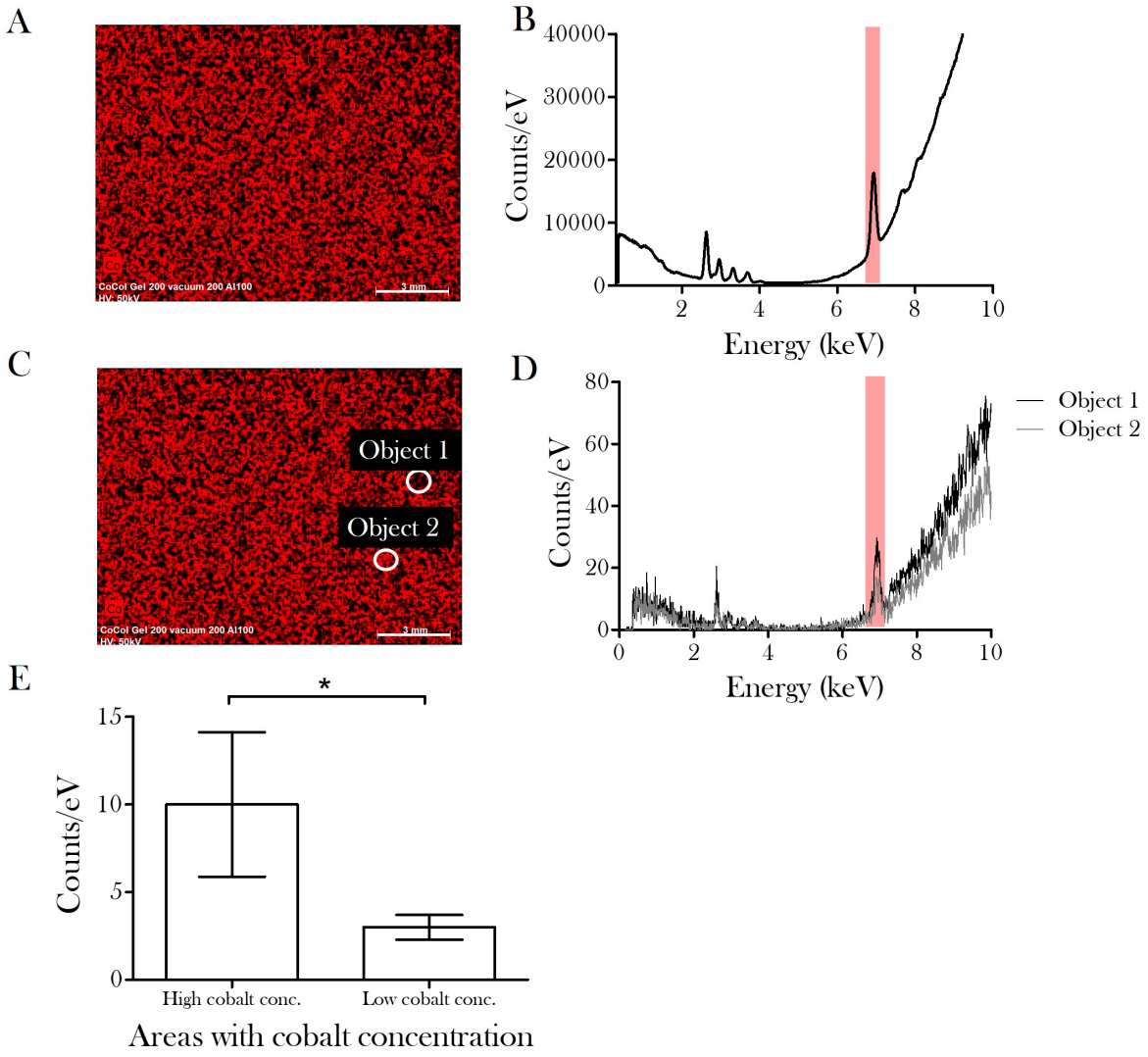



Figure 3.4: XRF fluorescent measurements depicting the dispersion of cobalt throughout the bulk of a 200 ppm CoCol gel. (A) Scan depicting relative cobalt dispersion throughout the entire area, (B) spectrum indicating cobalt is being measured (highlighted peak). (C) A scan depicting an example of two objects showing relative high and low cobalt intensity. (D) An example of spectra of both object 1 and object 2 used within average concentration increase measurements. Here object 1 and 2 are the spectra of object 1 and 2 in part (C). (E) Average counts from five areas with high cobalt concentration and five areas with low cobalt concentration, * indicates a P value $\leq 0.05$. N = 5, error bars refer to $\pm$ standard deviation. Scale bar is 3 mm in length.

Oscillatory rheology measurements determined the effect of cobalt ions on the bulk mechanical properties of the collagen matrix. Overall there was a significant reduction in both the storage (G') and loss (G") moduli (Figure 3.5A,B) with the addition of even low concentrations of cobalt. This indicates that cobalt ions reduce the stiffness of the hydrogel. The cause of this reduction may be due to the areas of low collagen fibril density,

caused by cobalt-collagen interactions, as they are structurally weaker regions. The change in weight of cobalt-collagen hydrogels over 5 hrs was measured to further investigate the bulk effects of adding cobalt to collagen. There was found to be a correlation between a decrease in weight and an increase in cobalt concentration. This indicates that there is a higher level of water loss with the introduction of cobalt (Figure 3.5C). This shows that cobalt ions are influencing the structure of the matrix causing a reduction in the amount of water bound to the matrix.

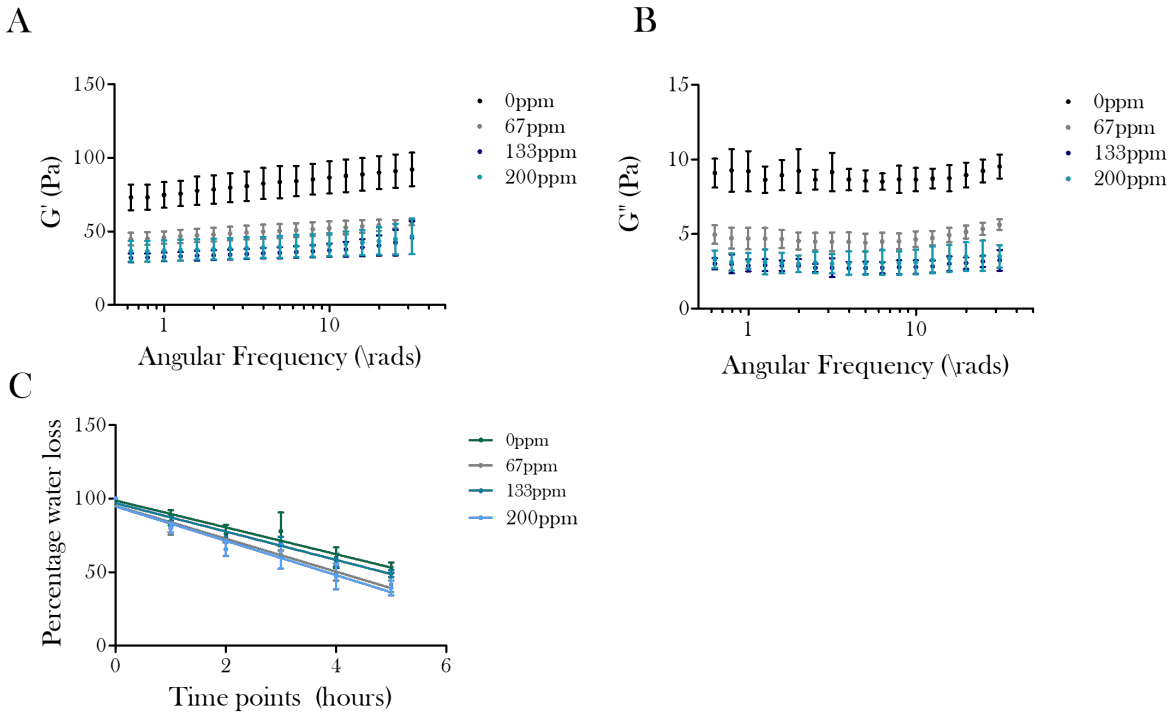



Figure 3.5: (A) G' and (B) G" from a frequency sweep of CoCol gels at increasing cobalt concentration ranging from 0.01 - 10 Hz. Sweep was taken with a strain of 0.01 determined from a strain sweep of 200 ppm CoCol gel sample. (C) Percentage weight decrease over five hours of collagen hydrogels doped with varying concentrations of cobalt. N = 3, error bars refer to ± standard deviation.

### 3.3.3 Cellular Response due to CoCol Gel Structure

As the underlying structure of a collagen matrix determines the growth and proliferation of cells, various biological experiments were undertaken to determine how the changes in formation, induced by cobalt, effect cellular growth. Cells maintained a relatively high viability when seeded onto CoCol gels up to a cobalt concentration of 133 ppm, as shown by confocal fluorescent images in Figure 3.6A. There is also a slight change in morphology with the presence of cobalt. In comparison, cells exposed to cobalt infused culture medium only maintained high viability up to a concentration of 67 ppm, shown in Figure 3.6B. This confirms that the underlying structure is determining cellular growth, due to a lack of direct cobalt-cell interaction. Therefore, all cellular responses shown in Figure 3.6A are due to the underlying matrix structure and not direct cell - cobalt interaction caused *via* leeching.

Quantification of the viability of cells, through a TrypanBlue assay (Figure 3.6C), also confirmed that there was a correlation between cell death and cobalt concentration with a significant decrease in the number of live cells with 133 ppm cobalt concentration. An alamarBlue assay indicated that there was a significant decrease in cell metabolism with the addition of cobalt ions even at low concentrations, as indicated by Figure 3.6D. This implies that cobalt decreases cell proliferation as proliferation correlates to metabolism. There was a larger decrease in metabolism when cells were cultured in cobalt infused media, which further confirms that any cell response from cells cultured onto collagen gels is not due to cobalt ion - cell interaction directly. Overall the underlying CoCol matrix structure is directly influencing how the cells attach and therefore proliferate, causing a reduction in viability that correlates with cobalt concentration.

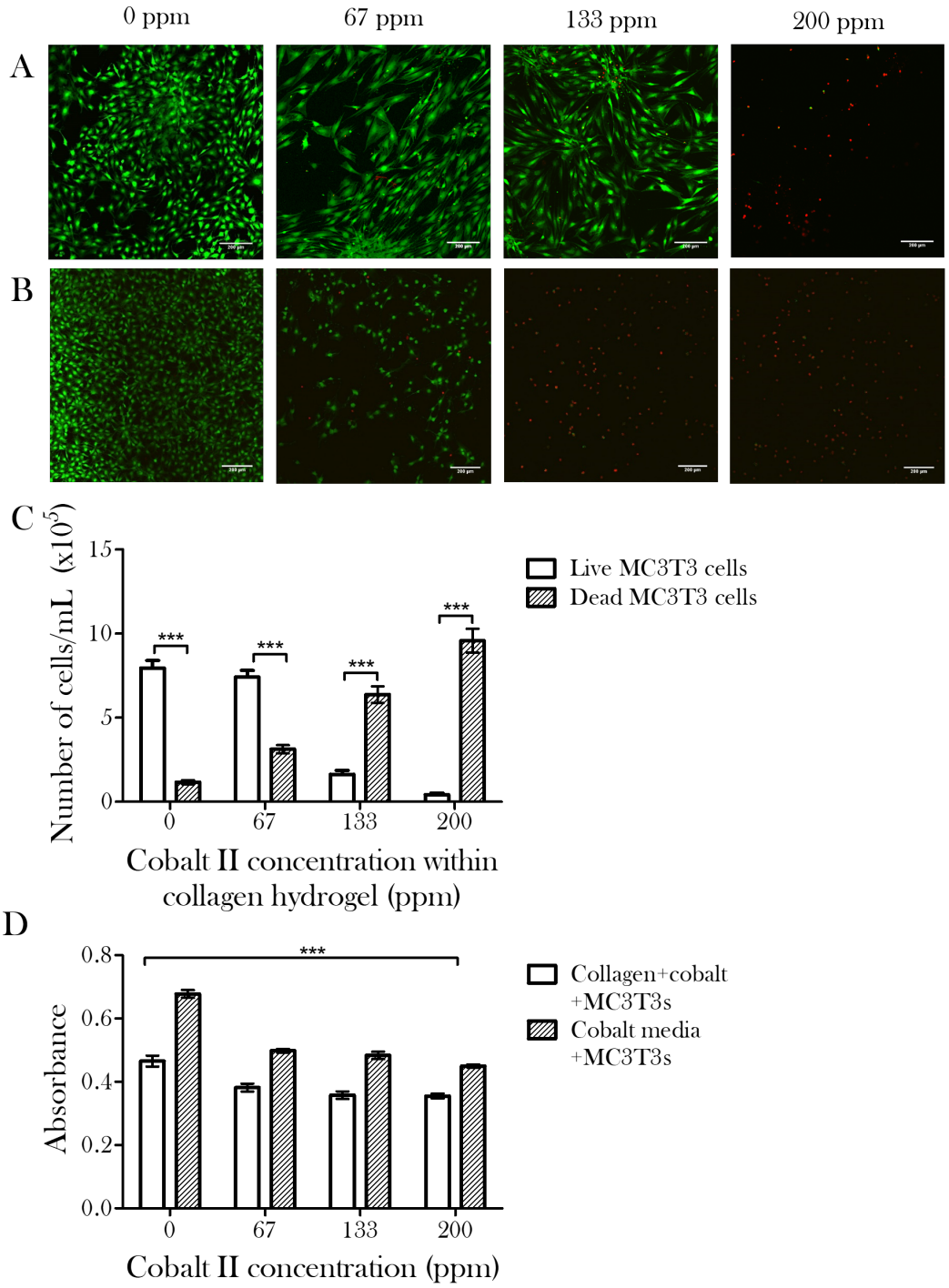



Figure 3.6: Confocal fluorescent images of MC3T3s stained with calcein AM and propidium iodide seeded onto both the surface of CoCol gels (A) and grown within cobalt infused media (B). Green cells indicate live cells, red indicate dead cells. (C) TrypanBlue assay quantifying both live and dead cells seeded onto CoCol gels. (D) alamarBlue assay of MC3T3 cells cultured on CoCol gels and in cobalt infused media. *** referes to a P value $\leq 0.001$. N = 3, error bars refer to $\pm$ standard deviation. Scale bar is 200 $\mu$m.

### 3.3.4 Cobalt-Collagen Molecular Mechanics

To experimentally determine the interaction site of cobalt ions to collagen, DSC and Raman spectroscopy measurements of both 0 ppm and 200 ppm CoCol samples were undertaken. Differential scanning calorimetry (DSC) results show that excess water within the bulk of the collagen matrix is not bound as strongly with the presence of cobalt. All water bound within the 200 ppm sample was removed at a temperature of 120.3 ℃, 5 ℃ lower than that of 0 ppm. In addition, the energy required to remove the bulk water within the 200 ppm sample is 14% lower than that of the 0 ppm sample, as shown in Figure 3.7A. This highly suggests that the cobalt is preventing any interaction with an important collagen hydration binding site, stopping water molecules from being tightly bound to the collagen fibrils.

Characteristic protein peaks were shown on the Raman spectra, such as the secondary amide peak at 1205-1207 $cm^{-1}$ and the C=O peak at 1606-1607 $cm^{-1}$ [271], as shown in Figure 3.7B. However, any differences between the two samples were subtle. To further analyse the spectra, PCA was performed on the dataset after cosmic ray removal. Most of the data was described by the first two principal components. The scores plot for all spectra is shown in Figure 3.7C, within which two clusters separating the 0 ppm sample and 200 ppm sample can be seen. The wavenumber of relative differences between each sample was obtained by plotting the loadings vectors with respect to wavenumber. The plot of the first loading indicates the largest variance within the dataset, indicated by a large intensity peak, shown in Figure 3.7D. From this plot, the largest variation between the samples occurred at 869 $cm^{-1}$ and 1000 $cm^{-1}$. These wavenumbers correspond to a C-O bond within the secondary alcohol [271], with the atomic vibration being suppressed within the 200 ppm sample.

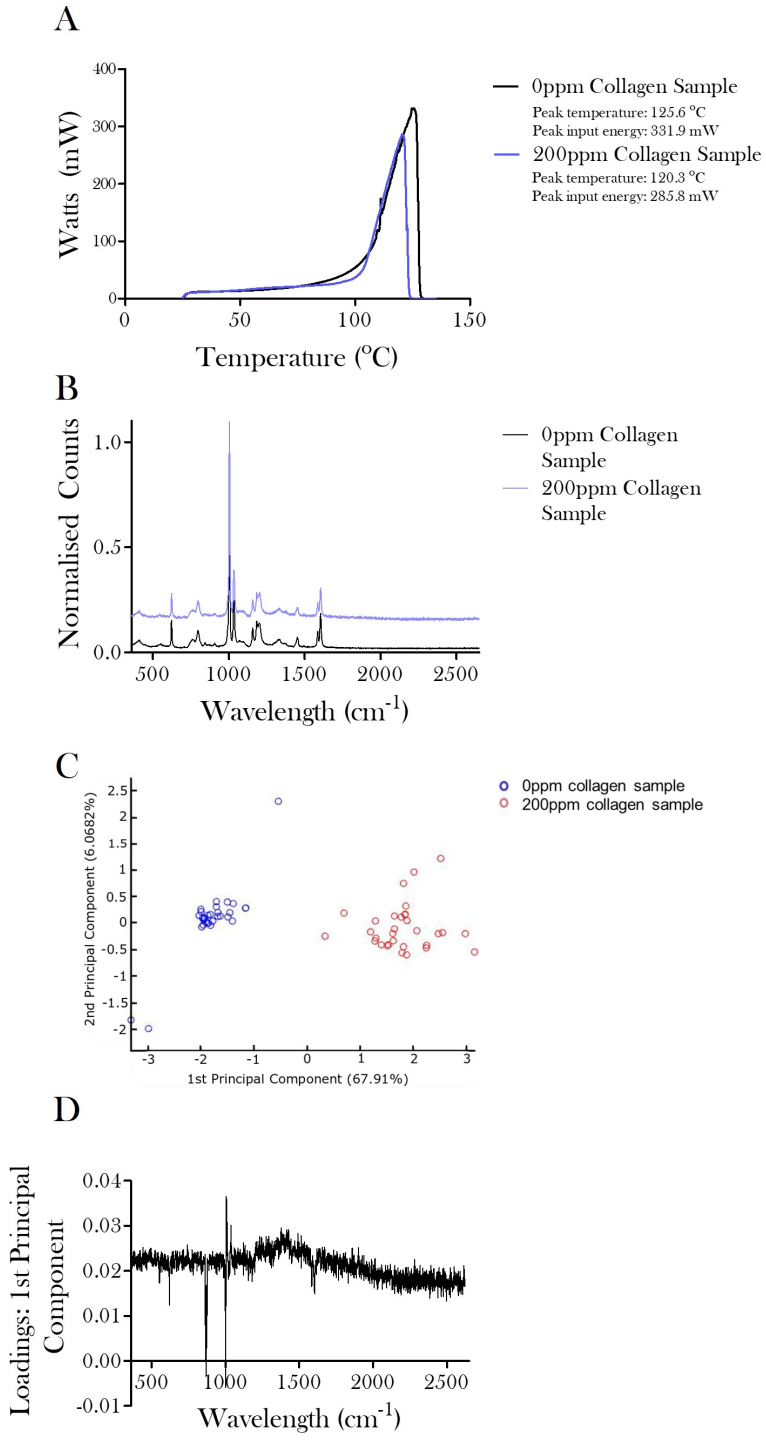



Figure 3.7: (A) DSC measurements between a 0 ppm and 200 ppm sample indicating a reduction in energy required to remove bulk water. (B) Raman spectroscopy using an immersion lens of both 0 ppm and 200 ppm CoCol gels, (C) scores plot of the first two principal components determined via PCA, (D) loadings plot of the first principal component indicating the largest change in variance at 869 $cm^{-1}$ and 1000 $cm^{-1}$. For DSC N = 3, for Raman and PCA N = 30.

## 3.4 Discussion

Collagen structure and its interaction with cells is highly influenced by the presence of cobalt ions. Nanoscale changes, indicated through AFM imaging, highlight how the presence of cobalt ions increase the heterogeneity of the collagen matrix, especially when comparing images of collagen hydrogels with 0 ppm and 200 ppm cobalt concentration. A density histogram indicated the increase in number of fibrils per unit area with cobalt addition. These areas seem to suggest that cobalt ions cause agglomeration of fibrils within the collagen matrix. This contributes to the increase in heterogeneity. Measurements of D-spacing indicate that there is an increase in spacing between collagen molecules with increasing cobalt concentration. This increase in D-spacing, as measured from AFM images, suggests that the cobalt ions interact at an early stage of the hierarchical formation process, affecting the parallel quasi-staggered arrangement of tropocollagen. However, 67 ppm was not a high enough concentration to produce a significant difference in D-spacing with respect to control, showing that there is a lower threshold on the concentration required to cause changes in D-spacing length. This may indicate why unexpected failures of this nature occur in patients years after the initial MOM implant, as cobalt concentrations need to accumulate above a threshold concentration. These changes within the fibril formation appear to disrupt crucial interaction points between collagen molecules from aligning. This in turn causes the fibril diameter to decrease with increasing cobalt concentration. Comparatively, 67 ppm is a high enough concentration to affect fibril diameter implying that cobalt interacts not only at fibril formation but at other points in the hierarchical formation.

Visual changes of the collagen hydrogel with increasing cobalt concentration indicate that cobalt ions are not only effecting the localised structure but also bulk structure. There was a visual reduction in structural integrity of the CoCol gels, with increasingly less force required to break the gel with increasing cobalt concentration. There was also an increase in excess water produced with increasing cobalt concentration, reducing the gel's ability to store water. To determine whether the change in both bulk and local collagen structure

was due to bulk cobalt distribution, XRF analysis of a 200 ppm sample was conducted. Results indicated that there was a three-fold increase in relative cobalt concentration at high intensity sites over the entire XRF scan area. It can be assumed that these areas cause the increase in collagen fibril agglomeration at higher cobalt concentrations. Oscillatory rheology measurements show a decrease in the storage and loss moduli, even with low concentrations of cobalt, indicating a reduction in bulk stiffness. Regions of high- and low-density collagen cause the overall bulk structure to be less stiff as low density areas of collagen may act as weak points within the structure due to a reduction of collagen fibrils available for fibril - fibril interactions. The increase in cobalt - collagen interactions prevent interactions forming between collagen fibrils themselves, due to either blocking the binding site or by altering the physical structure so that binding sites are no longer accessible. This, therefore reduces the overall stiffness.

A decrease in cell viability, caused by changes in collagen matrix assembly due to the presence of cobalt ions, was shown via fluorescent imaging. Live/dead staining on cells cultured on the surface of CoCol gels indicated that complete cellular death did not occur until cobalt ion concentration reached that of 200 ppm, however, due to the heterogeneous distribution of collagen fibrils caused by the presence of cobalt ions, cell viability varied between 67 ppm and 133 ppm. The addition of cobalt concentration beyond 133 ppm also caused a change in cell morphology with an increase in elongation of the cytoskeleton. This may be due to the increased area of low-density collagen resulting in greater cell-fibril distances, causing an increase in cell stress and consequently elongation. The reduction in stiffness of the matrix may indicate why cellular death significantly increased at 200 ppm cobalt as the matrix no longer provides sufficient structural support. In addition to this, the significant reduction in fibril diameter may result in the obstruction of cell - collagen binding sites within the new fibril structure preventing cellular growth. The TrypanBlue assay quantified the viability of cells seeded onto CoCol gels in the presence of culture media, again confirming there is a decrease in viability with increasing cobalt concentration. The alamarBlue assay determined that there was a decrease in

cell metabolism with the increase in cobalt concentration. When cells are alive they are able to reduce resazurin, a reagent of the alamarBlue assay that is blue in colour, to resorufin, a compound that is both red in colour and highly fluorescent. If the cells are not metabolising the resazurin at the expected rate and therefore not proliferating normally, there will be a decrease in overall fluorescence and change of colour. As both metabolism and proliferation have closely linked cellular pathways, any reduction in metabolism can be correlated to a reduction in proliferation [272]. Both assays further suggest that the manipulation of the collagen fibrils by cobalt ions prevents cells from behaving normally. The decrease in cell proliferation and viability with increased concentration of cobalt ions may imply that the poorly formed collagen fibrils cannot facilitate signalling between cells. It may also suggest that the local structural environment is not sufficient for supporting cellular growth.

Molecular binding mechanics need to be understood to determine the complete effect of cobalt ions on a collagen matrix. When solid cobalt (II) chloride is dissolved in water, the predominant cation is $[Co(H_2O)_6]^{2+}$, as shown via X-ray diffraction analysis [273]. As $[Co(H_2O)_6]^{2+}$ is a positive complex, it will interact with the negatively charged species on collagen chains. Negatively charged collagen chains also interact with water molecules and form a strongly bound, dense hydration monolayer [67, 274]. Four water molecules bind with the carboxyl and hydroxyl groups of both the glycine and hydroxyproline residues in collagen to create the monolayer, as shown in Figure 3.8A. This is discussed more in depth in Chapter 1 Section 1.3. Initial hydration of the collagen molecule (surface water layer) is formed when water binds to the polar amino acid residues of collagen. Once all polar sites are filled, water binds to non-polar regions of the collagen, completing the hydration monolayer, Figure 3.8B.

It is assumed that hydrogen bonding of water bridges between residues in neighbouring collagen molecules contributes to matrix assembly rather than direct collagen interactions. Intrachain water bridges are typically 2 - 3 molecules long and are dependent on the local environment. There are three ways in which water bridges can form between collagen

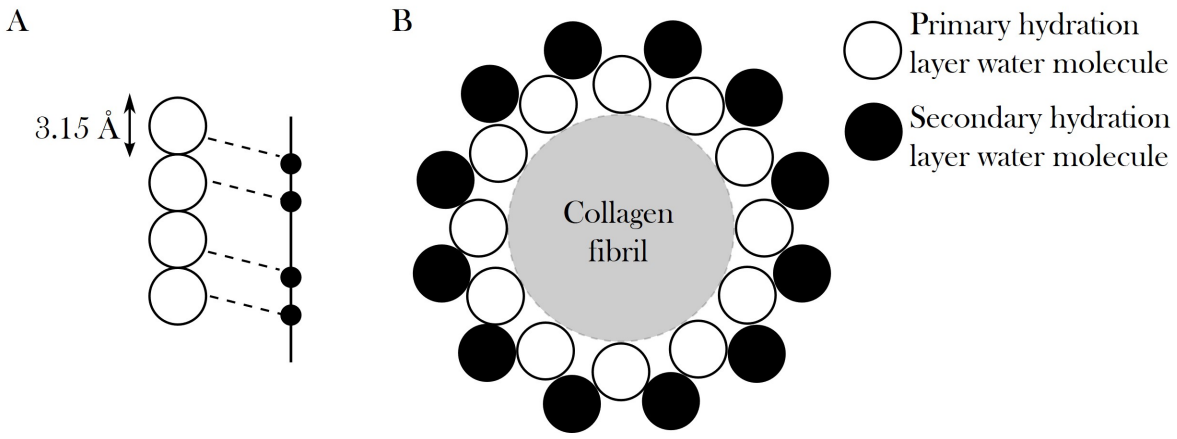



Figure 3.8: Schematic diagram depicting the cross-section of the binding sites of water with a collagen fibril. (A) Four water molecules per three collagen residues. (B) Polar and non-polar bound water layers surrounding the collagen fibril. Image is not to scale.

molecules; between two carbonyl groups $C{=}O$ ---- $water_n$ ---- $C{=}O$, between two hydroxyl groups $C\text{-}O$ ---- $water_n$ ---- $C\text{-}O$, or between a hydroxyl group and a carbonyl group $C\text{-}O$ ---- $water_n$ ---- $C{=}O$.

When $[Co(H_2O)_6]^{2+}$ is incorporated into the collagen matrix, it will either interact with the surface hydration layer of the collagen fibril, or with the fibril itself, as depicted in Figure 3.9A,B. There are four potential underlying mechanisms responsible for cobalt collagen interaction. If the cobalt ions interact with the collagen molecule directly, it will occur either with carbonyl groups present in both glycine and hydroxyproline (Figure 3.9C), the hydroxyl group present in hydroxyproline alone (Figure 3.9D) or with the carboxylic terminal at the end of the collagen molecule (Figure 3.9E). However, if the cobalt interacts with the hydration layer, it may be incorporated into the water bridge (Figure 3.9F) replacing one of the water molecules in the three molecule long chain.

In order to determine the binding site of collagen and cobalt, DSC and Raman measurements were taken. DSC measurements showed a 14% decrease in energy required to remove bound water from a 200 ppm CoCol gel. This suggests cobalt interactions prevent water binding either due to a blocking water binding sites or by altering the assembly of the collagen molecules, hindering the access of water binding sites. There was also a reduction in the temperature required to remove all excess water from the 200 ppm

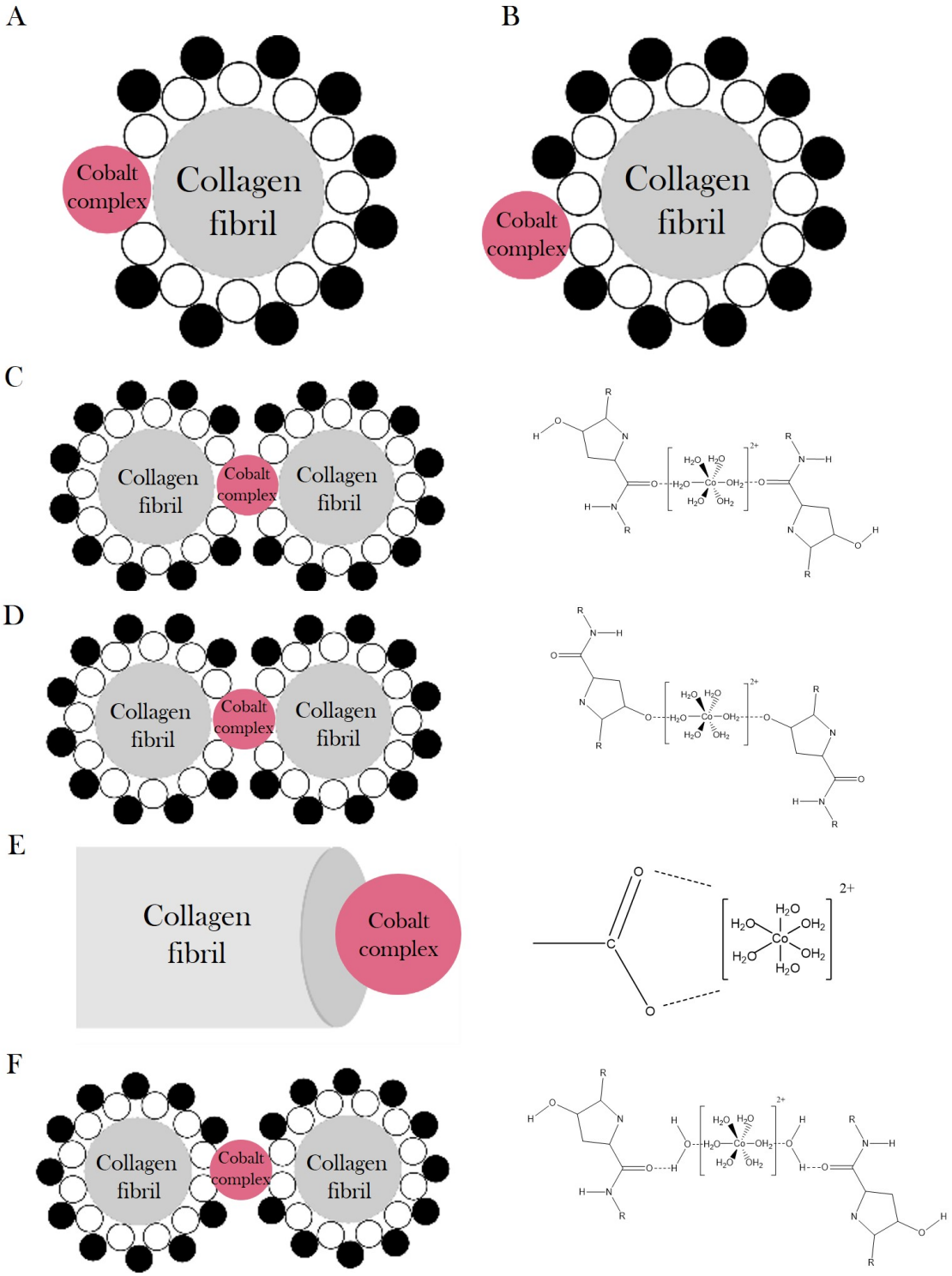



Figure 3.9: Schematic diagram depicting the potential binding sites of collagen with cobalt (not to scale). (A) Binding of cobalt to the collagen fibril directly. (B) Binding of cobalt to the first hydration layer. (C) Cobalt binding to the collagen fibril via a carboxylic bond. (D) Cobalt binding to the collagen fibril via a hydroxyl bond. (E) Cobalt binding to collagen at the carboxylic terminal. (F) Cobalt forming a water bridge between two collagen molecules.

collagen sample. This shows that the bulk water is less tightly bound within the collagen matrix. Due to the changes observed *via* AFM regarding local collagen formation, it is likely that the binding sites on the surface of the fibrils essential for hydration are no longer accessible. Raman spectroscopy showed a suppression of a secondary alcohol vibration due to a reduction in the C-O peak between samples containing 0 ppm and 200 ppm of cobalt. This suggests that the cobalt ions interact specifically with a hydroxyl group [275, 276]. Suppression of a peak seems to indicate that the oxygen within the bond can no longer vibrate as before, suggesting that there is another molecule interacting in conjunction with the carbon causing an overall reduction in the vibration peak produced. A carbonyl group is present in both hydroxyproline and the carboxylic acid terminal of collagen, however, previous studies into complex interaction with collagens show preferential binding to terminal sites of the molecule [277]. The significant increase in D-spacing with increasing cobalt concentration further suggests an interaction with the carboxylic acid terminal of the collagen molecule. An increase in D-spacing would be due to an increase in spacing between collagen molecules, indicating an interaction with the collagen terminal. Therefore, the proposed binding site of cobalt ions to collagen fibrils is that of the carbonyl group within the carboxylic acid terminal of the collagen fibril.

## 3.5 Conclusion

This work indicates that cobalt ions have an adverse effect on the formation of collagen fibrils. An increase in the cobalt ion concentration not only elongates the D-spacing but also decreases the fibril diameter. This causes an increase in matrix heterogeneity as shown from frequency of local fibril density. Visually there is a decrease in structural integrity of CoCol hydrogels with an increase in cobalt concentration. Local cobalt concentration varies from high concentration to low concentration with a three-fold increase, which may explain the localised density change of collagen fibrils. These differences caused a reduction in the overall stiffness of the collagen hydrogel. This change in matrix formation

prevents osteoblasts from attaching and proliferating at a normal rate, changing both cell morphology and metabolism, ultimately decreasing cell viability. Changes in characteristic DSC and Raman collagen fibril measurements indicate that the likely interaction site of cobalt - collagen is at the carboxylic acid terminal rather than interactions with either the side of the collagen fibril or incorporated within a water bridge. This leads toward a reduction in crucial stabilizing bonds within matrix formation, explaining the decrease in matrix stiffness and reduction in energy required for bulk water loss.

These results give further insight into the underlying mechanisms that cause unexpected failures of MOM implants. As we have shown, the collagen matrix is adversely affected, and it is likely that the extensive necrosis seen is more a result of the metal debris changing the ECM structure rather than interacting with the surrounding cells directly. Overall, manipulation of collagen matrix formation *via* inorganic ions can produce an inflamed wound-like environment. Investigations into new materials for medical implants need to focus on not only two-dimensional cell culture but also on three-dimensional cell culture interactions, specifically focusing on any adverse effects the material may have towards the ECM.

# CHAPTER 4

# THE EFFECT OF CALCIUM AND PHOSPHATE ON COLLAGEN ASSEMBLY

Early stage bone formation is characterised by the mineralisation of collagen type I fibrils. These fibrils act as a scaffold on which hydroxyapatite (HA) crystals form. Collagen type I fibrils consist of over 90% of all organic matter within bone and are crucial for both formation and mechanical strength. The fundamental process behind the role of collagen in early stage mineralization is still largely unknown. As collagen is a hierarchical protein, we investigated the influence of calcium, phosphate and calcium phosphate on collagen formation from the nano- to the macro- scale. This chapter found that calcium and phosphate alter the conformation of the collagen triple helix, yet when calcium phosphate is present, the conformation of the triple helix matches that of native collagen. It was also found that the addition of calcium causes a significant reduction in the size of the collagen triple helix, alongside phosphate ions, however this is not the case with the addition of calcium phosphate. Investigations found calcium to be detrimental to the fibrillogenesis process, causing a significant decrease in the growth phase. Calcium phosphate also has an effect on fibrillogenesis but not as detrimentally as calcium alone. When looking at near physiological ratios of calcium to phosphate (1:0.6), it was found that calcium phosphate has a larger influence over later stage fibril development rather than early stage. The data in this chapter suggests that these effects are due to the size of individual calcium and phosphate ions and the size of the calcium phosphate complex they form. Calcium phosphate clusters (Posner clusters) are five times larger than that of calcium and phosphate ions alone. When interacting with surface groups on the collagen, smaller ions will be able to deform the triple helix more than larger ions or complexes. In this way the collagen molecule is able to maintain its triple helix conformation only in the presence of Posner clusters, preventing disruption to the fibril formation process and overall matrix assembly.

## 4.1 Introduction

Bone is a hierarchical structure with multiple stages of organisation [278, 279]. Early bone formation involves the organisation of type I collagen fibrils alongside hydroxyapatite (HA) crystals [$Ca_{10}(PO_4)_6(OH)_2$] [280–284]. The interaction is a complex physical and chemical process dependent on intermolecular interactions between collagen and HA [281]. The initial step in crystallization is nucleation of the extracellular matrix, in which supersaturation of both calcium and phosphate allows for the first nuclei within the system to form [285, 286]. As the collagen fibrils self-assemble, they regulate the nucleation and growth of HA crystals so that the crystals form within the fibrils [280]. Within these early forming HA crystals, the ratio of calcium to phosphate is 1.5 [287, 288]. Collagen type I fibrils consists of more than 90% of all organic matter within bone [278, 289]. The fibrils orientate in a way that provides a template for the deposition of HA mineral, forming a dense matrix [278, 282, 289]. By ordering mineralisation through fibril organisation, a structure is produced which has optimal mechanical properties [289]. Both structure and formation of collagen fibrils play a role in maintaining the mechanical properties of bone, as one of the influential factors regarding the biomechanical strength of tissues is collagen fibril diameter [278]. Mineralization of bone matrix provides the stiffness of bone with the collagen matrix contributing to its toughness [279].

Phosphate ions predominately exist as $HPO_4^{2-}$ or $HPO_4^-$ ions at physiological pH [290–292]. However the ratio of divalent to monovalent phosphate ions is 4:1 [291]. As there are more divalent phosphate ions present, preferential binding with positive divalent ions is prevalent. As calcium is a divalent ion, the nucleation and growth of mineral complexes forms when phosphate interacts with surrounding calcium. An amorphous form of calcium phosphate, called a Posner cluster, is considered to be the precursor to crystalline calcium phosphate minerals, such as HA, which are crucial to bone mineralisation and formation [293]. These clusters are comprised of particulates made of spherical domains ranging in size from 0.7 – 1 nm in diameter [294]. The particulates then aggregate creating clusters ranging from 30 - 100 nm in diameter, referred to as amorphous calcium phosphate (ACP).

The ratio of calcium to phosphate within ACP has been found to be $1.45 \pm 0.05$ [283, 288]. ACP in turn creates a more stable phase and aggregates to form calcium phosphate chains [288, 295]. The mineral crystals grow along the long axis of the collagen fibrils and lie in parallel to the surface of the collagen [286].

It was initially believed that early nucleation sites formed at the carboxylic terminals of the collagen molecule [280, 286]. In this way, calcium phosphate crystals fill the space between adjacent collagen molecules arranged in a staggered array [282, 286]. These gaps range from 35 - 40 nm in length and 1.5 - 3 nm width so are therefore able to accommodate microcrystal formation [286]. This process is shown in Figure 4.1.

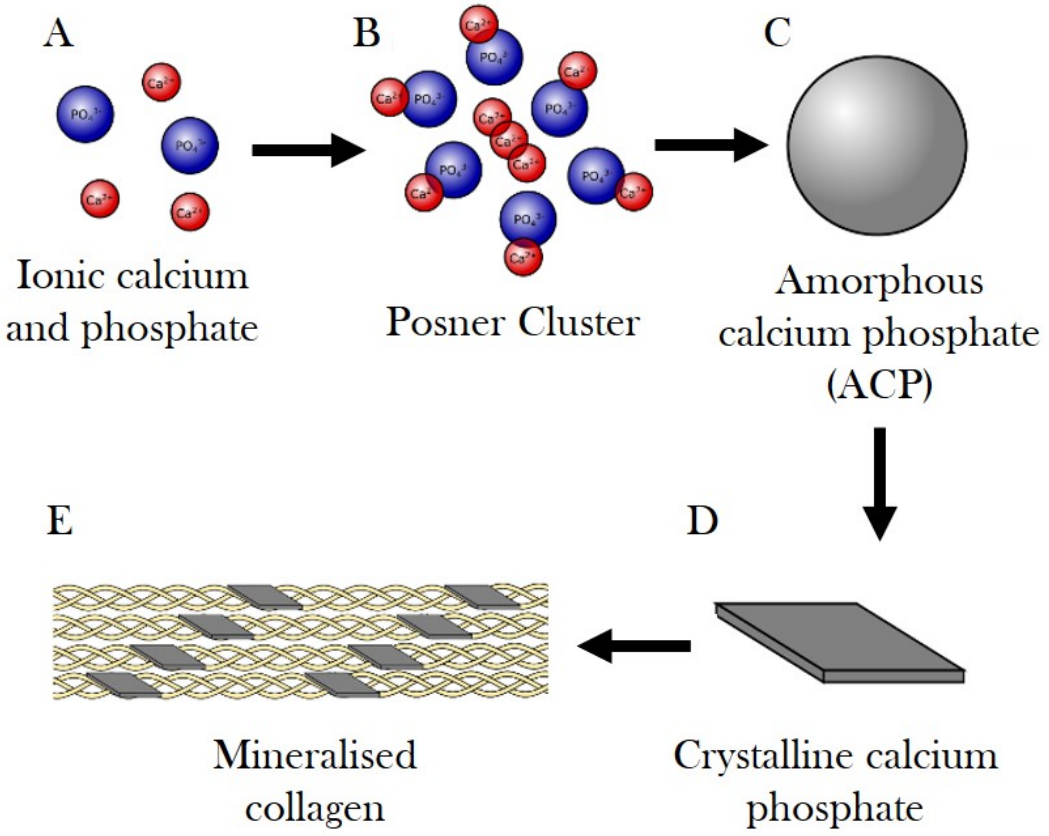



Figure 4.1: Mineralisation process of calcium (Ca) and phosphate ($PO_4$) ions aggregating to form mineralised collagen. (A) $Ca^{2+}$ and $PO_4^{3-}$ ions within the surrounding environment. (B) $Ca^{2+}$ and $PO_4^{3-}$ ions aggregate to form Posner Clusters (0.1 - 1 nm). (C) Posner clusters aggregate to form amorphous calcium phosphate (ACP) particles (30 - 100 nm). (D) ACP becomes crystalline, in which it forms a platelet morpholoy (50 nm x 25 nm x 23 nm). (E) Crystalline calcium phosphate nanocrystals incorporated into and mineralising collagen fibrils. Image adapted from [4].

However, studies have now shown, through Fourier-transform infrared spectroscopy, that both calcium and calcium phosphate can also interact with the surface of the collagen molecule through both carboxyl and carbonyl groups [280].

The mineralisation of collagen within bone is still largely unknown [282]. However, through evaluation of the kinetic process of fibril formation (fibrillogenesis) we can determine how different ions influence matrix assembly [225, 296]. Collagen fibrillogenesis is thermally driven, and due to the displacement of hydration layers surrounding the collagen molecules, is controlled by large positive entropy. Hydrogen bonding between polar residues within the collagen molecule contributes to a large part of fibrillogenesis [297]. As collagen is hierarchical, ions are able to influence both formation and assembly at many different stages [279, 296, 297].

In this chapter, the influence of calcium and phosphate ions (that are crucial to bone development) on collagen assembly is investigated. The hierarchical properties of collagen are investigated by an evaluation of the influence of these ions across the nano- to macro-scale. Through the fundamental understanding of how these ions interact both individually and within the same system, we can gain understanding of the early stage bio-processes involved in bone mineralisation.

## 4.2 Methodology

### 4.2.1 Ionic Buffers

Each ionic buffer was made to a concentration of 0.1 mM in deionised water. Deionised water was used to eliminate the effects of any other ions within the solution. The pH was then adjusted to match that of the deionised water with either 1 M sodium hydroxide (Sigma-Aldrich, UK) or 1 M hydrochloric acid (HCl, Sigma-Aldrich, UK) depedinging on the pH of the initial solution. Ionic buffers included potassium chloride (KCl, Sigma-Aldrich, UK), calcium chloride ($CaCl_2$, Sigma-Aldrich, UK), magnesium chloride ($MgCl_2$, Sigma, UK), sodium chloride (NaCl, Sigma, UK), ethylenediaminetetraacetic acid (EDTA, Invit-

rogen, CA, USA) and sodium phosphate (sodium phosphate dibasic heptahydrate (Acros Organics, UK) and sodium phosphate monobasic monohydrate (Sigma-Aldrich, UK) at a ratio of 1:0.46).

### 4.2.2 Freeze Drying

Samples were prepared as stated in Section 2.1.2 before being placed into -80 ℃ for 24 hrs at incubation time points of 35 mins and 120 mins. Samples were then freeze dried for 72 hrs using a Laylyo mini freeze dryer (Frozen in Time, UK). Freeze drying was performed under high (4 x $10^{-4}$ mbar) vacuum conditions with the condenser temperature set at -55 ℃. Freeze dried samples were imaged using AFM (sample preparation found in Chapter 2 Section 2.1.2) but images were acquired over a larger area of 75 x 75 $\mu m^2$.

### 4.2.3 Dynamic Light Scattering (DLS)

A Zetasizer NanoSeries (Malvern, UK) was used to measure dynamic light scattering of collagen in deionised water and collagen with excess calcium chloride ($CaCl_2$), sodium phosphate ($PO_4^{3-}$) and calcium phosphate at a ratio of 1:1 (Ca:$PO_4$ 1:1). Collagen was at a concentration of 1 mg $mL^{-1}$ with a buffer concentration of 0.1 mM. A refractive index of 1.430 and absorption of 0.05 was used for collagen [298]. The dispersant used was water with a viscosity of 0.8872 cP and refective index of 1.330. 1 mL of each sample was placed in a disposable cuvette (Sarstedt ag & Co., DE) and 5 scans were taken for each sample with 11 runs per scan.

## 4.3 Results

### 4.3.1 The Influence of Calcium and Phosphate Ions on Collagen Assembly

To fully understand how calcium and phosphate ions impact collagen assembly, their ionic influence on the collagen molecule (triple helix) must be understood. Therefore, circular dichroism (CD), dynamic light scattering (DLS) and zeta potential measurements were undertaken. CD was performed on collagen dispersed in a buffer solution of excess calcium chloride ($CaCl_2$), sodium phosphate ($PO_4^{3-}$) and calcium phosphate ($Ca{:}PO_4$) at a ratio of 1:1, as shown in Figure 4.2A. This ensured that all potential binding sites on the collagen triple helix were occupied. The CD signal measured had a reduction in both the positive and negative peak with the addition of $CaCl_2$ and $PO_4^{3-}$, indicating that both interact with the collagen molecule and cause conformational changes. However, the buffer solution of $Ca{:}PO_4$ 1:1 did not cause a reduction in either peak, with the signal matching that of the control. This shows that the addition of both calcium and phosphate together prevents conformational changes to the collagen molecule that occur when $CaCl_2$ or $PO_4^{3-}$ are added individually. Ratios of positive to negative peaks (Figure 4.2B) quantify that both $CaCl_2$ and $PO_4^{3-}$ interfere with the conformation of a collagen molecule, with $Ca{:}PO_4$ 1:1 not having an effect on the triple helix structure.

To further understand how each ionic complex is interfering with the molecular confirmation of collagen, DLS was implemented to evaluate molecule size. Figure 4.2C,D show that the introduction of $CaCl_2$ causes a reduction in the size of the collagen molecule, with $PO_4^{3-}$ also reducing the size but not as significantly. The addition of collagen to $Ca{:}PO_4$ 1:1 causes a reduction in molecule size yet it is a non-significant reduction. This correlates with CD measurements, showing how calcium and phosphate separately change the conformation of the collagen molecule from that of its native form. DLS measurements suggest that the presence of calcium causes a tightening of the collagen molecule, with phosphate and calcium phosphate interacting but less strongly. Collagen molecule

size peaks have been correlated to the peaks at 100 nm, as DLS is a technique optimised for spherical products there will be a discrepancy from the established 300 nm size of a collagen molecule [299].

Zeta potential measurements, Figure 4.2E, show that there is an increase in aggregation with the presence of both calcium and phosphate within the medium. This indicates that collagen molecules are less stable within a Ca:$PO_4$ 1:1 buffer, suggesting an increase in rate of fibril self-assembly.

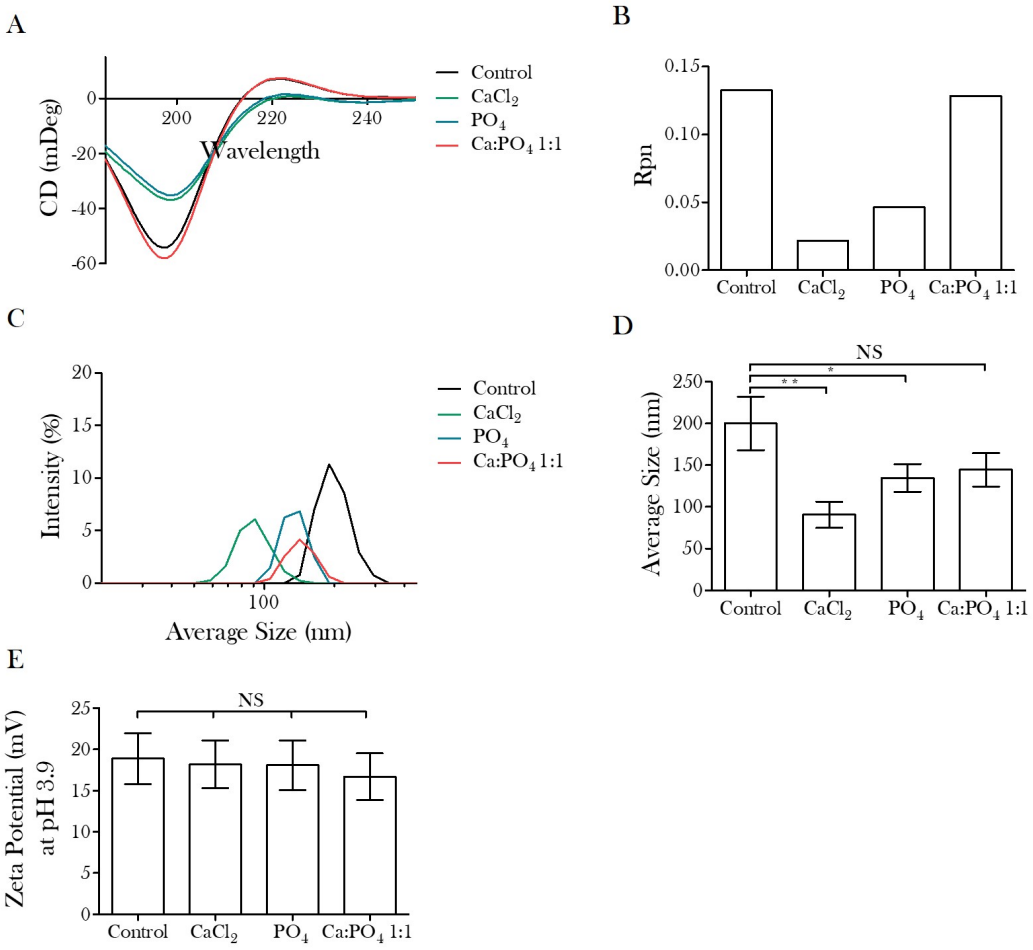



Figure 4.2: (A) Circular dichroism measurements of collagen in excess calcium chloride ($CaCl_2$), excess sodium phosphate ($PO_4^{3-}$) and excess calcium phosphate at a Ca:$PO_4$ ratio of 1:1 (Ca:$PO_4$ 1:1). (B) Ratio of positive to negative (Rpn) peaks of circular dichroism data shown in (A). (C) Dynamic light scattering measurements of collagen in excess $CaCl_2$, excess $PO_4^{3-}$ and excess Ca:$PO_4$ 1:1. It has been assumed that the collagen molecule size is located at approximately 100 nm. (D) Quantification of the dynamic light scattering measurements shown in (C). (E) Zeta potential measurements at a pH of 3.9 of collagen in excess $CaCl_2$, excess $PO_4^{3-}$ and excess Ca:$PO_4$ 1:1. ** refers to a P value $\leq$ 0.01, * refers to a P value of $\leq$ 0.05 and NS refers to a non-significant result. N = 3, error bars refer to $\pm$ standard deviation.

As collagen is assembled in a hierarchical manner, it is important to understand how changes to collagen molecule conformation influence fibril growth and formation. Therefore, a series of fibrillogenesis studies were undertaken.

Turbidity measurements to investigate fibrillogenesis required optimisation. A 2 hr absorbance scan of a 3 mg $mL^{-1}$ collagen gel found the absorbance peak of collagen to be 380 nm (over a range of 300 - 700 nm), as shown by Figure 4.3A. Therefore, fibrillogenesis measurements at an absorbance of 380 nm were taken over a range of collagen concentrations (0.5, 1, 1.5 and 2 mg $mL^{-1}$). These measurements determined that a concentration of 2 mg $mL^{-1}$ provided an optimal fibrillogenesis curve, as shown by Figure 4.3B. Concentrations lower than 2 mg $mL^{-1}$ were not high enough to produce a fibrillogenesis curve. This collagen concentration was then used in the optimisation of further fibirllogenesis methods.

In order to ensure the reliability of absorbance measurements, multiple repeats of 2 mg $mL^{-1}$ gels were scanned, as shown in Figure 4.4A. By using the initial method involving the addition of 2.2 $\mu$L 1 M NaOH to each 96 well-plate individually, neither accurate nor reproducible results were produced. Therefore, a stock solution of buffer containing the required amount of NaOH for cross-linking (130 $\mu$L per 5 mL buffer) was made for all repeats. Results from this method were more reliable, with a reduction in standard deviation, as shown in Figure 4.4B,C. Therefore, this methodology was continued to determine chemical influence on collagen assembly.

Although the concentration of NaOH required to fully cross-link a control collagen gel was already established, the concentration required to cross-link a collagen matrix with the addition of new ions still needed to be determined. Figure 4.5A shows absorbance scans (over 300 - 700 nm) of varying NaOH concentrations with 2 mg $mL^{-1}$ collagen. A concentration of 26 $\mu$L $mL^{-1}$ gave the largest absorbance reading so was used for future experiments. Next, the optimal concentration of ionic buffer was determined by varying the concentrations of KCl, as shown by the absorbance scans in Figure 4.5B. As there was little difference between scans, a concentration of 0.1 mM was chosen. To ensure that

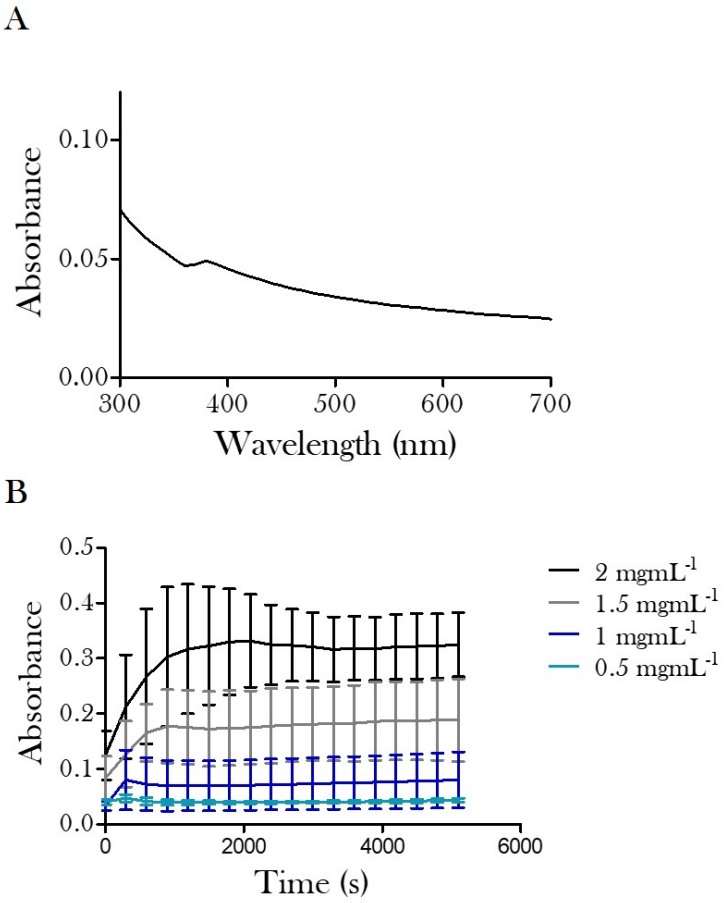



Figure 4.3: (A) Absorbance of 3 mg $mL^{-1}$ collagen taken over the range 300 - 700 nm, peak was taken to be at a wavelength of 380 nm. (B) Fibrillogenesis of 2, 1.5, 1 and 0.5 mg $mL^{-1}$ collagen, with 2 mg $mL^{-1}$ giving the most expected response. All scans were baselined to that of uncross-linked collagen at each corresponding concentration. N = 3, error bars refer to ± standard deviation.

an absorbance wavelength of 380 nm was appropriate for all ionic solutions when added to collagen, an absorbance scan of all ions combined with 2 mg $mL^{-1}$ collagen was taken over the range of 300 - 700 nm (Figure 4.5C). It determined that a more appropriate absorbance wavelength was 360 nm and not the original 380 nm.

These established parameters (2 mg $mL^{-1}$ collagen concentration, 0.1 mM ionic buffer concentration, 360 nm absorbance) were then used to understand the fibrillogenesis process in the presence of calcium and phosphate. Fibrillogenesis experiments show that calcium chloride had the most detrimental effect on collagen fibril assembly (Figure 4.6A). To see whether the addition of phosphate prevented these effects, sodium phosphate so-

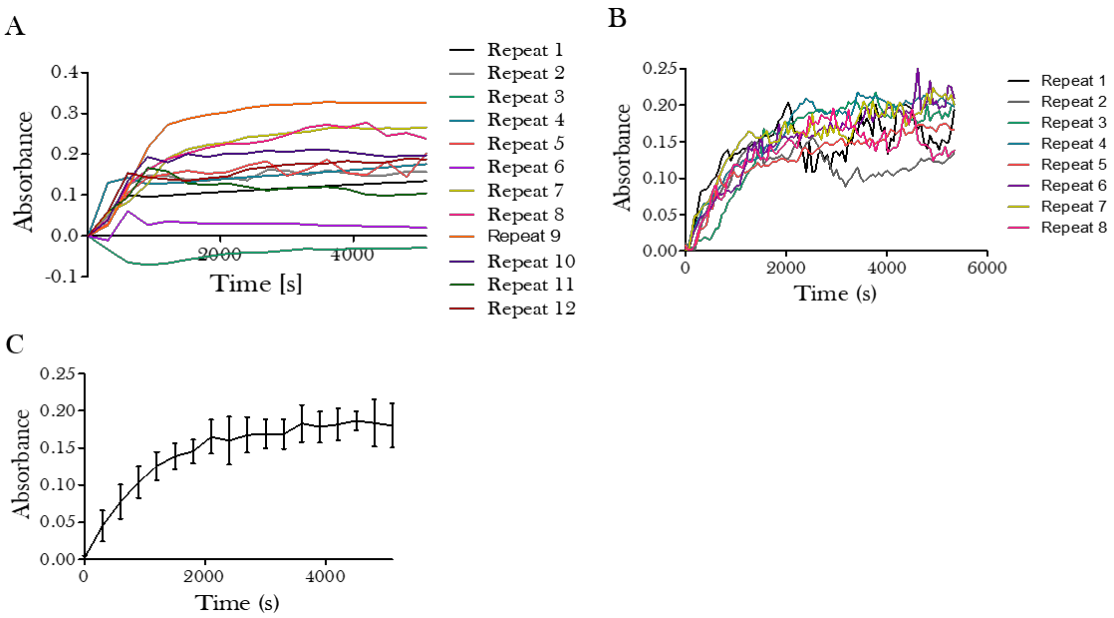



Figure 4.4: (A) Fibrillogenesis repeats of 2 mg $mL^{-1}$ when initial method was undertaken. This involved small volumes of NaOH being added to buffer within a 96-well individually. (B) Fibrillogenesis repeats of 2 mg $mL^{-1}$ using alternative method. This method involved adding NaOH to a working buffer stock prior to addition of both to the 96-well. (C) Average of (B) with standard deviation. N = 12 for (A) and N = 8 for (B), (C). Error bars refer to ± standard deviation.

lution was added to calcium chloride at a Ca:$PO_4$ ratio of 1:1. Both solutions were mixed to create a final concentration of 0.1 mM. Figure 4.6C shows that adding phosphate into the solution prevents the adverse effects on fibril formation. Figure 4.6B shows the fibrillogenesis profile of collagen with added excess sodium phosphate only. This shows that sodium phosphate alone does not influence collagen fibril assembly detrimentally. A control of the fibrillogenesis profile of NaCl and $CaCl_2$ (Appendix I, Figure 7.6) indicated that changes in the Ca:$PO_4$ 1:1 profile were not due to any NaCl within the solution.

To ensure that any changes in fibrillogenesis profile were not due to the presence of chloride ions within the buffer, a fibrillogenesis assay of varying chloride complexes was undertaken. In order to achieve this, stock solutions of KCl, $MgCl_2$ and NaCl were made at a concentration of 0.1 mM. Kinetic fibrillogenesis measurements determined that chloride ions were not influencing turbidity due to the changes in turbidity profiles with different cations, as shown in Figure 4.7. $CaCl_2$ still had the most detrimental effect on collagen

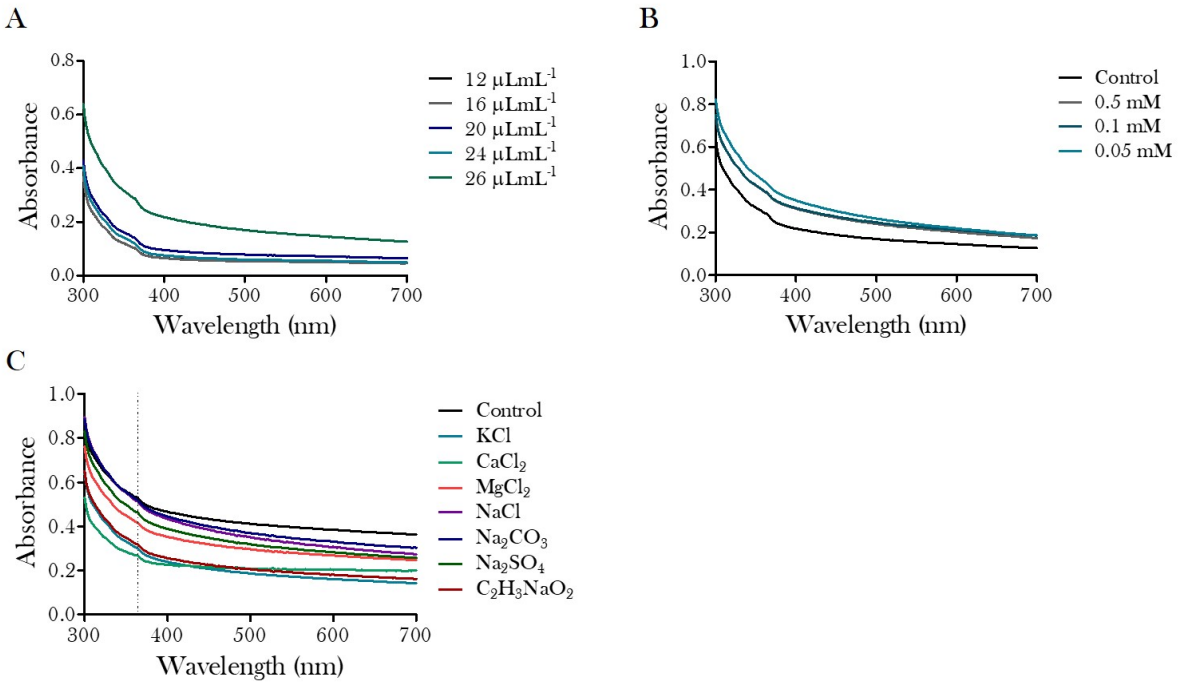



Figure 4.5: (A) Varying concentrations of NaOH (12-26 $\mu$L mL$^{-1}$) required for gelation to occur. (B) Absorbance scan between 300-700 nm of varying concentrations of KCl to determine what concentration of ion was optimal. (C) Absorbance scan between 300-700 nm of 0.1 mM ion with 2 mg mL$^{-1}$ collagen to ensure wavelength used for fibrillogenesis was optimal. N = 3.

fibril formation, yet it was also shown that KCl adversely effected collagen fibril assembly just not as drastically (Figure 4.7B). The fibrillogenesis profile with the addition of excess $MgCl_2$ was within one standard deviation of the control, alongside NaCl, however this seemed to enhance the rate of fibril formation.

This was also confirmed by determining the growth phase of collagen when dispersed within each ionic buffer. The growth phase is a product of both collagen molecule concentration and the coalescence of collagen molecules [224]. As the concentration of molecules is consistent, it can be determined that any changes in the growth phase are due to changes in rate of fibril formation. Therefore, it can be used to determine characteristic changes within matrix assembly. When looking at the growth phase for ionic solutions containing chlorides, there was a significant difference when introducing both potassium and calcium to the collagen matrix, as shown in Figure 4.7E. This seems to suggest that the chloride ions are not effecting the fibrillogenesis process and any changes to fibrillogenesis, when

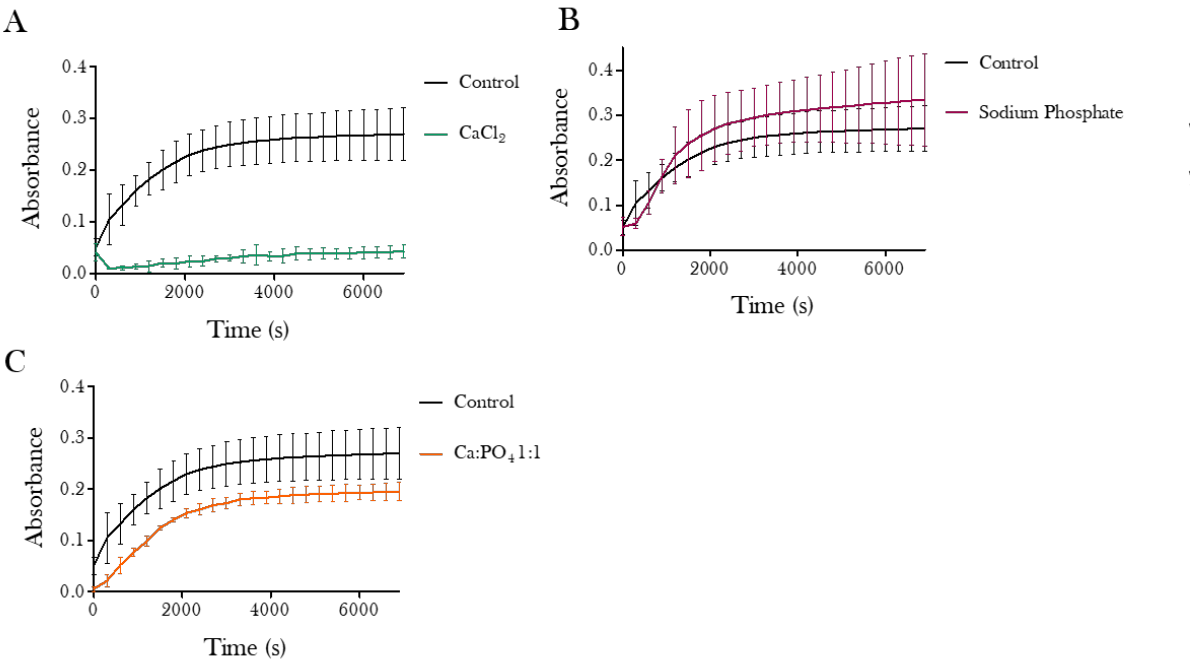



Figure 4.6: Fibrillogenesis of (A) $CaCl_2$, (B) sodium phosphate solution and (C) calcium phosphate solution at a ratio of Ca:$PO_4$ 1:1. N = 3, error bars refer to ± standard deviation.

investigating calcium and phosphate, are from those ions alone. Investigations into alternative anions were also conducted, concluding that cations had the largest influence over collagen fibril assembly (Appendix I, Figures 7.7, 7.8 and 7.9)

To visualise changes caused by altering the chemical environment of the collagen, AFM images of dehydrated collagen gelled in each ionic buffer were taken, as shown in Figure 4.8A. It was shown that the addition of KCl, $CaCl_2$ and $MgCl_2$ prevented the formation of smooth, intact collagen aggregates, leaving agglomerated areas of collagen monomers and rough bundles. This correlates with fibrillogenesis results as these ions had an adverse effect on matrix formation, as indicated by Figure 4.7E. However, regardless of which ion was added to the collagen, there was a decrease in fibril diameter, as shown in Figure 4.8B. Examples of how fibril diameter was measured can be found in Appendix I Figure 7.10. This indicates that all cations added to the collagen gel have an influence on fibril assembly.

Growth phase measurements for collagen in the presence of excess calcium (0.1 mM),

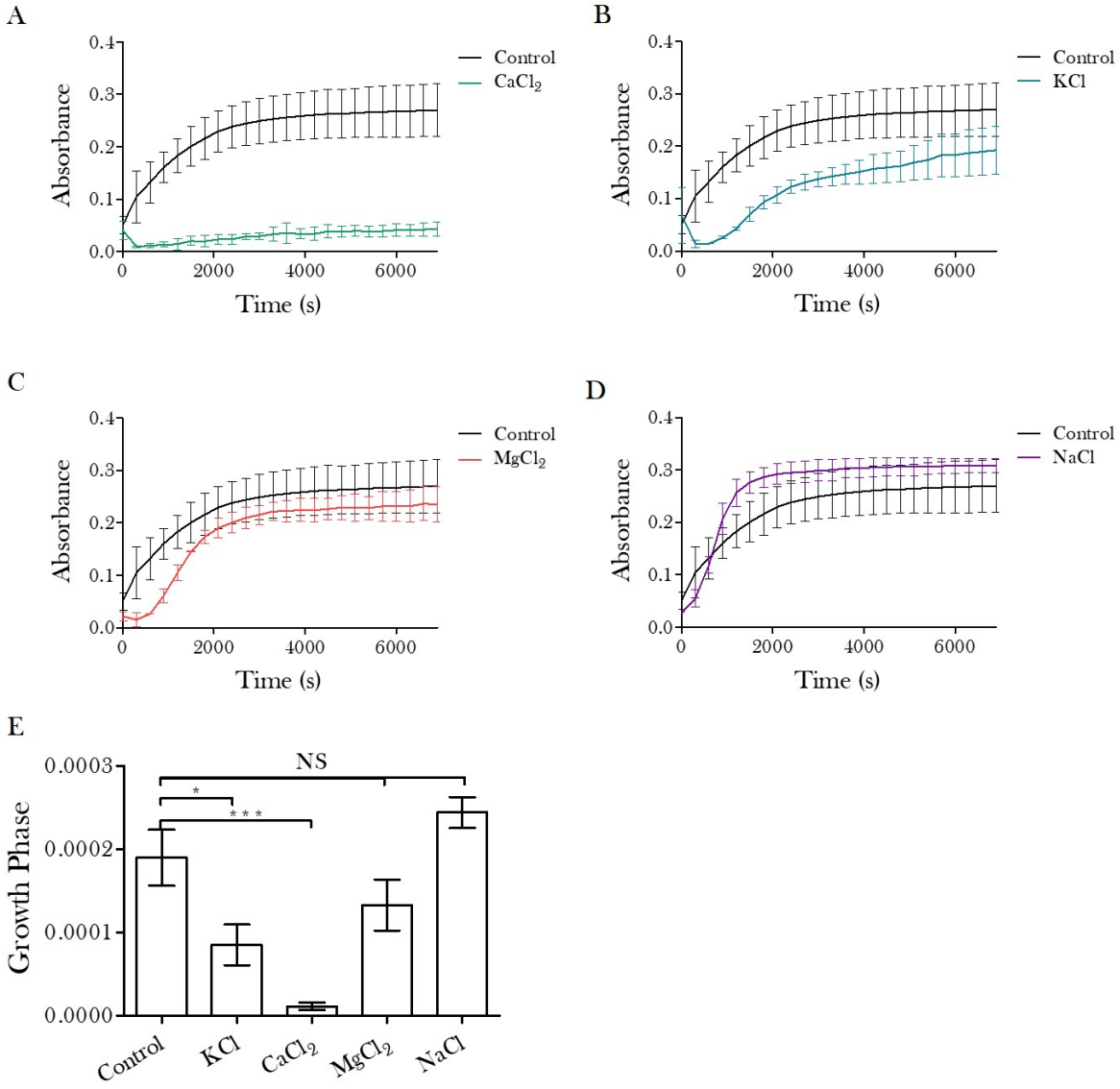



Figure 4.7: Fibrillogenesis measurements of (A) $CaCl_2$, (B) KCl, (C) $MgCl_2$, and (D) NaCl at a concentration of 0.1 mM added to 2 mg $mL^{-1}$ collagen. Growth phase of collagen in excess KCl, $CaCl_2$, $MgCl_2$ and NaCl. *** refers to a P value $\leq 0.001$, * refers to a P value $\leq 0.05$, NS refers to a statistically non significant result. N = 3, error bars refer to $\pm$ standard deviation.

excess phosphate (0.1 mM) and excess calcium phosphate (0.1 mM) in a ratio of Ca:$PO_4$ 1:1 were then undertaken. Measurements were calculated from the fibrillogenesis profiles shown in Figure 4.6. Growth phase measurements, shown in Figure 4.9A, further confirm that the addition of phosphate reduces the negative effects of calcium on fibril formation, as there is less of a significant difference between the growth phase of calcium phosphate and calcium chloride. To determine the lowest ratio of phosphate required to reverse the

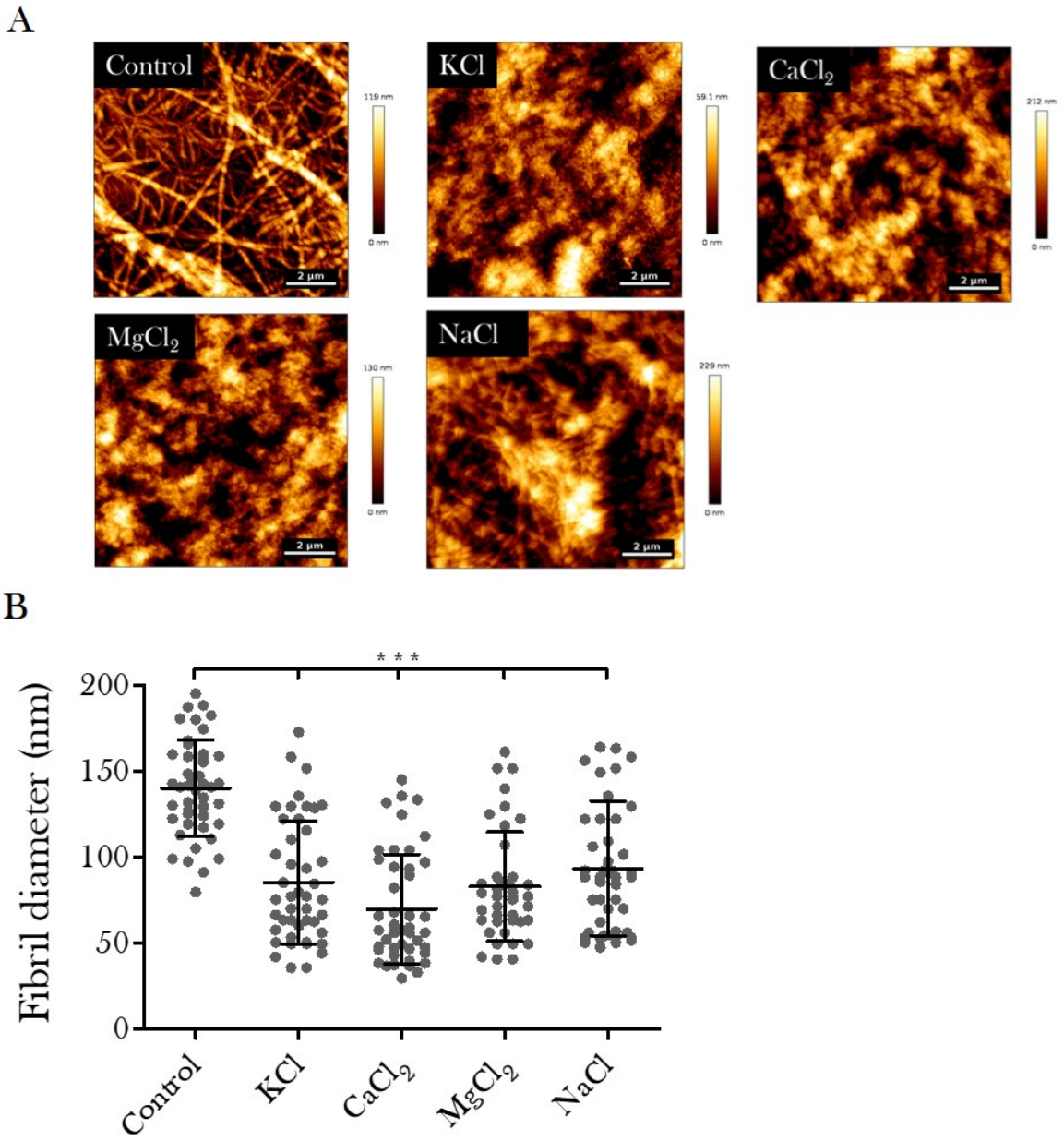



Figure 4.8: (A) AFM images of 2 mg $mL^{-1}$ collagen with added KCl, $CaCl_2$, $MgCl_2$ and NaCl at a concentration of 0.1 mM. (B) Fibril diameter measured from triplicates of each AFM image. *** refers to a P value of $\leq 0.001$. N = 75 across 3 biological repeats, error bars refer to $\pm$ standard deviation. Scale bar is 2 $\mu$m.

effects of calcium on collagen fibril formation, a range of Ca:$PO_4$ ratios were also investigated. Growth phase measurements of these lower ratios (Figure 4.9B) confirmed that a ratio of 1:1 was the only ratio to show a significant ($P \leq 0.01$) reduction, with all other ratios having a non-significant effect on the growth phase in comparison to the control.

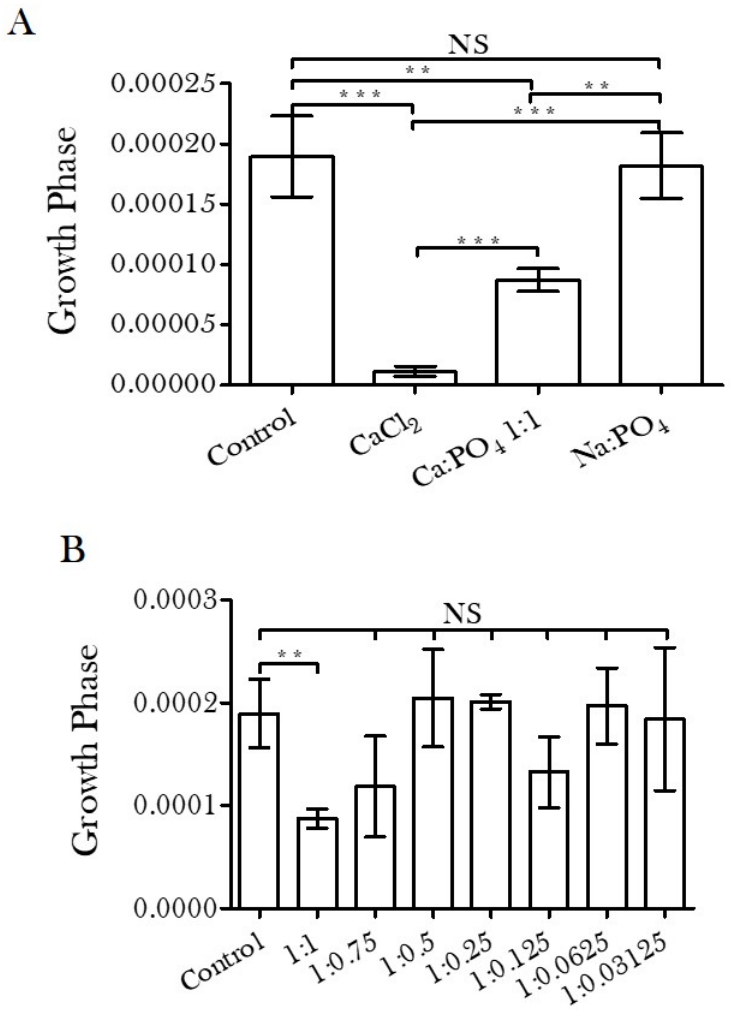



Figure 4.9: (A) Growth phase of $CaCl_2$, sodium phosphate solution ($Na:PO_4$) and calcium phosphate solution ($Ca:PO_4$)at a ratio of 1:1. (B) Growth phase measurements of $Ca:PO_4$ with decreasing ratios of phosphate. Fibrillogenesis profiles used to measure ratio growth phase can be found in Appendix I Figures 7.2 and 7.11. *** refers to a P value of $\leq 0.001$, ** refers to a P value of $\leq 0.01$, * refers to a P value of $\leq 0.05$, NS refers to a statistically non-significant result. N = 3, error bars refer to $\pm$ standard deviation.

Fibrillogenesis profiles for these $Ca:PO_4$ ratios can be found in Appendix I, Figure 7.11.

To visualise the difference between how calcium and calcium phosphate effected collagen fibrils, AFM images were acquired. Figure 4.10A shows that the presence of calcium chloride does not allow for defined collagen bundles to form. Visually, it shows a mass of small protein agglomerates within the system. In comparison, the presence of calcium phosphate allows for larger, more well-defined bundles to form. This is further confirmed with fibril diameter measurements, as Figure 4.10B is showing a significant reduction in

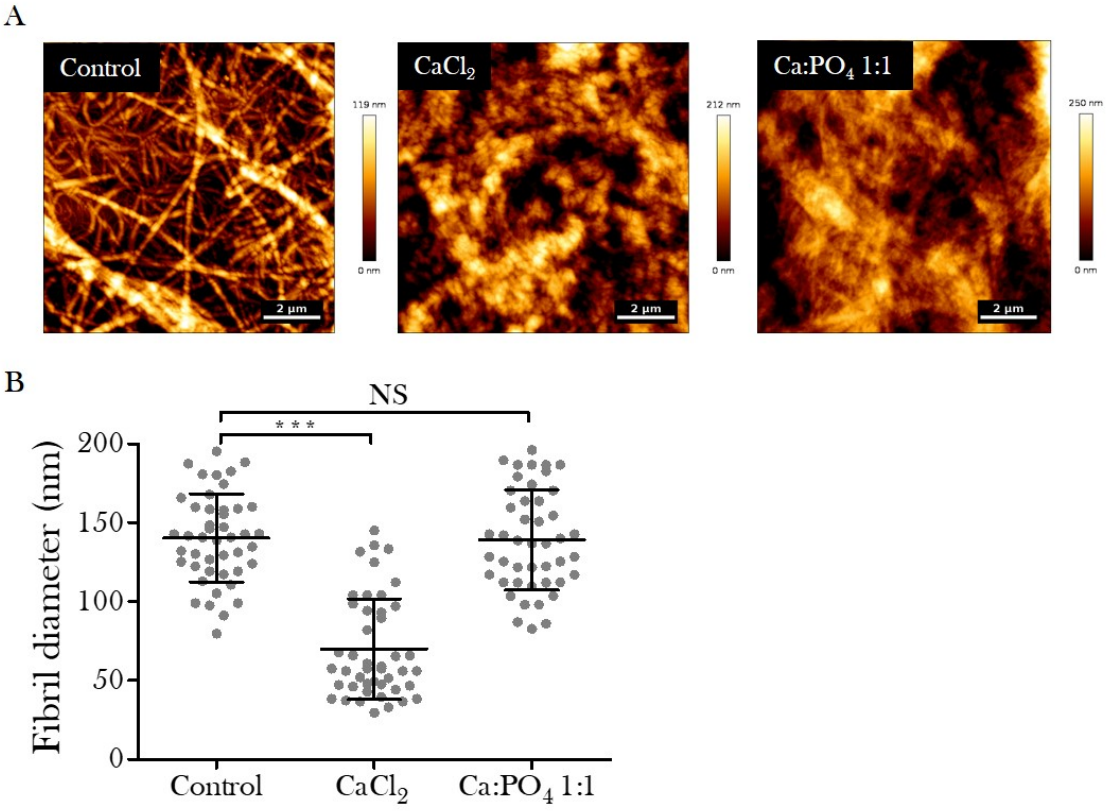



Figure 4.10: (A) AFM images of 2 mg $mL^{-1}$ collagen with added $CaCl_2$ and calcium phosphate in a ratio of $Ca:PO_4$ 1:1 at a concentration of 0.1 mM. (B) Fibril diameter measured from triplicates of each AFM image. *** refers to a P value of $\leq 0.001$. N = 75 across 3 biological samples, error bars refer to $\pm$ standard deviation. Scale bar is 2 $\mu$m.

fibril diameter in the presence of $CaCl_2$ ($P \leq 0.001$) and a non-significant reduction in fibril diameter in the presence of $Ca:PO_4$ 1:1.

Although these AFM images provide a visualisation of any changes within the collagen nanostructure, they do not provide definitive quantitative analysis. Dimensions such as fibril diameter have been measured from these images, yet techniques such as high-resolution transmission electron microscopy would have been able to provide further and more definitive measurements. This would have provided a more robust understanding of how each chemical is influencing the formation of collagen and therefore its assembly, however this technique was not available during the project.

To understand the process by which phosphate may be preventing the detrimental effects of calcium on collagen assembly, a calcium chelator was added in excess to collagen.

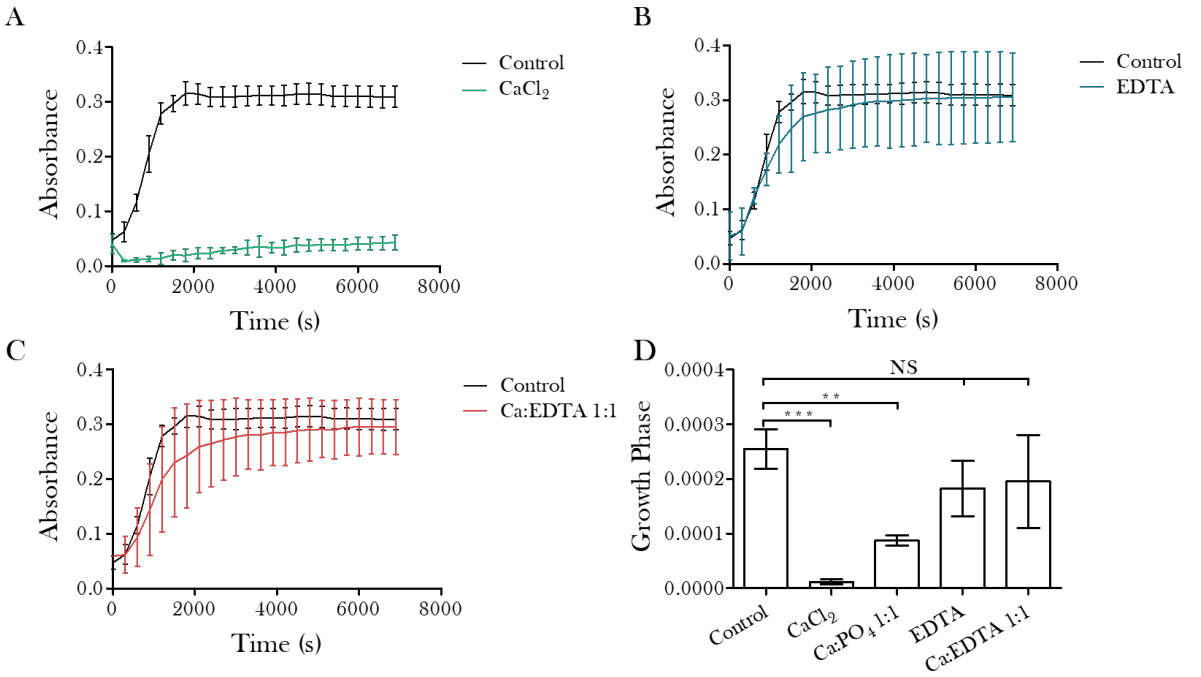



Figure 4.11: Fibrillogenesis measurements of (A) $CaCl_2$, (B) EDTA, (C) Ca:EDTA at a ratio of 1:1. (D) Quantification of growth phase measurements for $CaCl_2$, Ca:$PO_4$ at a ratio of 1:1, EDTA, Ca:EDTA at a ratio of 1:1. *** refers to a P value of $\leq 0.001$, ** refers to a P value of $\leq 0.01$, NS refers to a statistically non-significant result. N = 3, error bars refer to $\pm$ standard deviation.

A buffer consisting of ethylenediaminetetraacetic acid (EDTA) and $CaCl_2$ was made at an overall ionic concentration of 0.1 mM, with the knowledge that calcium preferentially binds to EDTA. It was found that the addition of EDTA alone did not have a significant effect on collagen assembly, as shown by Figure 4.11B. When added to calcium at a ratio of 1:1 it was also found that it prevented the detrimental effects of calcium on collagen (Figure 4.11C) much the same as when phosphate was added to the solution. This was further confirmed when looking at growth phase measurements (Figure 4.11D). The quantification indicated that the addition of EDTA produced no significant difference in growth phase in comparison to the control, unlike the addition of calcium alone. This indicates that the calcium is preferentially binding to EDTA instead of collagen allowing the collagen to form without interference. From this we can infer that the calcium is also potentially interacting with phosphate, preventing it from influencing the collagen molecule as drastically as it would if on its own.

### 4.3.2 Investigation of the Early Mineralisation of Collagen

Early mineralisation of collagen is not well understood. Therefore, fibrillogenesis profiles of early stage precipitation ratios of Ca:$PO_4$ were measured. Initially Ca:$PO_4$ ratios ranging from 1:0.2 - 1:1 were investigated, with a consistent calcium concentration of 2 mM. The absorbance of each ratio of Ca:$PO_4$ was measured to determine which ratio gave the initial signs of precipitation. Collagen was gelled within a calcium phosphate buffer, with a calcium concentration of 2 mM and phosphate concentration ranging from 0 - 2 mM. Gels were incubated for 2 hrs to ensure they were fully gelled before maximum absorbance was measured. Figure 4.12 shows that a phosphate concentration of 1.2 mM gave an initial increase in absorbance, corresponding to a Ca:$PO_4$ ratio of 1:0.6. Therefore this ratio was further investigated.

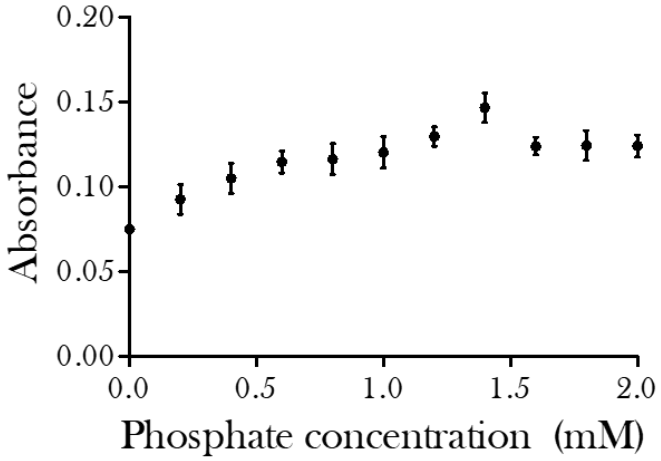



Figure 4.12: Maximum absorbance measurements of collagen with excess calcium at a concentration of 2 mM and phosphate at a concentration ranging from 0 - 2 mM. N = 3, error bars refer to ± standard deviation.

Figure 4.13A-C shows the fibrillogenesis profile of Ca:$PO_4$ ratios of 1:0, 1:0.6 and 1:1 respectively, indicating that the presence of each ion does not have a significantly detrimental effect on collagen assembly. Growth phase measurements, Figure 4.13D, show how only high ratios of calcium and phosphate alter early stage fibril formation, with there being no significant difference at early precipitation. Figure 4.13E, however, shows how early precipitation does have an effect on plateau time. Plateau time is defined

as the time at which turbidity stops increasing indicating changes in fibril assembly alone [297]. This seems to indicate that early stage mineralisation, while not effecting fibril formation, does effect fibril-fibril interaction at later stages of matrix formation.

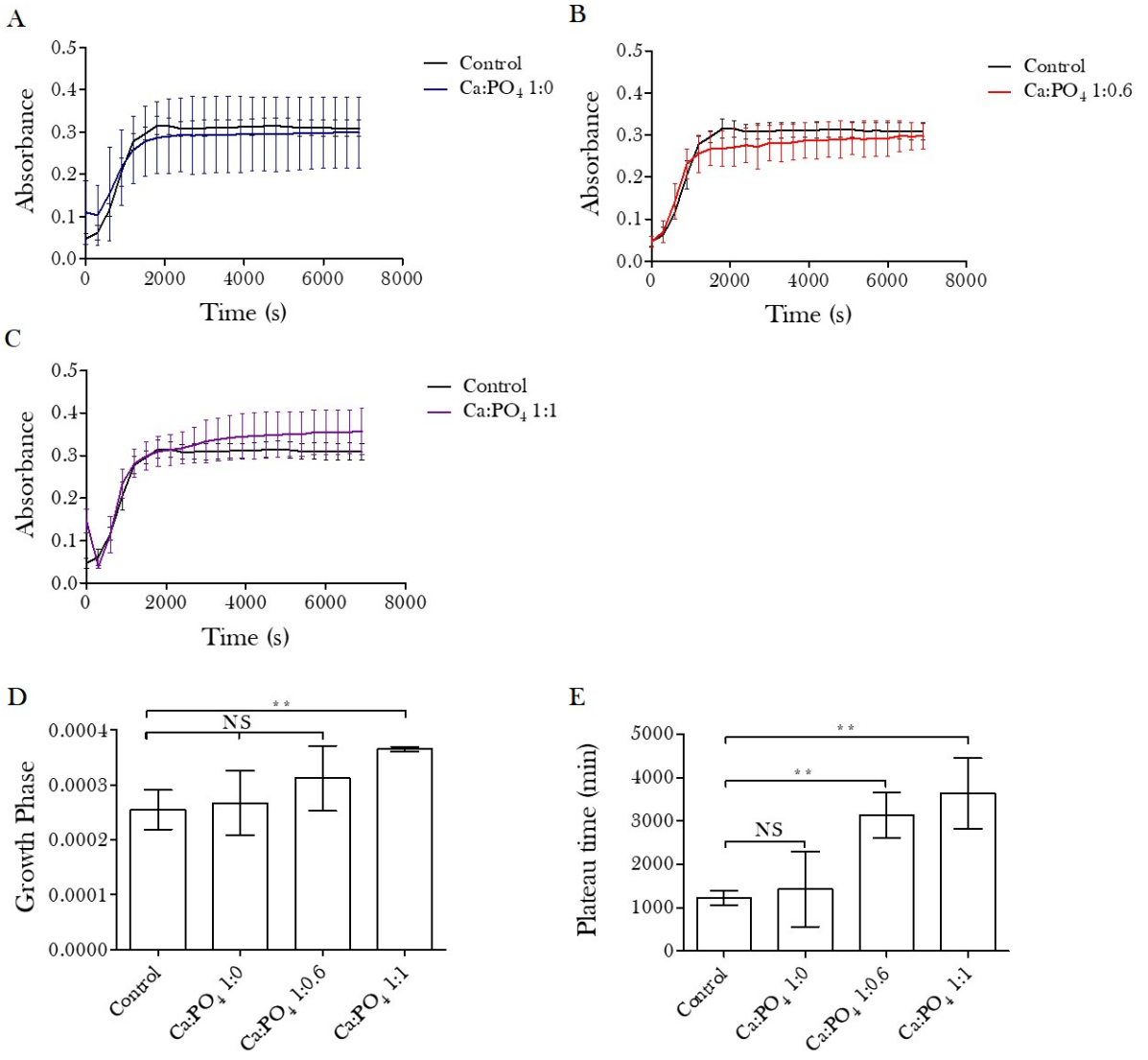



Figure 4.13: Fibrillogenesis of (A) $Ca:PO_4$ at a ratio of (A) 1:0, (B) 1:0.6 and (C) 1:1 all with calcium at a concentration of 2 mM. Growth phase (D) and plateau time (E) of each ratio. ** refers to a P value of $\leq 0.01$, NS refers to a statistically non significant result. N = 3, error bars refer to $\pm$ standard deviation.

AFM images of $Ca:PO_4$ at ratios of 1:0.6 and 1:1 at precipitation concentrations indicated a change in fibril formation at 35 min and 120 min, as shown in Figure 4.14A. Initial fibril formation can be seen in both the control and $Ca:PO_4$ 1:0.6 at 35 min, which is not visible at a ratio of 1:1. Full fibril formation is visible within all samples, with more

defined fibrils in the control sample and Ca:$PO_4$ ratio of 1:1. Figure 4.14B shows the fibril diameter of each sample after an incubation period of 120 min. Fibril diameter indicated that a Ca:$PO_4$ ratio of 1:0.6, had a significant decrease in fibril concentration, with a ratio of 1:1 having a non significant difference between 1:0.6, and a significant difference with respect to the control.

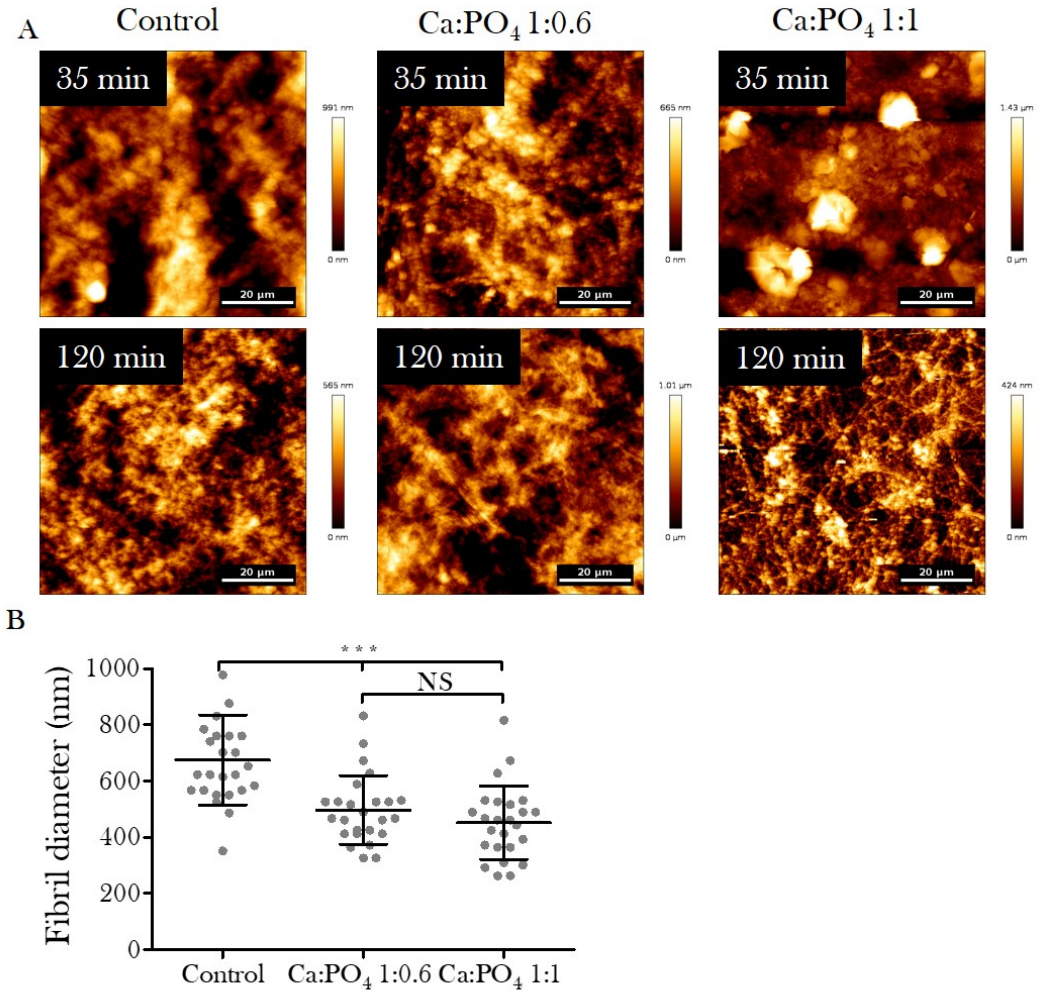



Figure 4.14: (A) AFM images of control collagen, Ca:$PO_4$ at a ratio of 1:0.6 and Ca:$PO_4$ at a ratio of 1:1 at a higher calcium concentration of 2 mM. (B) Fibril diameter measured from AFM images of each sample. ** refers to a P value of $\leq 0.01$, NS refers to a statistically non significant result. N = 75 across 3 biological samples, error bars refer to $\pm$ standard deviation. Scale bar is 2 $\mu$m.

## 4.4 Discussion

Both CD and zeta potential investigations indicated that both calcium and phosphate interacted with collagen molecules. CD data showed how excess calcium ions and excess phosphate ions caused a change in conformation of the triple helix. However, when in the presence of both calcium and phosphate ions, the triple helix retains its structure. DLS measurements also indicated that the addition of calcium and phosphate in excess caused a reduction in molecule size, with calcium ions causing a more significant hydrodynamic radius reduction. However, although calcium phosphate causes a slight reduction it is not significantly less than that of control collagen.

We hypothesise that the change in conformation is due to the size of the individual ions and calcium phosphate complex. If each ion/complex is able to interact with the surface of the collagen molecule it would be able to distort the triple helix structure resulting in a change in molecule confirmation. A smaller ion would cause surface groups which are attracted to it to be more greatly displaced than a larger ion/complex. Calcium ions have a radius of 217 pm [300] and phosphate ions have a radius of 238 pm [301], so are both small enough to cause a drastic conformational change. However, Posner clusters (clusters of both calcium and phosphate indicative of early stage mineralisation) have a radius of 1000 pm [302]. This means that Posner clusters are approximately five times larger than each individual component. Therefore, interactions between a calcium ion and a collagen surface group would result in larger distortion of the triple helix than a Posner cluser, as schematically depicted in Figure 4.15.

This would explain why CD shows an intact triple helix when collagen is in the presence of excess calcium phosphate as the cluster is unable to drastically alter the shape of the triple helix, preventing detrimental conformational changes. We hypothesise that interaction happens across the entire collagen molecule as CD titration data (Appendix 1, Figure 7.12) indicated that there are 6000 binding sites for both calcium and phosphate respectively, equating to approximately two binding sites per amino acid residue. Zeta potential indicated that the addition of calcium phosphate interacted with the collagen

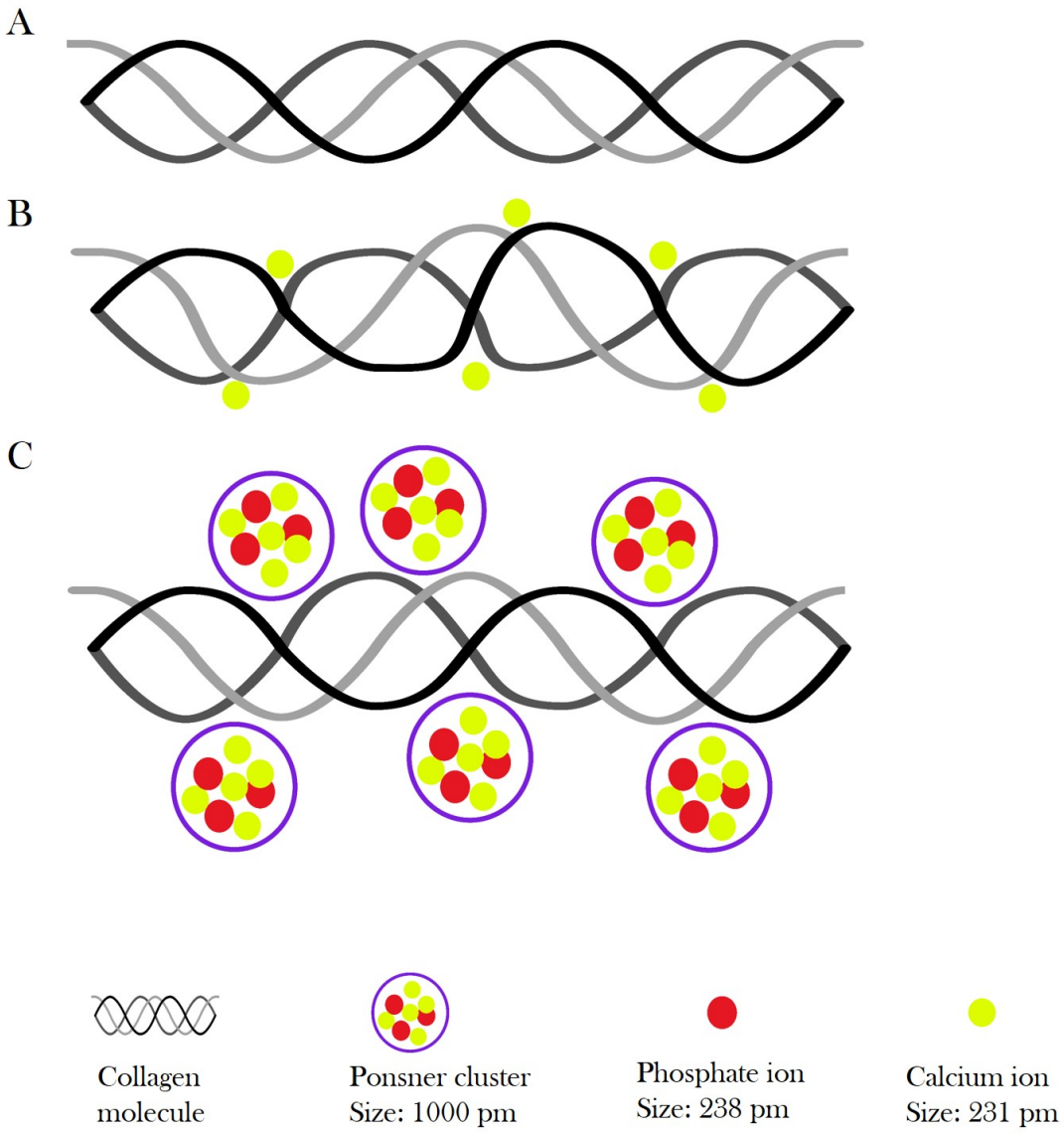



Figure 4.15: Schematic showing (A) an unaffected collagen molecule, (B) a collagen molecule distorted by calcium ions and (C) a collagen molecule distorted by Posner's clusters. Not to scale.

present within the sample, increasing its likelihood of aggregation.

As there was a change in zeta potential, we know any changes in molecule or fibril formation are still due to an interaction between collagen and calcium phosphate, rather than phosphate preferentially binding to calcium ions preventing them from adversely interacting with collagen. As calcium is divalent it has a strong affinity for the peptide groups in collagen. The large dipole moment on specific groups, such as carboxyl or amino groups, in collagen seem to provide preferential adsorption of divalent ions due to both

the positive and negative charges on each collagen group [225]. This suggests that it is the calcium which interacts with the surface of the collagen molecule, with electrostatic repulsion forcing the phosphate to form a layer on the outer most edge of the calcium. As phosphate is a negative ion, it provides the same interaction sites that would be present from the hydroxyl and carbonyl groups present in collagen. These sites are essential for water bridges which form the backbone of collagen aggregation [274].

This process is also confirmed by the fibrillogenesis profile of collagen and calcium phosphate. The growth phase of collagen when in the presence of Ca:$PO_4$ 1:1 is less significantly different from the control than when collagen is in the presence of $CaCl_2$ alone. This shows how calcium phosphate interacts with the collagen molecule in a way which still allows for intermolecular binding and therefore fibril formation. However, this process is slower than that of control collagen. The addition of lower ratios of phosphate to calcium indicates that the size of the Posner cluster has an effect on the rate of growth of fibrils. Even low concentrations of phosphate were still able to prevent calcium from interacting with the collagen molecules in a way that prevented fibril formation. This process is further confirmed by AFM images. By adding excess $CaCl_2$, collagen fibrils were unable to form, leaving only aggregation of globular proteins rather than fully defined fibrils. Calcium phosphate, however, produced highly defined fibrils, similar to that of control collagen. Fibril diameter measurements also show that calcium chloride interacts with the collagen molecule in a way that significantly reduces fibril diameter. In comparison, the addition of excess calcium phosphate did not alter the fibril diameter significantly from that of the control, further determining that calcium phosphate interaction with collagen molecules does not hinder fibril formation.

By looking at calcium phosphate ratios that were slightly higher than that of HA, at concentrations that had visible precipitation, it was clear that fibrillogenesis profiles were similar to that of the control. Growth phase measurements showed how physiological ratios only effected later stage fibril formation (plateau phase) rather than early stage (growth phase). This further indicates that calcium phosphate is interacting with the

collagen molecule in a way that allows for unaffected fibril formation, effecting only fibril assembly and not formation. AFM images visualise this change, as ratios of Ca:$PO_4$ 1:1 at a calcium concentration of 2 mM do not have the early stages of fibril formation at 35 min. Only globular regions of proteins are present at 35 min, although fully formed fibrils are present at 120 min. For physiological ratios early stage fibril formation can be seen at 35 min, also indicating that this ratio does not influence early stage development as shown from fibrillogenesis and growth phase measurements. Quantification of fibril diameter at higher calcium concentration further shows that the interaction of calcium chloride with collagen molecules causes a decrease in the fibril diameter. This again suggests that calcium phosphate influence only effects later stage assembly of fibrils.

## 4.5 Conclusion

Calcium and phosphate have an adverse effect on collagen formation. Both, when added in excess, cause changes in the conformation of collagen molecules and prevent fibril formation. However, when calcium phosphate is present, collagen molecule conformational changes do not occur and fibril formation is similar to that of control collagen. We suggest that is due to the size of each individual ion and the size of Posner clusters. Both calcium and phosphate ions are much smaller than Posner clusters. Any deformation caused from the ions interacting with the surface will be more significant with smaller ions than the Posner complex. This allows for fibril formation and assembly that matches that of control collagen. When looking at physiological ratios of calcium phosphate (Ca:$PO_4$ 1:0.6) it is clear that surface interaction of calcium phosphate with collagen only interferes with later stage development yet still provides intact fibrils.

This data seems to support the idea that early fibril mineralisation occurs after Posner clusters have formed. As there are multiple binding sites along the surface of the collagen molecule, as indicated by CD data, it is clear that mineralisation occurs across the whole collagen molecule rather than at the terminals. Posner clusters must form prior to

mineralisation to prevent breakdown of collagen fibril formation, something that would be caused by each component of the cluster individually.

# CHAPTER 5

# INFLUENCE OF SURFACE CHEMISTRY AND TOPOGRAPHICAL CUES ON COLLAGEN MATRIX FORMATION

Corneal blindness is a worldwide problem caused by both traumatic injuries and disease. Corneal trauma is responsible for half a million new cases of blindness per year. The only treatment for corneal blindness as a result of corneal laceration is keratoplasty. This is heavily reliant on highly skilled surgeons, eye-banks and surgical facilities. Furthermore, there is a high risk of infection and graft rejection. These treatments are not so readily available within the developing world. The cornea is mainly comprised by the stroma (90%) which has extensively organized ECM. This ECM is responsible for both the transparency and mechanical properties of the cornea. However, during wound healing the ECM is deposited rapidly, resulting in abnormal protein content and organisation. This change in organisation within the corneal epithelium and stroma can result in scarring which alters the transparency and function of the cornea. This can result in scar induced blindness. Within this chapter, external manipulation of collagen type I to force orientation and alignment is investigated. Through the use of surface chemistry and topography collagen was perpendicularly aligned to the nanopatterned edge. A ridge to gap ratio of 1.5 and a depth of 1000 nm resulted in approximately 60% perpendicular collagen alignment. This structure was replicated in IP-DIP (a biocompatible, high resolution surface) to determine whether the collagen alignment preferentially aligns cells seeded onto the surface instead of the cells orientating with the pattern underneath. It suggested that the perpendicular alignment of collagen caused an increase in randomisation of cellular cytoskeleton, however due to the surface area of the IP-DIP being considerably smaller than cell size, quantification was not possible. The underlying mechanism as to why perpendicular alignment occurs is unclear, however it appears to be due to regular attachment points on the ridge edges alongside it being more energetically favourable for collagen to align perpendicular rather than parallel to the pattern.

## 5.1 Introduction

Corneal disease and corneal traumatic injuries are a major cause of worldwide blindness. Corneal ulceration and ocular trauma are responsible for 1.5-2 million new cases of blindness every year, with half a million of these being trauma alone [303, 304]. Commonly, patients who have suffered these types of corneal injuries are classed as visually disabled, due to the injuries being more commonly monocular [303]. Trauma is often the most significant cause of unilateral loss, especially within developing countries [305]. Currently, the only treatment for corneal blindness is keratoplasty. This relies heavily on highly skilled surgeons, good surgical facilities and reliable eye-bank facilities. In addition, there is a risk of graft rejection and infection following surgical procedure. Treatment to minimise these risks is not so readily available within the developing world [303, 306].

Many pharmaco-therapeutic products have been used to try and enhance wound healing properties [306–308]. For example, epidermal growth factor, once applied to the injury site, binds to its transmembrane receptor, causing an activation intercellularly of several metabolic events. This stimulates the proliferation and differentiation of epithelial cells in the limbus and peripheral cornea, therefore re-epithelializing the corneal surface [307]. These products are usually applied as an eye drop or incorporated into a contact lens. Applications are typically frequent, increasing the cost required to store multiple doses and for trained professionals to administer [307]. Adhesives have also been considered to improve wound healing rate following corneal traumatic injury. This process involves gluing the cornea at the sight of injury reducing scarring and inflammation effects. Although this process is more effective than using sutures, it is only suitable for ocular injury from lacerations. The process still requires trained professionals to administer and a time limitation on application of product [309, 310]. Although 80% of all corneal blindness is preventable, many developing countries do not have the economic support for ocular treatment [311].

The cornea is predominately constituted by the stroma, which encompasses 90% of the corneal depth. The anterior of the stroma is covered with epithelium, with the posterior

covered with endothelium. The predominant role of the ECM in the eye is to focus light towards the retina, therefore, it needs to be both transparent and curved. Both these qualities are due to the highly organised hierarchical extracellular matrix (ECM), consisting of regularly spaced collagen fibres with both uniform interfibrillar space and diameter [312, 313]. The ECM within the eye defines both tissue function and form. Mechanical properties and the protective outer layer of the connective ocular tissues define both the transparency and shape of the cornea. This allows light to be focussed into the back of the retina. The connective tissues are predominately comprised of collagen, with the properties of the ocular ECM determined by the unique spatial organisation of the tissue components [314].

Within the cornea, these collagen fibres weave together to form an orthogonal, 3- dimensional refractive lens. The cornea has distinct patterns at different depths. Multi-layered collagen lamellae, running from the central region of the stroma towards the anterior end of the stroma, are organised both parallel and traverse to the corneal surface, as shown in Figure 5.1. The anterior lamellae have complex linking patterns, due to branching between fibrils, with multiple fibres bisecting the direction of the corneal surface. This forms a tightly woven 3-dimensional pattern of intertwined fibrils interacting with adjacent lamellae. This allows for an increase in mechanical stiffness and therefore produces a more rigid structure, maintaining the overall corneal shape. In comparison, the posterior collagen lamellae run mostly parallel to the corneal surface, with little to no branching. The collagen molecules within a hydrated human cornea have a 1.6 nm spacing. The regular spacing (65 nm) and uniform diameter (32 nm) of the collagen fibrils is required for transparency of the cornea. Non-collagenous materials bind to the gap regions within the cornea. [314].

Different cells within the cornea heal in different ways. Epithelial cells heal via movement and differentiation of limbal stem cells, however the epithelial cells themselves do not re-differentiate. Stromal cells require keratocytes to transform to myofibroblasts and fibroblasts, with considerable contribution from immune system cells. Endothelium cells

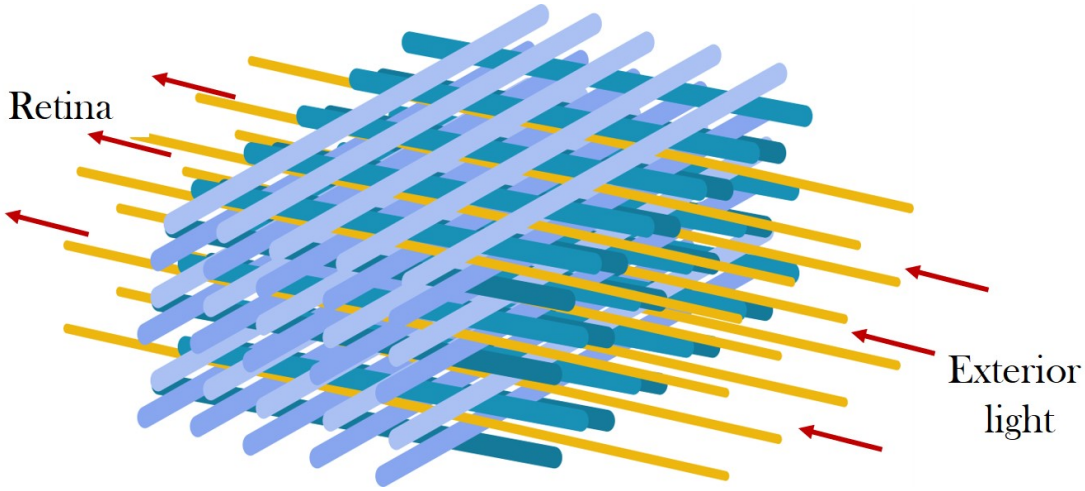



Figure 5.1: Structure of collagen within the cornea. Hash network of fibres at the anterior part of the eye which are regularly spaced to allow exterior light into the retina. Cartoon is not to scale. Blue lines represent collagen fibrils and yellow lines represent light. Shades only represent different layers of collagen fibrils.

heal via migration and spreading; re-differentiation may occur but only as a secondary process. All of these processes require the involvement of the ECM [315, 316].

Epithelium wound healing requires growth factors and ECM signal interactions to allow for a restoration of homeostasis and epithelial integrity. The ECM within the epithelium is basement membrane. During epithelium wound healing, the ECM undergoes degradation to allow for further production and reorganisation of the matrix. This remodelling, alongside the release of growth factors, creates a scaffold to direct migration of epithelial cells across the wound [315–318].

When wound healing occurs in the stroma, there are multiple changes to the surrounding cells such as keratocyte apoptosis and proinflammatory cytokine secretion. This in turn results in extensive ECM remodelling, from degradation to reassembly as close to native tissue as possible, to enhance structural support for wound healing cells. This new ECM often forms proteins that are atypical from the native ECM resulting in compositional and organisational changes. It is these changes to the newly deposited matrix which result in scar formation, reducing the function of the stromal tissue and resulting in a reduction in transparency [315, 318].

During corneal wound repair, it is essential that the surface maintains both a smooth

refractive surface (on the macro scale) - facilitated by a uniform epithelium, and a protective barrier [317, 319]. As the migration and differentiation of cells are dictated by the ECM, complete restoration of the corneal ECM is essential to maintain transparency and function of the cornea [317].

Therefore, in this chapter the external manipulation of collagen, resulting in organised and aligned fibrils, is investigated. This is achieved through the use of both surface chemistry and surface topography. The alignment, achieved in the perpendicular direction (from the patterned edge), was also used to determine whether collagen orientation and alignment is sufficient to influence cellular orientation over the underlying pattern.

## 5.2 Methodology

### 5.2.1 Patterned Surfaces

Surfaces were created originally using AutoCAD (2008). Images were extruded to the desired depths on AutoCAD and focus ion beam (FIB) milled into a silicon wafer by Datel (Datel Holdings Ltd, UK). Silicon wafers were n-type with a 100 crystal orientation. A NanoWizard® 4 NanoScience Atomic Force Microscope (JPK Instruments, DE) was used to determine parameters of each of the surfaces in contact mode. A PointProbe®Plus Non-Contact/Tapping Mode - High Resonance Frequency probe (Nanosensors, CH) with cantilever of 330 Hz frequency and 42 $Nm^{-1}$ spring constant was used to obtain each image. Scans were processed using JPK Data Processing Software (JPK Instruments, DE). Surfaces used to determine which pattern parameter was more significant in orientating collagen alignment were also created in AutoCAD, however samples were FIB milled using a Strata DB235 (FEI, OR, USA).

### 5.2.2 Alignment Measurements

Three biological repeats of each patterned surface with the desired collagen concentration were imaged *via* environmental scanning electron microscopy (ESEM), as described in

Section 2.1.11. Images were imported into ImageJ [207] and alignment angle with respect to ridge edge was measured. 25 random fibrils were measured over 3 biological samples (N=75) and results were analysed using a two-way paired t-test with respect to the control.

### 5.2.3 Surface Free Energy (SFE) of IP-DIP

Surfaces created via photolithography in IP-DIP had surface free energy measured following the protocol dictated in Section 2.1.13. However, a volume of 2 $\mu$L instead of 10 $\mu$L was used due to surface area of unpatterned IP-DIP. A two-way paired t-test was performed on the contact angle for pure water only measurements to determine any statistical significance between the data sets.

## 5.3 Results

### 5.3.1 Influence of Surface Chemistry

Having shown that the chemistry of the surrounding environment alters collagen assembly, the influence of surface chemistry was investigated. Polydimethylsiloxane (PDMS) was chosen as a starting material to chemically alter, due to its biocompatibility and wide use in medical devices [320–323]. The surface of PDMS can be altered *via* plasma treatment, silanization and sputtercoating providing a platform for surface chemistry changes.

To change the chemistry of PDMS, the surface was plasma treated (PDMSPlasma) for 10 mins. This changed the PDMS surface from hydrophobic to hydrophilic. In addition to this PDMS was sputtercoated with gold (PDMSAu) to provide another change in surface chemistry, as shown in Figure 5.2. To ensure that the gold coverage was significantly thick enough to alter the surface chemistry, both XRF and SEM images were taken. XRF images were taken of PDMS half sputtercoated with gold, clearly showing that there is a significant addition of gold to change the surface chemistry (Figure 5.2A). Furthermore, SEM images indicated that there was an uneven layer of gold on the PDMS surface with a clear distinction between gold treated and untreated PDMS (Figure 5.2B). Another

change in surface chemistry was created by first treating PDMS with plasma and then exposing to APTES (PDMSAPTES).

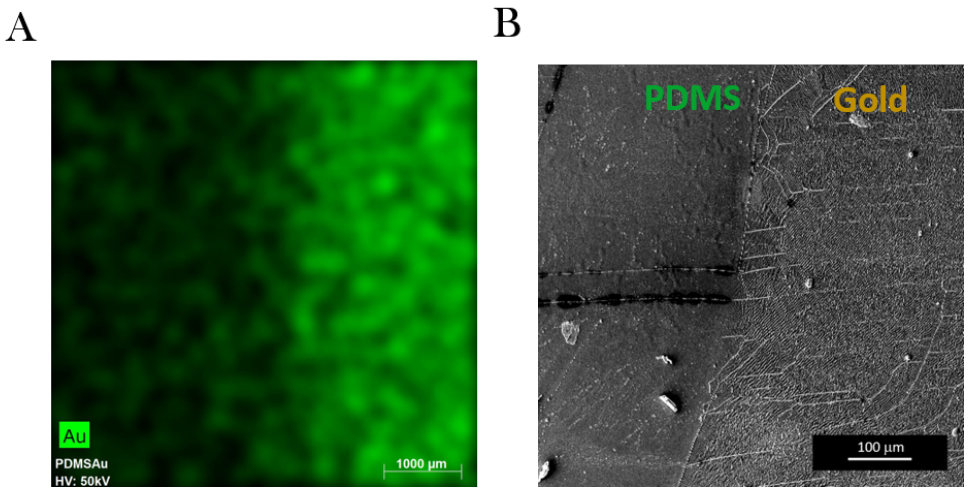



Figure 5.2: (A) XRF image of PDMS half sputtercoated with gold. Scale bar is 1000 $\mu$m. (B) SEM image of PDMS half sputtercoated with gold. Coating of gold is sufficient enough to result in a change in surface chemistry. Scale bar is 100 $\mu$m.

To determine the surface free energy (SFE) of each surface the contact angle of pure water, ethelyene glycol and diiodomethane on each of the five surfaces (silicon, PDMS, PDMSPlasma, PDMSAu and PDMSAPTES) was measured. A description of this methodology and the theory behind the calculation of surface free energy can be found in Section 2.1.13.

When looking at the contact angle of pure water alone, it is clear that PDMS is the most hydrophobic surface (Figure 5.3A). It also shows that PDMSPlasma is the most hydrophilic, with silicon chemistry being similar. By using the Zisman plot, as shown in Figure 5.3B, a specific profile can be determined for each surface. Through addition of the square of both the gradient and y-intercept of each line the surface free energy can be determined. These values are shown in Table 5.1. As PDMS is hydrophobic it had the lowest SFE, with PDMSPlasma having the highest as it is the most hydrophillic. The SFE for both silicon and PDMS lie within the range as stated in the literature [230, 324]. From SFE measurements it can be concluded that PDMSAu is the second most hydrophillic surface with PDMSAPTES lying between PDMSAu and silicon.

Collagen at a concentration of 0.5 mg $mL^{-1}$ was deposited onto all five of the surfaces

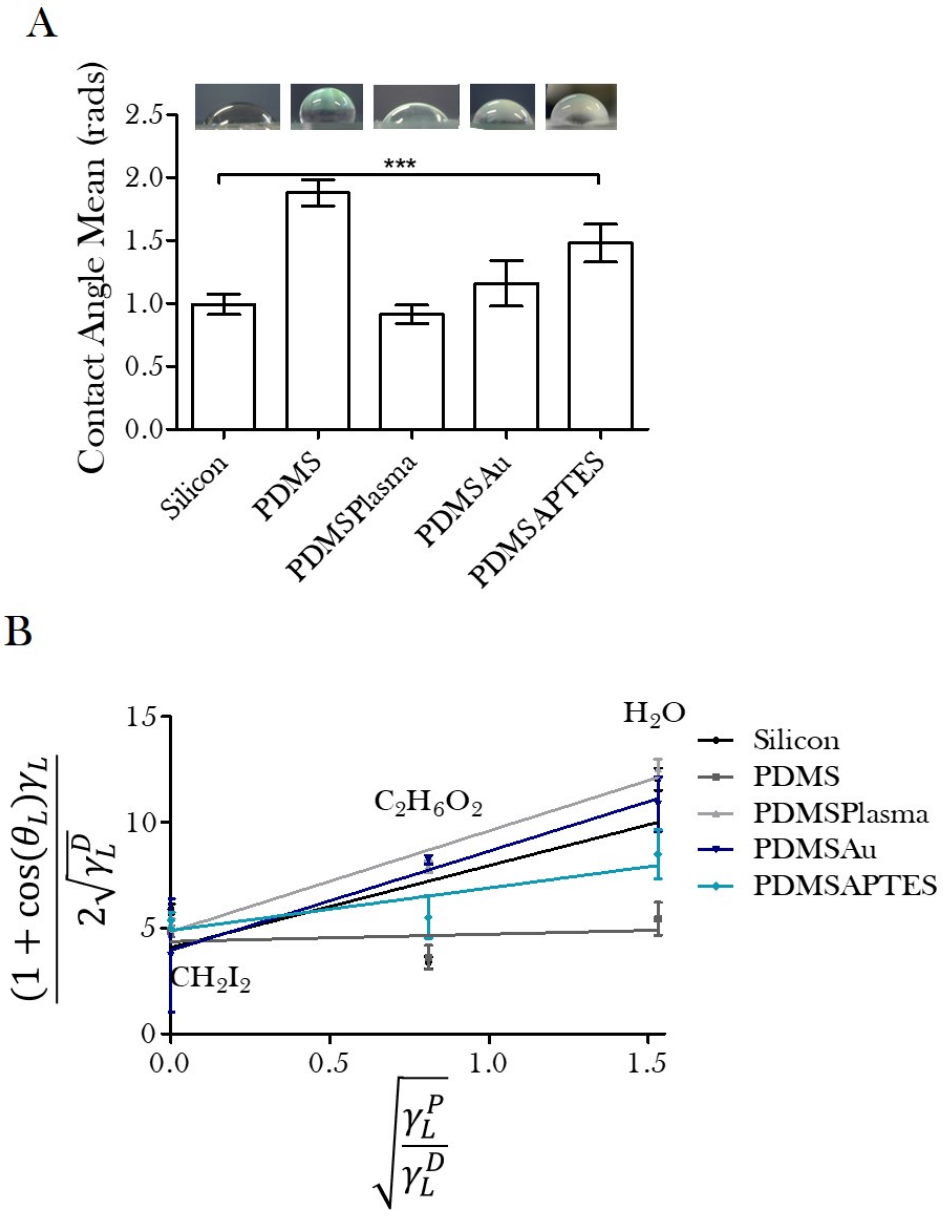



Figure 5.3: (A) Contact angle mean for each surface using pure water. (B) Zisman plot using diiodomethane ($CH_2I_2$), ethylene glycol ($C_2H_6O_2$) and pure water ($H_2O$) for each of the chemically altered surfaces. *** refers to a P value $\leq 0.001$ and ** refers to a P value $\leq 0.01$. N = 30, 5 measurements of both left and right side angles across 3 biological repeats. Error bars refer to $\pm$ standard deviation.

to determine collagen matrix formation. SEM images indicate that collagen fibrils formed on silicon, PDMSAu and PDMSAPTES as shown in Figure 5.4A-E. Although there is a difference in hydrophobicity between PDMS and PDMSPlasma, as shown from SFE, PDMSPlasma is a reversible process. Figure 5.4 indicates that the hydrophobic properties of PDMS prevent collagen from forming complete fibrils. Instead, collagen seems to form

Table 5.1: Surface free energy measurements calculated from Zisman plots for silicon, PDMS, PDMSPlasma, PDMSAu and PDMSAPTES

| **Surface** | **Surface free energy** ($\mathbf{mJ \cdot m^{-2}}$) |
|---|---|
| Silicon | 31.71 |
| PDMS | 19.18 |
| PDMSPlasma | 46.13 |
| PDMSAu | 37.64 |
| PDMSAPTES | 28.00 |

discrete globular masses. PDMSPlasma also produces similar results to PDMS, as the reversible properties of plasma treatment may occur faster than collagen fibrils take to form.

To quantify collagen fibril formation on each surface, alignment of fibrils with respect to the horizonal was measured. There was no significant difference between collagen formation on all surfaces except for PDMSAu as shown in Figure 5.4F. This indicates that surface chemistry does not have a large enough influence on collagen orientation to provide significant alignment changes, although Figure 5.4 clearly shows that surface chemistry has an influence on collagen assembly. However, PDMS sputtercoated with gold was the only surface with a topographical change. The increase in organisation of the collagen matrix may be influenced more due to surface topography rather than surface chemistry. Therefore, topographical influence on collagen assembly was investigated.

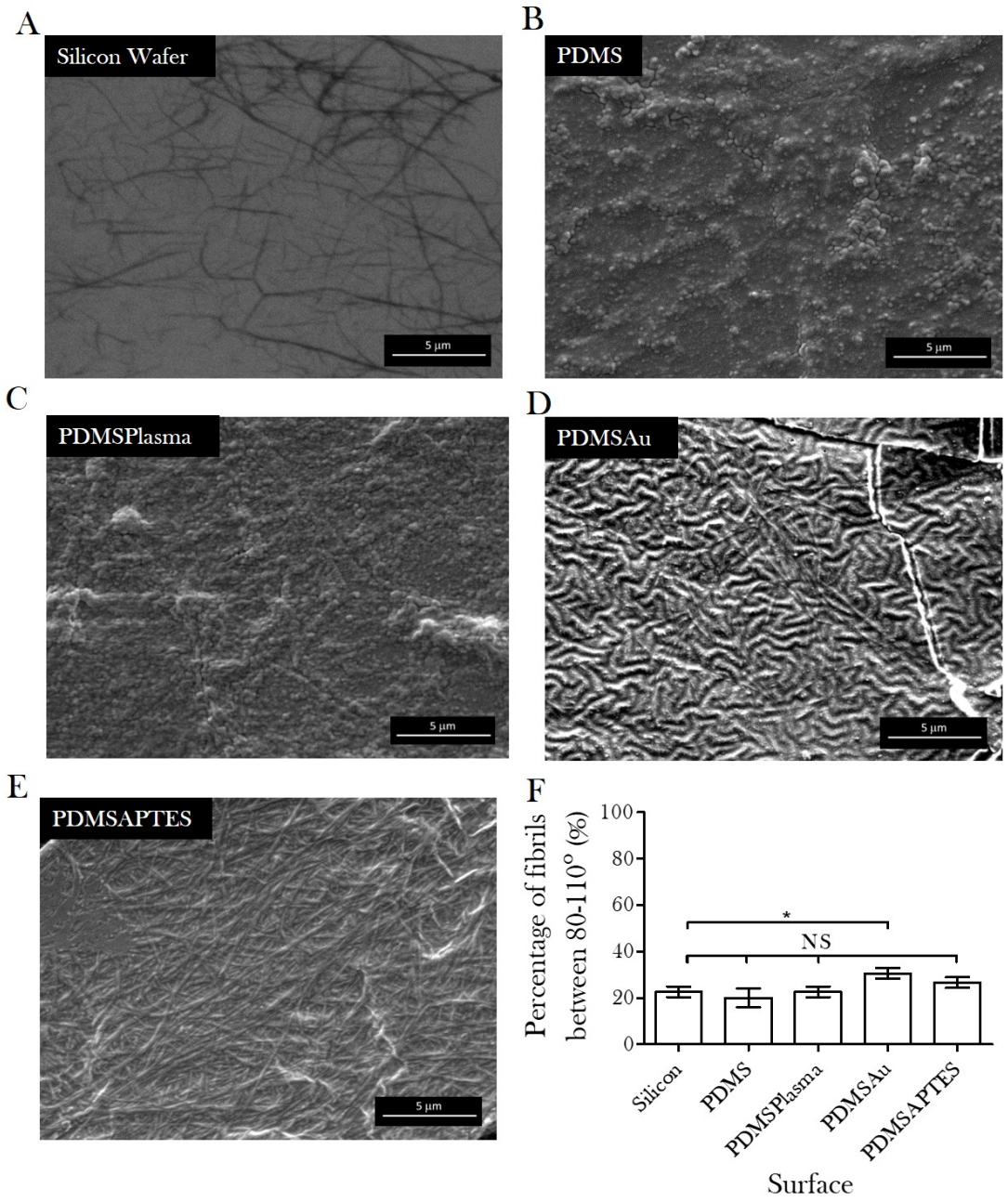



Figure 5.4: SEM images of 0.5 mg $mL^{-1}$ collagen deposited onto a (A) silicon wafer, (B) PDMS, (C) PDMSPlasma, (D) PDMSAu and (E) PDMSAPTES. PDMS and PDMSPlasma produced globular collagen rather than fully formed fibrils. The gold on PDMS formed an uneven layer changing the topography of the surface. (F) Percentage aligned of fibrils, measured from the horizontal, of 0.5 mg $mL^{-1}$ collagen deposited onto a silicon wafer, PDMS, PDMSPlasma, PDMSAu and PDMSAPTES. It was found that there was no significant difference in collagen assembly with respect to surface free energy, however PDMSAu, a surface with a topographical change, did provide a significant increase in organised collagen. * refers to a P value $\leq 0.05$, NS refers to a non-significant result. N = 3, error bars refer to $\pm$ standard deviation. Scale bar is 5 $\mu$m.

### 5.3.2 Topographical Influences

To determine the effect of topography on collagen alignment a total of 12 patterned surfaces were created using AutoCAD. The parameters of these surfaces can be found in Table 5.2.

Table 5.2: AutoCAD parameters for etching specific patterns into silicon wafers

| **Structure** | **Ridge Width (nm)** | **Gap Width (nm)** | **Gap Depth (nm)** | **Ridge to Gap (RG) Ratio** |
|---|---|---|---|---|
| 1.1 | 700 | 1000 | 1000 | 0.7 |
| 1.2 | 700 | 1000 | 500 | 0.7 |
| 1.3 | 700 | 1000 | 200 | 0.7 |
| 2.1 | 1000 | 700 | 1000 | 1.4 |
| 2.2 | 1000 | 700 | 500 | 1.4 |
| 2.3 | 1000 | 700 | 200 | 1.4 |
| 3.1 | 550 | 850 | 1000 | 0.6 |
| 3.2 | 550 | 850 | 500 | 0.6 |
| 3.3 | 550 | 850 | 200 | 0.6 |
| 4.1 | 850 | 550 | 1000 | 1.5 |
| 4.2 | 850 | 550 | 500 | 1.5 |
| 4.3 | 850 | 550 | 200 | 1.5 |

These surfaces were etched onto silicon wafers *via* focussed ion beam milling (Datel Holdings Ltd, UK). Three technical repeats were created to allow for surface reliability. AFM images of each surface allowed measurements of each parameter to be obtained, as shown in Figure 5.5. Each parameter was within one standard deviation from the original CAD file except for the ridge width of surface number 2 which was within two standard deviations of the original file, as indicated by Table 5.3. Masked average roughness was also measured from the AFM images for each of the four surfaces.

In order to determine the optimal topographical parameters for collagen alignment, a collagen concentration of 1 mg $mL^{-1}$ was deposited onto the etched silicon surface. SEM

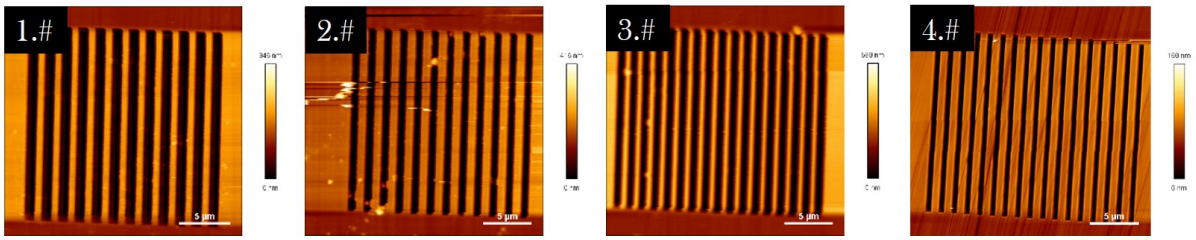



Figure 5.5: AFM images of each surface to ensure that the dimensions were the same as those created in the CAD file. Scale bar is 5 $\mu$m.

Table 5.3: Measured parameters from AFM images of etched silicon patterned surfaces

| **Structure** | **Ridge Width (nm)** | **Gap Width (nm)** | **Masked Average Roughness nm** |
|---|---|---|---|
| 1.1 | | | 141.00 |
| 1.2 | 698 ± 35 | 1008 ± 44 | 88.60 |
| 1.3 | | | 27.90 |
| 2.1 | | | 78.82 |
| 2.2 | 937 ± 47 | 708 ± 43 | 75.43 |
| 2.3 | | | 55.51 |
| 3.1 | | | 101.50 |
| 3.2 | 560 ± 51 | 830 ± 52 | 117.20 |
| 3.3 | | | 64.21 |
| 4.1 | | | 66.76 |
| 4.2 | 856 ± 59 | 537 ± 45 | 78.01 |
| 4.3 | | | 74.99 |

images were obtained for each surface as shown in Figure 5.6. Visually, surfaces with a RTG ratio of 0.7 did not allow for any form of collagen alignment (surface number 1). In comparison, surfaces 2, 3 and 4 seemed to indicated a preferential alignment of collagen in the perpendicular direction. The control image indicates that random deposition of collagen on a silicon wafer results in a randomised mesh-work of collagen fibrils, unlike that found on surfaces with RTG ratios of 1.4 and 1.5.

To determine which surfaces produced biologically reproducible results, images of three repeats were taken and alignment of collagen measured as the angle between ridge edge

and fibril. All surfaces which produced a perpendicular collagen alignment within 10° of each other were considered to be reliable, as shown in Figure 5.7 and are indicated by a red circle. Of those measurements which were reliable, only two patterns produced statistically significant results in comparison to the control, as indicated by a green circle.

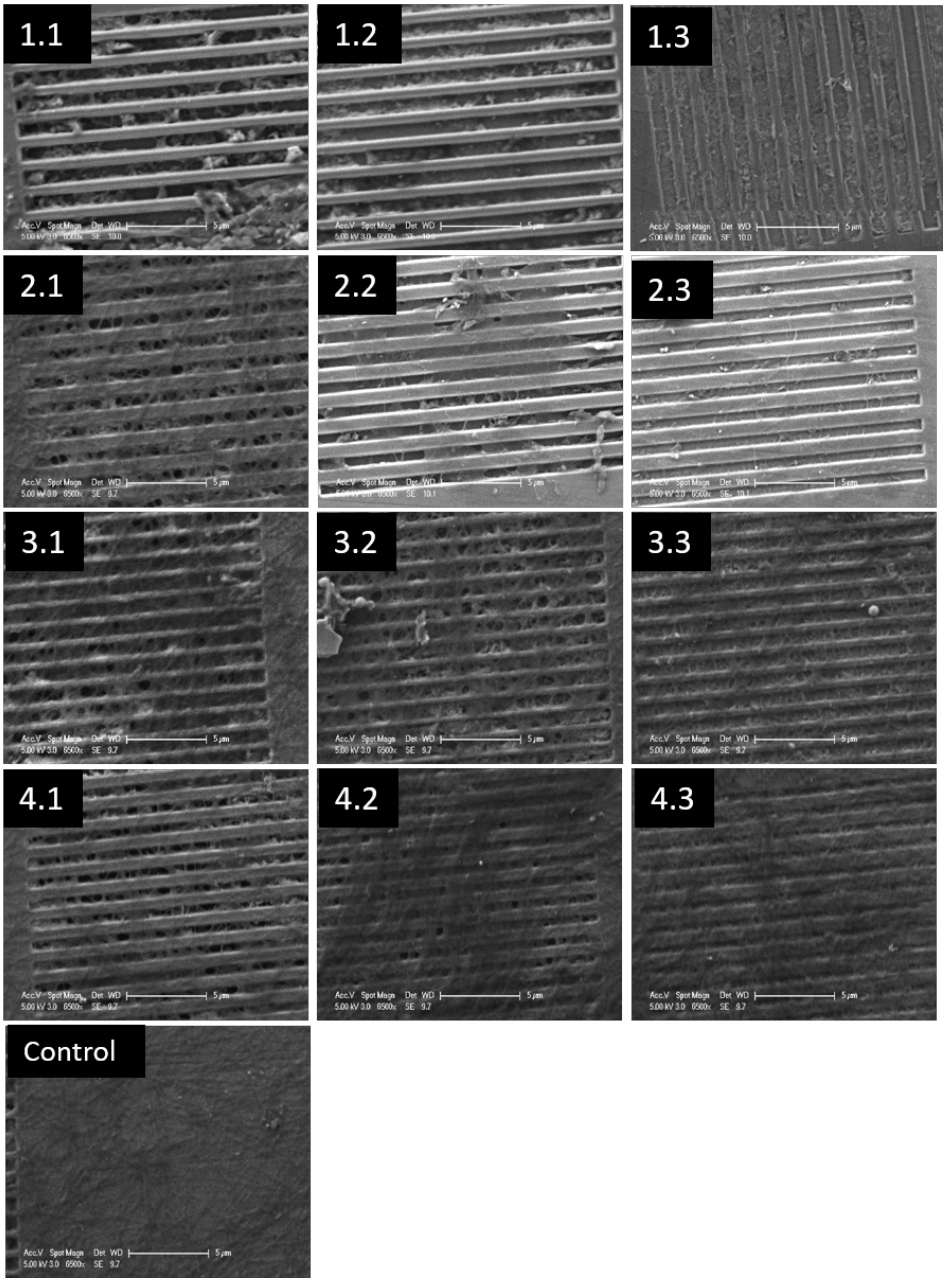



Figure 5.6: SEM images of 1 mg $mL^{-1}$ collagen deposited onto each patterned structure. Images taken in vacuum with a 5 kV beam. Scale bar is 5 $\mu$m. Ridge width (R), gap width (G) and depth (D) are as follows: 1.# (R) 700 nm, (G) 1000 nm, 2.# (R) 1000 nm, (G) 700 nm, 3.# (R) 550 nm, (G) 850 nm, 4.# (R) 850 nm, (G) 550 nm. #.1 (D) 1000 nm, #.2 (D) 500 nm, #.3 (D) 200 nm.

These patterns were RTG ratio of 1.4 and 1.5 with a depth of 500 nm and 1000 nm respectively. To determine whether surface roughness was a factor with regards to alignment, the percentage of fibrils perpendicularly aligned was correlated to the specific structural roughness. However Figure 5.7D clearly indicates that roughness does not have an effect on alignment orientation.

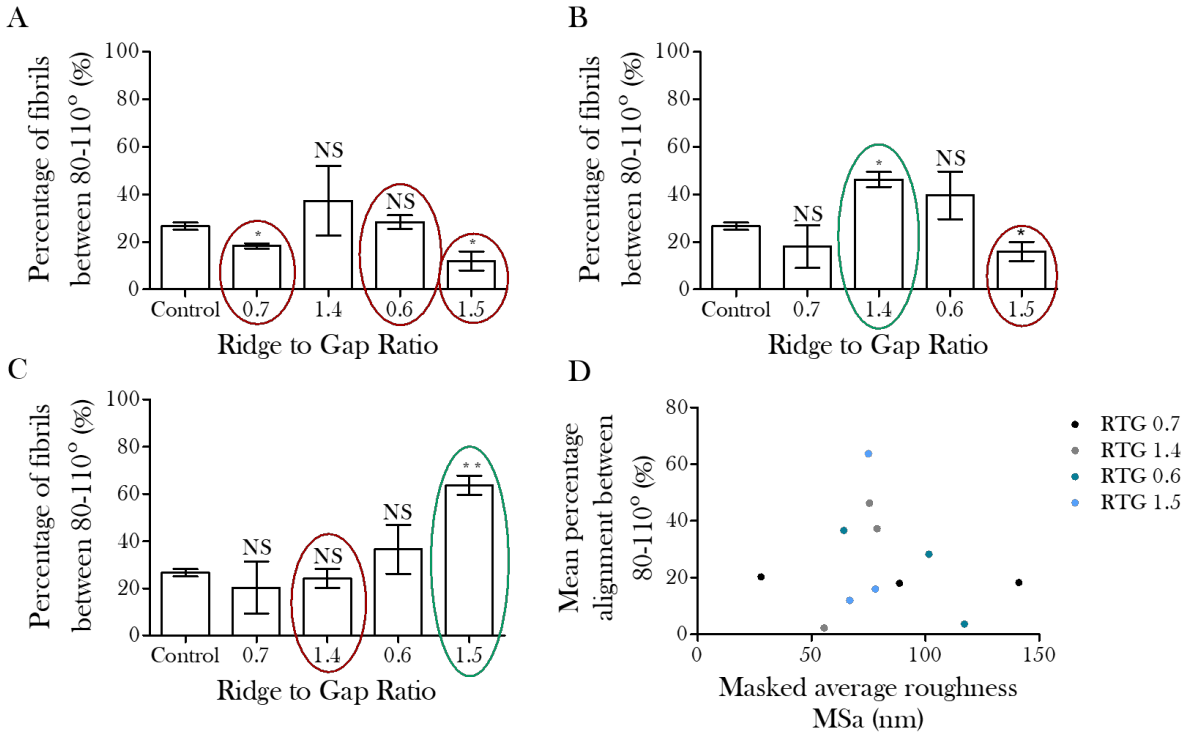



Figure 5.7: Percentage of fibrils aligned between 80-110° at depths of (A) 200 nm, (B) 500 nm, (C) 1000 nm. Red circles indicate biological repeats that are within 10° of each other, green circles indicate biological repeats that were statistically significant from the control. (D) Average percentage of fibrils at perpendicular alignment with respect to structural roughness.There is no correlation so roughness does not effect alignment organisation. ** refers to a P value $\leq 0.01$, * refers to a P value $\leq 0.05$ and NS refers to a non-significant result. N = 75 across 3 biological samples for (A), (B), and (C). N = 3 for (D). Error bars refer to $\pm$ standard deviation.

To ensure that alignment was not collagen concentration dependent concentrations of collagen at 0.5, 1, 1.25, 1.5 and 1.75 mg $mL^{-1}$ were all deposited onto patterns 2.2 (RTG 1.4 at 500 nm depth) and 4.1 (RTG 1.5 at 1000 nm depth). These were again imaged using SEM as shown in Figure 5.8. All concentrations visually preferred perpendicular alignment with little visual variation between concentrations.

To quantify collagen alignment at different concentrations the angle between the ridge

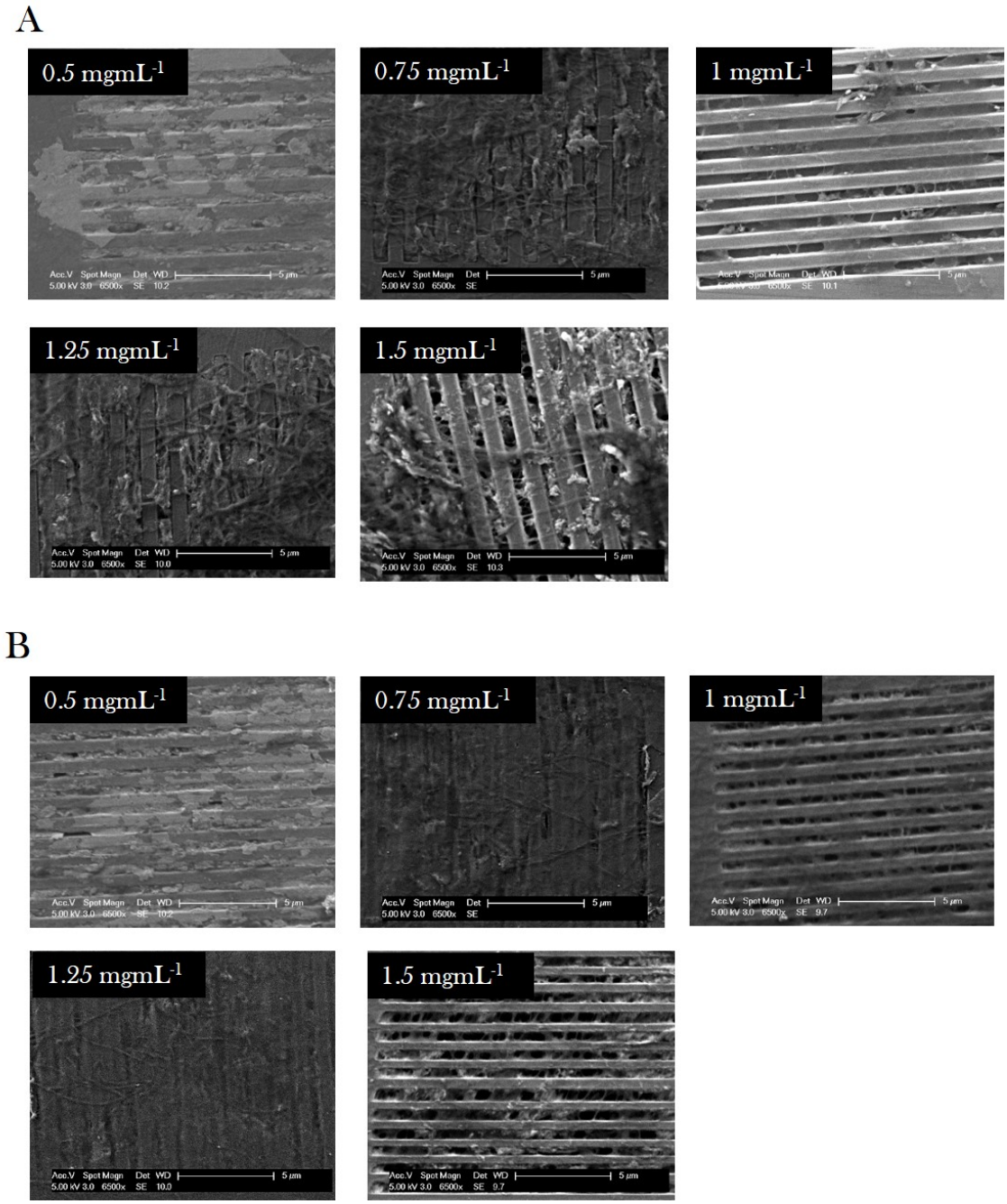



Figure 5.8: SEM images of varying concentrations of collagen on pattern structures with an RTG ratio of (A) 1.4 and (B) 1.5. Images taken in vacuum with a 5 kV beam. Scale bar is 5 $\mu$m.

edge and collagen fibril was again measured. It was found that all concentrations had a significant perpendicular alignment with the surface structure, however there was a higher degree of reliability between concentrations of collagen deposited onto the silicon patterned surface with a RTG ratio of 1.5. This quantification is shown in Figure 5.9.

As this surface provided both the highest percentage of fibril perpendicular alignment and lowest variability in collagen concentration it was deemed the most optimal surface pattern.

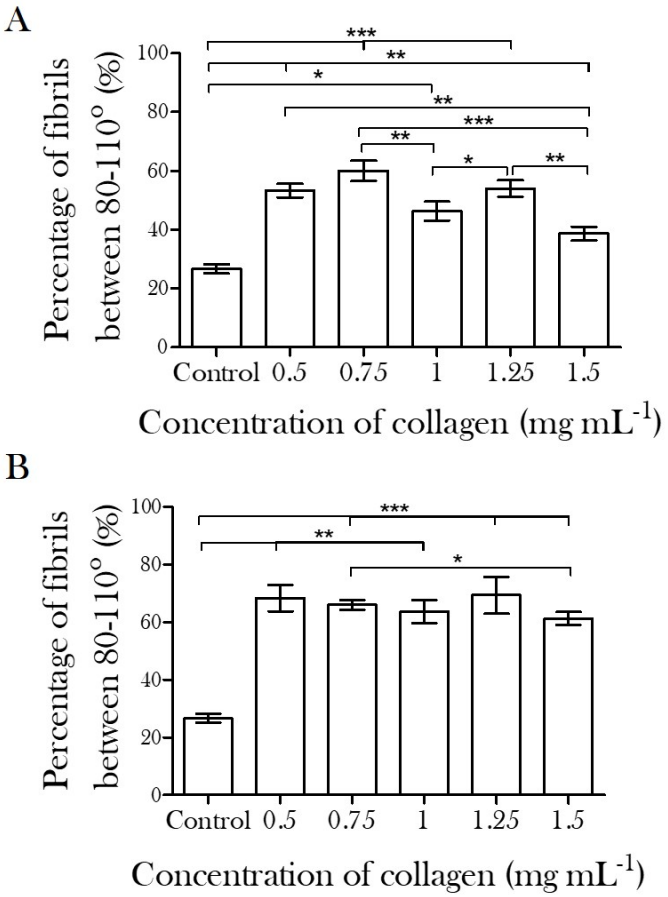



Figure 5.9: Quantification of percentage of fibrils aligned between 80 - 110° of the ridge edge. Alignment measured from SEM images of varying concentrations of collagen deposited onto pattern structures with a RTG ratio of (A) 1.4 and (B) 1.5. *** refers to a P value $\leq 0.001$, ** refers to a P value $\leq 0.01$, * refers to a P value $\leq 0.05$. N = 75 across 3 biological samples. Error bars refer to $\pm$ standard deviation.

### 5.3.3 Topographical Influence on Cell Alignment

In order to determine whether the underlying collagen alignment had a more significant influence on cell alignment than the patterned structure, patterned surfaces with ridge to gap ratio of 1.5 were created within a photoresist. Although silicon wafers were used to establish the optimal patterned surface for the highest percentage alignment, it is not a

suitable material for a corneal wound dressing. Therefore, an optically clear, biocompatible photoresist was chosen. IP-DIP was a suitable photoresist due to its biocompatability and high resolution as its refractive index matches the focusing optic required for fabrication [325–329].

To verify whether the surface chemistry of IP-DIP had an effect on collagen alignment, contact angle and surface free measurements were conducted. Figure 5.10A indicates that IP-DIP is a more hydrophobic surface than silicon. However, when looking at the Zisman plot (Figure 5.10B) and SFE values (Table 5.4) we can see that the surface free energy for silicon and IP-DIP are seemingly similar. This may indicate that they have similar surface chemistries and collagen will align in a similar manner.

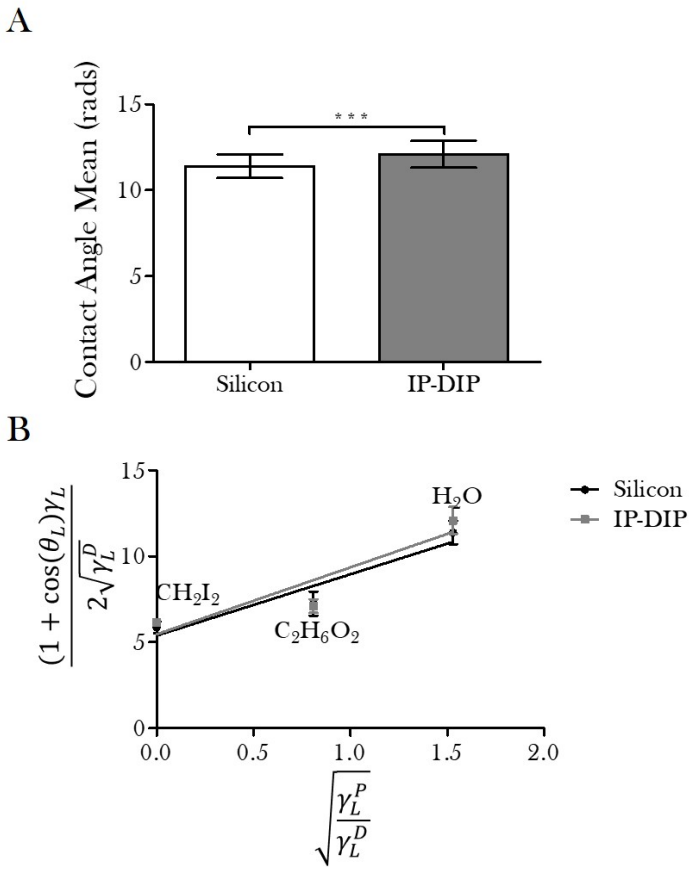



Figure 5.10: (A) Contact angle mean for both silicon wafer and IP-DIP non-patterned surface using pure water. (B) Zisman plot using diiodomethane ($CH_2I_2$), ethylene glycol ($C_2H_6O_2$) and pure water ($H_2O$) for silicon and IP-DIP. *** refers to a P value $\leq 0.001$. N = 30, 5 measurements of both left and right side angles across 3 biological repeats. Error bars refer to $\pm$ standard deviation.

Table 5.4: Surface free energy measurements calculated from Zisman plots for silicon and IP-DIP

| **Surface** | **Surface free energy** ($\mathbf{mJ \cdot m^{-2}}$) |
|---|---|
| Silicon | 41.82 |
| IP-DIP | 45.08 |

Collagen alignment was then investigated to ensure that patterned surfaces on IP-DIP still caused a high percentage of perpendicular alignment. Figure 5.11A shows a high level of alignment of 1 mg $mL^{-1}$ collagen when placed on the patterned surfaces. Figure 5.11B shows the random alignment of collagen when deposited onto a non-patterned section of IP-DIP.

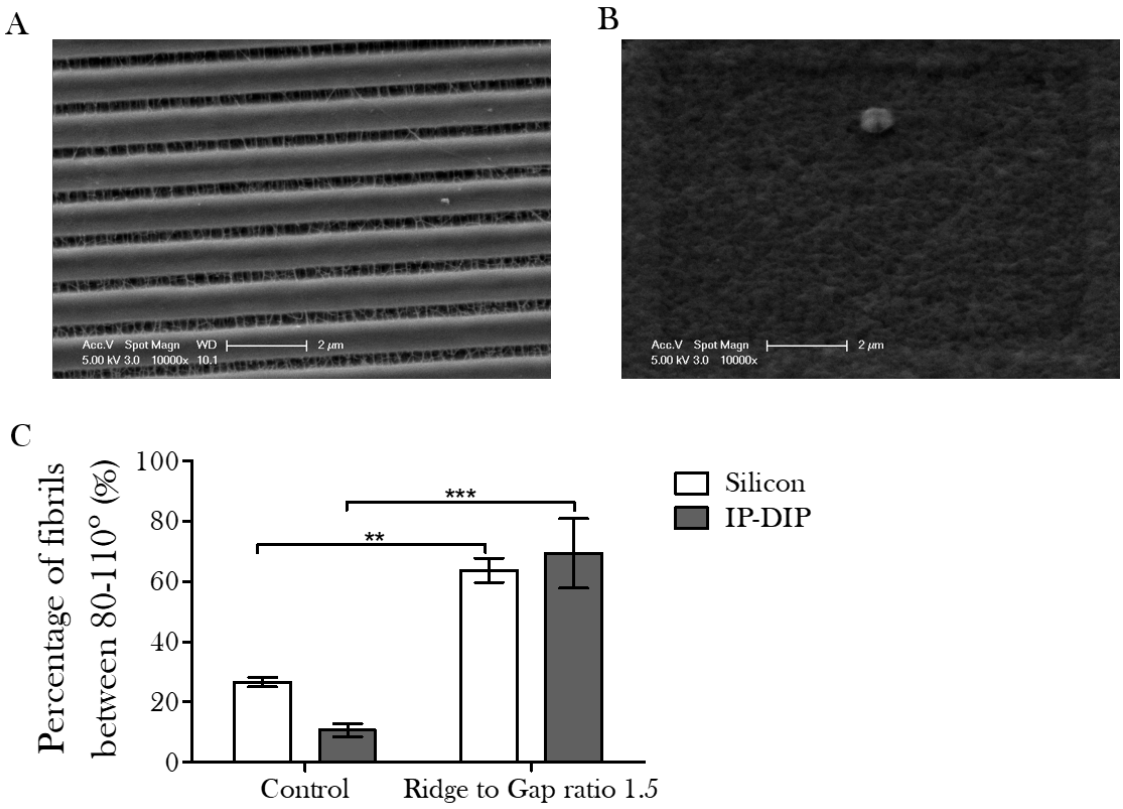



Figure 5.11: ESEM image of 1 mg $mL^{-1}$ collagen deposited onto (A) patterned IP-DIP and (B) non-patterned IP-DIP. (C) Quantification of the percentage of fibrils aligned between 80 - 110° of the ridge edge. ** refers to a P value $\leq 0.01$, *** refers to a P value $\leq 0.001$. N = 75 across 3 biological samples. Error bars refer to $\pm$ standard deviation. Scale bar is 2 $\mu$m.

Quantification of this alignment is shown in Figure 5.11C, with there being no significant difference between the percentage of fibrils that aligned perpendicular to the ridge edge between both silicon and IP-DIP. However, there is a significant difference between the percentage of fibrils aligned when compared to a non-patterned control surface of each material. This indicates that the underlying IP-DIP at a pattern with a ridge to gap ratio of 1.5 and depth of 1000 nm is highly aligning collagen aggregates.

To investigate biological influence corneal fibroblasts were cultured for 48 hrs on patterned and non-patterned IP-DIP surfaces and imaged under fluorescent and brightfield light. Figure 5.12 shows the difference between cellular alignment both with and without collagen present.

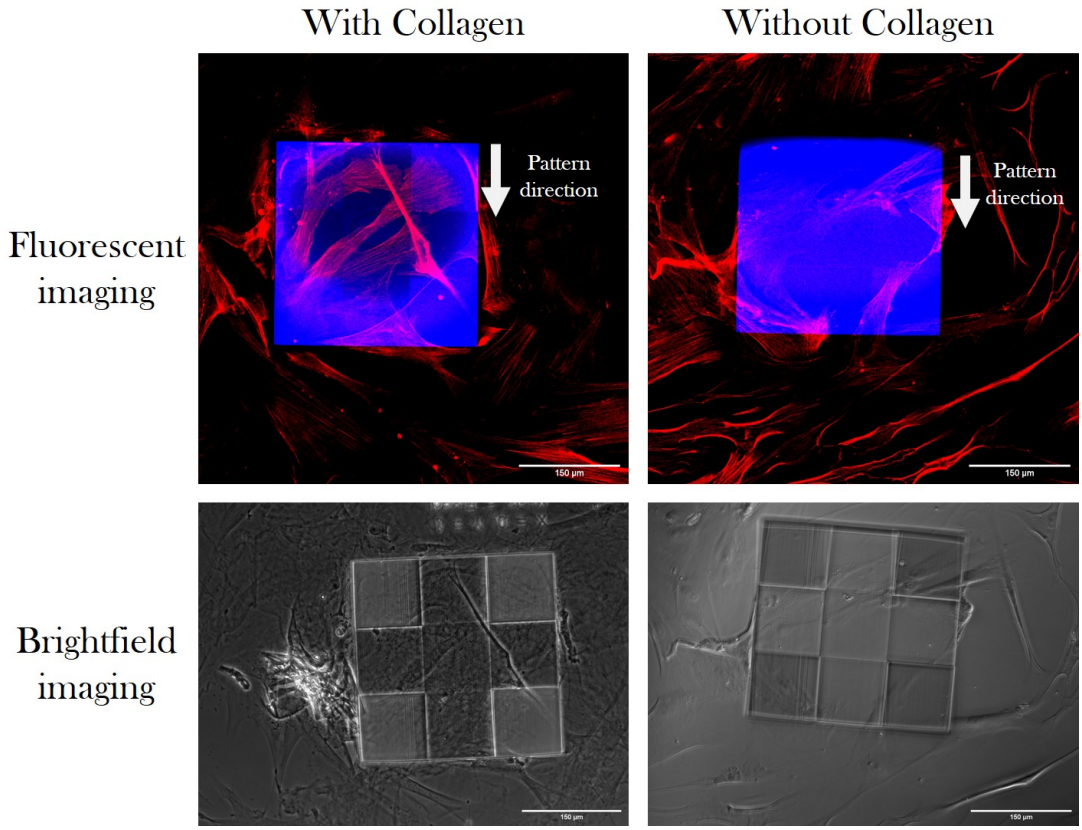



Figure 5.12: Fluorescent and brightfield images taken of corneal fibroblasts cultured for 48 hrs on patterened and non-pattered IP-DIP in the presence of collagen and without. Cells were stained with both Phalloidin (red) and DAPI (blue), however the DAPI dye stained the IP-DIP pattern very strongly preventing the visualization of cellular DNA. IP-DIP patterning was vertical as shown within brightfield images. Scale bar is 150 $\mu$m.

Visually, there is a potential that the presence of collagen causes an increase in the

random orientation of the cytoskeleton within the actin, however this is hard to quantify. This is shown by the red Phalloidin stain. Unfortunately, the DAPI dye stained the IP-DIP surface so strongly that visualization of cell DNA location was not possible. Therefore, the blue square only indicates the presence of the IP-DIP surface. Whether the underlying perpendicular alignment of collagen is sufficient to alter the alignment of cellular cytoskeleton is still unclear due to the size of the patterned surface (100 x 100 $\mu m^2$) in comparison to the cellular size (265.6 $\pm$ 10.65 $\mu$m [330]). Quantification could only be determined if there was a significant increase in the number of cells present on the patterned IP-DIP (all repeats can be found in Chapter 8 Figure 8.1, 8.2 and 8.3).

### 5.3.4 Understanding the Driving Forces Behind Alignment

As topographical investigations indicated that a ridge to gap ratio of 1.4 at 500 nm depth and a ridge to gap ratio of 1.5 at 1000 nm depth both gave significant increase in collagen alignment, it was still unclear whether ratio or depth was the largest influence on collagen matrix assembly. Nine surfaces, with ratios of 1.2, 1.4 and 1.6 each with depths of 500, 750 and 1000 nm, were investigated to look at collagen alignment more in depth. Focused ion beam milling was used to create the patterned surfaces, however the accuracy of the beam created surfaces with a ratio of 1.3 instead of 1.2.

Figure 5.13 shows SEM images of collagen deposited onto all nine surfaces. It can be seen that there are high levels of alignment on all surfaces with a ratio of both 1.3 and 1.4. However, it seems that collagen deposited onto the surface with a ratio of 1.6 were not so readily aligned in the perpendicular direction. It seems that less collagen overall grew across the gap and instead distinct globular areas of aggregation appear at the ridge edges.

Quantification confirmed that perpendicular alignment of collagen was preferred on surfaces with a ridge to gap ratio of 1.3 and 1.4. As there was no significant difference in percentage of fibrils aligned to the perpendicular between each depth, we can conclude that ratio is the greatest influential factor. All surfaces still had a significant increase in

collagen alignment in comparison to that of the control.

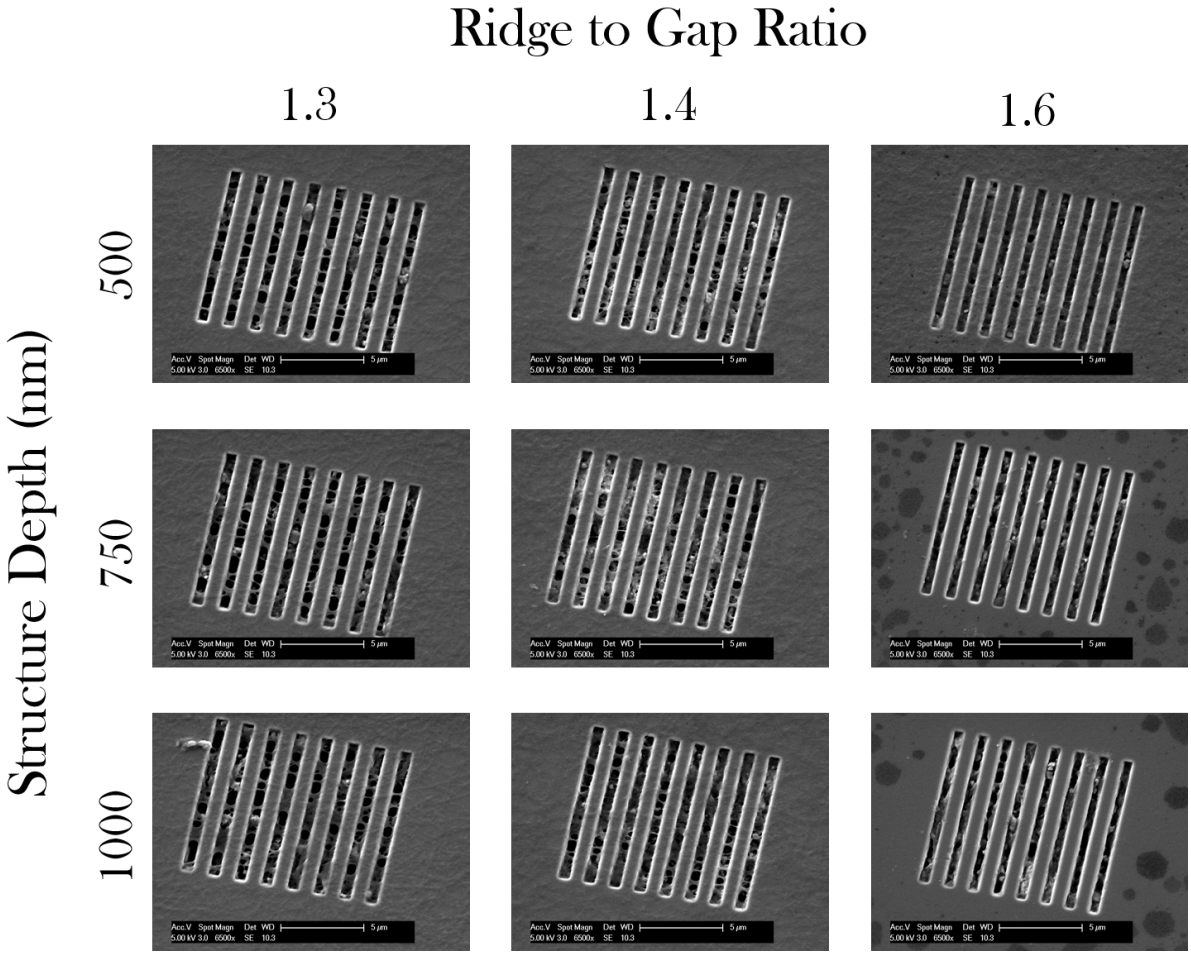



Figure 5.13: SEM images taken of collagen aligned on patterns with ridge to gap ratios of 1.3, 1.4 and 1.6 at depths of 500, 750 and 1000 nm to see whether ridge to gap ratio or depth is more influential for collagen alignment. Scale bar is 5 $\mu$m.

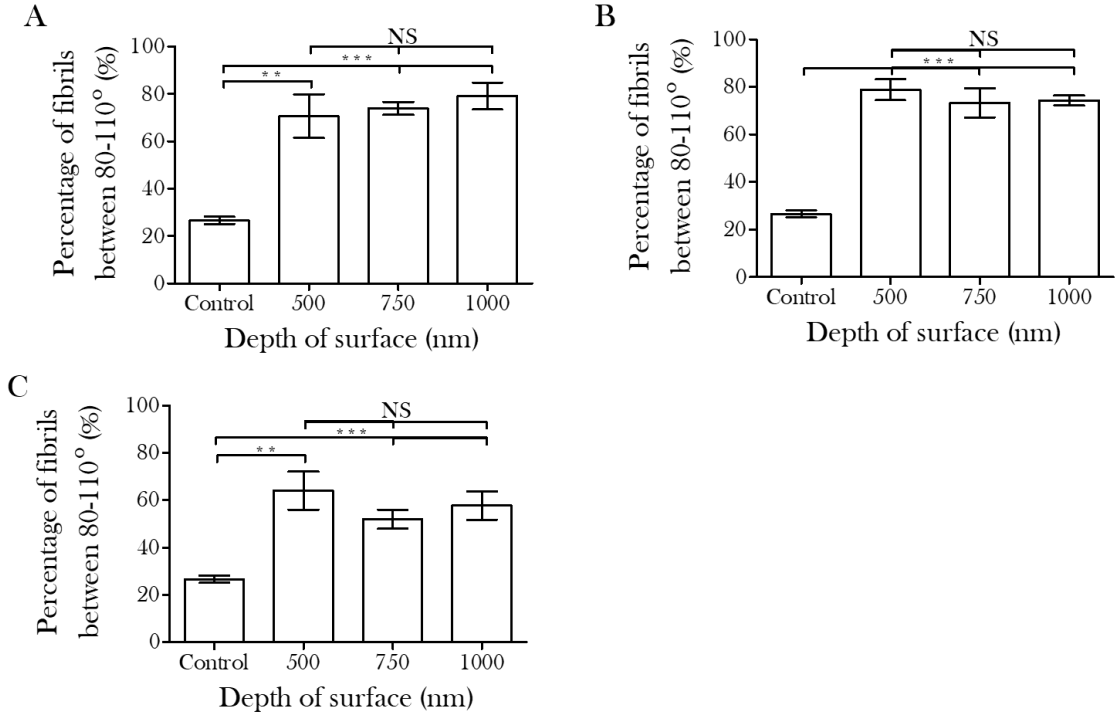



Figure 5.14: Quantification of percentage of fibrils aligned between 80 - 110° of the ridge edge. Alignment measured from SEM images of varying concentrations of collagen deposited onto pattern structures with an RTG ratio of (A) 1.3 (B) 1.4 and (C) 1.6. As there is no significant difference between the perpendicular alignment of collagen with respect to the depth we can conclude that ridge to gap ratio is the most influential factor in collagen alignment. N = 75 across 3 biological samples. Error bars refer to ± standard deviation.

## 5.4 Discussion

The chemical and physical environment in which collagen assembles influences its orientation. Surface chemistry was investigated to determine whether this had an overall influence on collagen assembly. Although multiple surface chemistries were investigated (Silicon wafer, PDMS, PDMSPlamsa, PDMSAu and PDMSAPTES) there was no overall influence on collagen orientation. There was a significant increase in collagen orientation in the perpendicular direction with gold sputtercoated PDMS, which during sputtercoating formed an uneven layer. This layer created a topographical structure, which may have influenced the collagen assembly. Therefore, topographical influence was investigated using the same surface material (to maintain similar surface chemistry).

A surface pattern created from a series of ridges and grooves (gaps) ranging in di-

mensions in the nanoscale (550-1000 nm in width, 200-1000 nm in depth) were created to determine collagen alignment. The surfaces were FIB-milled all with various RTG ratios. When collagen was deposited on the surface, it was found that it preferentially aligned perpendicular rather than parallel to the ridge/gap. It was found that an RTG ratio of 1.4 and gap depth of 500 nm and an RTG ratio of 1.5 and gap depth of 1000 nm gave the highest percentage of aligned collagen fibrils. To ensure that any alignment changes were not due to collagen concentration, collagen was deposited onto both surfaces at concentrations ranging from 0.5 – 1.5 mg $mL^{-1}$.

The surface with an RTG ratio of 1.5 was found to be the most consistent with fibril assembly and so was used to determine cellular alignment. Although previous experiments used a silicon wafer surface, this would not be sufficient for cellular imaging and analysis due to its opaqueness. Therefore, the surface pattern was recreated in IP-DIP, a biocompatible high-resolution photoresist. IP-DIP also allowed for a high level of collagen alignment in the perpendicular direction, with orientation being more statistically significant ($P \leq 0.001$) than that of silicon. It was still unclear, however, whether this alignment of collagen caused a change in the alignment of fibroblast cytoskeleton. Although visually there seems to be an increase in random cytoskeleton orientation with the presence of collagen, the surface area (100 x 100 $\mu m^2$) of the patterned IP-DIP was not sufficient to quantify alignment. Until this is repeated with a larger surface area of patterning, cellular alignment cannot be determined.

To fully understand whether depth or ratio had a more significant influence on collagen orientation, a smaller range of surface patterns were investigated. These surfaces indicated that RTG ratio had a larger influence on collagen alignment than depth of the gap. Overall, it was clear that RTG ratio caused a high percentage of collagen to align perpendicularly to the ridge edge.

Multiple studies have shown that a topographical surface consisting of ridges and grooves can orientate cells [331–334]. Patterned surfaces cause cells to orientate along the axis of the ridge using a phenomenon called contact guidance. This guidance is linked to

the orientation of intracellular matrix and deposited collagen, causing both to also align with the patterned surface [332, 334]. Although this has predominantly been shown to cause parallel alignment to the ridge edge, there are studies which have found that cells align perpendicular to repeating topographies if the dimensions are within the nanoscale (400–1200 nm) [333, 335].

It is theorised that discontinuities on the grooved surface cause the ECM to adsorb onto the surface, aligning attachment points and causing the contact guidance [331]. The edges of the ridges create mechanical grips allowing the cell and potentially collagen to adhere and force both to orientate and align in a preferential direction [335]. As the length of the collagen microfibril is much greater than that of any of the gap widths (all $\leq$ 1000 nm), it may be more energetically favourable for the collagen microfibrils to lay across the gap (perpendicular) rather than along it (parallel). However, there is currently very little understanding as to how collagen aligns with topographical patterning, especially when the alignment is perpendicular to the ridge edge. Although the mechanism is yet to be understood, changes in the surface energy because of interactions with both a solid surface and liquid (due to alternating ridge and gap interactions) could cause a repeating change in hydrophobicity and hydrophilicity which influences and guides the collagen orientation.

As there is guaranteed perpendicular alignment of collagen, a patterned surface of this nature could be used as a wound dressing to treat corneal scarring from laceration. Blindness as a result of corneal scarring is due to the random orientation of newly deposited ECM in an inflamed environment. As the function and transparency of the cornea is closely linked to the organisation of corneal epithelial cells, dictated by the ECM, it is essential that during wound repair the ECM remains a replica of the surrounding native tissue. In this way, topographical surfaces as shown within the chapter could dictate and force the direction of newly deposited ECM in one direction. This would directly manipulate cell orientation and therefore reduce the likelihood of a malformed corneal epithelium. Overall, this would result in a reduction of scarring and reduction in the likelihood of scar induced blindness.

## 5.5 Conclusion

In conclusion, it is clear that the substrate on which collagen is deposited has a large impact on orientation. Although surface chemistry seems to have little influence on collagen orientation, it is clear that specific patterning causes an increase in percentage alignment in a perpendicular orientation from a ridge edge. An RTG ratio of between 1.3 – 1.5 caused an increase in percentage alignment, regardless of the depth of the gap. Perpendicular collagen alignment resulted in a potential randomisation of fibroblast cytoskeleton alignment, as indicated from fluorescent and brightfield staining. Although it is still unclear as to whether the alignment of collagen influences cellular alignment, nanoscale topographical structures can still be used to orientate collagen. This could allow for tailored assembly of other ECM proteins. This can be used to treat ailments such as scar induced corneal blindness, a tissue which requires highly ordered ECM to maintain both transparency and function. Overall, the use of topographical structures to manipulate ECM orientation and alignment can be used to obtain highly specialised, tissue specific wound dressings.

# CHAPTER 6

# CONCLUSIONS AND FUTURE ASPECTS

## 6.1 Chapter Summary and Future Perspectives

### 6.1.1 Influence of Cobalt Ions on Collagen Assembly

When investigating the influence of cobalt ions on collagen assembly it was clear that cobalt disrupted the self-assembly process of collagen. Cobalt ions caused an increase in heterogeneity of the collagen matrix resulting in a reduction in bulk matrix stiffness. Cobalt ions also aggregated in clusters, causing an increase in collagen concentration in certain areas, further increasing the heterogeneity of the matrix. This change in matrix structure prevented cells seeded onto the doped collagen surface to proliferate and grow, decreasing cell viability. The energy required to remove bulk water from the collagen network was also reduced with the presence of cobalt. This was attributed to cobalt interacting with the C-terminal of the collagen, blocking crucial hydration and helix stabilising binding sites.

Cobalt ions were investigated as they are the most abundant ion to be released from common metal-on-metal implants. The work investigated within Chapter 3 emphasises how important it is to test medical devices in a 3-dimensional environment, taking care to investigate how devices influence the extracellular matrix.

To further test how metal-on-metal implants influence a collagen matrix, wear particles corroded from metal-on-metal implants should be incorporated into the collagen hydrogel.

Characterisation of the collagen matrix, through density AFM images and rheology, with wear debris present will provide a deeper understanding of how these implants influence the most common protein within the extracellular matrix. It would also be beneficial to see how any changes to the collagen, caused by the presence of wear particles, would again influence cellular growth and proliferation. As the wear particles would contain multiple inorganic ions, not just cobalt, so a more succinct overview of how unexpected necrosis from implants is occurring can be established.

To fully understand how the ECM is influenced by wear debris *in vivo*, characterisation of ECM produced from fibroblasts in the presence of debris would be beneficial. Fibroblasts could be grown in the presence of low ($\leq$ 133 ppm) concentration wear debris until they produce a matrix. This could then be characterised in the same way collagen was characterised in Chapter 3 to establish any changes in density, stiffness and inorganic ion accumulation in newly synthesized matrix. This would give the most accurate *in vitro* model for how metal-on-metal implants effect the ECM.

This approach could be implemented on a range of individual ions and wear particles from other metal implants. For example, dental implants are predominately made of titanium alloys, most specifically Ti-6Al-4V (6% aluminium and 4% vanadium) [336]. The influence of these materials on the surrounding 3-dimensional extracellular environment could be tested as cobalt-collagen was tested. To continue using titanium dental implants as an example, newer studies are also trying to combat bacterial infection. This has been investigated by either changing the topography of the surfaces [337] or by changing the chemical composition of the material [338, 339]. These changes could again be tested against collagen to understand whether they will cause any unexpected detrimental effects on the extracellular matrix.

### 6.1.2 Calcium and Phosphate Influence on Collagen Formation

Calcium and phosphate had detrimental effects on collagen formation from the nano- to the macro-scale. Calcium and phosphate changed the conformational structure of the

collagen triple helix, resulting in a reduction in collagen molecule size. With the addition of calcium this resulted in a reduction in fibrillogenesis, predominately the rate of fibril formation. Changes to the collagen molecule by phosphate were less significant, which meant that the fibrillogenesis process was not affected. When calcium and phosphate were combined, there was no change in molecule conformation, a non-significant reduction in molecule size and a slight reduction in fibrillogenesis. This indicates that when both ions are present in the medium, they interact with each other as well as the collagen causing a reduction in the detrimental effects of each ion alone. Calcium phosphate ratios mimicking that of physiological HA further confirmed this, with no change to the rate of fibril formation but an increase in fibril-fibril interaction. This was hypothesised to be due to the sizes of the individual ions and how this compared to a Posner cluster (cluster of both calcium and phosphate). Posner clusters are five times the size of a calcium/phosphate ion. By assuming that both interact with the surface of a collagen molecule, a smaller ion would cause a more significant bend in the triple helix over a larger ion or complex. In this way, calcium and phosphate ions are able to cause a change in molecule conformation, leading to changes in fibrillogenesis, but a larger Posner cluster would not.

Although this chapter focussed on the underlying mechanisms behind how calcium, phosphate and calcium phosphate influenced collagen assembly, there were no investigations into how this effected matrix mechanics. Experiments measuring the rheological properties of the collagen matrix in the presence of each ion and calcium phosphate would give insight into how the mechanics of early stage collagen mineralisation change. As calcium causes a significant decrease in fibrillogenesis, it can be inferred that it would also cause a reduction in matrix stiffness. Nanoindentation measurements, looking at the mechanics of individual fibrils, would also give an in-depth assessment of how changes to the molecular structure are affecting fibril stiffness and compression on a localised scale.

Transmission electron microscopy (TEM) could be implemented to further investigate the interaction sites of each of the ions. Investigations in Chapter 4 indicate that there

are 6000 potential binding sites for calcium or phosphate, with ions interacting on the surface of the molecule. By forming collagen in excess $CaCl_2$, $PO_4$ and Ca:$PO_4$, without a cross-linking agent (NaOH), and imaging under TEM, interaction sites could be visualised. Investigations in this chapter also show that fibril formation ends at approximately 35 mins, from physiological calcium phosphate ratios, and full matrix assembly ends at 120 mins. Taking images of collagen in excess $CaCl_2$, $PO_4$ and Ca:$PO_4$, removed from incubation at these crucial times, would give insight into where these ions and Posner clusters are accumulating on the fibrils. Furthermore, it would show how they interact with collagen during the fibril formation stage.

Compression of the collagen matrix to remove excess water and create a denser matrix could also be investigated for visualisation of the collagen network via AFM and SEM imaging. Compression of collagen hydrogels results in the formation of a denser network without compromise of fibril formation and assembly [340]. This may give more accurate quantitative data regarding collagen characteristics such as fibril diameter and D-spacing. This would give clearer insight into how each ion is influencing fibril formation and matrix assembly.

No cellular experiments were conducted within Chapter 4, so the influence of these matrix changes on cellular formation, caused by $CaCl_2$, $PO_4$ and Ca:$PO_4$, has not been investigated. It would be important to understand how these changes in matrix formation influence proliferation and viability of cells seeded onto the surface of the doped collagen hydrogel. Analysis could be conducted in the same way as in Chapter 3. It would also be important to see how cells proliferate when incorporated into a collagen matrix in excess $CaCl_2$, $PO_4$ and Ca:$PO_4$. This may allow for more insight into early stage collagen mineralisation, especially when using physiological ratios of Ca:$PO_4$. Environmental scanning electron microscopy (ESEM) would be able to image cells and their interaction with the doped collagen matrix, without the need for cell fixation or damage. EDS could also be used alongside ESEM to establish which part of the mineral is interacting with both the cell and the collagen, and in turn how it interacts with any newly deposited ECM [341].

### 6.1.3 Topographical Influence on Collagen Assembly

When investigating the influence of surface properties on collagen assembly, it was initially clear that surface free energy was not a contributing factor. Both hydrophilic and hydrophobic surfaces were investigated, and, although hydrophobic surfaces influenced the formation of collagen fibrils, the orientation of collagen fibrils was still randomised. However, the self-assembled layer caused by gold on a PDMS surface alluded that topography may have a larger influence on collagen fibril orientation. Investigations into nano-topography concluded that a ridge to gap (RTG) ratio of 1.4 and 1.5 with gap depth of 500 and 1000 nm respectively resulted in a reproducible perpendicular alignment of collagen to the ridge edge. Further studies revealed that only the surface with an RTG ratio of 1.5 was unaffected by collagen concentration. These optimal parameters were then imprinted onto IP-DIP (a high resolution, biocompatible photoresist) to investigate how the perpendicular alignment of the collagen fibrils influenced cellular alignment. Although it was unclear, the presence of collagen potentially caused an increase in randomisation of cytoskeleton alignment. Deeper investigations into whether RTG ratio or depth was the most influential factor concluded that RTG ratio was the driving force behind the perpendicular alignment, with an RTG ratio of 1.3-1.5 causing the highest percentage of fibril alignment.

The largest limitation within this investigation was the size of the patterned surface area and the size of the pattern parameters. It is essential that a larger surface area is investigated before exploring other avenues. A larger patterned surface area, ideally $\geq 0.25$ mm$^2$, would allow for SFE characterisation of the patterned surface. SFE is dependent on any surface roughness or topography, so therefore there will be a difference in SFE of the patterned and non-patterned surfaces [342]. By measuring SFE for a large patterned surface area, more insight may be achieved into why the fibrils are orientating within a perpendicular direction. A larger surface area would also allow for cellular cytoskeleton quantification to determine whether collagen alignment can influence cellular alignment in this way. Phalloidin staining was sufficient to determine cytoskeleton orien-

tation, however DAPI also stained the IP-DIP surface, indicating that potentially a lower concentration might be more appropriate. Once cellular experiments have been undertaken for the same nano-parameters used within previous experiments, investigations into the RTG ratio can start.

As RTG ratio was the most influential parameter, it would be crucial to investigate whether a similar percentage of perpendicularly aligned collagen fibrils can be achieved when scaling up the topographical pattern. The biggest limitation within Chapter 5 was the difficulty in printing reproducible nano-patterns in a range of materials. If high percentages of perpendicular collagen alignment can be achieved with larger structures, which maintain an RTG ratio of 1.3-1.5, then this alignment phenomenon could be used within a medical device.

To further analyse how these surfaces influence cellular alignment, live cell imaging could be implemented. This process involves the accumulation of multiple brightfield images over a range of time, giving insight into early stage interaction between the cells, collagen and the surface. Imaging using polarising light would also allow for an in-depth analysis of how cells migrate over these surfaces with and without the presence of collagen. This would give a robust model of how these surfaces would act *in vivo*.

This level of collagen alignment caused by the repeating pattern could be used as a medical device to combat blindness as a result of a corneal laceration. When a wound within the eye begins to heal, a scar can form. This scar causes scattering of light within the cornea, resulting in the surface becoming opaque and leaving the patient blind. If a medical device is created that would improve the alignment of collagen during the wound healing stage in a perpendicular direction, there would likely be a reduction in the formation of a debilitating scar.

To turn the current topographical surface into a product, a material that could be patterned and curved would need to be investigated. Contact lenses are most commonly made of silicone- or polymer-hydrogels. The manufacturing of these gels can be altered, with parameters such as oxygen permeability, wettability, water content, lens thickness

and mechanical properties being the main constituents required for a contact lens [343]. Creating a material that could be used as a contact lens with the RTG ratio of 1.3-1.5 etched onto the curved surface would be a substantial development in creating a useable product. This would be made easier if a scaled up ratio had already been established, residing more within the micro-scale rather than the nano-scale. Analysis of collagen alignment on a curved surface could be achieved through SEM imaging of sections of the surface, however this would not give the clearest overview. By cutting slits within the sides of the curved surface, the surface could be flattened, allowing for SEM imaging. Staining of the collagen with PicroSirius red would also allow for brightfield imaging, capturing both the direction of the pattern and the direction of the collagen [344].

It would also be beneficial to understand how these surfaces influence newly synthesised ECM. Growing cells on the patterned surfaces until they produce ECM would give further insight into how the surfaces would act *in vivo*. Fluorescent staining of collagen, and other ECM proteins, such as fibronectin, would establish whether newly synthesised ECM also aligns perpendicularly to the ridge edge and whether it is at the same high percentage. To further model wound healing, these cells could be placed in an inflamed environment to mimic rapid ECM deposition. Analysis of the ECM could be achieved as before, through fluorescent imaging, live cell imaging and brightfield imaging using stains such as PicroSirius red. A comparison of this to the alignment of ECM from cells in a controlled environment would give insight as to whether these surfaces would be a suitable medical device to help combat blindness caused from corneal scarring.

It is still unclear what the underlying mechanism causing perpendicular alignment of collagen fibrils over these nanopatterns. Therefore, it would be important to try and computationally model how the collagen molecules interact with these structures. Molecules should be investigated initially, as when the solution is deposited onto the surface the collagen has not yet self-assembled, meaning the initial interaction is that of collagen molecules and the surface. It should be assumed that the molecules are interacting with both a solid and a liquid due to the space within the gaps. Initial assumptions should

be made by modelling the molecules as stiff rods or cylinders, reducing the complications within the problem. Although they are flexible, for this purpose assuming they are solid rods would be sufficient. Multiple collagen molecule rods should then be introduced to see how they interact with each other as well as the underlying pattern. Ideally, modelling the full process would account for the liquid medium that the collagen molecules are being deposited in, that they are being dropped onto the patterned surface and that they are interacting across multiple phases; solid and liquid.

## 6.2 Overall Conclusion

Collagen is a hierarchical protein and can therefore be influenced at multiple stages of assembly. The environment in which collagen forms highly affects the alignment, orientation and fibril formation. Within this thesis, the chemical environment in which the collagen matrix forms has been investigated. It emphasises how complexes of certain ions can have no effect on collagen formation or matrix assembly, yet when ions present within the complex interact individually, there can be detrimental effects. It also shows how not only the chemical environment, but the physical environment plays a crucial role in collagen orientation and alignment. It showcases how surface patterns with specific RTG ratios can cause a perpendicular (to the ridge edge) percentage alignment of $\leq$ 60 %. This concludes that collagen can be manipulated through a combination of chemical and physical parameters to mimic that of native tissue. This is extremely important during the wound healing phase, as debilitating scars, caused from misaligned collagen, can be eradicated by exposing the newly synthesised collagen to parameters which will force formation, orientation and alignment to match that of the surrounding native tissue.

# CHAPTER 7

# APPENDIX I

Enclosed within this appendix is a list of supplementary figures relating to data found in Chapter 4.

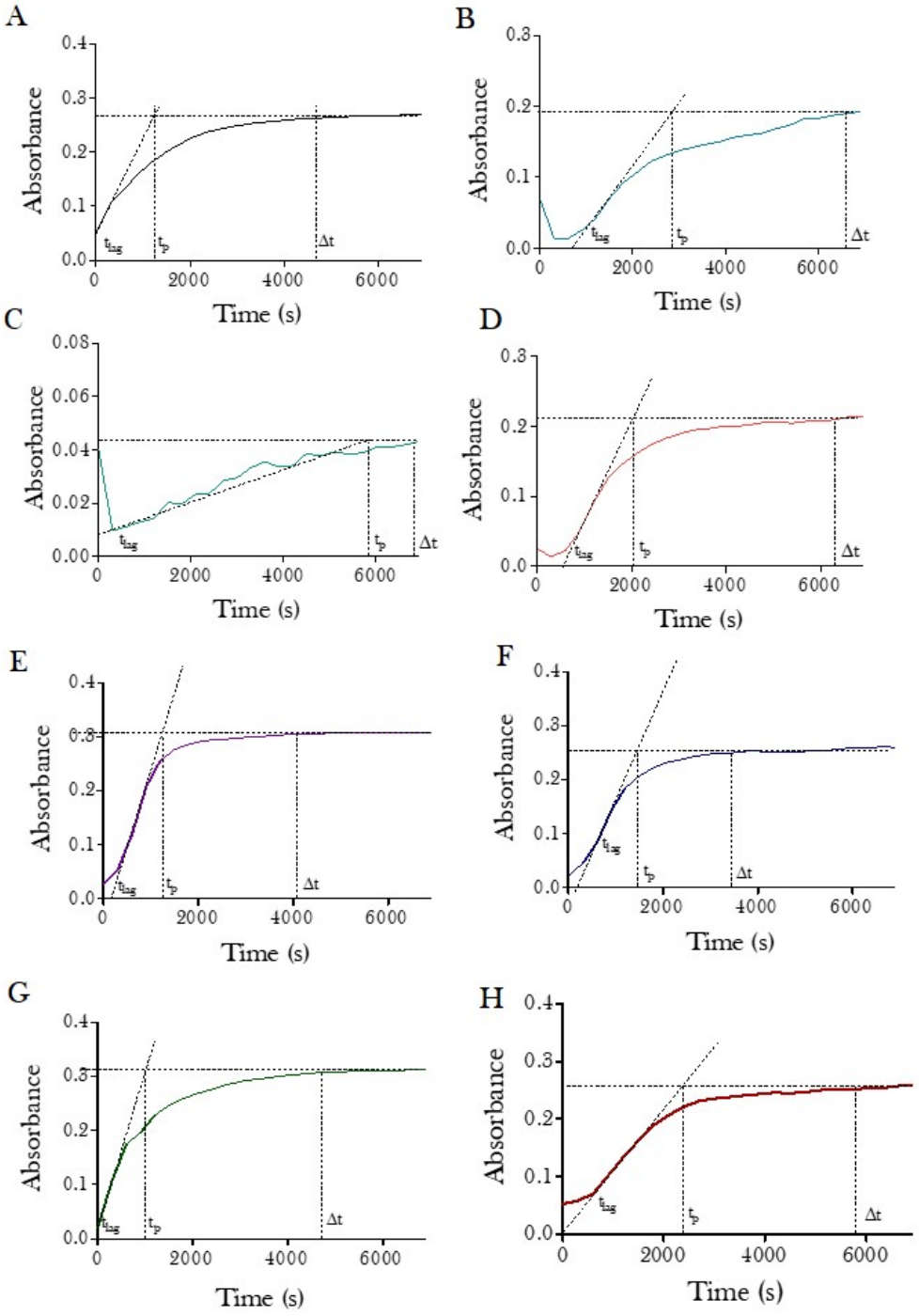



Figure 7.1: Fibrillogenesis profiles used to calculate growth phase measurements (only average shown). (A) Control collagen, (B) potassium chloride, (C) calcium chloride, (D) magnesium chloride, (E) sodium chloride, (F) sodium carbonate, (G) sodium sulphate, (H) sodium acetate. $t_{lag}$ refers to the lag time, $t_p$ refers to the time point when the plateau time begins and $\Delta t$ refers to the time at which collagen fibril formation ends. N = 3.

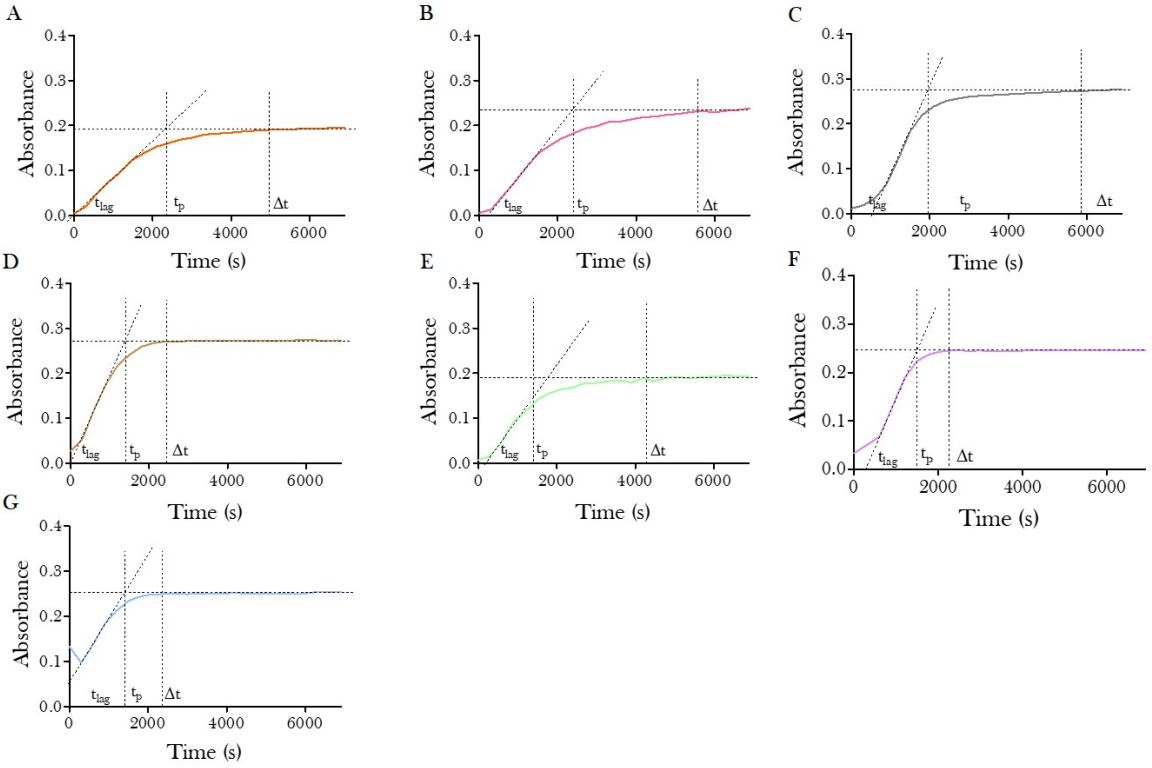



Figure 7.2: Fibrillogenesis profiles indicating how growth phase was measured for decreasing ratios of $Ca:PO_4$. (A) $Ca:PO_4$ 1:1, (B) $Ca:PO_4$ 1:0.75, (C) $Ca:PO_4$ 1:0.5, (D) $Ca:PO_4$ 1:0.25, (E) $Ca:PO_4$ 1:0.125, (F) $Ca:PO_4$ 1:0.0625, (G) $Ca:PO_4$ 1:0.03125. $t_{lag}$ refers to the lag time, $t_p$ refers to the time point when the plateau time begins and $\Delta t$ refers to the time at which collagen fibril formation ends. N = 3.

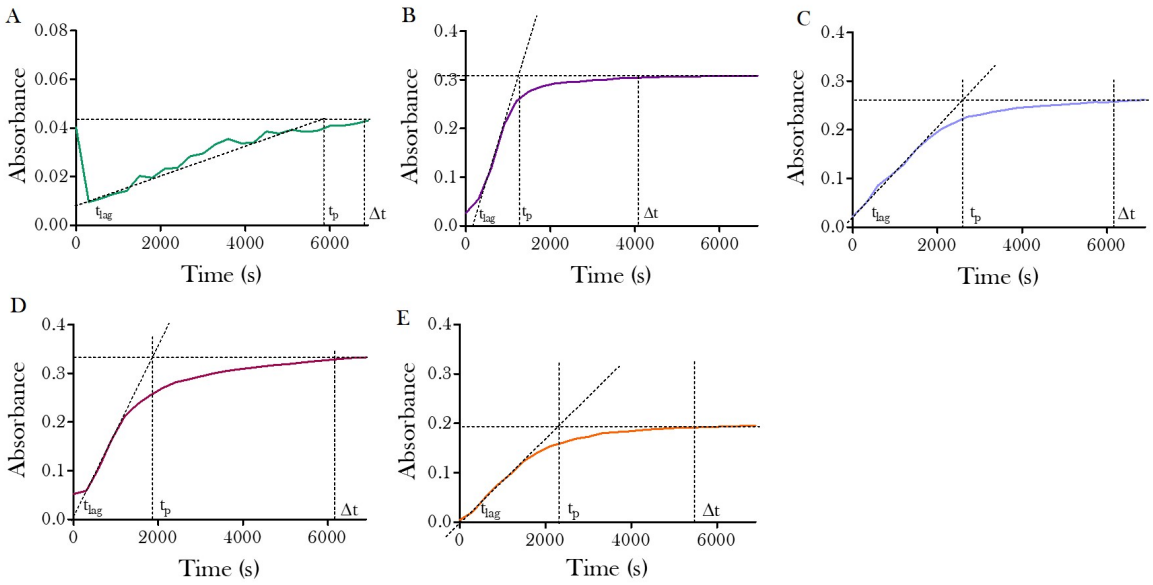



Figure 7.3: Fibrillogenesis profiles indicating how growth phase was measured for (A) $CaCl_2$, (B) NaCl, (C) NaCl + $CaCl_2$, (D) sodium phosphate, and (E) Ca:$PO_4$ 1:1. $t_{lag}$ refers to the lag time, $t_p$ refers to the time point when the plateau time begins and Δt refers to the time at which collagen fibril formation ends. N = 3.

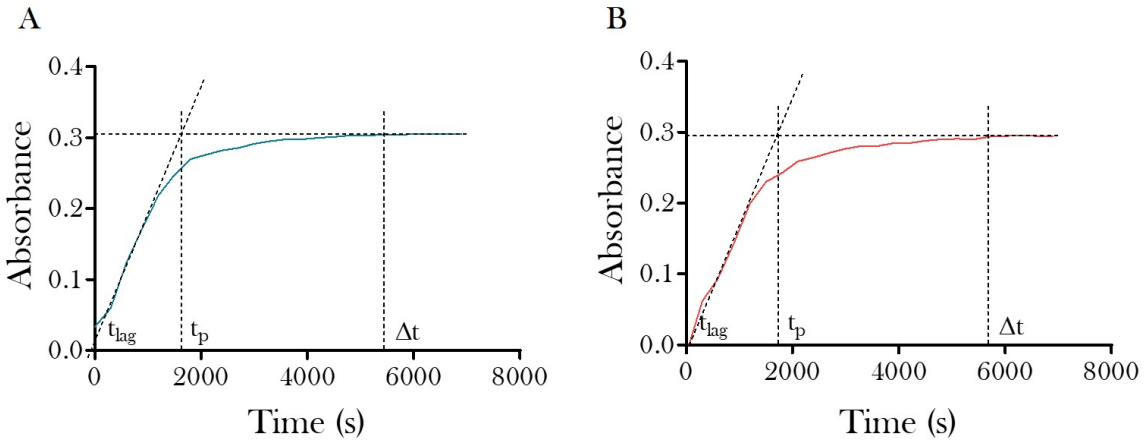



Figure 7.4: Fibrillogenesis profiles indicating how growth phase was measured for collagen doped with (A) EDTA and (B) Ca:EDTA. $t_{lag}$ refers to the lag time, $t_p$ refers to the time point when the plateau time begins and Δt refers to the time at which collagen fibril formation ends. N = 3.

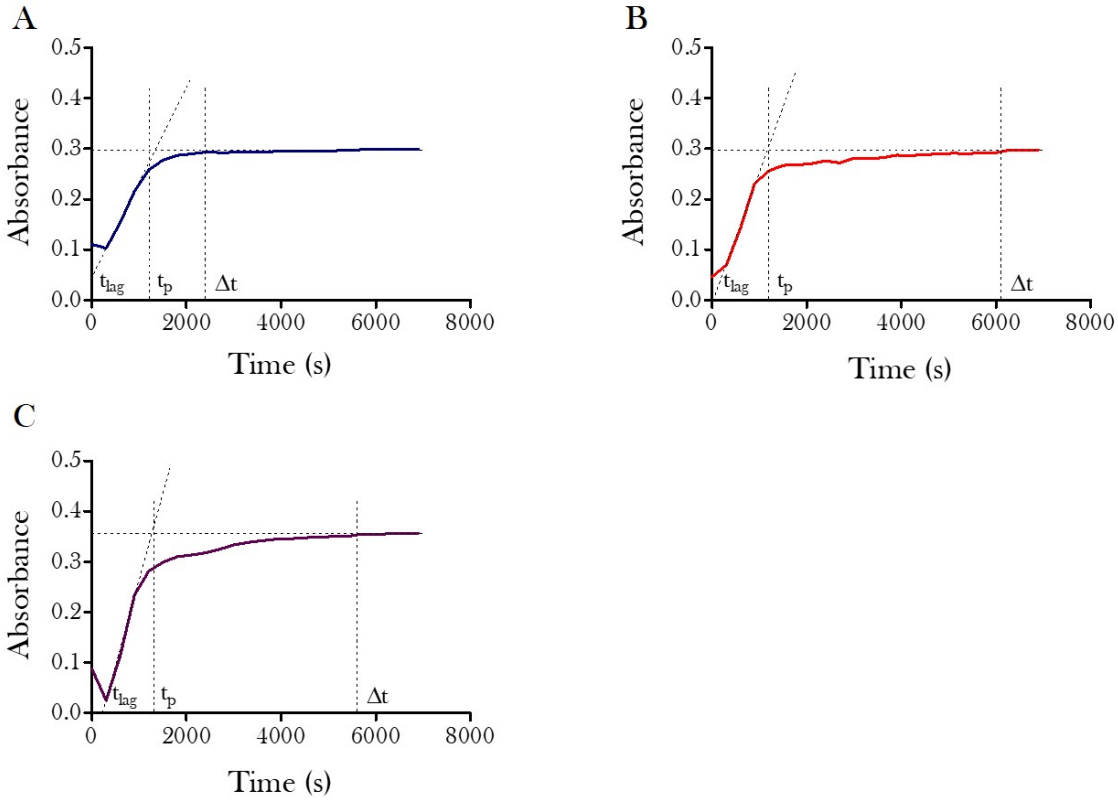



Figure 7.5: Fibrillogenesis profiles indicating how growth phase was measured for collagen doped with a higher concentration of Ca (2 mM), (A) Ca:$PO_4$ 1:0, (B) Ca:$PO_4$ 1:0.6, and (C) Ca:$PO_4$ 1:1.. $t_{lag}$ refers to the lag time, $t_p$ refers to the time point when the plateau time begins and $\Delta$t refers to the time at which collagen fibril formation ends. N = 3.

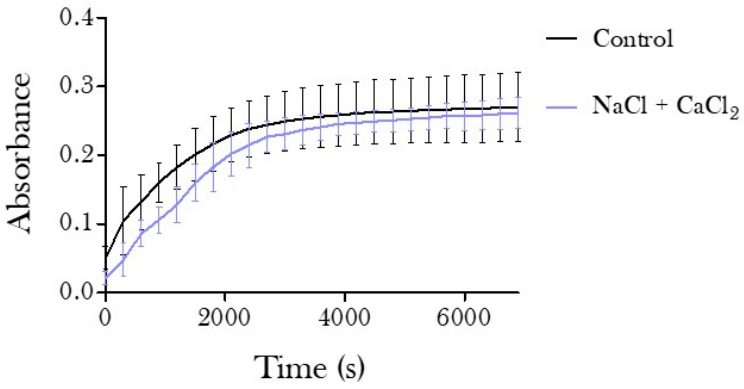



Figure 7.6: Control indicating that the addition of both sodium chloride (NaCl) and calcium chloride ($CaCl_2$) does not result in any change in fibrillogenesis. N = 3, error bars refer to $\pm$ standard deviation.

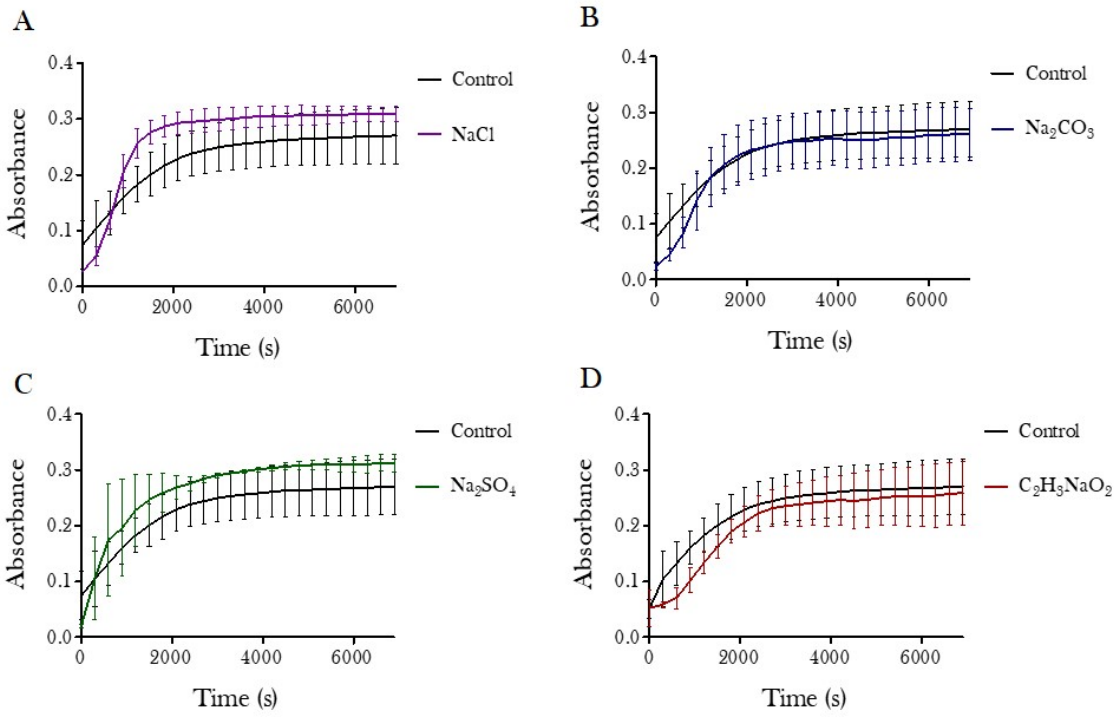



Figure 7.7: Fibrillogenesis assays indicating that changing the anion does not result in a change in fibrillogenesis profile. (A) NaCl, (B) $Na_2CO_3$, (C) $Na_2SO_4$, (D) $C_2H_3NaO_2$. N = 3, error bars refer to ± standard deviation.

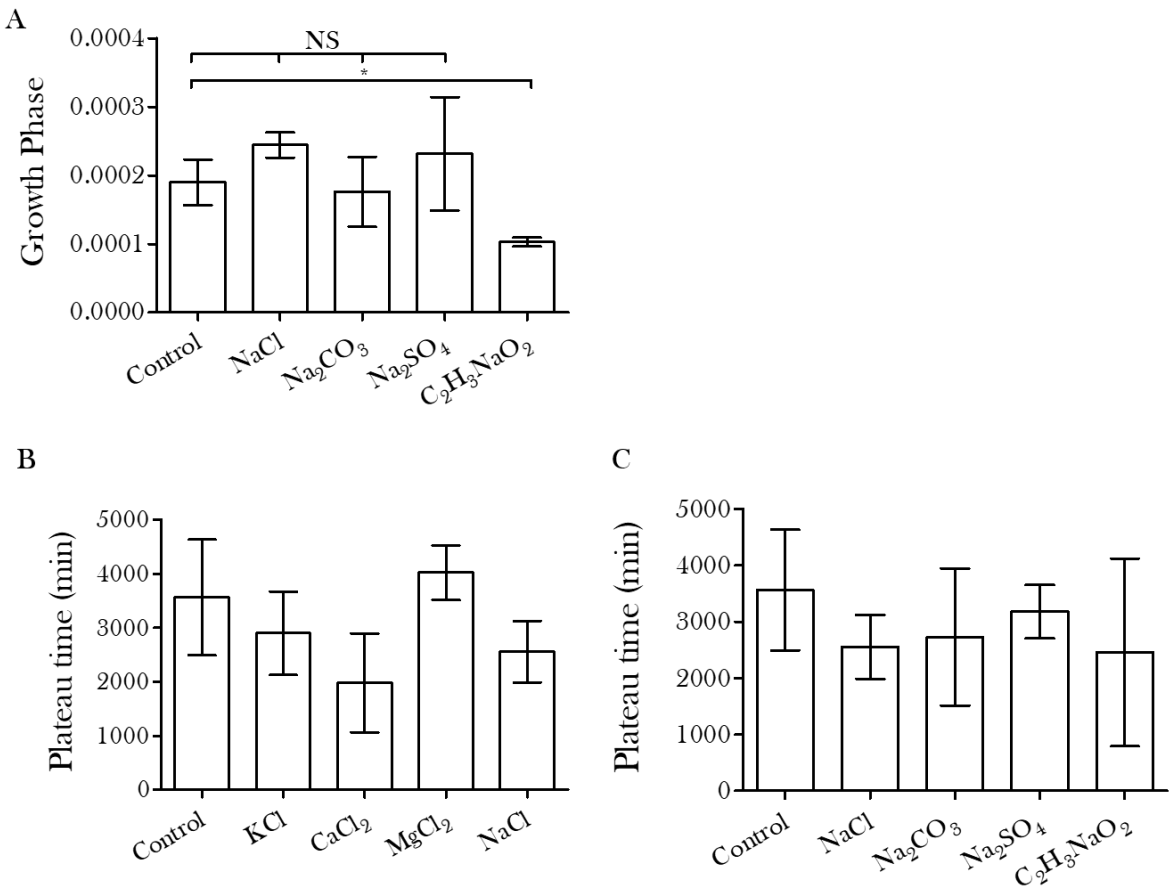



Figure 7.8: (A) Growth phase measurements for anion experiments. Plateau measurements for (B) cations and (C) anions. N = 3, error bars refer to ± standard deviation.

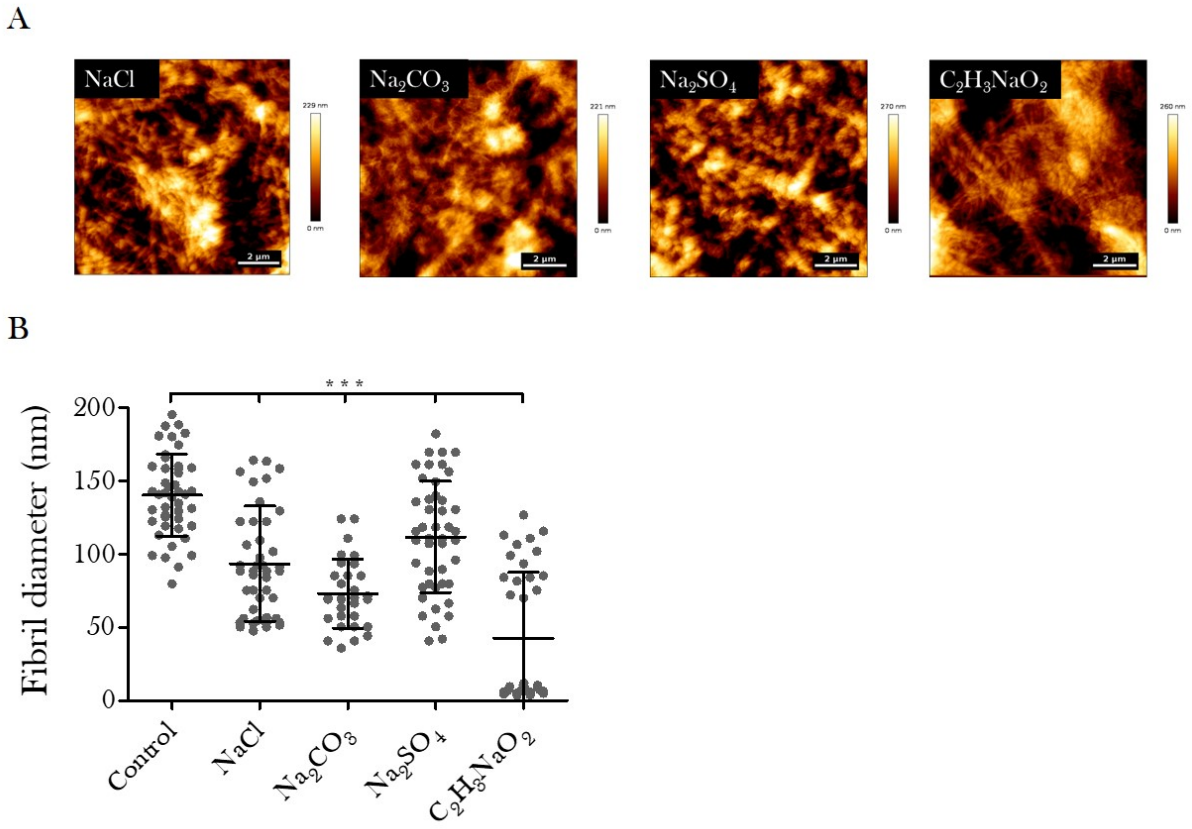



Figure 7.9: (A) AFM images of collagen and excess NaCl, $Na_2CO_3$, $Na_2SO_4$, $C_2H_3NaO_2$. (B) Fibril diameter measured from triplicates of each AFM images. *** refers to a P value $\leq 0.001$. N = 75 across 3 biological samples. Error bars refer to $\pm$ standard deviation.

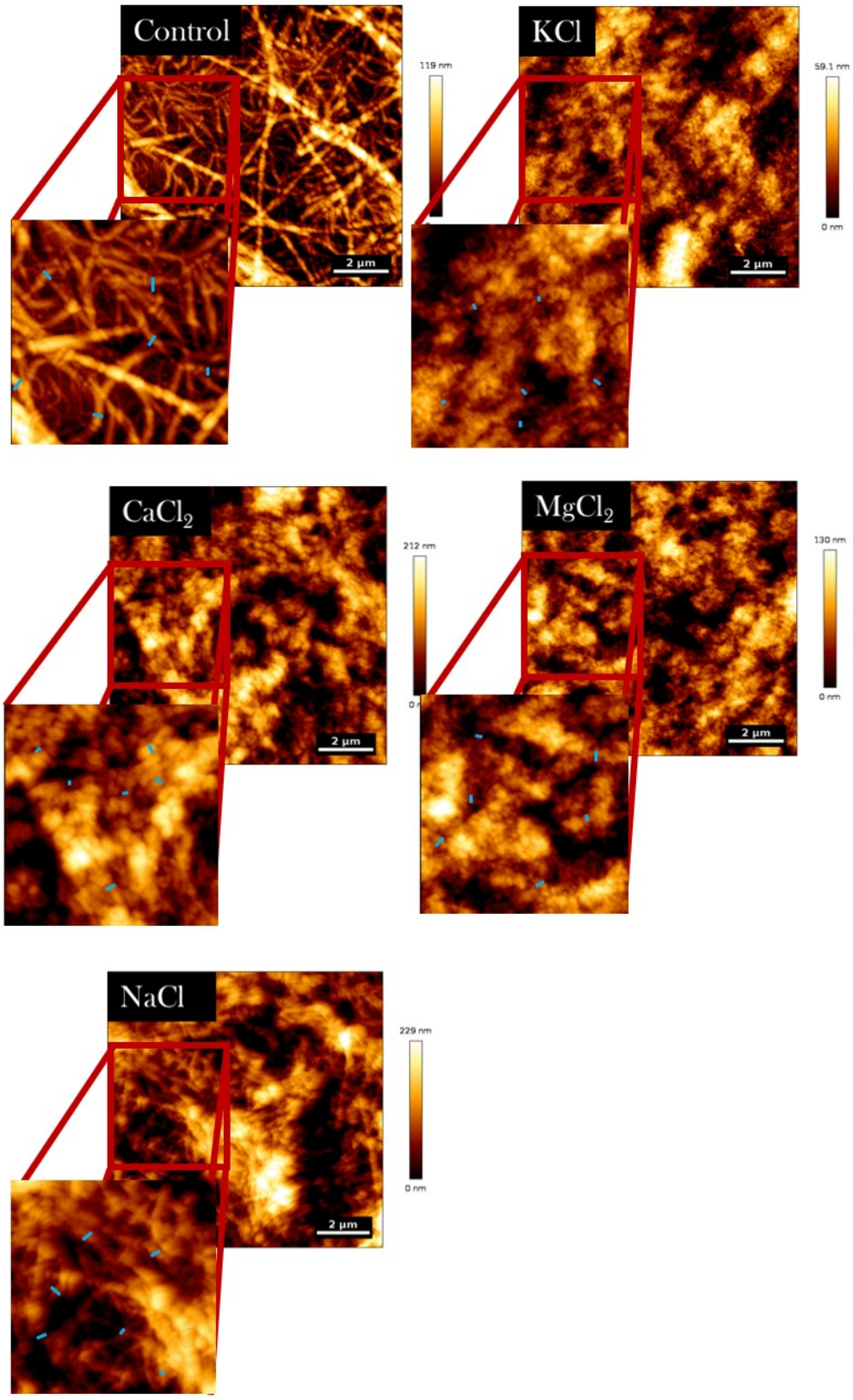



Figure 7.10: Examples of how measurements of fibrils were taken from AFM images to determine fibril diameter. Lines drawn across fibrils, on AFM images acquired from triplicate samples, were measured in ImageJ at random in order to establish mean fibril diameter and standard deviation. N = 75 across 3 biological samples.

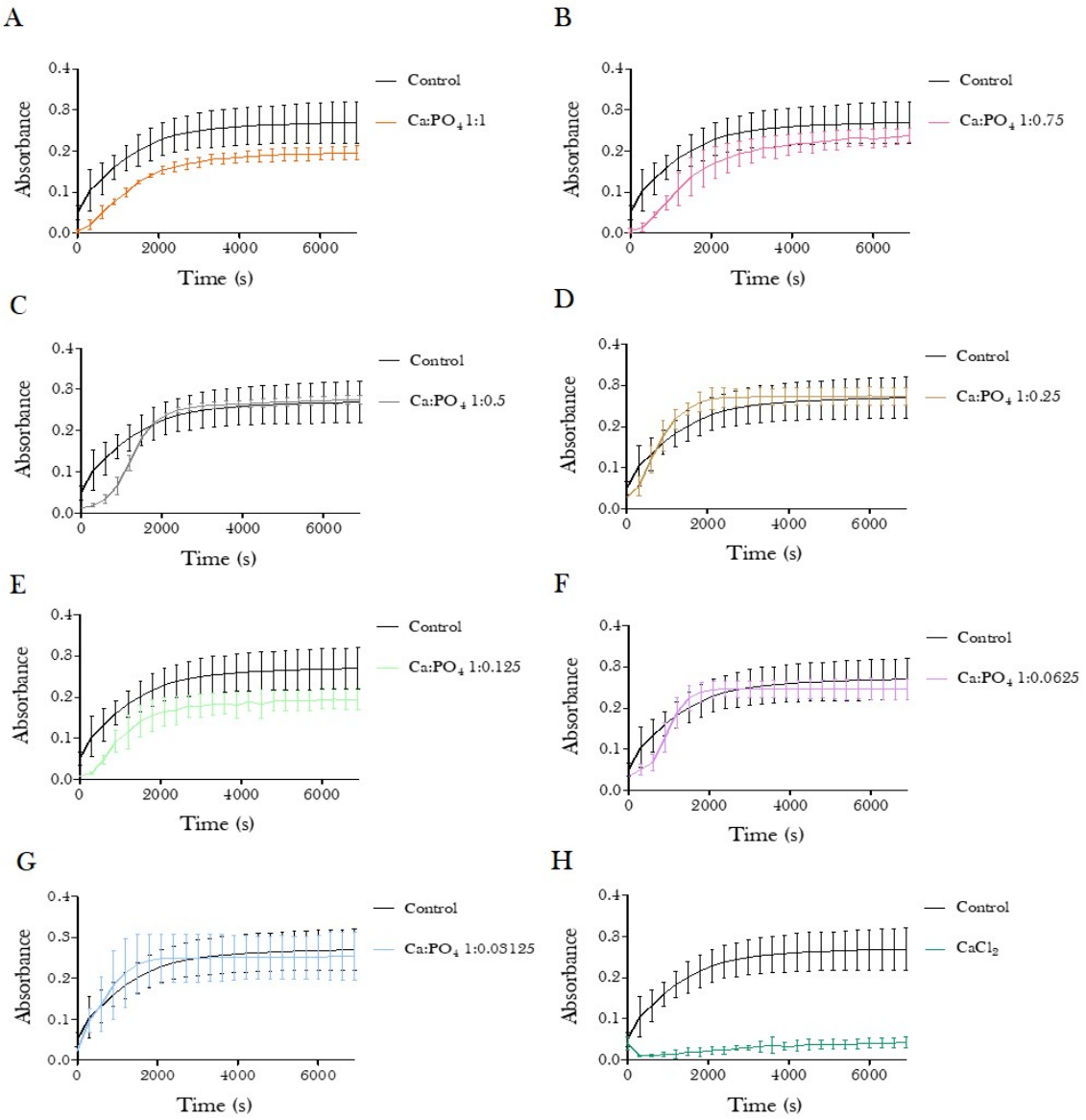



Figure 7.11: Fibrillogenesis profiles for decreasing ratios of $Ca:PO_4$. (A) $Ca:PO_4$ 1:1, (B) $Ca:PO_4$ 1:0.75, (C) $Ca:PO_4$ 1:0.5, (D) $Ca:PO_4$ 1:0.25, (E) $Ca:PO_4$ 1:0.125, (F) $Ca:PO_4$ 1:0.0625, (G) $Ca:PO_4$ 1:0.03125. N = 3, error bars refer to ± standard deviation.

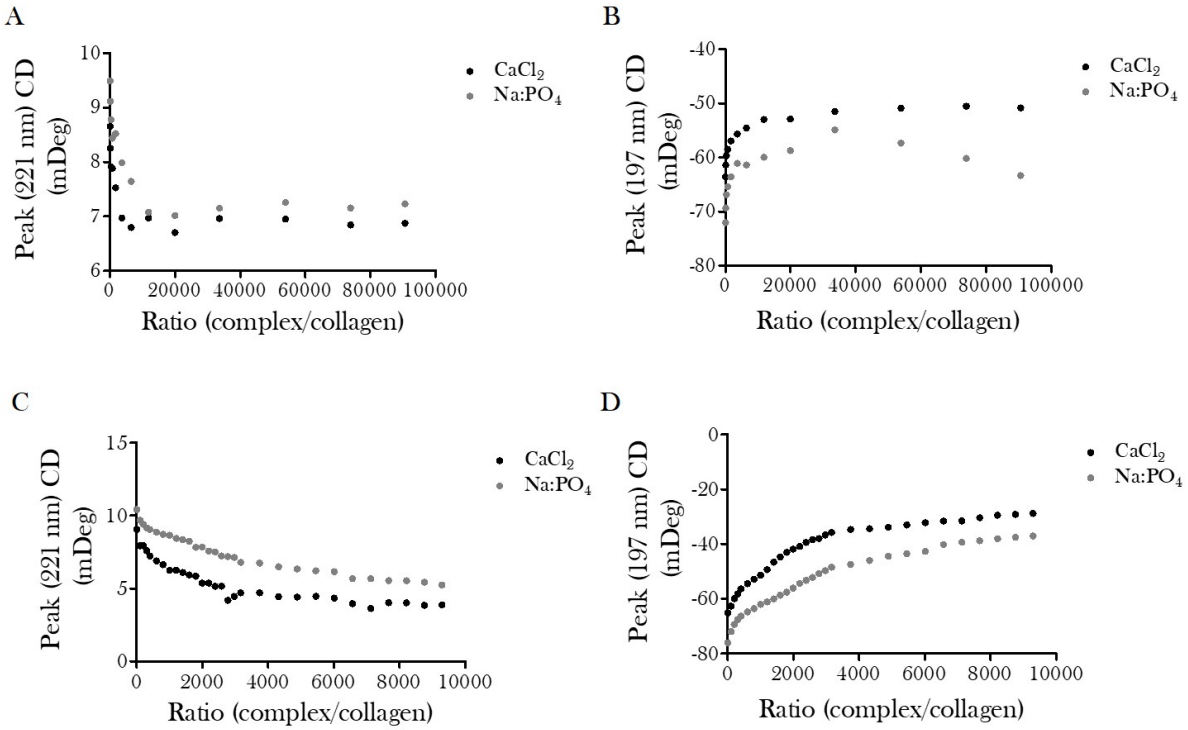



Figure 7.12: Circular dichroism (CD) titration of calcium chloride ($CaCl_2$) and sodium phosphate ($Na:PO_4$) added at large volumes to collagen to determine approximate number of surface binding sites of each molecule. CD measurements for the peak at 221 nm (A) and for 197 nm (B). To further gain the number of available binding sites for $CaCl_2$ and $Na:PO_4$ more measurements in a smaller range were taken. (C) CD measurements for the peak at 221 nm for the smaller range. (D) CD measurements for the peak at 197 nm for the smaller range. N = 3.

# CHAPTER 8

# APPENDIX II

Enclosed within this appendix is a list of supplementary figures relating to data found in Chapter 5.

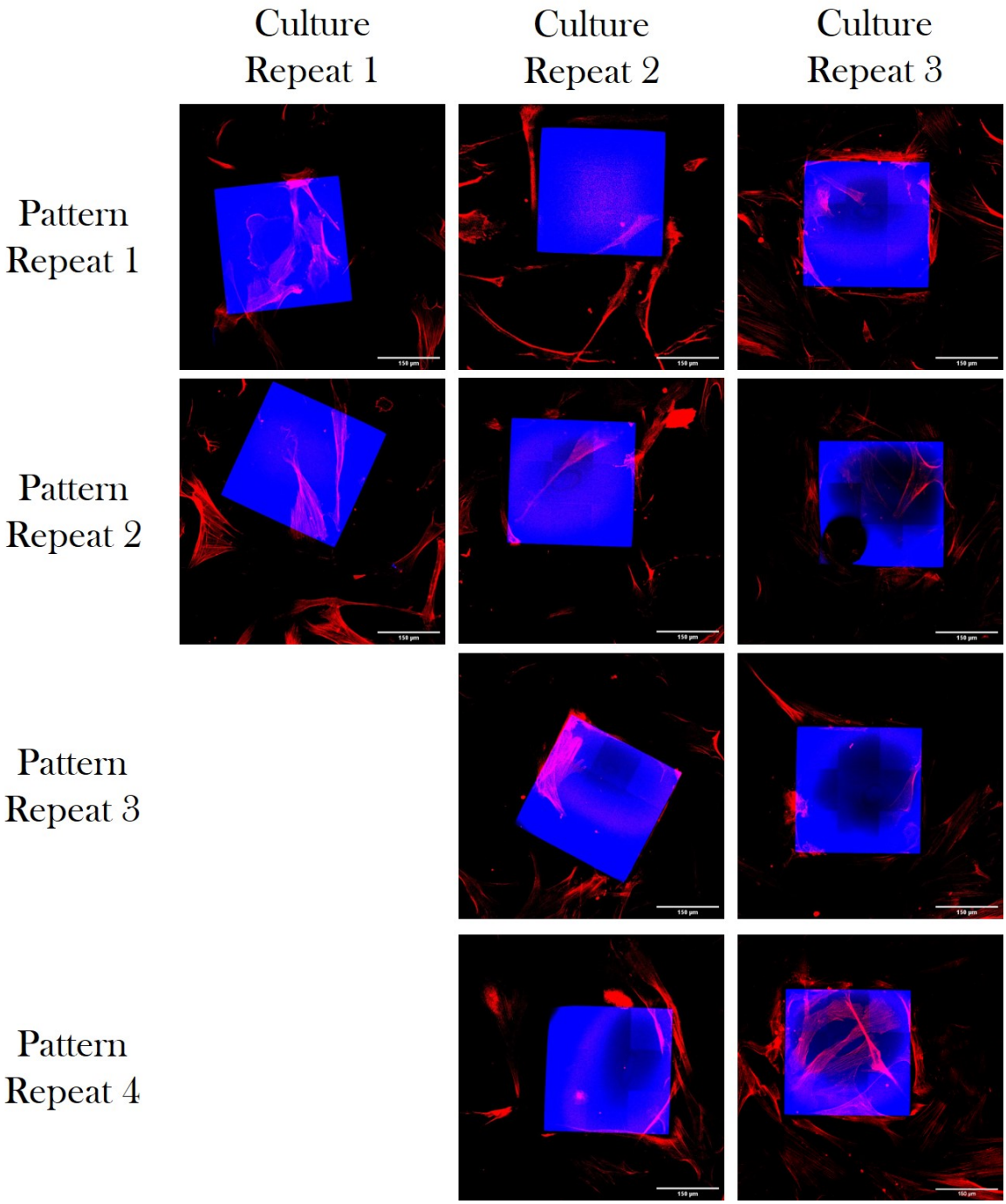



Figure 8.1: Fluorescent images of corneal fibroblasts cultured onto patterned and non-patterned IP-DIP in the presence of collagen. Three culture repeats were imaged with a total of four patterns per repeat. Two patterns within repeat 1 were lost in the cell fixing process. Red staining is Phalloidin and blue staining is DAPI. DAPI stained the IP-DIP pattern very strongly preventing the visualization of cellular DNA. Scale bar is 150 $\mu$m.

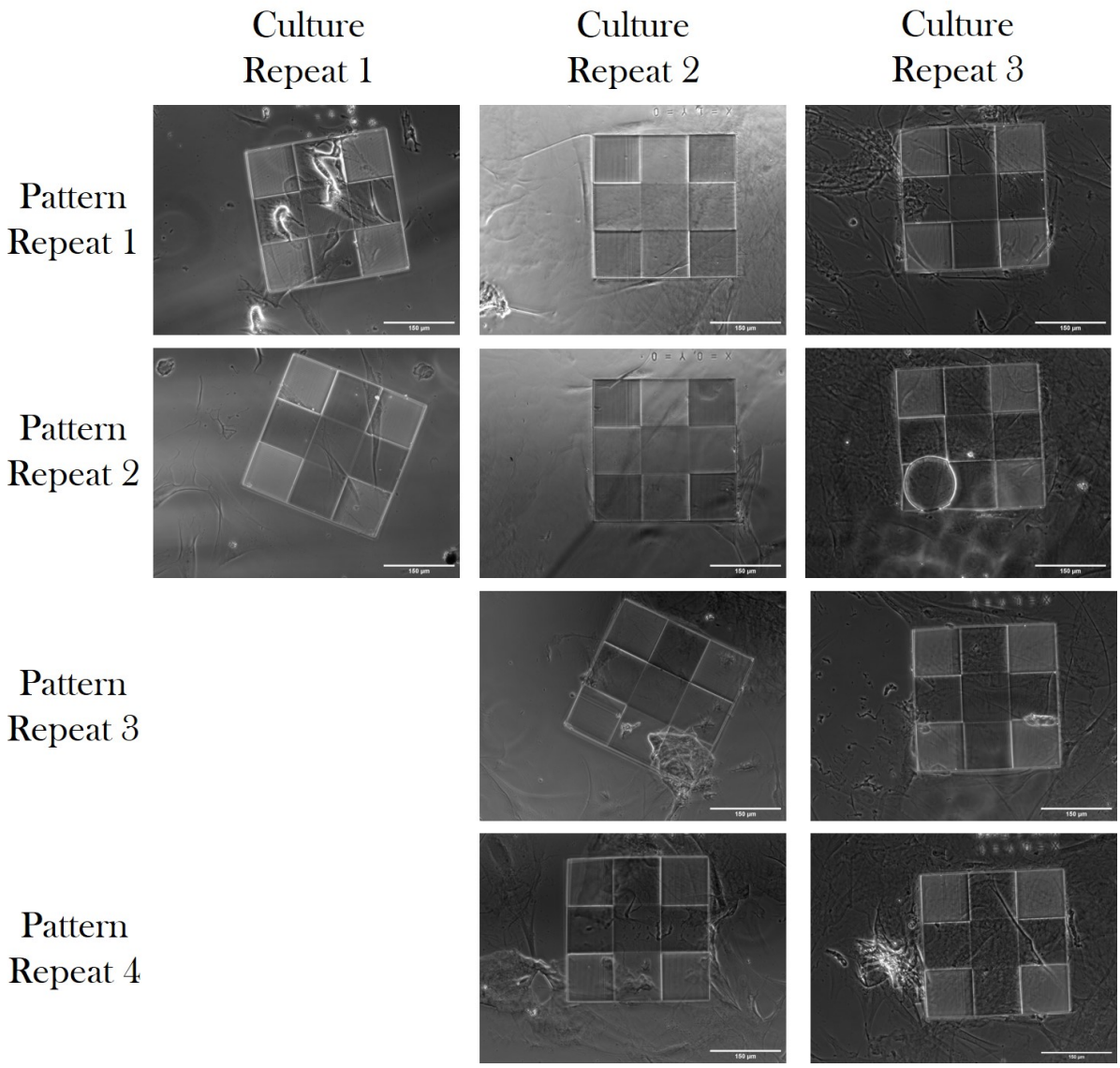



Figure 8.2: Brightfield images of corneal fibroblasts cultured onto patterned and non-patterned IP-DIP in the presence of collagen. Three culture repeats were imaged with a total of four patterns per repeat. Two patterns within repeat 1 were lost in the cell fixing process. Scale bar is 150 $\mu$m.

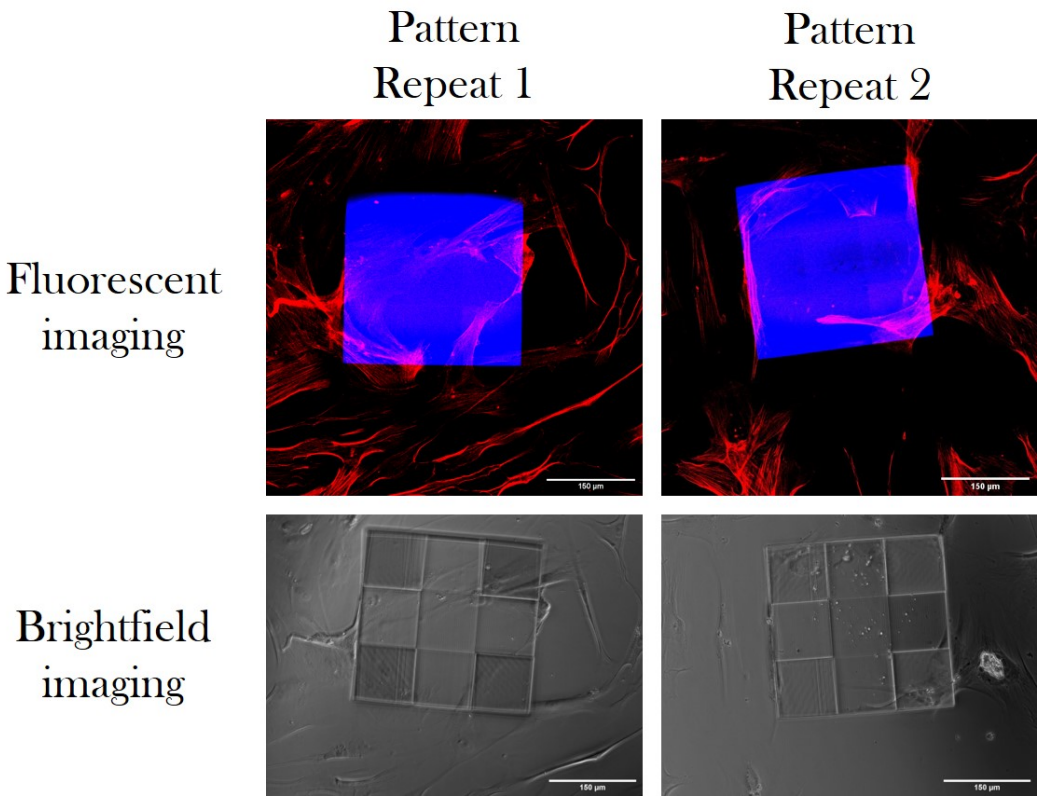



Figure 8.3: Fluorescent and brightfield images of corneal fibroblasts cultured onto patterned and non-patterned IP-DIP without the presence of collagen. Although there were three culture repeats seeded, only two pattern repeats from one culture repeat was not lost in the cell fixing and washing process. Red staining is Phalloidin and blue staining is DAPI. Scale bar is 150 $\mu$m.

# CHAPTER 9

# APPENDIX III

A version of Chapter 3 has been previously published in ACS Omega.

Emma M. McCarthy, Hayley Floyd, Owen Addison, Zhenyu J. Zhang, Pola Goldberg Oppenheimer, Liam M. Grover. Influence of Cobalt Ions on Collagen Gel Formation and Their Interaction with Osteoblasts. *ACS Omega*, 3(8):10129-10138, 2018. doi: 10.1021/acsomega.8b01048

A copy of this can be found enclosed:

This is an open access article published under a Creative Commons Attribution (CC-BY) License, which permits unrestricted use, distribution and reproduction in any medium, provided the author and source are cited.

ACS OMEGA

Article

Cite This: ACS Omega 2018, 3, 10129−10138

http://pubs.acs.org/journal/acsodf

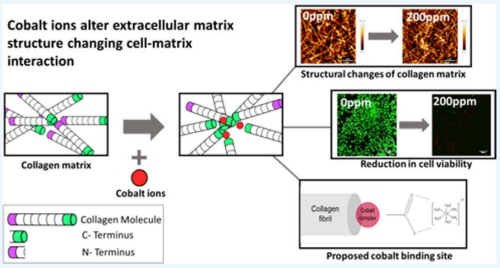
# Influence of Cobalt Ions on Collagen Gel Formation and Their Interaction with Osteoblasts

Emma M. McCarthy,[*,†,§] Hayley Floyd,[‡,§] Owen Addison,[∥] Zhenyu J. Zhang,[§] Pola Goldberg Oppenheimer,[§] and Liam M. Grover[*,§]

[†]Physical Sciences for Health, School of Chemistry, [‡]Physical Sciences of Imaging in the Biomedical Sciences, School of Chemistry, [§]Department of BioChemical Engineering, School of Chemical Engineering, and [∥]School of Dentistry, University of Birmingham, Edgbaston, B15 2TT Birmingham, U.K.

Supporting Information

**ABSTRACT:** Metals on metal implants have long been used in arthroplasties because of their robustness and low dislocation rate. Several relatively low-corrosion metals have been used in arthroplasty, including 316L stainless steel, titanium, and cobalt−chromium−molybdenum alloy. Debris from these implants, however, has been found to cause inflammatory responses leading to unexpected failure rates approaching 10% 7 years surgery. Safety assessment of these materials traditionally relies on the use of simple two-dimensional assays, where cells are grown on the surface of the material over a relatively short time frame. It is now well-known that the composition and stiffness of the extracellular matrix (ECM) have a critical effect on cell function. In this work, we have evaluated how cobalt ions influence the assembly of type I collagen, the principle component of the ECM in bone. We found that cobalt had a significant effect on collagen matrix formation, and its presence results in local variations in collagen density. This increase in heterogeneity causes an increase in localized mechanical properties but a decrease in the bulk stiffness of the material. Moreover, when collagen matrices contained cobalt ions, there was a significant change in how the cells interacted with the collagen matrix. Fluorescence images and biological assays showed a decrease in cell proliferation and viability with an increase in cobalt concentration. We present evidence that the cobalt ion complex interacts with the hydroxyl group present in the carboxylic terminal of the collagen fibril, preventing crucial stabilizing bonds within collagen formation. This demonstrates that the currently accepted toxicity assays are poor predictors of the longer-term biological performance of a material.




## INTRODUCTION

Cobalt−chromium−molybdenum alloys are one of the most common alloys used for both metal-on-metal (MOM) arthroplasties and implant resurfacing because of their high level of robustness and low risk of dislocation.[1−3] MOM implants have been found to have lower wear rates than metal-on-polyethylene implants and generate smaller wear particles;[4,5] however, there is a 500-fold increase in the generation rate of these small particles.[4−6] Metallic debris from MOM implants has been shown to initiate inflammatory responses which can lead to issues such as implant loosening and bone resorption.[7−10] In 2013, the Australian Orthopaedic Association National Joint Replacement Registry found unexpected failure rates approaching 10% after 7 years for MOM hip replacements alone.[1] Furthermore, MOM implants are 1.5 times more likely to fail 2 years post primary surgery in comparison with metal-on-polyethylene implants.[11] These failures were discovered because of the unexpected pain in patients, even in those with well-positioned implants, which suggested an adverse biological reaction to implant material derivatives rather than a biomechanical failure.[12] Damage as a consequence of the release of particles and ions from the implant surface has been shown to affect both the bone and the surrounding soft tissue.[13]

In addition to the production of particulate debris due to wear, MOM implants are also susceptible to corrosion processes in vivo that lead to the generation of small particles (including nanoscale) and the release of implant metal ions. Tribocorrosion occurs at the surface of articulating components of MOM implants as a consequence of the combination of mechanical wear and localized corrosion.[14] The unchallenged implant surface is protected from dissolution because of the presence of a passive surface oxide layer that limits corrosion. Disruption of this passive surface layer (due to mechanical damage) results in the exposure of the underlying metal, dissolution (anodic reaction), and the formation of

Received: May 18, 2018
Accepted: July 18, 2018
Published: August 30, 2018

ACS Publications © 2018 American Chemical Society



DOI: 10.1021/acsomega.8b01048
ACS Omega 2018, 3, 10129−10138

Downloaded via UNIV OF BIRMINGHAM on August 28, 2019 at 14:16:58 (UTC).
See https://pubs.acs.org/sharingguidelines for options on how to legitimately share published articles.

metal cations. The reaction produces electron flow from the corroding site to the metal surface (cathode), which is passive. Hydrolysis of released metal ions leads to a local acidification, which can subsequently allow free ions to easily migrate away from the original surface.[15,16] Cobalt−chromium−molybdenum alloys are protected by a passive oxide layer, which is 1−4 nm thick and primarily comprised chromium and cobalt oxides. The repetitive mechanical movement associated with load-bearing arthoplasties results in the abrasion of this thin oxide layer. Alongside the generation of particulate debris, the ionic cobalt and chromium released either remains in the solution or precipitates within the extracellular tissue space. As cobalt is more soluble than chromium, it is more likely to remain in the ionic form and interact with the extracellular matrix (ECM).[14]

Most investigations into how cobalt ions affect the surrounding tissue have focused on two-dimensional cell cultures, mimicking the osteolytic inflammatory response, driven by a direct interaction between macrophages and cobalt debris.[17−20] In particular, cobalt ions have been found to interact with DNA and nuclear proteins, ultimately causing cell death.[21] More specifically, cobalt ions are able to cross the cytoplasmic membrane, accumulating in the cell nucleus and subsequently the surrounding structures.[21−23] It has also been found that cobalt ions cause apoptosis in macrophages after 24 h and necrosis after 48 h.[24,25] Furthermore, cobalt ions exacerbate inflammation by increasing the amount of proinflammatory cytokines that are released from macrophages, such as tumor necrosis factor-a, IL-1b, and Il-6.[19−21,26,27] In addition to this, two-dimensional cell cultures looking at the direct effect of cobalt ions on osteoblast/mesenchymal stem cells have also been investigated. Studies showed how addition of cobalt ions into the cell media caused a decrease in the proliferation and function of osteoblasts and the differentiation of mesenchymal stem cells to osteoblasts.[28−31] In addition to being a degradation product from metallic prostheses, cobalt has been used to stimulate the HIF 1a pathway and angiogenesis. Glasses loaded with up to 1 wt % have proven to be nontoxic with a maximal dose of 5 wt % before toxicity occurs. At this point, there are no reports on how much concentration may influence the ECM or ECM interactions.[32−34] However, it is well-known that cell interactions are driven by small changes in the three-dimensional ECM, and therefore, two-dimensional studies are not sufficient.[35]

To date, studies in this area have investigated only the cellular effect of metal debris. However, it is the ECM that directly interacts with both implant and the surrounding tissue. The ECM mostly comprises collagen type I and provides not only structural support to cells and surrounding connective tissue but also plays a role within the differentiation of surrounding cells.[35−40] Collagen type I chains comprise a triple amino acid repeating sequence, Gly-X-Y, where glycine residues occupy every third position, and the X and Y residues are usually proline and hydroxyproline, respectively. Three collagen chains bind together via hydrogen bonding to form a triple helical structure, typically spanning 300 nm in length.[41] After both intra- and extracellular modification, the triple helix forms a collagen molecule.[42] As collagen matrix formation is hierarchical, multiple stages are required prior to collagen fiber formation. Five-stranded microfibrils super-twist and quasihexagonally stack, via covalent and hydrogen bonding, to form a collagen fibril. Because of the parallel staggering formed from the super-twist, a regular overlapping pattern, referred to as *d*-spacing, can be observed. This typically measures approximately 67 nm.[43−45] Fibrils can range from 50 to a few hundred nanometers in thickness and aggregate, via covalent bonding, to form fibers.[41] These fibers are cord-shaped and typically range within 1−20 $\mu$m in diameter.[43] Collagen fibers are the main constituents of the ECM and provide structural support to surrounding cells. As metallic ions produced from corrosion of MOM implants are so small, they can interact with the collagen fiber at much earlier stages of development. This can hinder the hierarchical process of collagen formation and may potentially alter both mechanical and structural properties of the matrix. Any changes to the structure of the ECM will drastically affect the way in which cells attach and thereby affect the tissue function. This study investigates how the presence of cobalt(II) ions affects collagen matrix formation and cell interactions to better understand unexpected MOM failures. Osteoblast cells were used to understand the effects of changes to the ECM without the influence of inflammatory changes. A maximum concentration of 200 ppm was used as this is the highest recorded cobalt concentration at the injury site.[46] This study highlights the importance of understanding the long-term biocompatibility of materials regarding not only cell response but also changes to the ECM.

## RESULTS

The effect of cobalt ions on the fibrillogenesis of collagen formation was analyzed using UV−vis spectrophotometry. Turbidity measurements, as shown in Figure 1A, suggest that the cobalt ion concentration has a detrimental effect on the kinetics of collagen fibril assembly. It takes much longer for the fibrils to fully form with the addition of cobalt as shown by the extension of the growth phase. This is further shown by comparing the growth phase ratios with respect to 0 ppm, as shown in Figure 1B. Turbidity results suggest that even at low concentrations, the cobalt ions interact with the collagen fibrils. To determine the loss of cobalt ions from collagen hydrogels, a leaching assay was performed, as shown in Figure 1C. The CoCol gel with a cobalt concentration of 200 ppm released only 8 ppm of cobalt ions into the surrounding media after 6 days. Given the small size of the cobalt ions,[4] it is unlikely that they are trapped sterically in the hydrogel matrix. This suggests that the ions are binding strongly within the hydrogel, preventing their diffusion into the media.

Atomic force microscopy (AFM) was performed to fully understand the effect of cobalt ions on the formation of collagen matrices. The microstructure of collagen fibrils doped with cobalt is shown in Figure 2. These images show that there are areas of both high- and low-density collagen fibrils in samples containing cobalt, as demonstrated in Figure 2A,B. These observations were also confirmed by reflectance microscopy images, shown in Figure 2C, as there is more collagen agglomeration with the addition of cobalt. This indicates that the cobalt ions alter the localized structure of the collagen matrix.

Force spectroscopy measurements on the CoCol gels were performed to determine the effect of cobalt addition on the adhesiveness of the samples. Because there is no alteration to the chemical nature of the collagen gel, nanomechanical properties could effectively reflect the localized arrangement of collagen fibrils. Large adhesion forces measured by the AFM tip are due to an increased contact area as a result of a readily



DOI: 10.1021/acsomega.8b01048
ACS Omega 2018, 3, 10129−10138

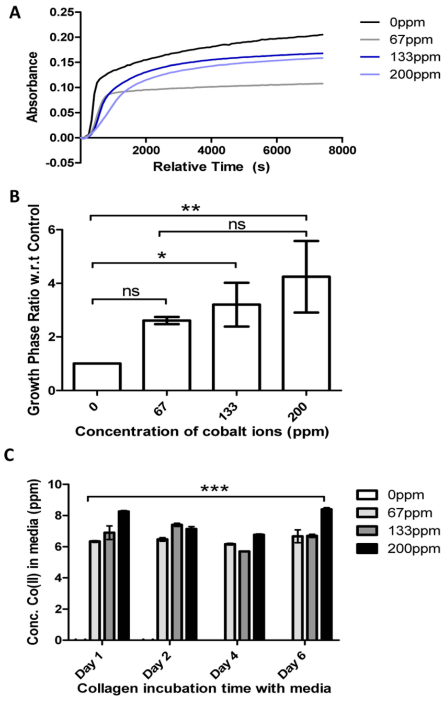



**Figure 1.** (A) Turbidity of cobalt-doped collagen at cobalt concentrations of 0, 67, 133, and 200 ppm. (B) Ratio of the growth phases at each cobalt concentration with respect to 0 ppm. (C) Leaching of cobalt ions from collagen hydrogels at varying time points. The initial cobalt concentrations were 0, 67, 133, and 200 ppm.

deformed collagen network and vice versa. Samples containing 0, 67, and 133 ppm of cobalt appear to have both stiff and soft fibrils. However, adhesion forces of the 200 ppm sample show that the fibrils are only soft, as shown in Figure 3. This result indicates that increased concentrations of cobalt ions could possibly block the important cross-linking binding sites for collagen and hence result in a porous matrix with enhanced local adhesiveness and reduced stiffness.

To analyze the dispersion of cobalt throughout the bulk matrix, X-ray fluorescence (XRF) measurements of CoCol gels were obtained, indicating the presence of cobalt ions, as depicted in Figure 4. It was shown that there were regions of localized cobalt, instead of an even dispersion, with an average 3-fold increase in cobalt concentration at areas of high intensity. This suggests that the increase in the heterogeneity of collagen fibrils within CoCol gels may be due to the uneven distribution of cobalt ions.

The effects of the heterogeneous dispersion of cobalt on the bulk material properties of collagen hydrogels were determined using oscillatory rheology, shown in Figure 5. Overall, there was a reduction in the storage and loss moduli of the gel with the addition of even low concentrations of cobalt. This indicates that the addition of cobalt ions reduces the stiffness of the hydrogel. This bulk property may be due to the areas of low-density collagen fibrils caused by cobalt collagen interactions as they are structurally weaker over the bulk gel structure.

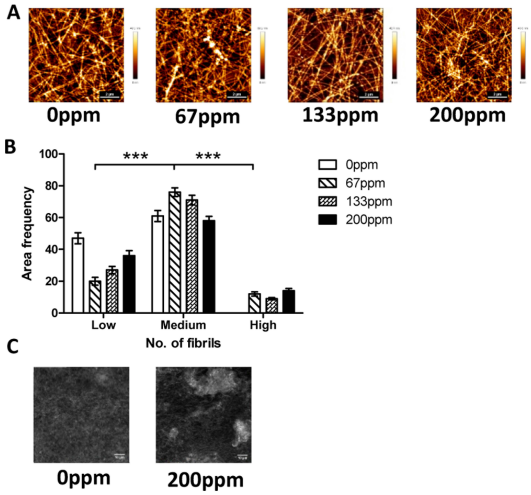



**Figure 2.** (A) AFM images of 1 mg $mL^{-1}$ collagen with increasing levels of cobalt ions. (B) Density histogram indicating the number of fibrils present within a 5000 $pixel^2$ area. Fibrils were separated into three categories, low (4−6 fibrils), medium (7−10 fibrils), and high (11−13 fibrils), and the number of areas with distinct number of fibrils was tallied to obtain the area frequency. (C) Confocal reflectance images of 1 mg $mL^{-1}$ collagen with added cobalt ions.

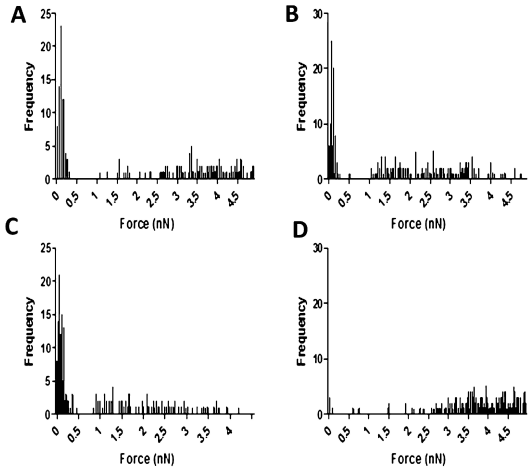



**Figure 3.** Force curves of CoCol gels at 0 (A), 67 (B), 133 (C), and 200 ppm (D) indicating the adhesion force of collagen fibrils.

As the underlying structure of collagen effects the growth and proliferation of cells, various biological assays were performed. MC3T3 cells maintain a relatively high viability when seeded onto CoCol gels up to a cobalt concentration of 133 ppm, as shown by the confocal fluorescence images in Figure 6A. In comparison, MC3T3 cells seeded within a cobalt-doped culture medium only maintained a relatively high viability up to a cobalt concentration of 67 ppm, as shown in Figure 6B. This further indicates that any cell response is not due to the direct interaction between the cells and the cobalt ions. Furthermore, the presence of cobalt ions within the



DOI: 10.1021/acsomega.8b01048
ACS Omega 2018, 3, 10129−10138

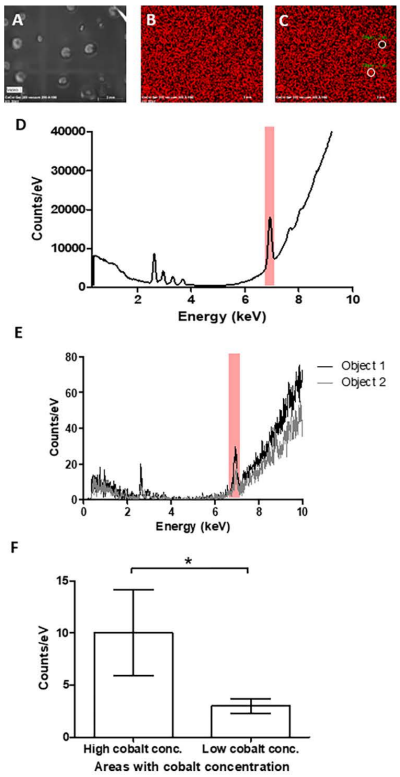



**Figure 4.** X-ray fluorescent measurements of cobalt distribution in a 200 ppm collagen hydrogel. (A) Bright-field image of bulk hydrogel, (B) relative cobalt intensity throughout hydrogel, (C) an example of positions of object 1 and object 2 in relation to bulk hydrogel, (D) spectra of gel with cobalt highlighted, (E) spectra of both object 1 and object 2 used to obtain an average of a 3-fold increase in cobalt fluorescence, and (F) average cobalt concentration of all object areas separated by relatively high and low concentrations, giving a $P$ value <0.1.

collagen hydrogel caused a change in the morphology, with an initial increase in actin filament elongation prior to reduction in the cellular cytoskeleton entirely, as shown in Figure 6C. Metabolic activity of the cells is reduced with the addition of cobalt ions as shown by the 3-(4,5-dimethylthiazol-2-yl)-2,5-diphenyltetrazolium bromide (MTT) assay. Figure 6D shows an 82% decrease in the absorbance showing a decrease in active mitochondria at a cobalt concentration of 100 ppm. The alamarBlue assay and trypan blue assay indicate that the proliferation of cells significantly decreased when low concentrations of cobalt ions were added to the collagen structure. This decrease was significant for both cells seeded onto CoCol gels and cells seeded within a cobalt-doped culture medium as shown in Figure 6E,F. This suggests that the structure of CoCol gels is directly affecting the way in which cells attach and therefore proliferate, causing a reduction in viability that correlates with the cobalt concentration.

To experimentally determine the preferential binding site between cobalt ions and collagen, Raman spectroscopy and differential scanning calorimetry (DSC) of both 0 and 200 ppm of cobalt-doped collagen samples were performed. Raman

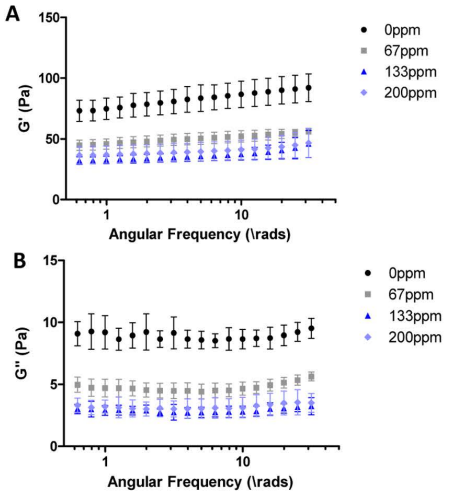



**Figure 5.** $G'$ (A) and $G''$ (B) from a frequency sweep of collagen hydrogels with the addition of an increasing concentration of cobalt ions.

spectra of both 0 and 200 ppm collagen samples showed characteristic protein peaks such as the C═O peak at 1606.75/1607.76 $cm^{-1}$ and the secondary amide peak at 1205.08/1207.25 $cm^{-1}$, as shown in Figure 7A.[47] However, in order to determine any subtle differences between each sample, principal component analysis (PCA) was performed on the data set after cosmic ray removal. The majority of information was described by the first two principal components. Figure 7B corresponds to the scores plot[48] for all the Raman spectra, within which two clusters separating the 0 ppm sample and 200 ppm sample were obtained. The position of relative differences between the 0 and 200 ppm samples was determined through plotting the loading vectors as a function of wavenumber.[49] The plot of the first loading, shown in Figure 7C, indicates the most prominent changes between the spectra through intense peaks.[48] It was found that the largest variation between the Raman spectra of the 0 ppm sample and the 200 ppm sample occurred at 869 and 1000 $cm^{-1}$, respectively.

These wavenumbers correspond to a C−O bond,[47] with this vibration being suppressed within the 200 ppm sample. DSC results show that bulk water within the 200 ppm collagen sample is not bound as strongly as that within the 0 ppm collagen sample. All the bound water within the 200 ppm collagen sample is removed at a temperature of 120.3, 5 °C lower than that of the 0 ppm collagen sample. In addition, the energy required to completely remove the water bound within the 0 ppm collagen sample is 14% more than that within the 200 ppm collagen, as shown in Figure 7D. This highly suggests that cobalt is binding to the collagen fibril, reducing the number of tightly bound water molecules surrounding the protein.

## DISCUSSION

The introduction of cobalt ions to collagen hydrogels causes significant effects in both the gel structure and the way in which cells attach to the collagen. These ions cause a change in the kinetics of fibril formation. The elongation of the growth



DOI: 10.1021/acsomega.8b01048
ACS Omega 2018, 3, 10129−10138

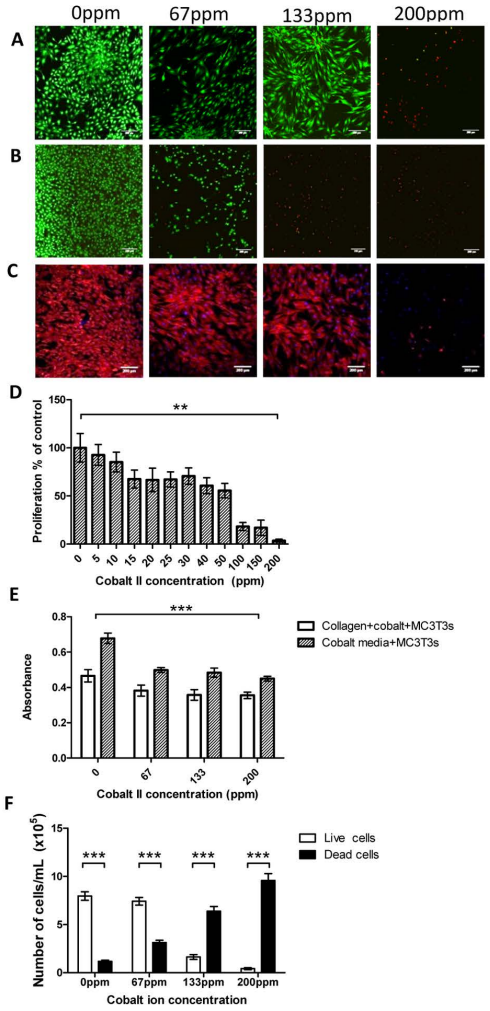



**Figure 6.** Live/dead images of MC3T3 cells stained with calcein AM and propidium iodide seeded onto both CoCol gels (A) and into cobalt-infused media (B). (C) Actin and 4′,6-diamidino-2-phenylindole (DAPI) staining of MC3T3 cells cultured onto CoCol gels. (D) MTT assay of MC3T3 cells cultured in cobalt-infused media. (E) alamarBlue assay of MC3T3 cells cultured on CoCol gels and in cobalt-infused media. (F) Trypan blue assay quantifying the number of live and dead cells with increasing cobalt concentration.

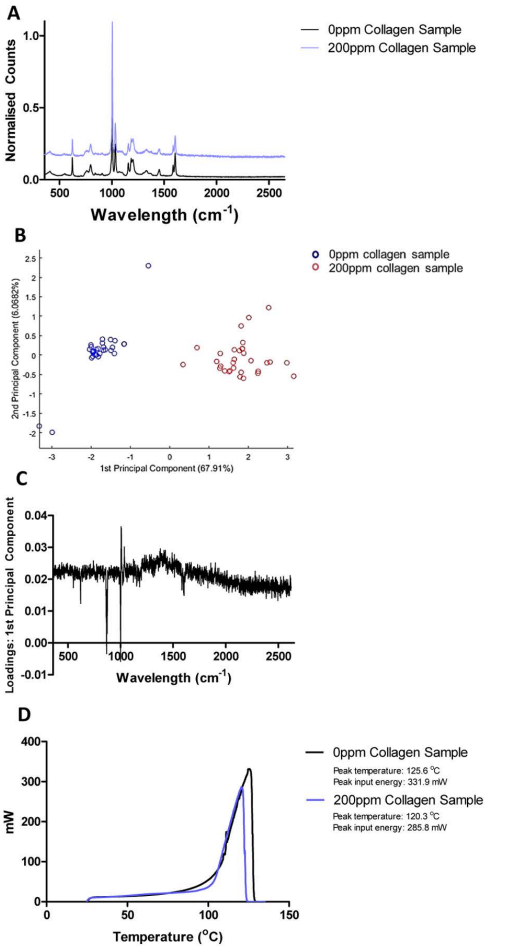



**Figure 7.** (A) Raman spectra of both 0 ppm collagen and 200 ppm collagen hydrogels, (B) score plots of the first two principal components, (C) loading plots of the first principal component indicating changes at 1000 and 869 $cm^{-1}$, and (D) DSC measurements indicating a reduction in energy required to remove bulk water between 0 and 200 ppm CoCol gels.

phase indicates that cobalt ions directly interact with the collagen fibrils. On incubation, the CoCol gels released a maximum of only 8 ppm of cobalt, suggesting that there is a strong interaction between the cobalt ions and the hydrogel, preventing the cobalt ions from diffusing out of the gel. AFM and confocal reflectance images show how increasing the concentration of cobalt increases areas of high-density collagen. A density histogram indicates that the addition of cobalt to the collagen matrix causes a high number of fibrils per unit area. These regions suggest that the cobalt ions ionically interact with the matrix to create areas of agglomeration, indicating that the cobalt ions are most likely present within these high-density regions. Overall, this causes an increase in the heterogeneity of the local collagen matrix. Force spectroscopy measurements indicated that a concentration of 200 ppm produced softer fibrils than that of 0 ppm. Furthermore, samples containing 67 and 133 ppm had areas of both stiff and soft fibrils, whereas 200 ppm only had soft fibrils. This may be due to a decrease in cross-linking sites between fibrils, as they are blocked by cobalt ions.

Cobalt distribution throughout the bulk of the hydrogel, determined via XRF—, further indicates that the collagen fibril agglomeration sites are formed because of an increase in the localized cobalt concentration. As there was a 3-fold relative increase in cobalt concentrations at select sites, it can be assumed that these areas correspond to high-density collagen areas.



DOI: 10.1021/acsomega.8b01048
ACS Omega 2018, 3, 10129−10138

Regions of high and low densities of collagen make the overall bulk structure less stiff. Oscillatory rheology shows a decrease in the storage and loss moduli with even low concentrations of cobalt, indicating a reduction in overall stiffness. This may be due to the low-density areas of collagen which act as weak points within the structure. The increase in ionic bonding between collagen fibrils and cobalt ions prevents the interactions forming between collagen fibrils themselves and therefore reduces the overall stiffness of the hydrogel structure.

As we determined from Figure 1C, there was insignificant leaching of cobalt ions from the collagen hydrogel to have any effect on cell proliferation and viability. Therefore, any decrease is due to the change in the matrix formation alone. Fluorescence images suggest that the manipulation of collagen fibrils by the introduction of cobalt ions results in not only a decrease in cell viability but also a change in the morphology of the cells. This was further confirmed by phalloidin and DAPI staining, showing that at low concentrations of cobalt, there was an elongation of actin filaments, preventing the alignment of cells. Increasing the concentration of cobalt ions also caused a reduction in the actin filament production. This may be due to an increase in the heterogeneity of the bulk matrix. Cell viability staining indicated that there was no overall cell death until 200 ppm of cobalt was added, however, because the heterogeneous distribution of cobalt in collagen cell viability varied between 67 and 133 ppm. Force measurements indicated that at 200 ppm, fibrils formed an overall soft material. This may explain why cell death significantly increased at 200 ppm as the fibrils were not stiff enough to support cell growth. The MTT assay, alamarBlue assay, and trypan blue assay further suggest that the manipulation of collagen fibrils by cobalt ions prevents cells from behaving normally. The decrease in cell proliferation with an increase in cobalt ions may imply that poorly formed collagen fibrils, resulting in a heterogeneous matrix, cannot facilitate signaling between cells. The reduction in attachment sites between the cell and the collagen fibril results in a rounding-off of the cells, preventing the cells from signaling to each other and proliferating.

When cobalt(II) chloride is dissolved in water, the predominant cation is $[Co(H_2O)_6]^{2+}$.[50] As $[Co(H_2O)_6]^{2+}$ is a positive complex in solution, it will interact with negatively charged amino acid residues along the collagen chains. Negatively charged collagen chains can interact with water molecules and form a dense and strongly bound hydration monolayer. Four water molecules of the monolayer bind with the carbonyl and hydroxyl groups of both glycine and hydroxyproline in collagen, as shown in Figure 8A.[51,52] Proline, however, is not associated with collagen hydration, participating only in interchain hydrogen bonding.[53] Initial hydration of the collagen molecule, referred to as nonfreezing bound water, is formed when water binds to hydrophilic amino acid residues of the collagen. Once all hydrophilic sites are filled, the water binds to nonpolar regions of the collagen, referred to as freezing bound water, completing the hydration monolayer, Figure 8B.[52]

As there is a lack of direct interactions between neighboring collagen molecules, it is assumed that hydrogen bonding of water bridges between residues in neighboring molecules contributes to the matrix assembly. Intrachain water bridges are dependent on the local environment and are typically two to three molecules long. Water bridges form in three ways,

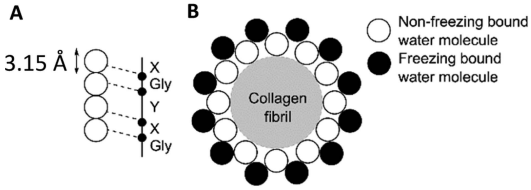



**Figure 8.** Schematic diagram depicting the cross section of the binding sites of water with a collagen fibril, not to scale. (A) Four water molecules per three collagen residues. (B) Nonfreezing and freezing bound water layers surrounding the collagen fibril. Image adapted from Fullerton and Amurao.[49]

either between two hydroxyl groups, C−O···water$_n$···O−C; between two carboxyl groups, C═O···water$_n$···O═C; or between a hydroxyl group and a carbonyl group in adjacent molecules, C−O···water$_n$···O═C.[47]

When $[Co(H_2O)_6]^{2+}$ is introduced into the collagen matrix, it may interact either directly with individual collagen fibrils or with water molecules of the nonfreezing bound water layer, depicted in Figure 9A,B. We then examined possible underlying mechanisms responsible for cobalt collagen

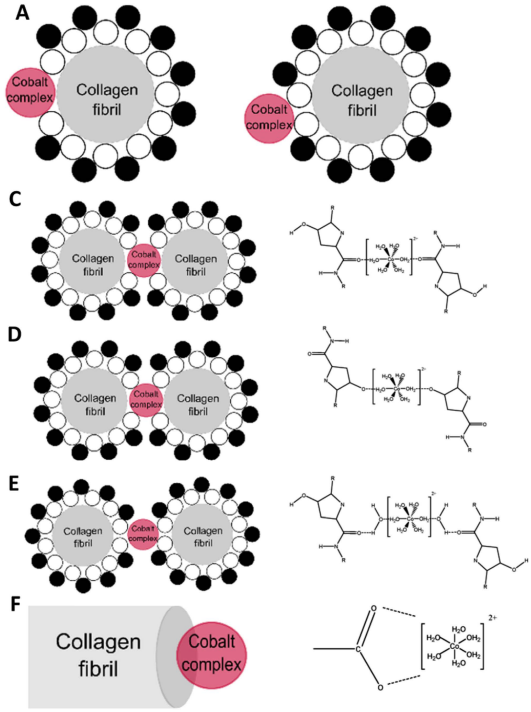



**Figure 9.** Schematic diagram depicting the binding sites of a cobalt complex with a collagen fibril, not to scale. (A) Cobalt complex interacting with the collagen fibril directly. (B) Cobalt complex interacting with the nonfreezing water layer surrounding the collagen fibril. Proposed binding sites of a cobalt complex with a collagen fibril where interactions occur with the carboxylic group (C), hydroxyl group (D), forming a water bridge (E), or interactions with the hydroxyl structure in the carboxylic terminal (F).



DOI: 10.1021/acsomega.8b01048
ACS Omega 2018, 3, 10129−10138

interaction. Direct interaction of cobalt complexes with collagen molecules occurs through either the carbonyl groups present in both glycine and hydroxyproline or the hydroxyl group present in hydroxyproline alone, shown in Figure 9C,D. If the cobalt complex interacts with the nonfreezing bound water layer, then hydrogen bonds will form between the water molecules and the cobalt complex, incorporating the complex into the water bridge, shown in Figure 9E. In addition, cobalt may also interact with the carboxylic terminal of the collagen molecule, as shown in Figure 9F.

Raman spectroscopy showed suppression of a secondary alcohol vibration, with a reduction in the C−O bond peak, between 0 and 200 ppm collagen samples. This suggests that cobalt ions interact specifically with a hydroxyl group.[52−54] Although this is present within the hydroxyproline, previous studies into complex interactions with collagens show preferential binding to terminal sites of the molecule.[55] Therefore, it is more likely that the cobalt ions interact with the hydroxyl structure at the carboxylic terminal. DSC measurements showed that a 14% decrease in energy is required to remove bound water from the 200 ppm CoCol gel. This suggests that cobalt ion interactions prevent water binding either by blocking of the binding sites or altering the assembly of the collagen molecules, preventing these binding sites from being accessible.

## ■ CONCLUSIONS

We have shown that cobalt ions have an adverse effect on the way in which collagen fibrils form. An increase in the cobalt ion concentration lengthens the time it takes for a collagen matrix to form and produce areas of both high-density and low-density collagen fibrils. This causes an increase in the structural heterogeneity, reducing the overall stiffness of the collagen hydrogel. This change in matrix formation prevents osteoblasts from attaching and proliferating at a normal rate, changing the cell morphology and ultimately resulting in a decrease in cell viability. We have also suggested that the binding site for cobalt ions lies with the hydroxyl group present in the C-terminal. This leads toward a reduction in crucial stabilizing bonds within matrix formation, explaining the decrease in matrix stiffness and reduction in energy required for bulk water loss.

This gives further insights into the underlying mechanisms that result in unexpected failures of MOM implants. As we have shown, the collagen matrix is adversely affected, and it is likely that the extensive necrosis seen is more a result of the metal debris changing the ECM structure rather than interacting with the surrounding cells directly.

## ■ MATERIALS AND METHODS

Cobalt-doped collagen hydrogels (CoCol gels): Cultrex rat collagen type I (AMS Biotechnology Europe Marketplace, UK) supplied at a concentration of 5 mg $mL^{-1}$ was diluted to 3 mg $mL^{-1}$ using a phosphate-buffered saline (PBS) stock (NaCl 0.137 M, KCl 0.003 M, $Na_2HPO_4$ 0.008 M, $KH_2PO_4$ 0.0015 M). This stock was created by dissolving two Oxoid PBS tablets (Thermo Fisher Scientific, UK) in 200 mL of distilled water. The cobalt(II) chloride stock was made to a concentration of 72.67 mg $mL^{-1}$ with double-distilled water. Collagen was further diluted to the desired concentrations using Dulbecco's modified Eagle's medium (DMEM) (Sigma-Aldrich, UK) or cobalt-infused DMEM and neutralized with 1 M sodium hydroxide (Sigma-Aldrich, UK) prior to incubation for 3 h to ensure gelation.

**Turbidity.** A UV−vis spectrophotometer (Cecil Instruments, UK) was used to measure the turbidity of collagen dispersion during the process of fibril formation. Temperature was maintained at 37 °C, and samples were placed into a disposable 1 cm plastic cuvette, with absorbance measured at 620 nm.

**Leaching Assay.** CoCol gels were prepared using Co concentrations of 0, 67, 133 and 200 ppm within a 12-well plate. PBS (2 mL) (as prepared above) was added to the wells, removed at the fixed time points, and frozen. A 7500ce inductively coupled plasma optical emission spectrometer (Agilent Technologies, USA) was used to determine the concentration of leached cobalt ions from the frozen PBS samples. A two-way analysis of variance (ANOVA) was used to obtain the statistics.

**Atomic Force Microscopy.** CoCol gels were prepared as indicated above but with a buffer of PBS to reduce building up of salt during dehydration. Samples were deposited onto a pressure cleaned silicon wafer using an adjustable micropipette, resulting in a thin collagen layer on the solid substrate. The gel was dehydrated in an incubator over 24 h and subsequently washed three times with distilled water. A 10 × 10 $\mu m^2$ area of each sample was imaged by a NanoWizard 4 NanoScience AFM (JPK Instruments, Germany), using a cantilever with a frequency of 20 kHz and a spring constant of 0.9 N $m^{-1}$ in the intermitted contact mode. Fibril density was determined by counting the number of fibrils present in a 5000 × 5000 pixel area. For each concentration, 108 areas were allocated over three samples to determine overall fibril density. Fibril density was classified as low (4−6 fibrils), medium (7−10 fibrils), and high (11−13 fibrils) and determined by separating the number of fibrils into three distinct groups. A two-way ANOVA was used to obtain the statistics.

**Reflectance Microscopy.** CoCol gels were prepared within a 35 mm imaging dish with an N#1.5 coverslip base. The gels were imaged with a 60× water immersion lens with a 488 nm laser on an Olympus FX1000 microscope in the reflection mode. A three-dimensional stack of fixed volume was acquired via multiple images in the $z$-direction and compressed into a two-dimensional plane.

**Force Spectroscopy.** CoCol gel (16 $\mu$L) was added to a silicon wafer. A Dimension 3100 AFM with a NanoScope IV controller (Veeco, Santa Barbara, USA) was used to perform nanomechanical adhesion measurements. Silicon nitride cantilevers (Budget Sensors, UK), with a nominal spring constant of 0.3 N $m^{-1}$, were used to carry out these force measurements in the PBS solution. One hundred force curves were acquired over a 10 × 10 $\mu m^2$ area from each location (three separate locations on each CoCol gel sample) for analysis. The control experiment, without the presence of a collagen film, was conducted on a titanium substrate. Overall adhesion forces between the AFM tip and the collagen film, which is reflected by the hysteresis between approaching and retraction curves, were analyzed using Carpick's toolbox, which is a suite of MATLAB scripts.

**X-ray Fluorescence.** A high-resolution measurement of a 4.9 mL sample of 200 ppm CoCol gel was analyzed using a TORNADO M4 XRF (Bruker, UK). A scan area of 100 ms $pixel^{-1}$ was used with a speed of 30 m $s^{-1}$ for three cycles. Ten object areas were taken over the entirety of the scan area over both high- and low-intensity regions. The differences in the



DOI: 10.1021/acsomega.8b01048
ACS Omega 2018, 3, 10129−10138

height of the peaks were measured, and the average difference is used to give an increase in the relative concentration of cobalt ions. Mann−Whitney test was performed to determine the statistics between average cobalt counts with respect to high- and low-density areas.

**Rheology.** CoCol gels were prepared in Petri dishes at a collagen concentration of 1 mg $mL^{-1}$ and a gel height of 1 mm. Samples were maintained at a temperature of 37 °C for 5 min prior to measurement. Rheological measurements were taken with an AR-G2 rheometer (TA Instruments), using a parallel plate geometry with a gap of 1 mm. A sandblasted plate was used to minimize the wall slip, and samples remained in the Petri dishes during measurement. Strain sweeps were taken, at a frequency of 1 Hz, in order to establish the limit of the linear viscoelastic region, the lowest value of which was found to be 0.01, for samples doped with 200 ppm of cobalt. Frequency sweeps were therefore performed at a strain of 0.01 over a frequency range of 0.01−10 Hz.

**Cell Culture.** Mouse MC3T3-E1 (passage 23, ATCC CRL-2593) osteoblast precursor cells were cultured in a $\alpha$-minimum essential medium ($\alpha$-MEM) (Sigma-Aldrich, UK) supplemented with 1% penicillin−streptomycin (Sigma-Aldrich, UK), 10% fetal bovine serum (Sigma-Aldrich, UK), and 4% L-glutamine (Sigma-Aldrich, UK). Cells were maintained at 37 °C and 5% $CO_2$ within a humidified incubator.

**Confocal Fluorescent Imaging.** CoCol gels, at a collagen concentration of 1 mg $mL^{-1}$, were gelled within a 12-well uncoated 10 mm glass diameter MatTek dish. For cell viability experiments, MC3T3 cell suspensions were seeded at a density of 200 000 cells $mL^{-1}$ onto the gel surface and grown within the supplemented $\alpha$-MEM (culture medium). In addition to this, MC3T3 cells were seeded at the same density onto the base of the wells. These were grown within the culture medium which had been doped with cobalt concentrations of 0, 67, 133, and 200 ppm. After culturing for 3 days, the medium was removed, and samples were washed with PBS. Calcein AM (Thermo Fisher Scientific, UK) and propidium iodide (Thermo Fisher Scientific, UK) dyes were prepared, with 300 $\mu$L added to each well and incubated for 30 min. For morphology experiments, MC3T3 cell suspensions were seeded at a density of 200 000 cells $mL^{-1}$ onto the surface of the CoCol gel and cultured for 3 days. The culture medium was then removed, and surfaces of the CoCol gel were washed twice with PBS (as prepared above). Cells were fixed within 4% formaldehyde for 15 min and washed as described before. Cells were then permeabilized with 0.5% Triton X-100 for 5 min. Staining with Alexa Fluor 488 Phalloidin and DAPI (Thermo Fisher Scientific, UK) allowed for visualization of the cytoskeleton and nuclei. Images were taken on a FV10-ASW confocal microscope with a 10× lens with image dimensions of 800 × 800 pixels.

**MTT (3-(4,5-Dimethylthiazol-2-yl)-2,5-diphenyltetrazolium bromine) Assay.** MC3T3 cells were seeded into a 48-well plate at a density of 7500 cells per well. Cells were initially cultured using supplemented $\alpha$-MEM for 24 h. This was then aspirated and replaced with a cobalt-infused culture medium. Culture media containing Co(II) ions were prepared by adding the stock cobalt solution to the supplemented $\alpha$-MEM up to a concentration of 200 ppm. The pH was adjusted using 1 M sodium hydroxide to neutral and diluted to the desired cobalt concentrations. Cells were cultured in cobalt media for a further 24 h prior to performing the MTT assay (Merck, USA). A stock solution of sterile-filtered 5 mg $mL^{-1}$ MTT (Sigma, UK) in PBS was prepared and stored at 4 °C in light-deprived conditions. After culturing for 3 days, cobalt media was aspirated and replaced with 200 $\mu$L of supplemented $\alpha$-MEM and 0.5 mg $mL^{-1}$ of MTT within each well. This was incubated for 2 h at 37 °C to allow for the formation of formazan crystals. The MTT and $\alpha$-MEM solution was then removed, and 200 $\mu$L of 0.22 $\mu$m sterile filtered dimethyl sulfoxide was added to each well. The plate was then agitated for another 2 h at room temperature to dissolve formazan crystals. Absorbance was measured at 570 nm using a microplate reader (Promega, UK). A one-way ANOVA was conducted to determine the statistics.

**alamarBlue Assay.** MC3T3 cell suspensions were seeded onto the surface of the cobalt-doped collagen hydrogel at a concentration of 200 000 cells $mL^{-1}$ in 12-well plates. After culturing for 3 days, the culture medium was aspirated, and 300 $\mu$L of fresh medium mixed with 10% alamarBlue dye (Thermo Fisher Scientific, UK) was added. This was incubated at 37 °C for 4 h before 100 $\mu$L of the medium was removed and placed into a 96-well plate. Absorption was read at 570 nm. A two-way ANOVA was conducted to determine the statistics.

**Trypan Blue Assay.** CoCol gels at concentrations of 0, 67, 133, and 200 ppm were gelled within a 12-well plate. MC3T3 cell suspensions were seeded onto the gels at a concentration of 100 000 cells $mL^{-1}$. Samples were cultured for 3 days within a humidified incubator. In order to detach cells from the collagen hydrogel, 0.1% collagenase was added to each sample followed by incubation for an hour. To count cells, 100 L of media was added to 100 L of trypan blue, to produce a diluting factor of 2, and both live and dead cells were counted using a hemocytometer. A two-way ANOVA was conducted to determine the statistics.

**Raman Spectroscopy.** Two 1 mL samples of 0 and 200 ppm of cobalt-doped collagen gels were analyzed using the inVia Qontor Confocal Raman microscope (Renishaw, UK). PBS was used as a buffer within these gels to remove any additional signal from DMEM. A 60× water immersion lens was used to obtain Raman spectra. An extended scan over the spectral range of 100−4500 $cm^{-1}$ was taken at random positions throughout each sample. Each scan had a 30 s acquisition using a 785 nm laser with the pinhole in at 10% power. Thirty scans of each sample were obtained, with cosmic ray removal performed on a wire. Averaging and normalizing of the data were obtained using Microsoft Office 365 Excel (2013). Reduction of the spectral range of 350−2650 $cm^{-1}$ was performed using Prism 5 (GraphPad Software, 2007) to remove any background effects.

**Principal Component Analysis.** Raman spectra from both 0 and 200 ppm CoCol samples were imported into MATLAB software (R2017a). The data set comprised 60 spectra in total, 30 from each sample. Before PCA, all spectra were normalized and reduced to a spectral range of 350−2650 $cm^{-1}$ to remove any background interference. Once PCA was conducted over the data set, principal components were chosen based on the highest fraction of variance. Both the scores and loadings values were plotted with respect to wavelength to aid data interpretation.

**Differential Scanning Calorimetry.** Samples of 0 and 200 ppm of cobalt-doped collagen gels were analyzed using a METTLER TOLEDO DSC 1 (METTLER TOLEDO, Schwerzenbach, Switzerland). Samples were weighed into 46 $\mu$L aluminum DSC pans (METTLER TOLEDO), capped with



DOI: 10.1021/acsomega.8b01048
ACS Omega 2018, 3, 10129−10138

aluminum DSC lids (METTLER TOLEDO), and sealed with a press (METTLER TOLEDO). This was calibrated with indium and zinc standards. PBS was used as a buffer within the gels to remove any additional signal from DMEM. Experiments were conducted under a nitrogen flow rate of 50 mL $min^{-1}$, and samples were heated from 25 to 135 °C after gelation at a rate of 5 °C $min^{-1}$.

## ■ ASSOCIATED CONTENT

### Supporting Information

The Supporting Information is available free of charge on the ACS Publications website at DOI: 10.1021/acsomega.8b01048.

Circular dichroism data, further AFM data, and turbidity data relating to matrix formation with increasing cobalt ion concentration (PDF)

## ■ AUTHOR INFORMATION


### Corresponding Authors

*E-mail: emm502@bham.ac.uk (E.M.M.).
*E-mail: L.M.Grover@bham.ac.uk (L.M.G.).

### ORCID

Emma M. McCarthy: 0000-0002-4318-2890
Zhenyu J. Zhang: 0000-0003-0243-2109


### Author Contributions

All authors contributed to the design of the research. Experimental research was performed and analyzed predominately by E.M.M. and H.F. with force spectroscopy measurements completed by Z.J.Z. The manuscript was written by E.M.M. All authors reviewed and commented on the manuscript

### Notes

The authors declare no competing financial interest.

## ■ ACKNOWLEDGMENTS

This work is supported in part by the EPSRC Sci-Phy-4-Health Centre for Doctoral Training (EP/L016346/1 to E.M.M.) and the NHIR Surgical Reconstruction and Microbiology Research (NIHR SRMRC to E.M.M.). All the data that were required to evaluate the conclusions made within this paper are present within the data presented and/or the supplementary data.

## ■ REFERENCES


(1) Nawabi, D. H.; Nassif, N. A.; Do, H. T.; Stoner, K.; Elpers, M.; Su, E. P.; Wright, T.; Potter, H. G.; Padgett, D. E. What causes unexplained pain in patients with metal-on metal hip devices? A retrieval, histologic, and imaging analysis. *Clin. Orthop. Relat. Res.* **2104**, *472*, 543−554.

(2) Mahendra, G.; Pandit, H.; Kliskey, K.; Murray, D.; Gill, H. S.; Athanasou, N. Necrotic and inflammatory changes in metal-on-metal resurfacing hip arthroplasties. *Acta Orthop.* **2009**, *80*, 653−659.

(3) Matthies, A. K.; Racasan, R.; Bills, P.; Blunt, L.; Cro, S.; Panagiotidou, A.; Blunn, G.; Skinner, J.; Hart, A. J. Material loss at the taper junction of retrieved large head metal-on-metal total hip replacements. *J. Orthop. Res.* **2013**, *31*, 1677−1685.

(4) Kwon, Y.-M.; Xia, Z.; Glyn-Jones, S.; Beard, D.; Gill, H. S.; Murray, D. W. Dose-dependent cytotoxicity of clinically relevant cobalt nanoparticles and ions on macrophages in vitro. *Biomed. Mater.* **2009**, *4*, 025018.

(5) Doorn, P. F.; Campbell, P. A.; Worrall, J.; Benya, P. D.; McKellop, H. A.; Amstutz, H. C. Metal wear particle characterization from metal on metal total hip replacements: Transmission electron microscopy study of periprosthetic tissues and isolated particles. *J. Biomed. Mater. Res.* **1998**, *42*, 103−111.

(6) Sieber, H.-P.; Rieker, C. B.; Küttig, P. Analysis of 118 second-generation metal-on-metal retrieved hip implants. *J. Bone Jt. Surg.* **1999**, *81*, 46−50.

(7) Koch, K. M.; Koff, M. F.; Bauer, T. W.; Shah, P. H.; Nencka, A. S.; Kaushik, S. S.; Potter, H. G. Off-resonance based assessment of metallic wear debris near total hip arthroplasty. *Magn. Reson. Med.* **2018**, *79*, 1628−1637.

(8) Lohmann, C. H.; Singh, G.; Willert, H.-G.; Buchhorn, G. H. Metallic debris from metal-on-metal total hip arthroplasty regulates periprosthetic tissues. *World J. Orthoped.* **2014**, *5*, 660−666.

(9) Langton, D. J.; Jameson, S. S.; Joyce, T. J.; Gandhi, J. N.; Sidaginamale, R.; Mereddy, P.; Lord, J.; Nargol, A. V. F. Accelerating failure rate of the ASR total hip replacement. *J. Bone Joint Surg. Br. Vol.* **2011**, *93*, 1011−1016.

(10) Davies, A. P.; Willert, H. G.; Campbell, P. A.; Learmonth, I. D.; Case, C. P. An Unusual Lymphocytic Perivascular Infiltration in Tissues around Contemporary Metal-on-Metal Joint Replacements. *J. Bone Jt. Surg.* **2005**, *87*, 18−27.

(11) Pearson, M. J.; Williams, R. L.; Floyd, H.; Bodansky, D.; Grover, L. M.; Davis, E. T.; Lord, J. M. The effects of cobalt-chromium-molybdenum wear debris in vitro on serum cytokine profiles and T cell repertoire. *Biomaterials* **2015**, *67*, 232−239.

(12) Hart, A. J.; Matthies, A.; Henckel, J.; Ilo, K.; Skinner, J.; Noble, P. C. Understanding Why Metal-on-Metal Hip Arthroplasties Fail. *J. Bone Jt. Surg., Am. Vol.* **2012**, *94*, e22.

(13) Panichkul, P.; Fricka, K. B.; Hopper, R. H.; Engh, C. A. Greater Trochanteric Fragmentation after Failed Metal-on-Metal Hip Arthroplasty. *Orthopedics* **2015**, *38*, e447−e451.

(14) Sinnett-Jones, P. E.; Wharton, J. A.; Wood, R. J. K. Micro-abrasion-corrosion of a CoCrMo alloy in simulated artificial hip joint environments. *Wear* **2005**, *259*, 898−909.

(15) Jacobs, J. J.; Gilbert, J. L.; Urban, R. M. Corrosion of Metal Orthopaedic Implants*. *J. Bone Jt. Surg., Am. Vol.* **1998**, *80*, 268−282.

(16) Oldfield, J. W. Electrochemical theory of galvanic corrosion. *Am. Soc. Test. Mater.* **1998**, *978*, 5−22.

(17) Posada, O. M.; Tate, R. J.; Grant, M. H. Toxicity of cobalt-chromium nanoparticles released from a resurfacing hip implant and cobalt ions on primary human lymphocytes in vitro. *J. Appl. Toxicol.* **2015**, *35*, 614−622.

(18) Posada, O.; Tate, R.; Meek, R. M.; Grant, M. In Vitro Analyses of the Toxicity, Immunological, and Gene Expression Effects of Cobalt-Chromium Alloy Wear Debris and Co Ions Derived from Metal-on-metal Hip Implants. *Lubricants* **2015**, *3*, 539−568.

(19) Haynes, D. R.; Rogers, S. D.; Hay, S.; Pearcy, M. J.; Howie, D. W. The differences in toxicity and release of bone-resorbing mediators induced by titanium and cobalt-chromium-alloy wear particles. *J. Bone Jt. Surg., Am. Vol.* **1993**, *75*, 825−834.

(20) Hallab, N. J.; Jacobs, J. J. Chemokines associated with pathologic responses to orthopedic implant debris. *Front. Endocrinol.* **2017**, *8*, 5.

(21) Ortega, R.; Bresson, C.; Fraysse, A.; Sandre, C.; Devès, G.; Gombert, C.; Tabarant, M.; Bleuet, P.; Seznec, H.; Simionovici, A.; Moretto, P.; Moulin, C. Cobalt distribution in keratinocyte cells indicates nuclear and perinuclear accumulation and interaction with magnesium and zinc homeostasis. *Toxicol. Lett.* **2009**, *188*, 26−32.

(22) Sargeant, A.; Goswami, T. Hip implants - Paper VI - Ion concentrations. *Mater. Des.* **2007**, *28*, 155−171.

(23) Jomova, K.; Valko, M. Advances in metal-induced oxidative stress and human disease. *Toxicology* **2011**, *283*, 65−87.

(24) Catelas, I.; Petit, A.; Vali, H.; Fragiskatos, C.; Meilleur, R.; Zukor, D. J.; Antoniou, J.; Huk, O. L. Quantitative analysis of macrophage apoptosis vs. necrosis induced by cobalt and chromium ions in vitro. *Biomaterials* **2005**, *26*, 2441−2453.

(25) Catelas, I.; Petit, A.; Zukor, D. J.; Antoniou, J.; Huk, O. L. TNF-$\alpha$ secretion and macrophage mortality induced by cobalt and chromium ions in vitro-Qualitative analysis of apoptosis. *Biomaterials* **2003**, *24*, 383−391.

(26) Caicedo, M. S.; Pennekamp, P. H.; McAllister, K.; Jacobs, J. J.; Hallab, N. J. Soluble ions more than particulate cobalt-alloy implant debris induce monocyte costimulatory molecule expression and release of proinflammatory cytokines critical to metal-induced lymphocyte reactivity. *J. Biomed. Mater. Res., Part A* **2010**, *93*, 1312−1321.
(27) Samelko, L.; Caicedo, M. S.; Lim, S.-J.; Della-Valle, C.; Jacobs, J.; Hallab, N. J. Cobalt-Alloy Implant Debris Induce HIF-1α Hypoxia Associated Responses: A Mechanism for Metal-Specific Orthopedic Implant Failure. *PLoS One* **2013**, *8*, e67127.
(28) Shah, K. M.; Wilkinson, J. M.; Gartland, A. Cobalt and chromium exposure affects osteoblast function and impairs the mineralization of prosthesis surfaces in vitro. *J. Orthop. Res.* **2015**, *33*, 1663−1670.
(29) Schrück, K.; Lutz, J.; Mändl, S.; Hacker, M. C.; Kamprad, M.; Schulz-Siegmund, M. Co(II)-mediated effects of plain and plasma immersion ion implanted cobalt-chromium alloys on the osteogenic differentiation of human mesenchymal stem cells. *J. Orthop. Res.* **2015**, *33*, 325−333.
(30) Anissian, L.; Stark, A.; Dahlstrand, H.; Granberg, B.; Good, V.; Bucht, E. Cobalt ions influence proliferation and function of human osteoblast-like cells. *Acta Orthop. Scand.* **2002**, *3*, 369−374.
(31) Pajarinen, J.; Lin, T.-h.; Nabeshima, A.; Jämsen, E.; Lu, L.; Nathan, K.; Yao, Z.; Goodman, S. B. Mesenchymal stem cells in the aseptic loosening of total joint replacements. *J. Biomed. Mater. Res., Part A* **2016**, *105*, 1195−1207.
(32) Hoppe, A.; Brandl, A.; Bleiziffer, O.; Arkudas, A.; Horch, R. E.; Jokic, B.; Janackovic, D.; Boccaccini, A. R. *In vitro* cell response to Co-containing 1393 bioactive glass. *Mater. Sci. Eng., C* **2015**, *57*, 157−163.
(33) Wu, C.; Zhou, Y.; Fan, W.; Han, P.; Chang, J.; Yuen, J.; Zhang, M.; Xiao, Y. Hypoxia-mimicking mesoporous bioactive glass scaffolds with controllable cobalt ion release for bone tissue engineering. *Biomaterials* **2012**, *33*, 2076−2085.
(34) Hoppe, A.; Jokic, B.; Janackovic, D.; Fey, T.; Greil, P.; Romeis, S.; Schmidt, J.; Peukert, W.; Lao, J.; Jallot, E.; Boccaccini, A. R. Cobalt-Releasing 1393 Bioactive Glass-Derived Scaffolds for Bone Tissue Engineering Applications. *ACS Appl. Mater. Interfaces* **2014**, *6*, 2865−2877.
(35) Hay, E. D. *Cell Biology of Extracellular Matrix*, 2nd ed.; Plenum Press: New York and London, 1991; pp 7−40.
(36) Hynes, R. O. The extracellular matrix: not just pretty fibrils. *Science* **2009**, *326*, 1216−1219.
(37) Frantz, C.; Stewart, K. M.; Weaver, V. M. The extracellular matrix at a glance. *J. Cell Sci.* **2010**, *123*, 4195−4200.
(38) Daley, W. P.; Yamada, K. M. ECM-modulated cellular dynamics as a driving force for tissue morphogenesis. *Curr. Opin. Genet. Dev.* **2013**, *23*, 408−414.
(39) Bonnans, C.; Chou, J.; Werb, Z. Remodelling the extracellular matrix in development and disease. *Nat. Rev. Mol. Cell Biol.* **2014**, *15*, 786−801.
(40) Mayne, R.; Burgeson, R. E. *Structure and Function of Collagen Types*, 1st ed.; Academic Press: US, 1987; pp 1−37.
(41) Fratzl, P. *Collagen: Structure and Mechanics*; Springer: New York, 2008; pp 1−52.
(42) Kadler, K. E.; Baldock, C.; Bella, J.; Boot-Handford, R. P. Collagens at a glance. *J. Cell Sci.* **2007**, *120*, 1955−1958.
(43) Fang, M.; Goldstein, E. L.; Turner, A. S.; Les, C. M.; Orr, B. G.; Fisher, G. J.; Welch, K. B.; Rothman, E. D.; Holl, M. M. B. Type I Collagen D-Spacing in Fibril Bundles of Dermis, Tendon, and Bone: Bridging between Nano- and Micro-Level Tissue Hierarchy. *ACS Nano* **2012**, *6*, 9503−9514.
(44) Erickson, B.; Fang, M.; Wallace, J. M.; Orr, B. G.; Les, C. M.; Holl, M. M. B. Nanoscale structure of type I collagen fibrils: quantitative measurement of D-spacing. *Biotechnol. J.* **2012**, *8*, 117−126.
(45) USHIKI, T. Collagen fibers, reticular fibers and elastic fibers. A comprehensive understanding from a morphological viewpoint. *Arch. Histol. Cytol.* **2002**, *65*, 109−126.
(46) Dobbs, H. S.; Minski, M. J. Metal ion release after total hip replacement. *Biomaterials* **1980**, *1*, 193−198.
(47) Socrates, G. *Infrared and Raman Characteristic Group Frequencies Tables and Charts*, 3rd ed.; John Wiley & Sons LTD: Chichester, New York Weinheim, Toronto, Brisbane, Singapore, 2001; pp 11−339.
(48) Wold, S.; Esbensen, K.; Geladi, P. Principal Component Analysis. *Chemom. Intell. Lab. Syst.* **1987**, *2*, 37−52.
(49) González-Solís, J. L.; Martínez-Espinosa, J. C.; Salgado-Román, J. M.; Palomares-Anda, P. Monitoring of chemotherapy leukemia treatment using Raman spectroscopy and principal component analysis. *Laser Med. Sci.* **2014**, *29*, 1241−1249.
(50) Wertz, D. L.; Kruh, R. F. X-Ray Diffraction Study of Some Concentrated Cobalt(II) Chloride Solutions. *J. Chem. Phys.* **1969**, *50*, 4313−4317.
(51) Bella, J.; Brodsky, B.; Berman, H. M. Hydration structure of a collagen peptide. *Structure* **1995**, *3*, 893−906.
(52) Fullerton, G.; Amurao, M. Evidence that collagen and tendon have monolayer water coverage in the native state. *Cell Biol. Int.* **2006**, *30*, 56−65.
(53) Larkin, P. *Infrared and Raman Spectroscopy: Principles and Spectral Interpretation*, 2nd ed.; Elsevier: Netherlands, U.K., US, 2011; pp 85−113
(54) Frushour, B. G.; Koenig, J. L. Raman Scattering of Collagen, Gelatin, and Elastin. *Biopolymers* **1975**, *14*, 379−391.
(55) Birdi-Chouhan, G.; Shelton, R. M.; Bowen, J.; Goldberg-Oppenheimer, P.; Page, S. J.; Hanna, J. V.; Peacock, A.; Wright, A. J.; Grover, L. M. Soluble silicon patterns and templates: calcium phosphate nanocrystal deposition in collagen type 1. *RSC Adv.* **2016**, *6*, 99809−99815.



DOI: 10.1021/acsomega.8b01048
*ACS Omega* 2018, 3, 10129−10138

# LIST OF REFERENCES


[1] Goodsell DS, RCSB PDB. Collagen. RCSB Protein Data Bank. 2000 apr;Available from: http://pdb101.rcsb.org/motm/4https://creativecommons.org/licenses/by/4.0/legalcode.

[2] Malhotra V, Erlmann P. The Pathway of Collagen Secretion. Annual Review of Cell and Developmental Biology. 2015 nov;31(1):109–124. Available from: http://www.annualreviews.org/doi/10.1146/annurev-cellbio-100913-013002.

[3] Fang M, Goldstein EL, Turner AS, Les CM, Orr BG, Fisher GJ, et al. Type i collagen D-spacing in fibril bundles of dermis, tendon, and bone: Bridging between nano- and micro-level tissue hierarchy. ACS Nano. 2012 nov;6(11):9503–9514.

[4] Hughes EAB, Robinson TE, Bassett DB, Azoidis I, Cox SC, Grover LM. Critical and Diverse Roles of Phosphates in Human Biomineralisation Processes. Under Review. 2019;.

[5] Frantz C, Stewart KM, Weaver VM. The extracellular matrix at a glance. Journal of Cell Science. 2010;123(24):4195–200. Available from: http://jcs.biologists.org/content/123/24/4195.

[6] Venstrom KA, Reichardt LF. Extracellular matrix. 2: Role of extracellular matrix molecules and their receptors in the nervous system. FASEB journal : official publication of the Federation of American Societies for Experimental Biology. 1993 aug;7(11):996–1003. Available from: http://www.ncbi.nlm.nih.gov/pubmed/8370483.

[7] Bonnans C, Chou J, Werb Z. Remodelling the extracellular matrix in development and disease. Nature Reviews Molecular Cell Biology. 2014 nov;15(12):786–801. Available from: http://www.ncbi.nlm.nih.gov/pubmed/25415508http://www.pubmedcentral.nih.gov/articlerender.fcgi?artid=PMC4316204http://www.nature.com/doifinder/10.1038/nrm3904.

[8] Yanagishita M. Function of proteoglycans in the extracellular matrix. Acta pathologica japonica. 1993 jun;43(6):283–93. Available from: http://www.ncbi.nlm.nih.gov/pubmed/8346704.

[9] Schultz GS, Wysocki A. Interactions between extracellular matrix and growth factors in wound healing. Wound Repair and Regeneration. 2009 mar;17(2):153–162. Available from: http://doi.wiley.com/10.1111/j.1524-475X.2009.00466.x.

[10] Khan Academy. The extracellular matrix and cell wall (article) — Khan Academy;. Available from: https://www.khanacademy.org/science/biology/structure-of-a-cell/cytoskeleton-junctions-and-extracellular-structures/a/the-extracellular-matrix-and-cell-wall.

[11] Mouw JK, Ou G, Weaver VM. Extracellular matrix assembly: a multiscale deconstruction. Nature Reviews Molecular Cell Biology. 2014 nov;15(12):771–785. Available from: http://www.ncbi.nlm.nih.gov/pubmed/25370693http://www.pubmedcentral.nih.gov/articlerender.fcgi?artid=PMC4682873http://www.nature.com/doifinder/10.1038/nrm3902.

[12] Jarvelainen H, Sainio A, Koulu M, Wight TN, Penttinen R. Extracellular Matrix Molecules: Potential Targets in Pharmacotherapy. Pharmacological Reviews. 2009 jun;61(2):198–223. Available from: http://www.ncbi.nlm.nih.gov/pubmed/19549927http://www.pubmedcentral.nih.gov/articlerender.fcgi?artid=PMC2830117http://pharmrev.aspetjournals.org/cgi/doi/10.1124/pr.109.001289.

[13] Schaefer L, Schaefer RM. Proteoglycans: from structural compounds to signaling molecules. Cell and Tissue Research. 2010 jan;339(1):237–246. Available from: http://www.ncbi.nlm.nih.gov/pubmed/19513755http://link.springer.com/10.1007/s00441-009-0821-y.

[14] Koláčná L, Bakešová J, Varga F, Košťáková E, Plánka L, Nečas A, et al. Biochemical and Biophysical Aspects of Collagen Nanostructure in the Extracellular Matrix. Physiol Res. 2007;56:51–60. Available from: http://www.biomed.cas.cz/physiolres.

[15] Rozario T, DeSimone DW. The extracellular matrix in development and morphogenesis: A dynamic view. Developmental Biology. 2010 may;341(1):126–140. Available from: http://www.ncbi.nlm.nih.gov/pubmed/19854168http:

//www.pubmedcentral.nih.gov/articlerender.fcgi?artid=PMC2854274http://linkinghub.elsevier.com/retrieve/pii/S0012160609012858.

[16] De Wever O, Demetter P, Mareel M, Bracke M. Stromal myofibroblasts are drivers of invasive cancer growth. International Journal of Cancer. 2008 nov;123(10):2229–2238. Available from: http://www.ncbi.nlm.nih.gov/pubmed/18777559http://doi.wiley.com/10.1002/ijc.23925.

[17] Petty RE, Laxer RM, Lindsley CB, Wedderburn LR. Chapter 2 - Structure and Function. In: Textbook of Pediatric Rheumatology (Seventh Edition). 7th ed.; 2016. p. 5–13.

[18] Mak KM, Png CYM, Lee DJ. Type V Collagen in Health, Disease, and Fibrosis. The Anatomical Record. 2016 may;299(5):613–629. Available from: http://doi.wiley.com/10.1002/ar.23330.

[19] Segev F, Heon E, Cole WG, Wenstrup RJ, Young F, Slomovic AR, et al. Structural abnormalities of the cornea and lid resulting from collagen V mutations. Investigative Ophthalmology and Visual Science. 2006 feb;47(2):565–573.

[20] Velez AMA, Howard MS. Collagen IV in normal and in disease process. Wolters Kluwer – Medknow Publications; 2012.

[21] Varga J, Rosenbloom J, Jimenez SA. Transforming growth factor beta (TGF beta) causes a persistent increase in steady-state amounts of type I and type III collagen and fibronectin mRNAs in normal human dermal fibroblasts. The Biochemical journal. 1987 nov;247(3):597–604. Available from: http://www.ncbi.nlm.nih.gov/pubmed/3501287http://www.pubmedcentral.nih.gov/articlerender.fcgi?artid=PMC1148454.

[22] Bettinger DA, Yager DR, Diegelmann RF, Cohen IK. The effect of TGF-beta on keloid fibroblast proliferation and collagen synthesis. Plastic and reconstructive surgery. 1996 oct;98(5):827–33. Available from: http://www.ncbi.nlm.nih.gov/pubmed/8823022.

[23] Ignotz RA, Massague J. Transforming growth factor-beta stimulates the expression of fibronectin and collagen and their incorporation into the extracellular matrix. Journal of Biological Chemistry. 1986;261:4337–45. Available from: http://www.jbc.org/content/261/9/4337.short.

[24] Vanhoutte D, Schellings M, Pinto Y, Heymans S. Relevance of matrix metalloproteinases and their inhibitors after myocardial infarction: A temporal

and spatial window. Cardiovascular Research. 2006 feb;69(3):604–613. Available from: https://academic.oup.com/cardiovascres/article-lookup/doi/10.1016/j.cardiores.2005.10.002.

[25] Kukačka J, Průša R, Kotaška K, Pelouch V. Matrix Metalloproteinases and their function in Myocardium; 2005. Available from: http://biomed.papers.upol.cz/pdfs/bio/2005/02/07.pdf.

[26] Janssens S, Lijnen H. What has been learned about the cardiovascular effects of matrix metalloproteinases from mouse models? Cardiovascular Research. 2006 feb;69(3):585–594. Available from: https://academic.oup.com/cardiovascres/article-lookup/doi/10.1016/j.cardiores.2005.12.010.

[27] Ito S, Nagata K. Biology of Hsp47 (Serpin H1), a collagen-specific molecular chaperone. Seminars in Cell & Developmental Biology. 2017 feb;62:142–151. Available from: http://www.ncbi.nlm.nih.gov/pubmed/27838364https://linkinghub.elsevier.com/retrieve/pii/S1084952116303846.

[28] Peter Fratzl, editor. Collagen Structure and Mechanics. 1st ed. Germany: Springer; 2008.

[29] Graham HK, Holmes DF, Watson RB, Kadler KE. Identification of collagen fibril fusion during vertebrate tendon morphogenesis. The process relies on unipolar fibrils and is regulated by collagen-proteoglycan interaction. Journal of molecular biology. 2000 jan;295(4):891–902. Available from: http://www.ncbi.nlm.nih.gov/pubmed/10656798.

[30] Canty EG, Lu Y, Meadows RS, Shaw MK, Holmes DF, Kadler KE. Coalignment of plasma membrane channels and protrusions (fibripositors) specifies the parallelism of tendon. The Journal of Cell Biology. 2004 may;165(4):553–563. Available from: http://www.jcb.org/lookup/doi/10.1083/jcb.200312071.

[31] Canty EG, Kadler KE. Procollagen trafficking, processing and fibrillogenesis. Journal of cell science. 2005 apr;118(Pt 7):1341–53. Available from: http://www.ncbi.nlm.nih.gov/pubmed/15788652.

[32] Canelón SP, Wallace JM, Burr D, al E. $\beta$-Aminopropionitrile-Induced Reduction in Enzymatic Crosslinking Causes In Vitro Changes in Collagen Morphology and Molecular Composition. PLOS ONE. 2016 nov;11(11):e0166392. Available from: http://dx.plos.org/10.1371/journal.pone.0166392.

[33] Kadler KE, Baldock C, Bella J, Boot-Handford RP. Collagens at a glance. Journal of Cell Science. 2007;120(12).

[34] Yamaguchi S, Yamaguchi S, Yamamoto E, Mannen T, al E. Nanoscale structure of type I collagen fibrils: Quantitative measurement of D-spacing;Available from: http://citeseerx.ist.psu.edu/viewdoc/summary?doi=10.1.1.721.8769.

[35] Kadler KE, Holmes DF, Trotter JA, Chapman JA. Collagen fibril formation. The Biochemical journal. 1996 may;p. 1–11. Available from: http://www.ncbi.nlm.nih.gov/pubmed/8645190http://www.pubmedcentral.nih.gov/articlerender.fcgi?artid=PMC1217307.

[36] Chang SW, Shefelbine S, Buehler M. Structural and Mechanical Differences between Collagen Homo- and Heterotrimers: Relevance for the Molecular Origin of Brittle Bone Disease. Biophysical Journal. 2012 feb;102(3):640–648. Available from: https://www.sciencedirect.com/science/article/pii/S0006349511053471.

[37] Information NCfB. Glycine, CID=750; 2019. Available from: https://pubchem.ncbi.nlm.nih.gov/compound/Glycine.

[38] Lodish H, Berk A, Zipursky SL, Matsudaira P, Baltimore D, Darnell J. Collagen: The Fibrous Proteins of the Matrix. In: Molecular Cell Biology. 4th ed. New York: W. H. Freeman; 2000. Available from: https://www.ncbi.nlm.nih.gov/books/NBK21582/.

[39] Boudko SP, Engel J, Bächinger HP. The crucial role of trimerization domains in collagen folding. The International Journal of Biochemistry & Cell Biology. 2012 jan;44(1):21–32. Available from: http://linkinghub.elsevier.com/retrieve/pii/S1357272511002615.

[40] Peterkofsky B, Udenfriend S. Conversion of Proline to Collagen Hydroxyproline in a Cell-free system from Chick Embryo. J Biol Chem. 1963;238:3966.

[41] Peterkofsky B, Udenfriend S. Enzymatic hydroxylation of proline in microsomal polypeptide leading to formation of collagen. Proceedings of the National Academy of Sciences USA. 1964;53(2):335–3423.

[42] Ito S, Nagata K. Biology of Hsp47 (Serpin H1), a collagen-specific molecular chaperone. Seminars in Cell & Developmental Biology. 2016;.

[43] Ishikawa Y, Rubin K, Bächinger HP, Kalamajski S. The endoplasmic reticulum–resident collagen chaperone Hsp47 interacts with and

promotes the secretion of decorin, fibromodulin, and lumican. Journal of Biological Chemistry. 2018 aug;293(35):13707–13716. Available from: http://www.ncbi.nlm.nih.gov/pubmed/30002123http://www.pubmedcentral.nih.gov/articlerender.fcgi?artid=PMC6120207http://www.jbc.org/lookup/doi/10.1074/jbc.RA117.000758.

[44] Kadler KE, Hill A, Canty-Laird EG. Collagen fibrillogenesis: fibronectin, integrins, and minor collagens as organizers and nucleators. Current Opinion in Cell Biology. 2008 oct;20(5):495–501. Available from: http://linkinghub.elsevier.com/retrieve/pii/S095506740800118X.

[45] Boyadjiev SA, Kim SD, Hata A, Haldeman-Englert C, Zackai EH, Naydenov C, et al. Cranio-lenticulo-sutural dysplasia associated with defects in collagen secretion. Clinical genetics. 2011 aug;80(2):169–76. Available from: http://www.ncbi.nlm.nih.gov/pubmed/21039434http://www.pubmedcentral.nih.gov/articlerender.fcgi?artid=PMC4143380.

[46] Sarmah S, Barrallo-Gimeno A, Melville DB, Topczewski J, Solnica-Krezel L, Knapik EW. Sec24D-Dependent Transport of Extracellular Matrix Proteins Is Required for Zebrafish Skeletal Morphogenesis. PLoS ONE. 2010 apr;5(4):e10367. Available from: http://dx.plos.org/10.1371/journal.pone.0010367.

[47] Townley AK, Feng Y, Schmidt K, Carter DA, Porter R, Verkade P, et al. Efficient coupling of Sec23-Sec24 to Sec13-Sec31 drives COPII-dependent collagen secretion and is essential for normal craniofacial development. Journal of Cell Science. 2008 aug;121(18):3025–3034. Available from: http://www.ncbi.nlm.nih.gov/pubmed/18713835http://jcs.biologists.org/cgi/doi/10.1242/jcs.031070.

[48] Venditti R, Scanu T, Santoro M, Di Tullio G, Spaar A, Gaibisso R, et al. Sedlin Controls the ER Export of Procollagen by Regulating the Sar1 Cycle. Science. 2012 sep;337(6102):1668–1672. Available from: http://www.ncbi.nlm.nih.gov/pubmed/23019651http://www.pubmedcentral.nih.gov/articlerender.fcgi?artid=PMC3471527http://www.sciencemag.org/cgi/doi/10.1126/science.1224947.

[49] Saito K, Chen M, Bard F, Chen S, Zhou H, Woodley D, et al. TANGO1 Facilitates Cargo Loading at Endoplasmic Reticulum Exit Sites. Cell. 2009 mar;136(5):891–902. Available from: http://www.ncbi.nlm.nih.gov/pubmed/19269366https://linkinghub.elsevier.com/retrieve/pii/S0092867408016309.

[50] Maiers JL, Kostallari E, Mushref M, DeAssuncao TM, Li H, Jalan-Sakrikar N, et al. The unfolded protein response mediates fibrogenesis and collagen I secretion through regulating TANGO1 in mice. Hepatology. 2017 mar;65(3):983–998. Available from: http://doi.wiley.com/10.1002/hep.28921.

[51] Saito K, Yamashiro K, Ichikawa Y, Erlmann P, Kontani K, Malhotra V, et al. cTAGE5 mediates collagen secretion through interaction with TANGO1 at endoplasmic reticulum exit sites. Molecular biology of the cell. 2011 jul;22(13):2301–8. Available from: http://www.ncbi.nlm.nih.gov/pubmed/21525241http://www.pubmedcentral.nih.gov/articlerender.fcgi?artid=PMC3128532.

[52] Nogueira C, Erlmann P, Villeneuve J, Santos AJ, Martínez-Alonso E, Martínez-Menárguez JÁ, et al. SLY1 and Syntaxin 18 specify a distinct pathway for procollagen VII export from the endoplasmic reticulum. eLife. 2014 may;3:e02784. Available from: http://www.ncbi.nlm.nih.gov/pubmed/24842878http://www.pubmedcentral.nih.gov/articlerender.fcgi?artid=PMC4054776https://elifesciences.org/articles/02784.

[53] Bonfanti L, Mironov AA, Martínez-Menárguez JA, Martella O, Fusella A, Baldassarre M, et al. Procollagen traverses the Golgi stack without leaving the lumen of cisternae: evidence for cisternal maturation. Cell. 1998 dec;95(7):993–1003. Available from: http://www.ncbi.nlm.nih.gov/pubmed/9875853.

[54] Machamer CE. Accommodation of large cargo within Golgi cisternae. Histochem Cell Biol. 2013;140(3):261–9.

[55] Ricard-Blum S. The collagen family. Cold Spring Harbor perspectives in biology. 2011 jan;3(1):a004978. Available from: http://www.ncbi.nlm.nih.gov/pubmed/21421911http://www.pubmedcentral.nih.gov/articlerender.fcgi?artid=PMC3003457.

[56] Vadon-Le Goff S, Hulmes DJS, Moali C. BMP-1/tolloid-like proteinases synchronize matrix assembly with growth factor activation to promote morphogenesis and tissue remodeling. Matrix Biology. 2015;44:14–23.

[57] Kelwick R, Desanlis I, Wheeler GN, Edwards DR. The ADAMTS (A Disintegrin and Metalloproteinase with Thrombospondin motifs) family. Genome Biology. 2015 dec;16(1):113. Available from: http://www.ncbi.nlm.nih.gov/pubmed/26025392http://www.pubmedcentral.nih.gov/articlerender.fcgi?artid=PMC4448532http://genomebiology.com/2015/16/1/113.

[58] Birk DE, Trelstad RL. Extracellular compartments in tendon morphogenesis: collagen fibril, bundle, and macroaggregate formation. The Journal of cell biology. 1986 jul;103(1):231–40. Available from: http://www.ncbi.nlm.nih.gov/pubmed/3722266http://www.pubmedcentral.nih.gov/articlerender.fcgi?artid=PMC2113791.

[59] Birk DE, Trelstad RL. Extracellular compartments in matrix morphogenesis: collagen fibril, bundle, and lamellar formation by corneal fibroblasts. The Journal of cell biology. 1984 dec;99(6):2024–33. Available from: http://www.ncbi.nlm.nih.gov/pubmed/6542105http://www.pubmedcentral.nih.gov/articlerender.fcgi?artid=PMC2113579.

[60] Holmes DF, Graham HK, Trotter JA, Kadler KE. STEM/TEM studies of collagen fibril assembly. Micron. 2001 apr;32(3):273–285. Available from: https://www.sciencedirect.com/science/article/pii/S0968432800000408?via{\%}3Dihub.

[61] Huijbregts PA, Smith SE. Tendon Injury: A Review. Journal of Manual & Manipulative Therapy. 1999 apr;7(2):71–80. Available from: http://www.tandfonline.com/doi/full/10.1179/106698199790811799.

[62] Fang M, Goldstein EL, Turner AS, Les CM, Orr BG, Fisher GJ, et al. Type I Collagen D -Spacing in Fibril Bundles of Dermis, Tendon, and Bone: Bridging between Nano- and Micro-Level Tissue Hierarchy. ACS Nano. 2012 nov;6(11):9503–9514. Available from: http://pubs.acs.org/doi/abs/10.1021/nn302483x.

[63] Lucero HA, Kagan HM. Lysyl oxidase: an oxidative enzyme and effector of cell function. Cellular and molecular life sciences : CMLS. 2006 oct;63(19-20):2304–16. Available from: http://www.ncbi.nlm.nih.gov/pubmed/16909208.

[64] Kurzweil-Segev Y, Popov I, Solomonov I, Sagit I, Feldman Y. Dielectric Relaxation of Hydration Water in Native Collagen Fibrils. The Journal of Physical Chemistry B. 2017 jun;121(21):5340–5346. Available from: https://pubs.acs.org/doi/10.1021/acs.jpcb.7b02404.

[65] Bella J, Brodsky B, Berman HM. Hydration structure of a collagen peptide. Structure. 1995 sep;3(9):893–906. Available from: https://www.sciencedirect.com/science/article/pii/S0969212601002246.

[66] Melacini G, Bonvin AMJJ, Goodman M, Boelens R, Kaptein R. Hydration dynamics of the collagen triple helix by NMR. Journal of Molecular Biology.

2000 jul;300(5):1041–1048. Available from: https://www.sciencedirect.com/science/article/pii/S0022283600939196.

[67] Fullerton G, Amurao M. Evidence that collagen and tendon have monolayer water coverage in the native state. Cell Biology International. 2006 jan;30(1):56–65. Available from: http://www.ncbi.nlm.nih.gov/pubmed/16488837http://doi.wiley.com/10.1016/j.cellbi.2005.09.008.

[68] Fullerton G, Nes E, Amurao M, Rahal A, Krasnosselskaia L, Cameron I. An NMR method to characterize multiple water compartments on mammalian collagen. Cell Biology International. 2006 jan;30(1):66–73. Available from: http://doi.wiley.com/10.1016/j.cellbi.2005.09.009.

[69] Neurath H, Hill RL, Boeder CL. The Proteins. Vol. 4. Academic Press; 1979.

[70] Herzog RO, Gonell HW. Über Kollagen. Berichte der deutschen chemischen Gesellschaft (A and B Series). 1925 oct;58(9):2228–2230. Available from: http://doi.wiley.com/10.1002/cber.19250580951.

[71] Herzog RO, Jancke W. Röntgenspektrographische Untersuchungen hochmolekularer Organischer Verbindungen. Zeitschrift für Angewandte Chemie. 1921 jul;34(59):385–386. Available from: http://doi.wiley.com/10.1002/ange.19210345902.

[72] Astbury W. The molecular structure of the fibres of the collagen group. London: Published by the International Society of leather trades' chemists; 1940. Available from: https://www.worldcat.org/title/molecular-structure-of-the-fibres-of-the-collagen-group/oclc/20387469.

[73] Cohen C, Bear RS. Helical polypeptide chain configuration in collagen. Journal of the American Chemical Society. 1953 jun;75(11):2783–2784. Available from: https://pubs.acs.org/doi/abs/10.1021/ja01107a523.

[74] Pauling L, Corey RB. The structure of fibrous proteins of the collagen-gelatin group. Proceedings of the National Academy of Sciences of the United States of America. 1951 may;37(5):272–81. Available from: http://www.ncbi.nlm.nih.gov/pubmed/14834150http://www.pubmedcentral.nih.gov/articlerender.fcgi?artid=PMC1063353.

[75] Bowes JH, Kenten RH. The amino-acid composition and titration curve of collagen. Biochemical Journal. 1948 jan;43(3):358–365. Available from: http://www.ncbi.nlm.nih.gov/pubmed/16748414http://www.pubmedcentral.nih.gov/articlerender.fcgi?artid=PMC1274697http://www.biochemj.org/cgi/doi/10.1042/bj0430358.

[76] Fidler AL, Boudko SP, Rokas A, Hudson BG. The triple helix of collagens - an ancient protein structure that enabled animal multicellularity and tissue evolution. Journal of cell science. 2018 apr;131(7):jcs203950. Available from: http://www.ncbi.nlm.nih.gov/pubmed/29632050http://www.pubmedcentral.nih.gov/articlerender.fcgi?artid=PMC5963836.

[77] Pauling L, Corey RB. The Pleated Sheet, A New Layer Configuration of Polypeptide Chains. Proceedings of the National Academy of Sciences. 1951 may;37(5):251–256. Available from: http://www.pnas.org/cgi/doi/10.1073/pnas.37.5.251.

[78] Pauling L, Corey RB, Branson HR. The structure of proteins: Two hydrogen-bonded helical configurations of the polypeptide chain. Proceedings of the National Academy of Sciences. 1951 apr;37(4):205–211. Available from: http://www.ncbi.nlm.nih.gov/pubmed/14816373http://www.pubmedcentral.nih.gov/articlerender.fcgi?artid=PMC1063337http://www.pnas.org/cgi/doi/10.1073/pnas.37.4.205.

[79] Watson JD, Crick FHC. Molecular Structure of Nucleic Acids: A Structure for Deoxyribose Nucleic Acid. Nature. 1953 apr;171(4356):737–738. Available from: http://www.nature.com/articles/171737a0.

[80] Pauling L, Corey RB. Compound Helical Configurations of Polypeptide Chains: Structure of Proteins of the $\alpha$-Keratin Type. Nature. 1953 jan;171(4341):59–61. Available from: http://www.nature.com/articles/171059a0.

[81] Schroeder WA, Kay LM, LeGette J, Honnen L, Green FC. The Constitution of Gelatin. Separation and Estimation of Peptides in Partial Hydrolysates. Journal of the American Chemical Society. 1954 jul;76(13):3556–3564. Available from: http://pubs.acs.org/doi/abs/10.1021/ja01642a062.

[82] Moore S, Stein WH. Chromatography of Amino Acids on Sulfonated Polystyrene Resins. J Biol Chem. 1951;192:663–681.

[83] Ramachandran GN, Kartha G. Structure of collagen. Nature. 1955 sep;176(4482):593–5. Available from: http://www.ncbi.nlm.nih.gov/pubmed/13265783.

[84] RICH A, CRICK FHC. The Structure of Collagen. Nature. 1955 nov;176(4489):915–916. Available from: http://www.nature.com/doifinder/10.1038/176915a0.

[85] Gross J. The Behavior of Collagen Units as a Model in Morphogenesis. The Journal of Cell Biology. 1956 jul;2(4):261–274. Available from: http://www.ncbi.nlm.nih.gov/pubmed/13357551http://www.pubmedcentral.nih.gov/articlerender.fcgi?artid=PMC2229734http://www.jcb.org/cgi/doi/10.1083/jcb.2.4.261.

[86] Monson JM, Borstein P. Identification of a disulfide-linked procollagen as the biosynthetic precursor of chick-bone collagen. Proceedings of the National Academy of Sciences of the United States of America. 1973 dec;70(12):3521–5. Available from: http://www.ncbi.nlm.nih.gov/pubmed/4519643http://www.pubmedcentral.nih.gov/articlerender.fcgi?artid=PMC427272.

[87] Fessler LI, Fessler JH. Protein assembly of procollagen and effects of hydroxylation. The Journal of biological chemistry. 1974 dec;249(23):7637–46. Available from: http://www.ncbi.nlm.nih.gov/pubmed/4474175.

[88] Nagata K, Saga S, Yamada KM. A major collagen-binding protein of chick embryo fibroblasts is a novel heat shock protein. The Journal of Cell Biology. 1986;103(1).

[89] Saga S, Nagata K, Chen WT, Yamada KM. pH-dependent function, purification, and intracellular location of a major collagen-binding glycoprotein. The Journal of Cell Biology. 1987;105(1).

[90] Hughes R C , Taylor A, Sage H, Hogan B L . Distinct patterns of glycosylation of colligin, a collagen-binding glycoprotein, and SPARC (osteonectin), a secreted Ca2+-binding glycoprotein. Evidence for the localisation of colligin in the endoplasmic reticulum. Eur J Biochem. 1987;163:57–65.

[91] Hirayoshi K, Kudo H, Takechi H, Nakai A, Iwamatsu A, Yamada KM, et al. HSP47: a tissue-specific, transformation-sensitive, collagen-binding heat shock protein of chicken embryo fibroblasts. Molecular and cellular biology. 1991 aug;11(8):4036–44. Available from: http://www.ncbi.nlm.nih.gov/pubmed/2072906http://www.pubmedcentral.nih.gov/articlerender.fcgi?artid=PMC361208.

[92] Traub W, Yonath A. Polymers of Tripeptides as Collagen Models VIII. X-ray Studies of Four Polyhexapeptides. J Mol Biol. 1969;43:519–527.

[93] Miller MH, Scheraga HA. Calculation of the structures of collagen models. Role of interchain interactions in determining the triple-helical coiled-coil conformation. I. Poly(glycyl-prolyl-prolyl). J Polym Sci. 1976;54:171–200.

[94] Némethy G, Gibson KD, Palmer KA, Yoon CN, Paterlini G, Zagari A, et al. nergy parameters in polypeptides. 10. Improved geometrical parameters and nonbonded interactions for use in ECEPP/3 algorithm, with application to proline-containing peptides. JPhys Chem. 1992;96:6472–6484.

[95] Persikov AV, Ramshaw JA, Kirkpatrick A, Brodsky B. Amino acid propensities for the collagen triple-helix. Biochemistry. 2000 dec;39(48):14960–7. Available from: http://www.ncbi.nlm.nih.gov/pubmed/11101312.

[96] Rigby BJ, Hirai N, Spikes JD, Eyring H. The Mechanical Properties of Rat Tail Tendon. The Journal of General Physiology. 1959;43(2).

[97] Diamant J, Keller A, Baer E, Litt M, Arridge RG. Collagen; ultrastructure and its relation to mechanical properties as a function of ageing. Proceedings of the Royal Society of London Series B, Biological sciences. 1972 mar;180(1060):293–315. Available from: http://www.ncbi.nlm.nih.gov/pubmed/4402469.

[98] Millington PF, Brown IA. Scanning electron microscopy studies of some internal surfaces of human skin. Zeitschrift fur Sozialforschung und mikroskopische Anatomie. 1970;106:209–219.

[99] Hulmes DJ, Jesior JC, Miller A, Berthet-Colominas C, Wolff C. Electron microscopy shows periodic structure in collagen fibril cross sections. Proceedings of the National Academy of Sciences of the United States of America. 1981 jun;78(6):3567–71. Available from: http://www.ncbi.nlm.nih.gov/pubmed/6943556http://www.pubmedcentral.nih.gov/articlerender.fcgi?artid=PMC319611.

[100] Baselt DR, Revel JP, Baldeschwieler JD. Subfibrillar structure of type I collagen observed by atomic force microscopy. Biophysical journal. 1993 dec;65(6):2644–55. Available from: http://www.ncbi.nlm.nih.gov/pubmed/8312498http://www.pubmedcentral.nih.gov/articlerender.fcgi?artid=PMC1226004.

[101] Ushiki T. Collagen Fibers, Reticular Fibers and Elastic Fibers. A Comprehensive Understanding from a Morphological Viewpoint. Archives of Histology and Cytology. 2002;65(2):109–126. Available from: http://joi.jlc.jst.go.jp/JST.JSTAGE/aohc/65.109?from=CrossRef.

[102] Erickson B, Fang M, Wallace JM, Orr BG, Les CM, Banaszak Holl MM. Nanoscale structure of type I collagen fibrils: quantitative measurement of D-spacing. Biotechnology journal. 2013 jan;8(1):117–26. Available from: http://www.ncbi.nlm.nih.gov/pubmed/23027700http://www.pubmedcentral.nih.gov/articlerender.fcgi?artid=PMC3535565.

[103] Levene CI, Gross J. Alterations in state of molecular aggregation of collagen induced in chick embryos by beta-aminopropionitrile (lathyrus factor). The Journal of experimental medicine. 1959 nov;110(5):771–90. Available from: http://www.ncbi.nlm.nih.gov/pubmed/14416144http://www.pubmedcentral.nih.gov/articlerender.fcgi?artid=PMC2137026.

[104] Tanzer ML, Hunt RD. Experimental Lathyrism. The Journal of Cell Biology. 1964;22(3).

[105] Bailey AJ, Robins SP, Balian G. Biological significance of the intermolecular crosslinks of collagen. Nature. 1974 sep;251(5471):105–109. Available from: http://www.nature.com/doifinder/10.1038/251105a0.

[106] Butler E, Hardin J, Benson S. The role of lysyl oxidase and collagen crosslinking during sea urchin development. Experimental Cell Research. 1987;173(1):174–182.

[107] Sampath Narayanan A, Siegel RC, Martin GR. On the inhibition of lysyl oxidase by $\beta$-aminopropionitrile. Biochemical and Biophysical Research Communications. 1972;46(2):745–751.

[108] Bornstein P, Kang AH, Piez IA. The Nature and Location of Intramolecular Crosslinks in Collagen. Biochemistry. 1966;5(11):3460–3473.

[109] Byers PH, Siegel RC, Holbrook KA, Narayanan AS, Bornstein P, Hall JG. X-Linked Cutis Laxa. New England Journal of Medicine. 1980 jul;303(2):61–65. Available from: http://www.nejm.org/doi/abs/10.1056/NEJM198007103030201.

[110] Kenyon K, Modi WS, Contente S, Friedman RM. A novel human cDNA with a predicted protein similar to lysyl oxidase maps to chromosome 15q24-q25. The Journal of biological chemistry. 1993 sep;268(25):18435–7. Available from: http://www.ncbi.nlm.nih.gov/pubmed/7689553.

[111] Jourdan-Le Saux C, Tronecker H, Bogic L, Bryant-Greenwood GD, Boyd CD, Csiszar K. The LOXL2 gene encodes a new lysyl oxidase-like protein and is expressed at high levels in reproductive tissues. The Journal of biological chemistry. 1999 apr;274(18):12939–44. Available from: http://www.ncbi.nlm.nih.gov/pubmed/10212285.

[112] Maki JM, Kivirikko KI. Cloning and characterization of a fourth human lysyl oxidase isoenzyme. Biochemical Journal. 2001;355(2).

[113] Ito H, Akiyama H, Iguchi H, Iyama K, Miyamoto M, Ohsawa K, et al. Molecular cloning and biological activity of a novel lysyl oxidase-related gene expressed in cartilage. The Journal of biological chemistry. 2001 jun;276(26):24023–9. Available from: http://www.ncbi.nlm.nih.gov/pubmed/11292829.

[114] Rajagopalan R, Misialek S, Huang JX, Hooi L, Ramesha H, Nicholas J, et al. Biochemical and functional characterization of lysyl oxidase like 2 (LOXL2) inhibitors. European Respiratory Journal. 2014;44(Suppl 58).

[115] Roberts J, Lunn K, Tear V, Jones M, Davies D, Cao L, et al. Inhibition of collagen cross-links by novel LOXL2 selective inhibitors in an in-vitro model of fibroblastic foci of IPF. European Respiratory Journal. 2016;48(suppl 60).

[116] Alzahrani F, Al Hazzaa SA, Tayeb H, Alkuraya FS. LOXL3, encoding lysyl oxidase-like 3, is mutated in a family with autosomal recessive Stickler syndrome. Human Genetics. 2015 apr;134(4):451–453. Available from: http://link.springer.com/10.1007/s00439-015-1531-z.

[117] Spicer G, Young ST, Yi J, Shea LD, Backman V. ISOCT study of collagen crosslinking of collagen in cancer models (Conference Presentation). International Society for Optics and Photonics; 2016. p. 97190M. Available from: http://proceedings.spiedigitallibrary.org/proceeding.aspx?doi=10.1117/12.2212035.

[118] Jiang WP, Sima ZH, Wang HC, Zhang JY, Sun LS, Chen F, et al. Identification of the involvement of LOXL4 in generation of keratocystic odontogenic tumors by RNA-Seq analysis. International Journal of Oral Science. 2014 mar;6(1):31–38. Available from: http://www.nature.com/doifinder/10.1038/ijos.2013.96.

[119] Wu L, Zhu Y. The function and mechanisms of action of LOXL2 in cancer (Review). International Journal of Molecular Medicine. 2015 sep;Available from: http://www.spandidos-publications.com/10.3892/ijmm.2015.2337.

[120] Cano A, Santamaría PG, Moreno-Bueno G. LOXL2 in epithelial cell plasticity and tumor progression. Future Oncology. 2012 sep;8(9):1095–1108. Available from: http://www.futuremedicine.com/doi/10.2217/fon.12.105.

[121] Peng DH, Tong P, Byers LA, Wang J, Creighton CJ, Gibbons DL. Abstract A27: Zeb1 induces LOXL2-mediated collagen stabilization and deposition in the extracellular matrix to drive lung cancer invasion and metastasis. Cancer Research. 2016;76(7 Supplement).

[122] Li Y, Asadi A, Monroe MR, Douglas EP. pH effects on collagen fibrillogenesis in vitro: Electrostatic interactions and phosphate binding. Materials Science and Engineering: C. 2009 jun;29(5):1643–1649. Available from: https://www.sciencedirect.com/science/article/pii/S0928493109000058.

[123] Kadler KE, Holmes DF, Trotter JA, Chapman JA. Collagen fibril formation; 1996. Available from: http://www.biochemj.org/content/316/1/1.full-text.pdf.

[124] WOOD GC, KEECH MK. The formation of fibrils from collagen solutions. 1. The effect of experimental conditions: kinetic and electron-microscope studies. The Biochemical journal. 1960 jun;75(3):588–98. Available from: http://www.ncbi.nlm.nih.gov/pubmed/13845809http://www.pubmedcentral.nih.gov/articlerender.fcgi?artid=PMC1204515.

[125] Nihon Seikagakkai T, NAGAI Y. The Journal of biochemistry.. vol. 74. Japanese Biochemical Society; 1973. Available from: https://www.jstage.jst.go.jp/article/biochemistry1922/74/2/74{_}2{_}253/{_}article/-char/ja/.

[126] Achilli M, Mantovani D, Achilli M, Mantovani D. Tailoring Mechanical Properties of Collagen-Based Scaffolds for Vascular Tissue Engineering: The Effects of pH, Temperature and Ionic Strength on Gelation. Polymers. 2010 dec;2(4):664–680. Available from: http://www.mdpi.com/2073-4360/2/4/664.

[127] Harris JR, Soliakov A, Lewis RJ. In vitro fibrillogenesis of collagen type I in varying ionic and pH conditions. Micron. 2013 jun;49:60–68. Available from: https://www.sciencedirect.com/science/article/pii/S0968432813000486.

[128] Gobeaux F, Mosser G, Anglo A, Panine P, Davidson P, Giraud-Guille MM, et al. Fibrillogenesis in Dense Collagen Solutions: A Physicochemical Study. Journal of Molecular Biology. 2008 mar;376(5):1509–1522. Available from: https://www.sciencedirect.com/science/article/pii/S0022283607016762.

[129] Brodsky B, Eikenberry EF, Cassidy K. An unusual collagen periodicity in skin. Biochimica et Biophysica Acta (BBA) - Protein Structure. 1980 jan;621(1):162–166. Available from: http://www.ncbi.nlm.nih.gov/pubmed/7353029https://linkinghub.elsevier.com/retrieve/pii/0005279580900720.

[130] Stinson RH, Sweeny PR. Skin collagen has an unusual d-spacing. Biochimica et Biophysica Acta (BBA) - Protein Structure. 1980 jan;621(1):158–161. Available from: http://www.ncbi.nlm.nih.gov/pubmed/6965456https://linkinghub.elsevier.com/retrieve/pii/0005279580900719.

[131] Brodsky B, Eikenberry EF. [5] Characterization of fibrous forms of collagen. In: Methods in enzymology. vol. 82 Pt A; 1982. p. 127–174. Available from: http://www.ncbi.nlm.nih.gov/pubmed/7078437https://linkinghub.elsevier.com/retrieve/pii/0076687982820624.

[132] Brodsky B, Eikenberry EF, Belbruno KC, Sterling K. Variations in collagen fibril structure in tendons. Biopolymers. 1982 may;21(5):935–951. Available from: http://www.ncbi.nlm.nih.gov/pubmed/7082771http://doi.wiley.com/10.1002/bip.360210507.

[133] Roeder BA, Kokini K, Sturgis JE, Robinson JP, Voytik-Harbin SL. Tensile Mechanical Properties of Three-Dimensional Type I Collagen Extracellular Matrices With Varied Microstructure. Journal of Biomechanical Engineering. 2002 apr;124(2):214. Available from: http://www.ncbi.nlm.nih.gov/pubmed/12002131http://biomechanical.asmedigitalcollection.asme.org/article.aspx?articleid=1407736.

[134] Morozova S, Muthukumar M. Electrostatic effects in collagen fibril formation. The Journal of Chemical Physics. 2018 oct;149(16):163333. Available from: http://aip.scitation.org/doi/10.1063/1.5036526.

[135] Hattori S, Adachi E, Ebihara T, Shirai T, Someki I, Irie S. Alkali-Treated Collagen Retained the Triple Helical Conformation and the Ligand Activity for the Cell Adhesion via 2 1 Integrin. Journal of Biochemistry. 1999 apr;125(4):676–684. Available from: http://www.ncbi.nlm.nih.gov/pubmed/10101279https://academic.oup.com/jb/article-lookup/doi/10.1093/oxfordjournals.jbchem.a022336.

[136] Jackson DS, Neuberger A. Observations on the isoionic and isoelectric point of acid-processed gelatin from insoluble and citrate-extracted collagen. Biochimica et Biophysica Acta. 1957 dec;26(3):638–639. Available from: http://www.ncbi.nlm.nih.gov/pubmed/13499423https://linkinghub.elsevier.com/retrieve/pii/0006300257901129.

[137] Chang JS, Laframboise JG. Probe theory for arbitrary shape in a large Debye length, stationary plasma. Physics of Fluids. 1976 aug;19(1):25. Available from: https://aip.scitation.org/doi/10.1063/1.861324.

[138] Friedman R. Electrolyte Solutions and Specific Ion Effects on Interfaces. Journal of Chemical Education. 2013 aug;90(8):1018–1023. Available from: http://pubs.acs.org/doi/10.1021/ed4000525.

[139] Rosenblatt J, Devereux B, Wallace DG. Injectable collagen as a pH-sensitive hydrogel. Biomaterials. 1994 oct;15(12):985–995. Available from: https://www.sciencedirect.com/science/article/pii/0142961294900795.

[140] Raub CB, Unruh J, Suresh V, Krasieva T, Lindmo T, Gratton E, et al. Image Correlation Spectroscopy of Multiphoton Images Correlates with Collagen Mechanical Properties. Biophysical Journal. 2008 mar;94(6):2361–2373. Available from: http://www.ncbi.nlm.nih.gov/pubmed/18065452http://www.pubmedcentral.nih.gov/articlerender.fcgi?artid=PMC2257909https://linkinghub.elsevier.com/retrieve/pii/S0006349508705800.

[141] Pamula E, De Cupere V, Dufrene YF, Rouxhet PG. Nanoscale organization of adsorbed collagen: Influence of substrate hydrophobicity and adsorption time. Journal of Colloid and Interface Science. 2004 mar;271(1):80–91. Available from: https://www.sciencedirect.com/science/article/pii/S0021979703010695.

[142] Denis FA, Hanarp P, Sutherland DS, Gold J, Mustin C, Paul G Rouxhet PG, et al. Protein Adsorption on Model Surfaces with Controlled Nanotopography and Chemistry. 2002;Available from: https://pubs.acs.org/doi/abs/10.1021/la011011o.

[143] Denis FA, Pallandre A, Nysten B, Jonas AM, Dupont-Gillain CC. Alignment and Assembly of Adsorbed Collagen Molecules Induced by Anisotropic Chemical Nanopatterns. Small. 2005 oct;1(10):984–991. Available from: http://doi.wiley.com/10.1002/smll.200500116.

[144] Elliott JT, Woodward JT, Umarji A, Mei Y, Tona A. The effect of surface chemistry on the formation of thin films of native fibrillar collagen. Biomaterials. 2007 feb;28(4):576–585. Available from: https://www.sciencedirect.com/science/article/pii/S0142961206008301.

[145] Yu X, Tang C, Xiong S, Yuan Q, Gu Z, Li Z, et al. Modification of Collagen for Biomedical Applications: A Review of Physical and Chemical Methods. Current Organic Chemistry. 2016;20:1797–1812. Available from: https://www.ingentaconnect.com/content/ben/coc/2016/00000020/00000017/art00007.

[146] Ber S, Torun Köse G, Hasırcı V. Bone tissue engineering on patterned collagen films: an in vitro study. Biomaterials. 2005 may;26(14):1977–1986. Available from: https://www.sciencedirect.com/science/article/pii/S0142961204005836.

[147] Ratanavaraporn J, Damrongsakkul S, Sanchavanakit N, Banaprasert T, Kanokpanont S. Comparison of gelatin and collagen scaffolds for fibroblast cell cul-

ture. Journal of Metals, Materials and Minerals. 2017 apr;16(1). Available from: http://ojs.materialsconnex.com/index.php/jmmm/article/view/249.

[148] Davidenko N, Bax DV, Schuster CF, Farndale RW, Hamaia SW, Best SM, et al. Optimisation of UV irradiation as a binding site conserving method for crosslinking collagen-based scaffolds. Journal of Materials Science: Materials in Medicine. 2016 jan;27(1):14. Available from: http://link.springer.com/10.1007/s10856-015-5627-8.

[149] Kubyshkina G, Zupancic B, Stukelj M, Groselj D, Marion L, Emri I. The Influence of Different Sterilization Techniques on the Time-Dependent Behavior of Polyamides. Journal of Biomaterials and Nanobiotechnology. 2011;02(04):361–368.

[150] Liu C, McKenna FM, Liang H, Johnstone A, Abel EW. Enhanced Cell Colonization of Collagen Scaffold by Ultraviolet/Ozone Surface Processing. Tissue Engineering Part C: Methods. 2010 dec;16(6):1305–1314. Available from: https://www.liebertpub.com/doi/10.1089/ten.tec.2009.0769.

[151] Sionkowska A, Kozłowska J, Lazare S. Modification by UV radiation of the surface of thin films based on collagen extracted from fish scales. Biointerphases. 2014 jun;9(2):029003. Available from: http://www.ncbi.nlm.nih.gov/pubmed/24985207http://avs.scitation.org/doi/10.1116/1.4865753.

[152] Kontomaris SV, Yova D, Stylianou A, Balogiannis G. The effects of UV irradiation on collagen D-band revealed by atomic force microscopy. Scanning. 2015 mar;37(2):101–111. Available from: http://doi.wiley.com/10.1002/sca.21185.

[153] Kornacka EM, Przybytniak G, Zimek Z. Radicals initiated by gamma-rays in collagen and its main components. Radiation Physics and Chemistry. 2018 jan;142:4–8. Available from: https://www.sciencedirect.com/science/article/pii/S0969806X16305758.

[154] Tyan YC, Liao JD, Lin SP, Chen CC. The study of the sterilization effect of gamma ray irradiation of immobilized collagen polypropylene nonwoven fabric surfaces. Journal of Biomedical Materials Research. 2003 dec;67A(3):1033–1043. Available from: http://www.ncbi.nlm.nih.gov/pubmed/14613254http://doi.wiley.com/10.1002/jbm.a.10024.

[155] Shih YRV, Chen CN, Tsai SW, Wang YJ, Lee OK. Growth of Mesenchymal Stem Cells on Electrospun Type I Collagen Nanofibers. Stem Cells. 2006 nov;24(11):2391–2397. Available from: http://doi.wiley.com/10.1634/stemcells.2006-0253.

[156] Lee P, Lin R, Moon J, Lee LP. Microfluidic alignment of collagen fibers for in vitro cell culture. Biomedical Microdevices. 2006 mar;8(1):35–41. Available from: http://link.springer.com/10.1007/s10544-006-6380-z.

[157] Stegemann JP, Nerem RM. Altered response of vascular smooth muscle cells to exogenous biochemical stimulation in two- and three-dimensional culture. Experimental Cell Research. 2003 feb;283(2):146–155. Available from: https://www.sciencedirect.com/science/article/pii/S0014482702000411.

[158] Cukierman E, Pankov R, Stevens DR, Yamada KM. Taking Cell-Matrix Adhesions to the Third Dimension. Science. 2001 nov;294(5547):1708–1712. Available from: http://www.ncbi.nlm.nih.gov/pubmed/11721053http://www.sciencemag.org/cgi/doi/10.1126/science.1064829.

[159] O'Shaughnessy TJ, Lin HJ, Ma W. Functional synapse formation among rat cortical neurons grown on three-dimensional collagen gels. Neuroscience letters. 2003 apr;340(3):169–72. Available from: http://www.ncbi.nlm.nih.gov/pubmed/12672533.

[160] Matthews JA, Wnek GE, David G Simpson, , Bowlin GL. Electrospinning of Collagen Nanofibers. Biomacromolecules. 2002;3(2):232–238. Available from: https://pubs.acs.org/doi/full/10.1021/bm015533u.

[161] Boland ED, Matthews JA, Pawlowski KJ, Simpson DG, Wnek GE, Bowlin GL. Electrospinning collagen and elastin: Preliminary vascular tissue engineering. Frontiers in Bioscience. 2004;9(June):1422–1432.

[162] Burck J, Aras O, Bertinetti L, Ilhan CA, Ermeydan MA, Schneider R, et al. Observation of triple helix motif on electrospun collagen nanofibers and its effect on the physical and structural properties. Journal of Molecular Structure. 2018 jan;1151:73–80. Available from: https://www.sciencedirect.com/science/article/pii/S0022286017312085.

[163] Yang L, Fitié CFC, van der Werf KO, Bennink ML, Dijkstra PJ, Feijen J. Mechanical properties of single electrospun collagen type I fibers. Biomaterials. 2008 mar;29(8):955–962. Available from: https://www.sciencedirect.com/science/article/pii/S0142961207008666.

[164] Ficai A, Andronescu E, Trandafir V, Ghitulica C, Voicu G. Collagen/hydroxyapatite composite obtained by electric field orientation. Materials Letters. 2010 feb;64(4):541–544. Available from: https://www.sciencedirect.com/science/article/pii/S0167577X09009197.

[165] Ihlefeld JF. Fundamentals of Ferroelectric and Piezoelectric Properties. Ferroelectricity in Doped Hafnium Oxide: Materials, Properties and Devices. 2019 jan;p. 1–24. Available from: https://www.sciencedirect.com/science/article/pii/B9780081024300000012.

[166] Alahakoon AU, Oey I, Silcock P, Bremer P. Understanding the effect of pulsed electric fields on thermostability of connective tissue isolated from beef pectoralis muscle using a model system. Food Research International. 2017 oct;100:261–267. Available from: https://www.sciencedirect.com/science/article/pii/S0963996917304623.

[167] Thakral G, LaFontaine J, Najafi B, Talal TK, Kim P, Lavery LA. Electrical stimulation to accelerate wound healing. Diabetic Foot & Ankle. 2013 jan;4(1):22081. Available from: https://www.tandfonline.com/doi/full/10.3402/dfa.v4i0.22081.

[168] Zhao M. Electrical fields in wound healing—An overriding signal that directs cell migration. Seminars in Cell & Developmental Biology. 2009 aug;20(6):674–682. Available from: https://www.sciencedirect.com/science/article/pii/S1084952108001535.

[169] Wang Et, Zhao M. Regulation of tissue repair and regeneration by electric fields. Chinese Journal of Traumatology (English Edition). 2010 feb;13(1):55–61. Available from: https://www.sciencedirect.com/science/article/pii/S1008127510600119.

[170] Wang Y, Rouabhia M, Zhang Z. Pulsed electrical stimulation benefits wound healing by activating skin fibroblasts through the TGF$\beta$1/ERK/NF-$\kappa$B axis. Biochimica et Biophysica Acta (BBA) - General Subjects. 2016 jul;1860(7):1551–1559. Available from: https://www.sciencedirect.com/science/article/pii/S0304416516300782.

[171] Rossini M, Viapiana O, Gatti D, de Terlizzi F, Adami S. Capacitively Coupled Electric Field for Pain Relief in Patients with Vertebral Fractures and Chronic Pain. Clinical Orthopaedics and Related Research. 2010 mar;468(3):735. Available from: http://www.ncbi.nlm.nih.gov/pubmed/19756902http://www.pubmedcentral.nih.gov/articlerender.fcgi?artid=PMC2816769.

[172] Wu Z, Ding X, Lei G, Zeng C, Wei J, Li J, et al. Efficacy and safety of the pulsed electromagnetic field in osteoarthritis: a meta-analysis. BMJ open. 2018 dec;8(12):e022879. Available from: http://www.ncbi.nlm.nih.gov/pubmed/

30552258http://www.pubmedcentral.nih.gov/articlerender.fcgi?artid=PMC6303578.

[173] Nguyen EB, Wishner J, Slowinska K. The effect of pulsed electric field on expression of ECM proteins: Collagen, elastin, and MMP1 in human dermal fibroblasts. Journal of Electroanalytical Chemistry. 2018 mar;812:265–272. Available from: https://www.sciencedirect.com/science/article/pii/S1572665718300663.

[174] McLeod KJ, Lee RC, Ehrlich P. Freuqency Dependence of Electric Field Modulation of Fibroblast Protein Synthesis. Science. 1987;236(4807).

[175] Iskander MF. Electromagnetic fields and waves. Second edi ed. Long Grove, IL: Waveland Press; 2013. Available from: http://cds.cern.ch/record/1529891.

[176] Mucalo M. Hydroxyapatite (HAp) for biomedical applications. UK: Woodhead Publishing; 2015.

[177] Guo C, Kaufman LJ. Flow and magnetic field induced collagen alignment. Biomaterials. 2007 feb;28(6):1105–1114. Available from: https://www.sciencedirect.com/science/article/pii/S0142961206009008.

[178] Torbet J, Ronzière MC. Magnetic alignment of collagen during self-assembly. The Biochemical journal. 1984 may;219(3):1057–9. Available from: http://www.ncbi.nlm.nih.gov/pubmed/6743242http://www.pubmedcentral.nih.gov/articlerender.fcgi?artid=PMC1153582.

[179] Dubey N, Letourneau PC, Tranquillo RT. Neuronal contact guidance in magnetically aligned fibrin gels: effect of variation in gel mechano-structural properties. Biomaterials. 2001 may;22(10):1065–1075. Available from: https://www.sciencedirect.com/science/article/pii/S0142961200003410.

[180] Guido S, Tranquillo RT. A methodology for the systematic and quantitative study of cell contact guidance in orientated collagen gels. Journal of Cell Science. 1993 jun;105:317–331. Available from: https://jcs.biologists.org/content/105/2/317.short.

[181] Erikson A, Andersen HN, Naess SN, Sikorski P, Davies CdL. Physical and chemical modifications of collagen gels: Impact on diffusion. Biopolymers. 2008 feb;89(2):135–143. Available from: http://doi.wiley.com/10.1002/bip.20874.

[182] Kotani H, Iwasaka M, Ueno S, Curtis A. Magnetic orientation of collagen and bone mixture. Journal of Applied Physics. 2000 may;87(9):6191–6193. Available from: http://aip.scitation.org/doi/10.1063/1.372652.

[183] Glass Brudzinski J, Perizzolo D, Brunette DM. Effects of substratum surface topography on the organization of cells and collagen fibers in collagen gel cultures. Journal of Biomedical Materials Research. 2002 sep;61(4):608–618. Available from: http://doi.wiley.com/10.1002/jbm.10243.

[184] Mendonca DBS, Miguez PA, Mendonca G, Yamauchi M, Aragao FJL, Cooper LF. Titanium surface topography affects collagen biosynthesis of adherent cells. Bone. 2011 sep;49(3):463–472. Available from: https://www.sciencedirect.com/science/article/pii/S8756328211009410.

[185] Berry CC, Campbell G, Spadiccino A, Robertson M, Curtis ASG. The influence of microscale topography on fibroblast attachment and motility. Biomaterials. 2004 nov;25(26):5781–5788. Available from: https://www.sciencedirect.com/science/article/pii/S0142961204000729.

[186] Jayaraman M, Meyer U, Bühner M, Joos U, Wiesmann HP. Influence of titanium surfaces on attachment of osteoblast-like cells in vitro. Biomaterials. 2004 feb;25(4):625–631. Available from: https://www.sciencedirect.com/science/article/pii/S0142961203005714.

[187] Heydarkhan Hagvall S, Choi CH, Dunn J, Heydarkhan S, Schenke Layland K, MacLellan WR, et al. Influence of Systematically Varied Nano-Scale Topography on Cell Morphology and Adhesion. Cell Communication & Adhesion. 2007 jan;14(5):181–194. Available from: http://www.tandfonline.com/doi/full/10.1080/15419060701755594.

[188] Metavarayuth K, Sitasuwan P, Zhao X, Lin Y, Wang Q. Influence of Surface Topographical Cues on the Differentiation of Mesenchymal Stem Cells in Vitro. ACS Biomaterials Science & Engineering. 2016 feb;2(2):142–151. Available from: http://pubs.acs.org/doi/10.1021/acsbiomaterials.5b00377.

[189] Poole K, Khairy K, Friedrichs J, Franz C, Cisneros DA, Howard J, et al. Molecular-scale Topographic Cues Induce the Orientation and Directional Movement of Fibroblasts on Two-dimensional Collagen Surfaces. Journal of Molecular Biology. 2005 jun;349(2):380–386. Available from: https://www.sciencedirect.com/science/article/pii/S0022283605003542.

[190] Gelse K, Poschl E, Aigner T. Collagens — structure, function, and biosynthesis. Advanced Drug Delivery Reviews. 2003 nov;55(12):1531–1546. Available from: https://www.sciencedirect.com/science/article/pii/S0169409X03001820.

[191] van Zuijlen PPM, Ruurda JJB, van Veen HA, van Marle J, van Trier AJM, Groenevelt F, et al. Collagen morphology in human skin and scar tissue: no adaptations in response to mechanical loading at joints. Burns. 2003 aug;29(5):423–431. Available from: https://www.sciencedirect.com/science/article/pii/S0305417903000524.

[192] Osman OS, Selway JL, Harikumar PE, Stocker CJ, Wargent ET, Cawthorne MA, et al. A novel method to assess collagen architecture in skin. BMC Bioinformatics. 2013 aug;14(1):260. Available from: http://bmcbioinformatics.biomedcentral.com/articles/10.1186/1471-2105-14-260.

[193] Jor JWY, Nielsen PMF, Nash MP, Hunter PJ. Modelling collagen fibre orientation in porcine skin based upon confocal laser scanning microscopy. Skin Research and Technology. 2011 may;17(2):149–159. Available from: http://doi.wiley.com/10.1111/j.1600-0846.2011.00471.x.

[194] Benjamin M, Kaiser E, Milz S. Structure-function relationships in tendons: a review. Journal of Anatomy. 2008 mar;212(3):211–228. Available from: http://doi.wiley.com/10.1111/j.1469-7580.2008.00864.x.

[195] Screen HRC, Berk DE, Kadler KE, Ramirez F, Young MF. Tendon Functional Extracellular Matrix. Journal of Orthopaedic Research. 2015 jun;33(6):793–799. Available from: http://doi.wiley.com/10.1002/jor.22818.

[196] Canty EG, Kadler KE. Collagen fibril biosynthesis in tendon: a review and recent insights. Comparative Biochemistry and Physiology Part A: Molecular & Integrative Physiology. 2002 dec;133(4):979–985. Available from: https://www.sciencedirect.com/science/article/pii/S109564330200212X.

[197] Gillies AR, Lieber RL. Structure and function of the skeletal muscle extracellular matrix. Muscle & nerve. 2011 sep;44(3):318–31. Available from: http://www.ncbi.nlm.nih.gov/pubmed/21949456http://www.pubmedcentral.nih.gov/articlerender.fcgi?artid=PMC3177172.

[198] Jarvinen TAH, Jozsa L, Kannus P, Jarvinen TLN, Jarvinen M. Organization and distribution of intramuscular connective tissue in normal and immobilized skeletal muscles. Journal of Muscle Research and Cell Motility. 2002;23(3):245–254. Available from: http://link.springer.com/10.1023/A:1020904518336.

[199] Passerieux E, Rossignol R, Chopard A, Carnino A, Marini JF, Letellier T, et al. Structural organization of the perimysium in bovine skeletal muscle: Junctional

plates and associated intracellular subdomains. Journal of Structural Biology. 2006 may;154(2):206–216. Available from: https://www.sciencedirect.com/science/article/pii/S1047847706000165.

[200] Bowers SLK, Baudino TA. Laying the groundwork for growth: Cell-cell and cell-ECM interactions in cardiovascular development. Birth Defects Research Part C: Embryo Today: Reviews. 2010 mar;90(1):1–7. Available from: http://doi.wiley.com/10.1002/bdrc.20168.

[201] Lindsey ML, Borg TK. Understanding the role of the extracellular matrix in cardiovascular development and disease: where do we go from here? Journal of molecular and cellular cardiology. 2010 mar;48(3):431–2. Available from: http://www.ncbi.nlm.nih.gov/pubmed/19781548http://www.pubmedcentral.nih.gov/articlerender.fcgi?artid=PMC2823953.

[202] Pope AJ, Sands GB, Smaill BH, LeGrice IJ. Three-dimensional transmural organization of perimysial collagen in the heart. American Journal of Physiology-Heart and Circulatory Physiology. 2008 sep;295(3):H1243–H1252. Available from: https://www.physiology.org/doi/10.1152/ajpheart.00484.2008.

[203] Binnig G, Quate CF, Gerber C. Atomic Force Microscope. Physical Review Letters. 1986 mar;56(9):930–933. Available from: https://link.aps.org/doi/10.1103/PhysRevLett.56.930.

[204] Giessibl FJ. Advances in atomic force microscopy. Reviews of Modern Physics. 2003 jul;75(3):949–983. Available from: https://link.aps.org/doi/10.1103/RevModPhys.75.949.

[205] JPK. NanoWizard ® AFM Handbook JPK Instruments NanoWizard ® Handbook Version 2.2a 1; 2012. Available from: http://www.nanophys.kth.se/nanophys/facilities/nfl/afm/jpk/manuf-manuals/handbook-2.2a.pdf.

[206] Zhong Q, Inniss D, Kjoller K, Elings VB. Fractured polymer/silica fiber surface studied by tapping mode atomic force microscopy. Surface Science Letters. 1993 jun;290(1-2):L688–L692. Available from: https://www.sciencedirect.com/science/article/pii/016725849390906Y.

[207] Rueden CT, Schindelin J, Hiner MC, Al E. ImageJ2: ImageJ for the next generation of scientific image data. BMC Bioinformatics. 2017;18(529).

[208] Brouwer P. Theory of XRF: Getting acquainted with the principles. The Netherlands: PANalytical BV; 2003. Available from: www.panalytical.com.

[209] Murata H. Rheology-Theory and Application to Biomaterials Hiroshi Murata; 2012. p. 404–411. Available from: http://dx.doi.org/10.5772/48393.

[210] Hohne GWH, Hemminger WF, Flammersheim HJ. Differential Scanning Calorimetry. Berlin, Heidelberg: Springer Berlin Heidelberg; 2003. Available from: http://link.springer.com/10.1007/978-3-662-06710-9.

[211] Reading M, Hourston DJ. Modulated temperature differential scanning calorimetry : theoretical and practical applications in polymer characterisation. Springer; 2006.

[212] Banwell CN, McCash EM. Fundamentals of Molecular Spectroscopy. 5th ed. New Delhi: McGraw Hill; 2013. Available from: http://www.worldcat.org/title/fundamentals-of-molecular-spectroscopy/oclc/949745652?referer=di{\&}ht=edition.

[213] Luck WAP. D. J. Gardiner, P. R. Graves (Eds.): Practical Raman Spectroscopy, mit Beiträgen von H. J. Bowley, D. J. Gardiner, D. L. Gerrard, P. R. Graves, J. D. Louden, and G. Turrell, Springer-Verlag, Berlin, Heidelberg, New York 1989. 157 Seiten, brosch., Preis: D. Berichte der Bunsengesellschaft für physikalische Chemie. 1990 sep;94(9):1047–1047. Available from: http://doi.wiley.com/10.1002/bbpc.19900940938.

[214] González-Solís J. Discrimination of different cancer types clustering Raman spectra by a super paramagnetic stochastic network approach. PLOS ONE. 2019 mar;14(3):e0213621. Available from: http://dx.plos.org/10.1371/journal.pone.0213621.

[215] Wold S, Esbensen K, Geladi P. Principal Component Analysis. Chemometrics and Intelligent Laboratory Systems. 1987;2:37–52. Available from: http://pzs.dstu.dp.ua/DataMining/pca/bibl/Principalcomponentsanalysis.pdf.

[216] Aschheim MA, Black EF, Cuesta I. Theory of principal components analysis and applications to multistory frame buildings responding to seismic excitation. Engineering Structures. 2002 aug;24(8):1091–1103. Available from: https://www.sciencedirect.com/science/article/pii/S0141029602000366.

[217] Woody R W . Theory of Circular Dichroism of Proteins. In: Fasman G D , editor. Circular Dichroism and the Conformational Analysis of Biomolecules.. second edi ed. Springer, Boston, MA; 1996. p. 25–67. Available from: https://link.springer.com/chapter/10.1007{\%}2F978-1-4757-2508-7{_}2{\#}citeas.

[218] Lee H, Huttunen MJ, Hsu KJ, Partanen M, Zhuo GY, Kauranen M, et al. Chiral imaging of collagen by second-harmonic generation circular dichroism. Biomedical Optics Express. 2013 jun;4(6):909. Available from: https://www.osapublishing.org/abstract.cfm?URI=boe-4-6-909.

[219] Barron LD. Molecular Light Scattering and Optical Activity - Laurence D. Barron - Google Books. 2nd ed. Cambridge University Press; 2004. Available from: https://books.google.co.uk/books?hl=en{\&}lr={\&}id=rTx7aG18854C{\&}oi=fnd{\&}pg=PP1{\&}dq=L.+D.+Barron,+Molecular+Light+Scattering+and+Optical+Activity+(Cambridge+University+Press,+1982),+Chap.+5.{\&}ots=iGeqaCgVjZ{\&}sig=qiF0QJrMnThwyDfraGd3Ie{_}6my0{\#}v=onepage{\&}q=chapter5{\&}f.

[220] Hunter RJ. Zeta potential in colloid science : principles and applications; 1981.

[221] Clogston JD, Patri AK. Zeta Potential Measurement. In: Methods in Molecular Biology. Humana Press; 2011. p. 63–70.

[222] Kitchener BG, Wainwright J, Parsons AJ. A review of the principles of turbidity measurement. Progress in Physical Geography: Earth and Environment. 2017 oct;41(5):620–642. Available from: http://journals.sagepub.com/doi/10.1177/0309133317726540.

[223] Swineharf DF. The Beer-Lambert Law. Journal of Chemical Education. 1962;39(7):333–335. Available from: https://pubs.acs.org/doi/10.1021/ed039p333.

[224] Comper WD, Veis A. The mechanism of nucleation forin vitro collagen fibril formation. Biopolymers. 1977 oct;16(10):2113–2131. Available from: http://www.ncbi.nlm.nih.gov/pubmed/334277http://doi.wiley.com/10.1002/bip.1977.360161004.

[225] Li Y, Douglas EP. Effects of various salts on structural polymorphism of reconstituted type I collagen fibrils. Colloids and Surfaces B: Biointerfaces. 2013 dec;112:42–50. Available from: https://www.sciencedirect.com/science/article/pii/S0927776513004736.

[226] Joy DC. Scanning Electron Microscopy: Theory, History and Development of the Field Emission Scanning Electron Microscope. In: Biological Field Emission Scanning Electron Microscopy. Chichester, UK: John Wiley & Sons, Ltd; 2019. p. 1–6. Available from: http://doi.wiley.com/10.1002/9781118663233.ch1.

[227] Joy DC. The theory and practice of high-resolution scanning electron microscopy. Ultramicroscopy. 1991 aug;37(1-4):216–233. Available from: https://www.sciencedirect.com/science/article/pii/0304399191900207.

[228] Leuven KU. Environmental scanning electron microscope Philips XL30 ESEM FEG – Departement Materiaalkunde;. Available from: https://www.mtm.kuleuven.be/equipment/ESEM-XL30-FEG/ESEM-XL30-FEG.

[229] piezobrush® PZ2. piezobrush® PZ2 - Plasma handheld device for surface activation; 2016. Available from: https://www.relyon-plasma.com/relyon-plasma-products/piezobrush-pz2/?lang=en{\&}fbclid=IwAR13XNRxirwspFV2W7EMbKYGWIN68J0nCuvk0fh7fyN77hU0XAbLIHA7FV8.

[230] Hejda F, Solař P, Kousal J. Surface Free Energy Determination by Contact Angle Measu rements - A Comparison of Various Approaches; 2010. Available from: https://www.semanticscholar.org/paper/Surface-Free-Energy-Determination-by-Contact-Angle-Hejda-Sola/e5a0e7dc916cfeb7f0b4a3e24027cf7421d5d5e0.

[231] D Kingery BW. Determination of Surface Tension by Sessile Drop Method Surface Tension at Elevated Temperatures. I. Furnace and Method for use of the Sessile Drop Method; Surface Tension of Silicon, Iron and Nickel. 1953;Available from: https://pubs.acs.org/doi/10.1021/j150504a026.

[232] Kubiak KJ, Wilson MCT, Mathia TG, Carval P. Wettability versus roughness of engineering surfaces. Wear. 2011;271:523–528. Available from: http://dx.doi.org/10.1016/j.wear.2010.03.029.

[233] Owen MJ, Smith PJ. Plasma treatment of polydimethylsiloxane. Journal of Adhesion Science and Technology. 1994 jan;8(10):1063–1075. Available from: http://www.tandfonline.com/doi/abs/10.1163/156856194X00942.

[234] Bhalerao S, Kadam P. Sample size calculation. International Journal of Ayurveda Research. 2010;1(1):55.

[235] Guenther WC. Sample size formulas for normal theory t tests. American Statistician. 1981;35(4):243–244.

[236] Moser BK, Stevens GR, Watts CL. The Two-Sample T Test Versus Satterthwaite's Approximate F Test. Communications in Statistics - Theory and Methods. 1989;18(11):3963–3975.

[237] Scariano SM, Davenport JM. The Effects of Violations of Independence Assumptions in the One-Way ANOVA. American Statistician. 1987;41(2):123–129.

[238] Babu GJ, Padmanabhan AR, Puri ML. Robust One-Way ANOVA under Possibly Non-Regular Conditions. Biometrical Journal. 1999 jun;41(3):321–339.

[239] Nawabi DH, Nassif NA, Do HT, Stoner K, Elpers M, Su EP, et al. What causes unexplained pain in patients with metal-on metal hip devices? A retrieval, histologic, and imaging analysis. Clinical orthopaedics and related research. 2014 feb;472(2):543–54. Available from: http://www.ncbi.nlm.nih.gov/pubmed/23897506http://www.pubmedcentral.nih.gov/articlerender.fcgi?artid=PMC3890159.

[240] Mahendra G, Pandit H, Kliskey K, Murray D, Gill HS, Athanasou N. Necrotic and inflammatory changes in metal-on-metal resurfacing hip arthroplasties. Acta Orthopaedica. 2009 dec;80(6):653–659. Available from: http://www.tandfonline.com/doi/full/10.3109/17453670903473016.

[241] Matthies AK, Racasan R, Bills P, Blunt L, Cro S, Panagiotidou A, et al. Material loss at the taper junction of retrieved large head metal-on-metal total hip replacements. Journal of Orthopaedic Research. 2013 jul;31(11):n/a–n/a. Available from: http://doi.wiley.com/10.1002/jor.22431.

[242] Alvarado J, Maldonado R, Marxuach J, Otero R. Biomechanics of hip and knee prostheses 1. 2003;p. 1–20.

[243] Hu CY, Yoon TR. Recent updates for biomaterials used in total hip arthroplasty. Biomaterials research. 2018;22:33. Available from: http://www.ncbi.nlm.nih.gov/pubmed/30534414http://www.pubmedcentral.nih.gov/articlerender.fcgi?artid=PMC6280401.

[244] Kwon YM, Xia Z, Glyn-Jones S, Beard D, Gill HS, Murray DW. Dose-dependent cytotoxicity of clinically relevant cobalt nanoparticles and ions on macrophages in vitro. Biomedical Materials. 2009 apr;4(2):025018. Available from: http://www.ncbi.nlm.nih.gov/pubmed/19349653http://stacks.iop.org/1748-605X/4/i=2/a=025018?key=crossref.c1508392a59b753e08c1a82d8716e837.

[245] Doorn PF, Campbell PA, Worrall J, Benya PD, McKellop HA, Amstutz HC. Metal wear particle characterization from metal on metal total hip replacements: transmission electron microscopy study of periprosthetic tissues and isolated particles. Journal of biomedical materials research. 1998 oct;42(1):103–11. Available from: http://www.ncbi.nlm.nih.gov/pubmed/9740012.

[246] Sieber HP, Rieker CB, Köttig P. Analysis of 118 second-generation metal-on-metal retrieved hip implants. The Journal of bone and joint surgery British volume. 1999 jan;81(1):46–50. Available from: http://www.ncbi.nlm.nih.gov/pubmed/10068001.

[247] Koch KM, Koff MF, Bauer TW, Shah PH, Nencka AS, Sivaram Kaushik S, et al. Off-resonance based assessment of metallic wear debris near total hip arthroplasty. Magnetic Resonance in Medicine. 2017 jun;Available from: http://doi.wiley.com/10.1002/mrm.26807.

[248] Lohmann CH, Singh G, Willert HG, Buchhorn GH. Metallic debris from metal-on-metal total hip arthroplasty regulates periprosthetic tissues. World journal of orthopedics. 2014 nov;5(5):660–6. Available from: http://www.ncbi.nlm.nih.gov/pubmed/25405095http://www.pubmedcentral.nih.gov/articlerender.fcgi?artid=PMC4133474.

[249] Langton DJ, Jameson SS, Joyce TJ, Gandhi JN, Sidaginamale R, Mereddy P, et al. Accelerating failure rate of the ASR total hip replacement. The Bone & Joint Journal. 2011 aug;93-B(8):1011–1016. Available from: http://www.ncbi.nlm.nih.gov/pubmed/21768621http://www.bjj.boneandjoint.org.uk/cgi/doi/10.1302/0301-620X.93B8.26040.

[250] Davies AP. An Unusual Lymphocytic Perivascular Infiltration in Tissues Around Contemporary Metal-on-Metal Joint Replacements. The Journal of Bone and Joint Surgery (American). 2005 jan;87(1):18. Available from: http://jbjs.org/cgi/doi/10.2106/JBJS.C.00949.

[251] Panichkul P, Fricka KB, Hopper RH, Engh CA. Greater Trochanteric Fragmentation After Failed Metal-on-Metal Hip Arthroplasty. Orthopedics. 2015 may;38(5):e447–e451. Available from: http://www.healio.com/doiresolver?doi=10.3928/01477447-20150504-93.

[252] Sinnett-Jones PE, Wharton JA, Wood RJK. Micro-abrasion–corrosion of a CoCrMo alloy in simulated artificial hip joint environments. Wear. 2005 jul;259(7-12):898–909. Available from: http://www.sciencedirect.com/science/article/pii/S0043164805001328{\#}bib23.

[253] Jacobs J, Gilbert JL, Urban RM. Corrosion of metal orthopaedic implants. The Journal of Bone and Joint Surgery (American). 1998;80:268–82.

[254] Oldfield J. Electrochemical Theory of Galvanic Corrosion. In: Galvanic Corrosion. 100 Barr Harbor Drive, PO Box C700, West Conshohocken, PA 19428-2959: ASTM

International; 1988. p. 5–5–18. Available from: http://www.astm.org/doiLink.cgi?STP26188S.

[255] Posada OM, Tate RJ, Grant MH. Toxicity of cobalt-chromium nanoparticles released from a resurfacing hip implant and cobalt ions on primary human lymphocytes in vitro. Journal of Applied Toxicology. 2015 jun;35(6):614–622. Available from: http://doi.wiley.com/10.1002/jat.3100.

[256] Haynes DR, Rogers SD, Hay S, Pearcy MJ, Howie DW. The differences in toxicity and release of bone-resorbing me... : JBJS. Journal of Bone & Joint Surgery - American Volume. 1993;Available from: http://journals.lww.com/jbjsjournal/Abstract/1993/06000/The{_}differences{_}in{_}toxicity{_}and{_}release{_}of.4.aspx.

[257] Hallab NJ, Jacobs JJ. Chemokines Associated with Pathologic Responses to Orthopedic Implant Debris. Frontiers in Endocrinology. 2017 jan;8:5. Available from: http://journal.frontiersin.org/article/10.3389/fendo.2017.00005/full.

[258] Ortega R, Bresson C, Fraysse A, Sandre C, Devès G, Gombert C, et al. Cobalt distribution in keratinocyte cells indicates nuclear and perinuclear accumulation and interaction with magnesium and zinc homeostasis. Toxicology Letters. 2009 jul;188(1):26–32. Available from: http://linkinghub.elsevier.com/retrieve/pii/S0378427409001477.

[259] Yavuz Ö, Altunkaynak Y, Güzel F. Removal of copper, nickel, cobalt and manganese from aqueous solution by kaolinite. Water Research. 2003 feb;37(4):948–952. Available from: https://www.sciencedirect.com/science/article/pii/S0043135402004098.

[260] Sargeant A, Goswami T. Hip implants – Paper VI – Ion concentrations. Materials & Design. 2007 jan;28(1):155–171. Available from: http://linkinghub.elsevier.com/retrieve/pii/S026130690500124X.

[261] Jomova K, Valko M. Advances in metal-induced oxidative stress and human disease. Toxicology. 2011 may;283(2-3):65–87. Available from: http://www.ncbi.nlm.nih.gov/pubmed/21414382http://linkinghub.elsevier.com/retrieve/pii/S0300483X11000886.

[262] Shah KM, Wilkinson JM, Gartland A. Cobalt and chromium exposure affects osteoblast function and impairs the mineralization of prosthesis surfaces in vitro. Journal of Orthopaedic Research. 2015 nov;33(11):1663–1670. Available from: http://doi.wiley.com/10.1002/jor.22932.

[263] Anissian L, Stark A, Dahlstrand H, Granberg B, Good V, Bucht E. Cobalt ions influence proliferation and function of human osteoblast-like cells. Acta Orthopaedica Scandinavica. 2002 jan;73(3):369–374. Available from: http://www.tandfonline.com/doi/full/10.1080/000164702320155400.

[264] Schröck K, Lutz J, Mändl S, Hacker MC, Kamprad M, Schulz-Siegmund M. Co(II)-mediated effects of plain and plasma immersion ion implanted cobalt-chromium alloys on the osteogenic differentiation of human mesenchymal stem cells. Journal of Orthopaedic Research. 2015 mar;33(3):325–333. Available from: http://doi.wiley.com/10.1002/jor.22765.

[265] Pajarinen J, Lin TH, Nabeshima A, Jämsen E, Lu L, Nathan K, et al. Mesenchymal stem cells in the aseptic loosening of total joint replacements. Journal of biomedical materials research Part A. 2017;105(4):1195–1207. Available from: http://www.ncbi.nlm.nih.gov/pubmed/27977880http://www.pubmedcentral.nih.gov/articlerender.fcgi?artid=PMC5531266.

[266] Hay ED. Cell biology of extracellular matrix;. Available from: https://books.google.co.uk/books?hl=en{\&}lr={\&}id=uwPTBwAAQBAJ{\&}oi=fnd{\&}pg=PA2{\&}dq=extracellular+matrix+function{\&}ots=FHORottmb1{\&}sig=wb1KCCjAb7Xa1F{_}tZSmPp3klpqQ{\#}v=onepage{\&}q=extracellularmatrixfunction{\&}f=false.

[267] Hynes RO. The extracellular matrix: not just pretty fibrils. Science (New York, NY). 2009 nov;326(5957):1216–9. Available from: http://www.ncbi.nlm.nih.gov/pubmed/19965464http://www.pubmedcentral.nih.gov/articlerender.fcgi?artid=PMC3536535.

[268] Daley WP, Yamada KM. ECM-modulated cellular dynamics as a driving force for tissue morphogenesis. Current Opinion in Genetics & Development. 2013 aug;23(4):408–414. Available from: http://www.ncbi.nlm.nih.gov/pubmed/23849799http://www.pubmedcentral.nih.gov/articlerender.fcgi?artid=PMC3780589http://linkinghub.elsevier.com/retrieve/pii/S0959437X13000828.

[269] Mayne R, Burgeson RE. Structure and function of collagen types. Academic Press; 1987.

[270] Dobbs HS, Minski MJ. Metal ion release after total hip replacement. Biomaterials. 1980 oct;1(4):193–198. Available from: https://www.sciencedirect.com/science/article/pii/0142961280900162.

[271] Socrates G. Infrared and raman characteristic group frequencies : tables and charts. John Wiley & Sons; 2007. Available from: https://www.wiley.com/en-gb/Infrared+and+Raman+Characteristic+Group+Frequencies{\%}3A+Tables+and+Charts{\%}2C+3rd+Edition-p-9780470093078.

[272] Mason EF, Rathmell JC. Cell metabolism: An essential link between cell growth and apoptosis. NIH Public Access; 2011. Available from: http://www.ncbi.nlm.nih.gov/pubmed/20816705http://www.pubmedcentral.nih.gov/articlerender.fcgi?artid=PMC3010257.

[273] Wertz DL, Kruh RF. X-Ray Diffraction Study of Some Concentrated Cobalt(II) Chloride Solutions. The Journal of Chemical Physics. 1969 may;50(10):4313–4317. Available from: http://aip.scitation.org/doi/10.1063/1.1670896.

[274] Bella J, Brodsky B, Berman HM. Hydration structure of a collagen peptide. Structure. 1995 sep;3(9):893–906. Available from: http://www.ncbi.nlm.nih.gov/pubmed/8535783http://linkinghub.elsevier.com/retrieve/pii/S0969212601002246.

[275] Larkin PPJ. Infrared and Raman spectroscopy : principles and spectral interpretation;.

[276] Frushour BG, Koenig JL. Raman scattering of collagen, gelatin, and elastin. Biopolymers. 1975 feb;14(2):379–391. Available from: http://www.ncbi.nlm.nih.gov/pubmed/1174668http://doi.wiley.com/10.1002/bip.1975.360140211.

[277] Birdi-Chouhan G, Shelton RM, Bowen J, Goldberg-Oppenheimer P, Page SJ, Hanna JV, et al. Soluble silicon patterns and templates: calcium phosphate nanocrystal deposition in collagen type 1. RSC Advances. 2016 oct;6(102):99809–99815. Available from: http://xlink.rsc.org/?DOI=C6RA19784A.

[278] Tzaphlidou M. Bone architecture: collagen structure and calcium/phosphorus maps. Journal of biological physics. 2008 apr;34(1-2):39–49. Available from: http://www.ncbi.nlm.nih.gov/pubmed/19669491http://www.pubmedcentral.nih.gov/articlerender.fcgi?artid=PMC2577747.

[279] Viguet-Carrin S, Garnero P, Delmas PD. The role of collagen in bone strength. Osteoporosis International. 2006 mar;17(3):319–336. Available from: http://www.ncbi.nlm.nih.gov/pubmed/16341622http://link.springer.com/10.1007/s00198-005-2035-9.

[280] Zhang W, Huang ZL, Liao SS, Cui FZ. Nucleation Sites of Calcium Phosphate Crystals during Collagen Mineralization. Journal of the American Ceramic Society. 2003 jun;86(6):1052–1054. Available from: http://doi.wiley.com/10.1111/j.1151-2916.2003.tb03422.x.

[281] Reddi AH. Cell Biology and Biochemistry of Endochondral Bone Development. Collagen and Related Research. 1981 feb;1(2):209–226. Available from: https://www.sciencedirect.com/science/article/pii/S0174173X81800210.

[282] Nudelman F, Pieterse K, George A, Bomans PHH, Friedrich H, Brylka LJ, et al. The role of collagen in bone apatite formation in the presence of hydroxyapatite nucleation inhibitors. Nature Materials. 2010 dec;9(12):1004–1009. Available from: http://www.nature.com/articles/nmat2875.

[283] Nancollas GH. The mechanism of biological mineralization. Journal of Crystal Growth. 1977 dec;42:185–193. Available from: https://www.sciencedirect.com/science/article/pii/0022024877901944.

[284] Rodrigues CVM, Serricella P, Linhares ABR, Guerdes RM, Borojevic R, Rossi MA, et al. Characterization of a bovine collagen–hydroxyapatite composite scaffold for bone tissue engineering. Biomaterials. 2003 dec;24(27):4987–4997. Available from: https://www.sciencedirect.com/science/article/pii/S0142961203004101.

[285] Gebauer D, Cölfen H. Prenucleation clusters and non-classical nucleation. Nano Today. 2011 dec;6(6):564–584. Available from: https://www.sciencedirect.com/science/article/pii/S1748013211001174.

[286] Christoffersen J, Landis WJ. A contribution with review to the description of mineralization of bone and other calcified tissues in vivo. The Anatomical Record. 1991 aug;230(4):435–450. Available from: http://doi.wiley.com/10.1002/ar.1092300402.

[287] Kay MI, Young RA, Posner AS. Crystal Structure of Hydroxyapatite. Nature. 1964 dec;204(4963):1050–1052. Available from: http://www.nature.com/articles/2041050a0.

[288] Kanzaki N, Treboux G, Onuma K, Tsutsumi S, Ito A. Calcium phosphate clusters. Biomaterials. 2001 nov;22(21):2921–2929. Available from: https://www.sciencedirect.com/science/article/pii/S0142961201000394.

[289] Robey PG. Vertebrate Mineralized Matrix Proteins: Structure and Function. Connective Tissue Research. 1996 jan;35(1-4):131–136. Available from: http://www.tandfonline.com/doi/full/10.3109/03008209609029183.

[290] Mann S. Mineralization in biological systems. In: Inorganic Elements in Biochemistry. Berlin, Heidelberg: Springer Berlin Heidelberg; 1983. p. 125–174. Available from: http://www.springerlink.com/index/10.1007/BFb0111320.

[291] Tenenhouse HS. REGULATION OF PHOSPHORUS HOMEOSTASIS BY THE TYPE IIA NA/PHOSPHATE COTRANSPORTER. Annual Review of Nutrition. 2005 aug;25(1):197–214. Available from: http://www.ncbi.nlm.nih.gov/pubmed/16011465http://www.annualreviews.org/doi/10.1146/annurev.nutr.25.050304.092642.

[292] Calcium and Phosphorus Metabolism: R and D Systems; 2007. Available from: https://www.rndsystems.com/resources/technical/calcium-phosphorus-metabolism{\#}phosphorus.

[293] EANES ED, GILLESSEN IH, POSNER AS. Intermediate States in the Precipitation of Hydroxyapatite. Nature. 1965 oct;208(5008):365–367. Available from: http://www.nature.com/articles/208365a0.

[294] Onuma K, Ito A. Cluster Growth Model for Hydroxyapatite. Chem Mater. 1998;p. 3346–3351. Available from: https://pubs.acs.org/doi/10.1021/cm980062c.

[295] Cadez V, Erceg I, Selmani A, Domazet Jurasin D, Segota S, Lyons D, et al. Amorphous Calcium Phosphate Formation and Aggregation Process Revealed by Light Scattering Techniques. Crystals. 2018;8(6):254.

[296] Williams BR, Gelman RA, Poppke DC, Piez KA. Collagen fibril formation. Optimal in vitro conditions and preliminary kinetic results. The Journal of biological chemistry. 1978 sep;253(18):6578–85. Available from: http://www.ncbi.nlm.nih.gov/pubmed/28330.

[297] Li Y, Asadi A, Monroe MR, Douglas EP. pH effects on collagen fibrillogenesis in vitro: Electrostatic interactions and phosphate binding. Materials Science and Engineering: C. 2009 jun;29(5):1643–1649. Available from: https://www.sciencedirect.com/science/article/pii/S0928493109000058.

[298] Wang Xj, Milner TE, Chang MC, Nelson JS. Group refractive index measurement of dry and hydrated type I collagen films using optical low-coherence reflectometry. Journal of Biomedical Optics. 1996 apr;1(2):212. Available from:

http://www.ncbi.nlm.nih.gov/pubmed/23014687http://biomedicaloptics.spiedigitallibrary.org/article.aspx?doi=10.1117/12.227699.

[299] Chang SW, Buehler MJ. Molecular biomechanics of collagen molecules. Materials Today. 2014 mar;17(2):70–76. Available from: https://www.sciencedirect.com/science/article/pii/S1369702114000261.

[300] Batsanov SS. Van der Waals Radii of Elements. Inorganic Materials. 2001;37(9):871–885. Available from: http://link.springer.com/10.1023/A:1011625728803.

[301] Tawfik DS, Viola RE. Arsenate replacing phosphate: alternative life chemistries and ion promiscuity. Biochemistry. 2011 feb;50(7):1128–34. Available from: http://www.ncbi.nlm.nih.gov/pubmed/21214261http://www.pubmedcentral.nih.gov/articlerender.fcgi?artid=PMC3070116.

[302] Mancardi G, Hernandez Tamargo CE, Di Tommaso D, de Leeuw NH. Detection of Posner's clusters during calcium phosphate nucleation: a molecular dynamics study. Journal of Materials Chemistry B. 2017 sep;5(35):7274–7284. Available from: http://xlink.rsc.org/?DOI=C7TB01199G.

[303] Whitcher JP, Srinivasan M, Upadhyay MP. Corneal blindness: a global perspective. Bulletin of the World Health Organization. 2001;79:214–221. Available from: https://www.scielosp.org/scielo.php?pid=S0042-96862001000300009{\&}script=sci{_}arttext.

[304] Congdon NG, Friedman DS, Lietman T. Important Causes of Visual Impairment in the World Today. JAMA. 2003 oct;290(15):2057. Available from: http://jama.jamanetwork.com/article.aspx?doi=10.1001/jama.290.15.2057.

[305] Thylefors B. Epidemiological patterns of ocular trauma. Australian and New Zealand journal of ophthalmology. 1992 may;20(2):95–8. Available from: http://www.ncbi.nlm.nih.gov/pubmed/1389141.

[306] Hertsenberg AJ, Shojaati G, Funderburgh ML, Mann MM, Du Y, Funderburgh JL. Corneal stromal stem cells reduce corneal scarring by mediating neutrophil infiltration after wounding. PLOS ONE. 2017 mar;12(3):e0171712. Available from: http://dx.plos.org/10.1371/journal.pone.0171712.

[307] Ziaei M, Greene C, Green CR. Wound healing in the eye: Therapeutic prospects. Advanced Drug Delivery Reviews. 2018 feb;126:162–176. Available from: http://www.ncbi.nlm.nih.gov/pubmed/29355667https://linkinghub.elsevier.com/retrieve/pii/S0169409X18300061.

[308] Prabhasawat P. Amniotic Membrane: A Treatment for Prevention of Blindness from Various Ocular Diseases — Prabhasawat — Siriraj Medical Journal. Siriraj Medical Journal. 2007;59(3). Available from: http://www.smj.si.mahidol.ac.th/sirirajmedj/index.php/smj/article/view/641.

[309] Berdahl JP, Johnson CS, Proia AD, Grinstaff MW, Kim T. Comparison of Sutures and Dendritic Polymer Adhesives for Corneal Laceration Repair in an In Vivo Chicken Model. Archives of Ophthalmology. 2009 apr;127(4):442. Available from: http://www.ncbi.nlm.nih.gov/pubmed/19365021http://archopht.jamanetwork.com/article.aspx?doi=10.1001/archophthalmol.2008.582.

[310] Miki D, Dastgheib K, Kim T, Pfister-Serres A, Smeds KA, Inoue M, et al. A photopolymerized sealant for corneal lacerations. Cornea. 2002 may;21(4):393–9. Available from: http://www.ncbi.nlm.nih.gov/pubmed/11973389.

[311] Garg P, Krishna PV, Stratis AK, Gopinathan U. The value of corneal transplantation in reducing blindness. Eye. 2005 oct;19(10):1106–1114. Available from: http://www.nature.com/articles/6701968.

[312] Michelacci YM. Collagens and proteoglycans of the corneal extracellular matrix. Brazilian Journal of Medical and Biological Research. 2003 aug;36(8):1037–1046. Available from: http://www.scielo.br/scielo.php?script=sci{_}arttext{\&}pid=S0100-879X2003000800009{\&}lng=en{\&}tlng=en.

[313] Chen S, Mienaltowski MJ, Birk DE. Regulation of corneal stroma extracellular matrix assembly. Experimental Eye Research. 2015 apr;133:69–80. Available from: https://www.sciencedirect.com/science/article/pii/S0014483514002152.

[314] Quantock AJ, Winkler M, Parfitt GJ, Young RD, Brown DJ, Boote C, et al. From nano to macro: Studying the hierarchical structure of the corneal extracellular matrix. Experimental Eye Research. 2015 apr;133:81–99. Available from: https://www.sciencedirect.com/science/article/pii/S0014483514002061.

[315] Ljubimov AV, Saghizadeh M. Progress in corneal wound healing. Progress in retinal and eye research. 2015 nov;49:17–45. Available from: http://www.ncbi.nlm.nih.gov/pubmed/26197361http://www.pubmedcentral.nih.gov/articlerender.fcgi?artid=PMC4651844.

[316] Suzuki K, Saito J, Yanai R, Yamada N, Chikama Ti, Seki K, et al. Cell–matrix and cell–cell interactions during corneal epithelial wound healing. Progress in Retinal and Eye Research. 2003 mar;22(2):113–133. Available from: https://www.sciencedirect.com/science/article/pii/S1350946202000423.

[317] Agrawal VB, Tsai RJF. Corneal epithelial wound healing. Indian journal of ophthalmology. 2003 mar;51(1):5–15. Available from: http://www.ncbi.nlm.nih.gov/pubmed/12701857.

[318] Velazquez AJ, Carnahan MA, Kristinsson J, Stinnett S, Grinstaff MW, Kim T. New Dendritic Adhesives for Sutureless Ophthalmic Surgical Procedures. Archives of Ophthalmology. 2004 jun;122(6):867. Available from: http://archopht.jamanetwork.com/article.aspx?doi=10.1001/archopht.122.6.867.

[319] Sridhar MS. Anatomy of cornea and ocular surface. Indian Journal of Ophthalmology. 2018 feb;66(2):190–194.

[320] Kim SH, Moon JH, Kim JH, Jeong SM, Lee SH. Flexible, stretchable and implantable PDMS encapsulated cable for implantable medical device. Biomedical Engineering Letters. 2011 aug;1(3):199–203. Available from: http://link.springer.com/10.1007/s13534-011-0033-8.

[321] Khan Y, Ostfeld AE, Lochner CM, Pierre A, Arias AC. Monitoring of Vital Signs with Flexible and Wearable Medical Devices. Advanced Materials. 2016 jun;28(22):4373–4395. Available from: http://doi.wiley.com/10.1002/adma.201504366.

[322] Wang Y, Wang L, Yang T, Li X, Zang X, Zhu M, et al. Wearable and Highly Sensitive Graphene Strain Sensors for Human Motion Monitoring. Advanced Functional Materials. 2014 aug;24(29):4666–4670. Available from: http://doi.wiley.com/10.1002/adfm.201400379.

[323] Mannsfeld SCB, Tee BCK, Stoltenberg RM, Chen CVHH, Barman S, Muir BVO, et al. Highly sensitive flexible pressure sensors with microstructured rubber dielectric layers. Nature Materials. 2010 oct;9(10):859–864. Available from: http://www.ncbi.nlm.nih.gov/pubmed/20835231http://www.nature.com/articles/nmat2834.

[324] Diversified Enterprises. Surface Energy Data for PDMS: Polydimethylsiloxane, CAS #9016-00-6; 2009. Available from: http://www.accudynetest.com/polymer{_}surface{_}data/polydimethylsiloxane.pdf.

[325] Durisova J, Pudis D, Goraus M, Gaso P. IP-Dip photoresist surfaces for photonic applications prepared by laser lithography and studied by AFM. Applied Surface Science. 2018 dec;461:108–112. Available from: https://www.sciencedirect.com/science/article/pii/S0169433218317975.

[326] Spagnolo B, Brunetti V, Leménager G, De Luca E, Sileo L, Pellegrino T, et al. Three-dimensional cage-like microscaffolds for cell invasion studies. Scientific Reports. 2015 sep;5(1):10531. Available from: http://www.nature.com/articles/srep10531.

[327] Tottori S, Zhang L, Qiu F, Krawczyk KK, Franco-Obregón A, Nelson BJ. Magnetic Helical Micromachines: Fabrication, Controlled Swimming, and Cargo Transport. Advanced Materials. 2012 feb;24(6):811–816. Available from: http://doi.wiley.com/10.1002/adma.201103818.

[328] Hengsbach S, Lantada AD. Rapid prototyping of multi-scale biomedical microdevices by combining additive manufacturing technologies. Biomedical Microdevices. 2014;16(4):617–627.

[329] Lemma ED, Rizzi F, Sileo L, Spagnolo B, Dattoma T, Qualtieri A, et al. Static and Dynamic Mechanical Characterization of Two-photon Lithography Photoresists. 2015;p. 2–3. Available from: http://www.nanopt.org/16Abstracts/2016{_}Lemma{_}EnricoDomenico{_}jlroldan@phantomsnet.net{_}Abstract{_}NanoPT2016{_}Lemma.pdf.

[330] O'Neill C, Jordan P, Riddle P, Ireland G. Narrow linear strips of adhesive substratum are powerful inducers of both growth and total focal contact area. Journal of Cell Science. 1990 apr;95(4):577–586.

[331] Andersson AS, Olsson P, Lidberg U, Sutherland D. The effects of continuous and discontinuous groove edges on cell shape and alignment. Experimental cell research. 2003 aug;288(1):177–88. Available from: http://www.ncbi.nlm.nih.gov/pubmed/12878169.

[332] Brunette DM. The effects of implant surface topography on the behavior of cells. The International journal of oral & maxillofacial implants. 1988;3(4):231–46. Available from: http://www.ncbi.nlm.nih.gov/pubmed/3075965.

[333] Teixeira AI, McKie GA, Foley JD, Bertics PJ, Nealey PF, Murphy CJ. The effect of environmental factors on the response of human corneal epithelial cells to nanoscale substrate topography. Biomaterials. 2006 jul;27(21):3945–54. Available from: https://linkinghub.elsevier.com/retrieve/pii/S0142961206000810http://www.ncbi.nlm.nih.gov/pubmed/16580065http://www.pubmedcentral.nih.gov/articlerender.fcgi?artid=PMC4820342.

[334] Walboomers XF, Croes HJE, Ginsel LA, Jansen JA. Contact guidance of rat fibroblasts on various implant materials. Journal of Biomedical Materials Research. 1999 nov;47(2):204–212. Available from: http:

//doi.wiley.com/10.1002/{\%}28SICI{\%}291097-4636{\%}28199911{\%}2947{\%}3A2{\%}3C204{\%}3A{\%}3AAID-JBM10{\%}3E3.0.CO{\%}3B2-H.

[335] Fraser SA, Ting YH, Mallon KS, Wendt AE, Murphy CJ, Nealey PF. Sub-micron and nanoscale feature depth modulates alignment of stromal fibroblasts and corneal epithelial cells in serum-rich and serum-free media. Journal of biomedical materials research Part A. 2008;86(3):725. Available from: https://www.ncbi.nlm.nih.gov/pmc/articles/PMC3040512/.

[336] Saini M, Singh Y, Arora P, Arora V, Jain K. Implant biomaterials: A comprehensive review. World journal of clinical cases. 2015 jan;3(1):52–7. Available from: http://www.ncbi.nlm.nih.gov/pubmed/25610850http://www.pubmedcentral.nih.gov/articlerender.fcgi?artid=PMC4295219.

[337] Dhaliwal JS, Rahman NA, Knights J, Ghani H, de Albuquerque Junior RF. The effect of different surface topographies of titanium implants on bacterial biofilm: a systematic review. SN Applied Sciences. 2019 jun;1(6):615. Available from: http://link.springer.com/10.1007/s42452-019-0638-6.

[338] Ferraris S, Spriano S. Antibacterial titanium surfaces for medical implants. Materials Science and Engineering: C. 2016 apr;61:965–978. Available from: https://www.sciencedirect.com/science/article/pii/S0928493115306755.

[339] Grischke J, Eberhard J, Stiesch M. Antimicrobial dental implant functionalization strategies — A systematic review. Dental Materials Journal. 2016 jul;35(4):545–558. Available from: https://www.jstage.jst.go.jp/article/dmj/35/4/35{_}2015-314/{_}article.

[340] Hu K, Shi H, Zhu J, Deng D, Zhou G, Zhang W, et al. Compressed collagen gel as the scaffold for skin engineering. Biomedical microdevices. 2010 aug;12(4):627–35. Available from: http://www.ncbi.nlm.nih.gov/pubmed/20300856.

[341] Newbury DE, Ritchie NWM. Performing elemental microanalysis with high accuracy and high precision by scanning electron microscopy/silicon drift detector energy-dispersive X-ray spectrometry (SEM/SDD-EDS). Journal of Materials Science. 2015 jan;50(2):493–518. Available from: http://link.springer.com/10.1007/s10853-014-8685-2.

[342] Bracic M, Mohan T, Kargl R, Griesser T, Hribernik S, Kostler S, et al. Preparation of PDMS ultrathin films and patterned surface modification with cellulose. RSC Advances. 2014;4(23):11955–11961.

[343] Musgrave CSA, Fang F. Contact Lens Materials: A Materials Science Perspective. Materials (Basel, Switzerland). 2019 jan;12(2). Available from: http://www.ncbi.nlm.nih.gov/pubmed/30646633http://www.pubmedcentral.nih.gov/articlerender.fcgi?artid=PMC6356913.

[344] Vogel B, Siebert H, Hofmann U, Frantz S. Determination of collagen content within picrosirius red stained paraffin-embedded tissue sections using fluorescence microscopy. MethodsX. 2015 jan;2:124–134. Available from: https://www.sciencedirect.com/science/article/pii/S2215016115000102.